

Politecnico di Bari

Repository Istituzionale dei Prodotti della Ricerca del Politecnico di Bari

Methods for security enhancement in low-inertia and non-synchronous power systems

This is a PhD Thesis

Original Citation:
Methods for security enhancement in low-inertia and non-synchronous power systems / Iurlaro, Cosimo. - ELETTRONICO. - (2024). [10.60576/poliba/iris/iurlaro-cosimo_phd2024]

Availability:
This version is available at http://hdl.handle.net/11589/268900 since: 2024-04-16

Published version
DOI:10.60576/poliba/iris/iurlaro-cosimo_phd2024

Publisher: Politecnico di Bari

Terms of use:

(Article begins on next page)

21 July 2026



Politecnico di Bari

Department of Electrical and Information Engineering

Electrical and Information Engineering

Ph.D. Program

SSD: ING-IND/33-Electrical Energy Systems

Final Dissertation

Methods for Security Enhancement in Low-Inertia and Non-Synchronous Power Systems

---

by

Cosimo Iurlaro

Supervisor:
Prof. Massimo LA SCALA

Coordinator of Ph.D. Program:
Prof. Mario Carpentieri

XXXVI Cycle - November 1st, 2020 - January 31st, 2024

Politecnico di Bari

LIBERATORIA PER L'ARCHIVIAZIONE DELLA TESI DI DOTTORATO

Al Magnifico Rettore
del Politecnico di Bari

Il/la sottoscritto/a **Cosimo Iurlaro** nato/a a **Taranto** il **29/05/1995**

residente a **Torricella (TA)** in via **Vittorio Alfieri, 51** e-mail **cos.iurlaro@gmail.com**

iscritto al 3° anno di Corso di Dottorato di Ricerca in **Ingegneria Elettrica e dell'Informazione** ciclo **XXXVI**

ed essendo stato ammesso a sostenere l'esame finale con la prevista discussione della tesi dal titolo:

Methods for security enhancement in low-inertia and non-synchronous power systems

DICHIARA

1) di essere consapevole che, ai sensi del D.P.R. n. 445 del 28.12.2000, le dichiarazioni mendaci, la falsità negli atti e l'uso di atti falsi sono puniti ai sensi del codice penale e delle Leggi speciali in materia, e che nel caso ricorressero dette ipotesi, decade fin dall'inizio e senza necessità di nessuna formalità dai benefici conseguenti al provvedimento emanato sulla base di tali dichiarazioni;
2) di essere iscritto al Corso di Dottorato di ricerca **Ingegneria Elettrica e dell'Informazione** ciclo **XXXVI**, corso attivato ai sensi del "*Regolamento dei Corsi di Dottorato di ricerca del Politecnico di Bari*", emanato con D.R. n.286 del 01.07.2013;
3) di essere pienamente a conoscenza delle disposizioni contenute nel predetto Regolamento in merito alla procedura di deposito, pubblicazione e autoarchiviazione della tesi di dottorato nell'Archivio Istituzionale ad accesso aperto alla letteratura scientifica;
4) di essere consapevole che attraverso l'autoarchiviazione delle tesi nell'Archivio Istituzionale ad accesso aperto alla letteratura scientifica del Politecnico di Bari (IRIS-POLIBA), l'Ateneo archivierà e renderà consultabile in rete (nel rispetto della Policy di Ateneo di cui al D.R. 642 del 13.11.2015) il testo completo della tesi di dottorato, fatta salva la possibilità di sottoscrizione di apposite licenze per le relative condizioni di utilizzo (di cui al sito http://www.creativecommons.it/Licenze), e fatte salve, altresì, le eventuali esigenze di "embargo", legate a strette considerazioni sulla tutelabilità e sfruttamento industriale/commerciale dei contenuti della tesi, da rappresentarsi mediante compilazione e sottoscrizione del modulo in calce (Richiesta di embargo);
5) che la tesi da depositare in IRIS-POLIBA, in formato digitale (PDF/A) sarà del tutto identica a quelle **consegnate**/inviate/da inviarsi ai componenti della commissione per l'esame finale e a qualsiasi altra copia depositata presso gli Uffici del Politecnico di Bari in forma cartacea o digitale, ovvero a quella da discutere in sede di esame finale, a quella da depositare, a cura dell'Ateneo, presso le Biblioteche Nazionali Centrali di Roma e Firenze e presso tutti gli Uffici competenti per legge al momento del deposito stesso, e che di conseguenza va esclusa qualsiasi responsabilità del Politecnico di Bari per quanto riguarda eventuali errori, imprecisioni o omissioni nei contenuti della tesi;
6) che il contenuto e l'organizzazione della tesi è opera originale realizzata dal sottoscritto e non compromette in alcun modo i diritti di terzi, ivi compresi quelli relativi alla sicurezza dei dati personali; che pertanto il Politecnico di Bari ed i suoi funzionari sono in ogni caso esenti da responsabilità di qualsivoglia natura: civile, amministrativa e penale e saranno dal sottoscritto tenuti indenni da qualsiasi richiesta o rivendicazione da parte di terzi;
7) che il contenuto della tesi non infrange in alcun modo il diritto d'Autore né gli obblighi connessi alla salvaguardia di diritti morali od economici di altri autori o di altri aventi diritto, sia per testi, immagini, foto, tabelle, o altre parti di cui la tesi è composta.

Luogo e data **Bari, 28/03/2024** Firma _____

Il/La sottoscritto, con l'autoarchiviazione della propria tesi di dottorato nell'Archivio Istituzionale ad accesso aperto del Politecnico di Bari (POLIBA-IRIS), pur mantenendo su di essa tutti i diritti d'autore, morali ed economici, ai sensi della normativa vigente (Legge 633/1941 e ss.mm.ii.),

CONCEDE

- al Politecnico di Bari il permesso di trasferire l'opera su qualsiasi supporto e di convertirla in qualsiasi formato al fine di una corretta conservazione nel tempo. Il Politecnico di Bari garantisce che non verrà effettuata alcuna modifica al contenuto e alla struttura dell'opera.
- al Politecnico di Bari la possibilità di riprodurre l'opera in più di una copia per fini di sicurezza, back-up e conservazione.

Luogo e data **Bari, 28/03/2024** Firma _____



Politecnico
di Bari

Department of Electrical and Information Engineering

Electrical and Information Engineering

Ph.D. Program

SSD: ING-IND/33-Electrical Energy Systems

Final Dissertation

Methods for Security Enhancement in Low-Inertia and Non-Synchronous Power Systems

---

by

Cosimo Iurlaro

Supervisor:
Prof. Massimo LA SCALA

Coordinator of Ph.D. Program:
Prof. Mario Carpentieri

XXXVI Cycle - November 1st, 2020 - January 31st, 2024

Contents

Abstract **1**

Acknowledgments **2**

Author's Publications **3**

Introduction **6**

Background and Motivation 6

Contributions 7

Outline of the Thesis 8

1 Overview on Microgrids and Non-Synchronous Power Systems **10**

1.1 Concept of microgrid 11

1.2 Operation and control of microgrids 14

1.3 Integration of microgrids into the power system framework 18

1.4 Capacity enhancement for monitoring and control of power grids in Italy . 20

1.5 Isolated Distribution Grids 24

1.5.1 An example of a small Italian island: a benchmark 27

1.5.2 Operating reserve in small islands 37

2 Operational Planning in Islanded Microgrids **41**

2.1 Operational planning algorithm 43

2.1.1 Formulation of the predictive optimal dispatch problem 44

2.1.2 Formulation of the "greedy" control logic 49

2.2 Reserve evaluation methods for non-synchronous power systems 53

2.2.1 Method *A* 53

2.2.2 Method *B* 54

2.3 Testing the algorithm on a real case study 55
2.3.1 Influence of PV penetration 60
2.3.2 Influence of the confidence interval 62
2.4 Inclusion of energy stored by BESSs in operating reserve constraints . . . 63
2.4.1 Influence of the BESS' operating reserve 65
2.5 Conclusion 74

3 Real-Time Operating Reserve Assessment and Allocation 77
3.1 Control algorithm of microgrid controllers for isolated microgrids 80
3.1.1 Macro-state 1: Minimum power control for regulation 85
3.1.2 Macro-state 2: Downward available operating reserve control . . 86
3.1.3 Macro-state 3: Upward available operating reserve control 87
3.1.4 Real-time algorithm implementation in a finite-state machine model 89
3.1.5 Operating reserve requirement evaluation method for isolated microgrids 98
3.2 Modelling of a small island for real-time algorithms tests 101
3.2.1 Dynamic grid model of a reference small Italian island 103
3.2.2 Quasi-static grid model for the real-time algorithm testing 110
3.3 Finite-state machine model testing 120
3.3.1 Validation of the MGC model assuming an extreme load behavior 121
3.3.2 Validation of the MGC model assuming an extreme PV generation 128
3.4 Testing the real-time algorithm on real test scenarios 132
3.4.1 Test case of a typical summer day 133
3.4.2 Test case of a typical winter day 137
3.5 Verification of the effectiveness of actions processed by the microgrid controller 141
3.5.1 Dynamic analysis of key moments of the typical summer day test case 141
3.5.2 Dynamic analysis of key moments of the typical winter day test case 148
3.6 Conclusion 152

4 Innovative Solutions for the Provision of Fast Frequency Support Ancillary Services 155
4.1 Improved Synthetic Inertia Control Law for Distributed Grid-Following Inverter-Based Energy Resources 158

4.1.1 Concept of the Proposed Synthetic Inertia Control Law 158
4.2 A real-world application in the BLORIN research project framework . . . 164
4.2.1 Dynamic model of Favignana island 167
4.2.2 Experimental set-up for FFS validation by V2G electric vehicles . 171
4.2.3 FFS control scheme for V2G EVs 173
4.2.4 Test scenarios and results in Favignana island 174
4.2.5 Winter scenario in Favignana 176
4.2.6 Summer scenario in Favignana 179
4.3 Fast Frequency Support through LED Street Lighting in Low-Inertia Non-Synchronous Power Systems 186
4.3.1 Flexible Control Resources through LED Street Lamps 187
4.3.2 Characterization of the LED lamp power regulation response . . . 189
4.3.3 Synthetic Inertia and Fast Frequency Response Models 192
4.3.4 Power Hardware-in-the-Loop experimental set-up 195
4.3.5 Single-bus grid model Power Hardware-in-the-Loop experimental tests 196
4.3.6 Test Results on Single-bus grid model 197
4.3.7 Small Non-Synchronous Island Model Power Hardware-in-the-Loop Experimental Tests 200
4.3.8 Model of the LED Street Lighting System 201
4.3.9 Test Results on Small Non-Synchronous Island Model 202
4.4 A SOC-feedback Control Scheme for Fast Frequency Support 209
4.4.1 SOC-feedback method for fast frequency regulation 210
4.4.2 Open-loop test of the proposed controller 213
4.4.3 Closed-loop response analysis and controller parameters optimal tuning 217
4.4.4 Test results 222
4.5 Conclusion 228

Conclusion **231**

References **234**

Acronyms **252**

List of Figures

1.1 Timescales and classification of the MG control functions with hierarchical control structure 15
1.2 Interaction scheme between DSO and MGs 18
1.3 General scheme of the CCI system with related interfaces 22
1.4 Block diagram of the control loops in the CCI 23
1.5 Representation of the small Italian island 10 kV distribution network under investigation 27
1.6 Maximum, average, and minimum hourly load profiles obtained from measurements made on the island in the year 2019 32
1.7 Average quarter-hourly load profiles of the year 2021 35
1.8 Average load trends in various months of the year 2021 compared with maximum-average trends 2019 36
1.9 PV production trends in p.u. for the year 2020 38

2.1 Proposed closed-loop optimization routine 44
2.2 Method A. On the left: Cumulative curves of net-load positive (up) and negative (down) forecast errors; on the right: daily estimation of upward (up) and downward (down) operating reserve 54
2.3 Method B. On the left: Cumulative curve of net-load forecast errors; on the right: daily estimation of upward (up) and downward (down) operating reserve 55
2.4 Single-bus representation of the reference small Italian island distribution network under investigation 56
2.5 Comparison between different control methodologies on August 8 - Active power 57

2.6 Comparison between different control methodologies on August 8 - Planned upward operating reserve 58
2.7 Comparison between different control methodologies on August 8 - Planned Downward operating reserve 59
2.8 Comparison between different control methodologies on August 8 considering BESS' operating reserve in the operating reserve constraints (*Approach #2*) - Active power 66
2.9 Comparison between different control methodologies on August 8 considering BESS' operating reserve in the operating reserve constraints (*Approach #2*) - Upward operating reserve 67
2.10 Comparison between different control methodologies on August 8 considering BESS' operating reserve in the operating reserve constraints (*Approach #2*) - Downward operating reserve 68

3.1 Hierarchical scheme of the proposed control architecture 78
3.2 Representation of the small Italian island distribution network under investigation 81
3.3 Flowchart of the proposed RTA for MGCs for isolated MGs 84
3.4 Finite-state machine model of the MGC 89
3.5 MGC implemented algorithm 90
3.6 Graphical representation of the calculation of the maximum historical upward deviation 99
3.7 Characteristic relative upward operating reserve - measured load 100
3.8 Characteristic relative downward operating reserve - measured load . . . 101
3.9 Dynamic model of the small Italian island under study 103
3.10 Equivalent diesel generator model for the MPP 105
3.11 Residential load dynamic model 105
3.12 Interface protection system dynamic model 106
3.13 Battery energy storage system dynamic model 108
3.14 Graphical illustration of the CEI-SFPR control law 108
3.15 Photovoltaic power plant dynamic model 110
3.16 Quasi-static model of the Main Power Plant with the attached logic 112
3.17 Quasi-static model of the residential load 1 115
3.18 Quasi-static model of the PV power plant 116
3.19 BESS logic-mathematical model and local level control systems 117

3.20 Complete BESS model for quasi-static simulations and operating reserve calculation . . . 121
3.21 Change in the active power consumption imposed on the prosumer 122
3.22 Operational states of the MGC following the extreme load behavior . . . 122
3.23 Active power balance following the extreme load behavior 123
3.24 Upward operating reserves following the extreme load behavior 124
3.25 Downward operating reserves following the extreme load behavior 124
3.26 Diesel unit commitment following the extreme load behavior 125
3.27 Active power consumption of residential loads following the extreme load behavior . . . 126
3.28 Change in the generated power imposed on the PV power plant 128
3.29 Operational states of the MGC following the extreme PV generation . . . 129
3.30 Active power balance following the extreme PV generation 129
3.31 Upward operating reservesfollowing the extreme PV generation 130
3.32 Downward operating reserves following the extreme PV generation . . . 130
3.33 Diesel unit commitment following the extreme PV generation 131
3.34 MGC states during July 28 134
3.35 Energy balance during July 28 135
3.36 Upward operating reserves during July 28 135
3.37 Downward operating reserves during July 28 136
3.38 Main power plant diesel units active during July 28, with or without MGC actions . . . 136
3.39 Load shedding during July 28 137
3.40 MGC states during during February 5 139
3.41 Energy balance during February 5 139
3.42 Upward operating reserves during February 5 140
3.43 Downward operating reserves during February 5 140
3.44 Case 1 - 5:18 event on July 28: frequency (left) and active power balance (right) . . . 143
3.45 Case 2 - 07:42 event on July 28: frequency (left) and active power balance (right) . . . 145
3.46 Case 3 - 19:54 event on July 28: frequency (left) and active power balance (right) . . . 147

3.47 Case 4 - 08:51 event on February 5: frequency (left) and active power balance (right) . . . 150
3.48 Case 5 - 13:15 event on February 5: frequency (left) and active power balance (right) . . . 152

4.1 A single-bus grid model for frequency transient analysis . . . 159
4.2 Example of frequency behaviour and definition of areas where the SI contribution is useful . . . 160
4.3 Comparison between the useful RoCoF results of acting the proposed concept with the actual RoCoF . . . 161
4.4 Model of the proposed SI control law . . . 161
4.5 Frequency behaviour without SI, with classical SI and with proposed SI control . . . 162
4.6 Comparison between SI set-point behaviour with classical SI and with proposed SI control . . . 163
4.7 MV distribution grid of Favignana . . . 168
4.8 Grid model of Favignana . . . 169
4.9 Modeling of equivalent load and PV system within a substation subsystem, example of SS18 substation subsystem . . . 170
4.10 Experimental set-up for PHIL simulations: blue indicates the devices and connections used in all tests performed, green indicates the devices and connections used during validation of the V2G action, and orange indicates the devices and connections used during validation of the DR action. . . . 172
4.11 V2G Fast Frequency Support Control Scheme . . . 173
4.12 Winter scenario on Favignana - Frequency behaviour with and without the FFS contribution of 20 V2G EVs . . . 177
4.13 Winter scenario on Favignana - Active power behaviours with and without the effect of 20 V2G EVs . . . 178
4.14 Winter scenario on Favignana - Frequency behaviour for different numbers of connected V2G EVs . . . 178
4.15 Winter scenario on Favignana - Frequency behaviour for 35 connected vehicles on the island, with and without the additional SI control . . . 179
4.16 Winter scenario on Favignana - Control set-point and exchanged power of a V2G EV . . . 179

4.17 Summer scenario on Favignana - Frequency behaviour for 20 connected vehicles on the island w/o CEI-OFPL (upward), w/ ideal CEI-OFPL (middle) and real CEI-OFPL (downward) implemented to the island's PV power plants . . . 181
4.18 Summer scenario on Favignana - Frequency behaviour for different numbers of connected vehicles on the island w/o CEI-OFPL (upward), w/ ideal CEI-OFPL (middle) and real CEI-OFPL (downward) implemented to the island's PV power plants . . . 182
4.19 Summer scenario on Favignana - Frequency behaviour for 20 connected vehicles on the island, with real CEI-OFPL implemented to the island's PV power plants . . . 184
4.20 Summer scenario on Favignana - Frequency behaviour for 35 connected vehicles on the island, with and without the additional SI control, with real CEI-OFPL implemented to the island's PV power plants . . . 184
4.21 Summer scenario on Favignana - Active power behaviours for 20 connected vehicles on the island, with real CEI-OFPL implemented to the island's PV power plants . . . 185
4.22 Summer scenario on Favignana - Control set-point and exchanged power of a V2G EV . . . 185
4.23 Set-up for the LED street lamp characterization tests . . . 190
4.24 Power-Voltage characteristic curve of the LED Street Lamp . . . 190
4.25 Response of Upward and Downward Load Regulation . . . 192
4.26 Synthetic inertia and FFR control scheme . . . 193
4.27 Set-up of the Power Hardware-in-the-Loop simulation tests . . . 196
4.28 Power Hardware-in-the-Loop test bed architecture . . . 196
4.29 LED lamp response with SI control . . . 198
4.30 Frequency behaviour with and without SI contribution . . . 198
4.31 Power behaviours with SI contribution . . . 198
4.32 LED lamp contribution with FFR control . . . 199
4.33 Frequency behaviour with and without FFR contribution . . . 199
4.34 Power behaviours with FFR contribution . . . 199
4.35 Modelled small islanded distribution grid . . . 200
4.36 Set-up of the Power Hardware-in-the-Loop simulation tests . . . 203
4.37 Case 1. Frequency response with SI control . . . 204

4.38 Case 1. LED lamp response with SI control 204
4.39 Case 1. Active power response with SI control 205
4.40 Case 2. Frequency response with FFR control 206
4.41 Case 2. LED lamp response with FFR control 206
4.42 Case 2. Active power response with FFR control 206
4.43 Cases 3-5. Frequency response to a 3% (left), 2% (center) and 1% (right) load variation 208
4.44 Cases 3-5. LED lamp response to a 3% (left), 2% (center) and 1% (right) load variation 209
4.45 SOC-feedback control scheme for primary regulation proposed in literature 211
4.46 Proposed SOC-feedback control scheme for fast frequency regulation . . 211
4.47 Graphical determination of additional reference active power deviation . . 212
4.48 Proposed SOC-feedback control scheme applied to a Hybrid Energy Storage System 213
4.49 Frequency transient experienced during the Aug. 9th 2019 Great Britain power system disruption event 214
4.50 Active power responses of the HESS model for open-loop response analysis 215
4.51 SoC behaviours of the HESS model for open-loop response analysis . . . 215
4.52 BESS active power references for open-loop response analysis 216
4.53 SC active power references for open-loop response analysis 216
4.54 Power system model with hybrid storage connected 217
4.55 Frequency behaviour with RoCoF optimization 223
4.56 Battery active power response with RoCoF optimization 223
4.57 Supercapacitor active power response with RoCoF optimization 224
4.58 Battery SoC behaviour with RoCoF optimization 224
4.59 Supercapacitor SoC behaviour with RoCoF optimization 224
4.60 Frequency behaviour with battery response optimization 225
4.61 Battery active power response with battery response optimization 226
4.62 Supercapacitor active power response with battery response optimization . 226
4.63 Battery SoC behaviour with battery response optimization 226
4.64 Supercapacitor SoC behaviour with battery response optimization 227

List of Tables

1.1 PV penetration in Italian islands in 2021 compared with 2020 targets . . . 26
1.2 Main characteristics of the grid components 28
1.3 Diesel consumption of the island in the year 2021 31
1.4 Energy consumption of the island in the year 2021 31
1.5 Differences between maximum recorded load and minimum recorded load in kW, for each hour and for each month 33
1.6 Differences between maximum recorded load and minimum recorded load for each hour and for each month, related to the average load for the hour 34

2.1 Annual operating costs for different PV penetration levels (€) 61
2.2 Annual operating costs with different confidence intervals (€) 63
2.3 Comparison of annual operating costs between *Approach #1* and *Approach #2* with closed-loop routine, for different levels of PV penetration (€) 70
2.4 Comparison of annual operating costs between *Approach #1* and *Approach #2* with open-loop routine, for different levels of PV penetration (€) 71
2.5 Comparison of annual operating costs between *Approach #1* and *Approach #2* with closed-loop routine, for different confidence intervals (€) 72
2.6 Comparison of annual operating costs between *Approach #1* and *Approach #2* with closed-loop routine, for different confidence intervals (€) 73
2.7 Annual operating costs variation considering the BESS' operating reserve in the operating reserve constraints (*Approach #2* vs *Approach #1*) for different PV penetration levels (€) 73

2.8 Annual operating costs variation considering the BESS' operating reserve in the operating reserve constraints (*Approach #2* vs *Approach #1*) for different confidence interval (€) 74

3.1 All conditions and actions performed, in order of priority, during transitions between states within macro-state 1 95
3.2 All conditions and actions performed, in order of priority, during transitions between states within macro-state 2 96
3.3 All conditions and actions performed, in order of priority, during transitions between states within macro-state 3 97
3.4 Key moments during July 28 134
3.5 Key moments during February 5 138
3.6 MGC actions of the typical summer day analyzed in Section 3.4.1 that have been chosen to be examined dynamically 141
3.7 Grid operating conditions during the MGC actions of the typical summer day analyzed in Section 3.4.1 that have been chosen to be examined dynamically 141
3.8 Load shedding performed during the key moment of 19:54 of July 28 . . 146
3.9 Actions of the MGC dynamically examined for the typical winter day . . 148
3.10 Grid situation during MGC actions for the typical winter day 148

4.1 Frequency characteristics during the transient without SI, with classical SI and proposed SI control 163
4.2 Active and reactive power set in the equivalent loads in the base case . . . 171
4.3 Load correction factors (*LCF*) for the two scenarios, summer and winter . 175
4.4 Generation correction factors (*LCF*) for the two scenarios, summer and winter 176
4.5 Test results of LED Street Lamp Characterization 191
4.6 Power and number of lamps at each LV node 202
4.7 Characteristics of the equivalent distribution line of the lighting subsystems 203
4.8 Base parameters of the proposed SOC-feedback control scheme 214

Abstract

This doctoral thesis reports the results carried out by the author during the three-year activities of the XXXVI cycle of the Ph.D. course in Electrical and Information Engineering at Politecnico di Bari. The main goal of this work was to develop methodologies and controls for managing distributed energy resources with the aim to promote the deployment of isolated microgrids. Moreover, the goal was to enhance the hosting capacity of isolated distribution systems, ensuring their secure and stable operation.

The control and operation of an islanded microgrid have been addressed in their entirety, starting with the optimal management of resources and ending with the control of the dynamic operation of grid components. In these studies, the main focus has been on a small Italian reference island. Based on its structure, an operational planning algorithm (operating on the highest hierarchical control level and a time scale on the order of hours) and a real-time algorithm for operating reserve assessment and allocation (operating on an intermediate hierarchical control level and a time scale from 1 minute to 15 minutes) were developed. Furthermore, concerning the low system inertia of microgrids and isolated distribution networks, innovative solutions for the provision of fast frequency support ancillary services, operating on the lowest hierarchical control level and a time scale of a few seconds, were studied and implemented. All of the methodologies discussed in this thesis have enhanced the security and stability of isolated distribution systems and reduced operational costs and greenhouse gas emissions.

Acknowledgments

The research activities were made possible by funding from the Next Intelligence Research (NIR srl) company.
My sincerest thanks go to my mentor, Prof. Massimo La Scala, and all the people, past and present, associated with the LabZERO Laboratory research group. I am grateful for the support they have provided me during my PhD journey and for the meaningful moments we have shared.
Special thanks to Prof. Giovanni De Carne for allowing me to delve into my research topics at the Karlsruhe Institute of Technology (KIT), and to the members of his research group for welcoming me and enhancing my experience abroad.
I thank, against all expectations, the technological development, equipment, and software that enabled me to carry out the research activities from day one until the last word of this thesis was written.
Il ringraziamento più grande va alla mia famiglia che mi ha sempre sostenuto e continua a credere in me al di là degli eventi e delle decisioni prese. Ringrazio inoltre gli amici che sono stati presenti durante questi tre anni di duro lavoro e che mi hanno permesso di vivere in maniera più serena anche i momenti più stressanti.



Author's Publications

Publications resulting from this research work are listed below in chronological order.

Conferences

1. S. Bruno, G. Giannoccaro, C. Iurlaro, M. L. Scala, and C. Rodio, "A Low-cost Controller to Enable Synthetic Inertia Response of Distributed Energy Resources," in *2020 IEEE International Conference on Environment and Electrical Engineering and 2020 IEEE Industrial and Commercial Power Systems Europe (EEEIC / I&CPS Europe)*, 2020, pp. 1–6

2. S. Bruno, G. Giannoccaro, C. Iurlaro, M. L. Scala, L. Notaristefano, and C. Rodio, "Mapping Flexibility Region through Three-phase Distribution Optimal Power Flow at TSO-DSO Point of Interconnection," in *2021 AEIT International Annual Conference (AEIT)*, 2021, pp. 1–6

3. S. Bruno, G. De Carne, C. Iurlaro, C. Rodio, and M. Specchio, "A SOC-feedback Control Scheme for Fast Frequency Support with Hybrid Battery/Supercapacitor Storage System," in *2021 6th IEEE Workshop on the Electronic Grid (eGRID)*, 2021, pp. 1–8

4. S. Bruno, G. Giannoccaro, C. Iurlaro, M. L. Scala, C. Rodio, and R. Sbrizzai, "Fast Frequency Regulation Support by LED Street Lighting Control," in *2021 IEEE International Conference on Environment and Electrical Engineering and 2021 IEEE Industrial and Commercial Power Systems Europe (EEEIC / I&CPS Europe)*, 2021, pp. 1–6

5. S. Bruno, G. Giannoccaro, C. Iurlaro, M. L. Scala, and M. Menga, "Predictive Optimal Dispatch for Islanded Distribution Grids considering Operating Reserve

Constraints," in *2022 IEEE 21st Mediterranean Electrotechnical Conference (MELECON)*, 2022, pp. 518–523

6. S. Bruno, C. Iurlaro, M. L. Scala, and M. Menga, "Integration of Operating Reserve Constrains in the Predictive Optimal Dispatch of Energy and Storage Resources in Small Islands," in *2022 IEEE International Conference on Environment and Electrical Engineering and 2022 IEEE Industrial and Commercial Power Systems Europe (EEEIC / I&CPS Europe)*, 2022, pp. 1–6

7. M. M. Islam, S. Bruno, C. Iurlaro, and M. La Scala, "Robust adaptive integral backstepping control of FC-SC-battery and traction motor based hybrid electric vehicles," in *2022 AEIT International Annual Conference (AEIT)*, 2022, pp. 1–6

8. S. Bruno, G. Giannoccaro, M. Muzammal Islam, C. Iurlaro, M. La Scala, M. Menga, and C. Rodio, "Control and Power Hardware-in-the-Loop tests for low-inertia power systems," in *2022 AEIT International Annual Conference (AEIT)*, 2022, pp. 1–6

9. S. Bruno, C. Iurlaro, M. L. Scala, M. Menga, and M. Semeraro, "A Dynamic Model of the Favignana Island Non-Synchronous Power System for Power Hardware-in-the-Loop Tests," in *2022 Workshop on Blockchain for Renewables Integration (BLORIN)*, 2022, pp. 107–112

10. S. Bruno, G. Giannoccaro, M. M. Islam, C. Iurlaro, M. L. Scala, M. Menga, and C. Rodio, "Predictive Control Based Energy Management of a Residential Hybrid AC-DC Nanogrid," in *2022 4th International Conference on Electrical Engineering and Control Technologies (CEECT)*, 2022, pp. 1183–1187

11. C. Iurlaro, L. Barbato, G. Bianco, S. Bruno, G. Ceneri, M. La Scala, L. Mascolo, M. Menga, C. Micillo, F. Renna, and G. Sapienza, "Control Architecture and Algorithms for Isolated Microgrids," in *CIRED 2023 - The 27th International Conference and Exhibition on Electricity Distribution*, Rome, Italy, 2023

12. K. Rajashekaraiah, G. De Carne, C. Iurlaro, M. Semeraro, and S. Bruno, "P-q theory-based dynamic load modelling in short-circuit analysis," in *2023 8th IEEE Workshop on the Electronic Grid (eGRID)*, 2023, pp. 1–5

13. L. Barbato, G. Bianco, L. Mascolo, M. Menga, F. Renna, G. Sapienza, C. Micillo, S. Bruno, C. Iurlaro, and M. L. Scala, "Power hardware-in-the-loop tests of a control

architecture for isolated microgrids in a co-simulation framework," in *2023 8th IEEE Workshop on the Electronic Grid (eGRID)*, 2023, pp. 1–6

Journal

1. S. Bruno, G. Giannoccaro, C. Iurlaro, M. La Scala, and C. Rodio, "Power Hardware-in-the-Loop Test of a Low-Cost Synthetic Inertia Controller for Battery Energy Storage System," *Energies*, vol. 15, no. 9, 2022

2. S. Bruno, G. Giannoccaro, C. Iurlaro, M. L. Scala, M. Menga, C. Rodio, and R. Sbrizzai, "Fast Frequency Support Through LED Street Lighting in Small Non-Synchronous Power Systems," *IEEE Transactions on Industry Applications*, vol. 59, no. 2, pp. 2277–2287, 2023

3. K. Rajashekaraiah, C. Iurlaro, S. Bruno, and G. De Carne, "Modelling of 3-Phase p-q Theory-Based Dynamic Load for Real-Time Simulation," *IEEE Open Access Journal of Power and Energy*, vol. 10, pp. 654–664, 2023

4. G. Sciumè, C. Iurlaro, S. Bruno, R. Musca, G. Zizzo, E. R. Sanseverino, and M. La Scala, "An integrated architecture for power hardware-in-the-loop environment and blockchain for fast frequency response tracking and remuneration," *to be submitted for publication to Electric Power Systems Research (EPSR)*, 2024

Introduction

Background and Motivation

A Microgrid (MG) is largely defined as "an electricity distribution system containing loads and distributed energy resources, (such as distributed generators, storage devices, or controllable loads) that can be operated in a controlled, coordinated way either while connected to the main power network or while islanded," according to the *Conseil International des Grandes Réseaux Électriques (CIGRÉ) Working Group C6.22*. Microgrids can be either normally connected to the utility distribution grid or permanently isolated, as in the case of remote MGs. This thesis focuses its attention on the isolated distribution grids which are operated as MGs.

The entire network has to be monitored and controlled to ensure security and continuity of operation. Energy generation and load in an isolated distribution network like an isolated MG must be balanced at all times. Inadequacy, in fact, would inevitably lead to a collapse of the MG. Therefore, it is of paramount importance to dispatch operational reserves to enable the network to operate even in the event of a sudden lack of generation.

Another characteristic of an isolated MG is its very low electrical inertia due to the absence of large rotating generators and the use of energy resources that are almost all interfaced through inverters. The inverter, in fact, decouples the inertia of connected energy resources from the distribution network, making the inertial contribution of energy resources such as wind generators ineffective. To ensure that the isolated MG can cope with sudden power fluctuations and maintain frequency within certain ranges, the entire system must be supplied by sufficiently powerful grid-forming generators or fast resources capable of rapidly adjusting their exchanged power to provide frequency support in the early stages of a transient event (e.g., Synthetic Inertia and Fast Frequency Response).

Given its critical nature, isolated MGs provide an ideal scenario for testing new control methodologies and energy resources. However, due to these above-mentioned critical

issues, MGs are not usually designed to operate disconnected from the main grid for a long time. Disconnection is considered for short periods, for testing or studies, or as a temporary operation after an unintended protection trip following disturbances on the main grid.

There are cases, though, where the MG must necessarily be isolated. These cases are related to islands, especially those that are small and geographically remote from the mainland. These networks are usually powered by diesel generation groups, and the penetration of renewable sources must necessarily remain low due to hosting capacity limitations.

Developing methodologies, algorithms, and solutions for isolated MGs that can be implemented immediately, easily, and at a low cost is essential to increase hosting capacity on islands, increase the penetration of renewable sources, and reduce dependence on fuel. Fuel costs, in fact, have a dual impact on islands compared to mainland costs. In addition to the cost of the fuel itself, the cost of maritime transportation plays a fundamental role in supplying this energy carrier to the island. The cost of energy production on islands affects the energy cost of the entire state, making it more difficult to achieve decarbonization and greenhouse gas emissions reduction goals set by governments and non-governmental organizations.

Contributions

This thesis presents several methods and applications that can be used for the optimal management and secure operation of isolated MGs. These methodologies aim to increase the reliability of isolated MGs and promote their use in distribution and transmission networks. The main contributions are resumed below.

1. Development of an operational planning algorithm for the optimal management of small isolated networks;

2. Evaluation of the relevance of considering operating reserve constraints within an optimal predictive dispatch algorithm for reducing operational costs and load shedding and generation curtailment in isolated systems;

3. Assessment of the impact of increasing penetration of renewable energy sources in small islands on solving optimal dispatch problems and how this affects the choice of the reserve assessment method to be adopted;

4. Evaluation of the effect of including the operating reserve of storage systems in the operating reserve constraints on the overall operational costs of the network;

5. Implementation of a real-time algorithm for operating reserve assessment and allocation in islanded MGs, based on control architectures and devices already in use in the Italian power systems context;

6. Development of a MG controller for islanded MGs based on a finite-state machine;

7. Development of a synthetic inertia control law for controlling distributed resources interfaced through grid-following inverters. This control law represents an improvement over the classical synthetic inertia control law found in the literature, capable to block the control action when not needed, enhance the system stability, and safeguarding the resources used;

8. Assessment of the contribution that Vehicle-to-Grid (V2G) electric vehicles can provide for frequency support in isolated distribution systems;

9. Evaluation of the impact of countermeasures adopted by current regulations against over-frequency transients and the incidence of acquisition and command delays on these contributions;

10. Assessment of the fast frequency regulation support that can be provided by LED lighting systems, particularly street lighting systems;

11. Development of a control based on the state of charge variation of storage systems to reduce stress on these components during the provision of fast frequency support to the grid.

Outline of the Thesis

This thesis is organized into four Chapters. An overview of isolated MG management is initially provided in Chapter 1, to give the reader a solid foundation and understanding of the methodologies proposed in this work. The subsequent Chapters discuss tools and methodologies related to a different time-scale of a grid operation.

Chapter 1 - Overview of MGs and Non-Synchronous Power Systems: the concept of MG and its general control structure are introduced. It focuses mainly on non-synchronous networks, especially small networks, giving an overview of the state of the art of small islands in Italy.

Chapter 2 - Operational Planning in Islanded Microgrids: an operational planning algorithm of energy resources in an isolated MG is proposed, referring to a time-scale of grid operation on the order of hours. The proposed algorithm is applied to an actual isolated MG located in Italy. This algorithm is not only explained but also validated through economic evaluations over a one-year operation of the examined network.

Chapter 3 - Real-Time Operating Reserve Assessment and Allocation: a real-time algorithm for operating reserve assessment and allocation is introduced, referring to a time-scale of grid operation from 1 minute to 15 minutes. This algorithm is designed to be simple, easily implementable, and to use devices and components already in use in Italian distribution networks or specified in existing regulations. The algorithm is first described and then validated through simulations on quasi-static and dynamic grid models.

Chapter 4 - Innovative Solutions for Ancillary Services Provision: innovative solutions for providing ancillary services are proposed, referring to a time-scale of grid operation of a few seconds. These specific solutions represent an enhancement of some controls introduced in recent years in the literature and aim to make the use of distributed energy resources for fast frequency regulation services easier and more efficient, reducing system instability and safeguarding the deployed resources.

Chapter 1

Overview on Microgrids and Non-Synchronous Power Systems

The evolving landscape of power generation is marked by remarkable developments in Renewable Energy Sources (RES) and Distributed Generation (DG). This progress offers several advantages for the electricity system, such as enhanced service continuity and increased involvement of end-users in the electricity market. The proliferation of dispersed generation facilities across regions empowers specific sections of the distribution grid, spanning both Medium Voltage (MV) and Low Voltage (LV), to operate autonomously. In such islanded conditions, the stability of voltage and frequency, as well as the equilibrium between generation and load, can be reliably maintained.

Increasing The increase in RES and DG results to be critical for the evaluation of power systems and for meeting the growing energy demand. Forecasts in [18], for example, predict a 30% increase in energy demand by 2030 over 2012 levels and almost a 50% increase by 2040, mainly due to population growth and economic expansion. In addition, the International Energy Agency (IEA) predicts that incremental global investment in the energy sector will reach an impressive $40 trillion by 2035 [19].

DG technologies have emerged as a pivotal avenue for integrating renewable energies into the electricity market, leveraging the advantages of decentralization.

Over the past two decades, the European Union (EU) has been a pioneer in global renewable energy adoption. Setting long-term targets and enacting supportive policies has significantly boosted renewable energy consumption in the region, growing from 9% in 2005 to 16.7% in 2015. Building upon the 20% target for 2020, the recast Renewable Energy Directive 2018/2001/EU [20] introduced a binding renewable energy target of

at least 32% for 2030, with room for possible upward revisions by 2023. To align with the European Green Deal's higher climate ambitions [21], the Commission presented new 2030 climate targets on 14 July 2021 [22]. These included a proposal to amend the Renewable Energy Directive, raising the 32% target to at least 40% renewable energy sources in the EU's energy mix by 2030. On 18 May 2022, the Commission released the *REPowerEU* plan [23], which aimed to rapidly reduce the EU's reliance on Russian fossil fuels well before 2030 by accelerating the clean energy transition. This plan focused on saving energy, producing clean energy, and diversifying the EU's energy supplies. As part of this initiative to expand renewable energy in power generation, industry, buildings, and transport, the Commission proposed raising the directive's target to 45% by 2030. To further expedite renewable deployment, the Council, following a Commission proposal in November 2022 [24], enacted a temporary emergency regulation on 22 December 2022 [25], streamlining permit-granting procedures for renewable projects and facilitating power purchase agreements. Significantly, on 30 March 2023, the European Parliament and the Council reached a provisional agreement to raise the binding renewable energy target to at least 42.5% by 2030, significantly surpassing the earlier 32% target, with aspirations to reach 45% [26]. This amendment marks a substantial increase in the EU's renewable energy share. At the center of this transformative ecosystem are Microgrid (MG), which are poised to facilitate the decentralisation of generation and the deployment of RES, ensuring a more robust, adaptable and sustainable energy landscape.

1.1 Concept of microgrid

A Microgrid (MG) is an innovative concept in the field of energy distribution and management. It encompasses various definitions, but they all converge on a common set of features [27–34]:

- *Generation and Demand Control Systems*: Microgrids incorporate generation sources, both renewable and traditional, alongside demand control systems. This allows for a diverse mix of electricity sources, promoting resilience and sustainability.
- *Clearly Defined Electrical Boundaries*: Microgrids have well-defined boundaries that distinguish them from the broader power grid. These boundaries are typically smaller in scale, and MGs can be situated at various voltage levels, often at LV but sometimes at MV.

- *Island Capabilities*: The ability to operate independently, or in an "islanded" mode, is a defining feature of MGs. For this purpose, a MG must have an installed generation capacity exceeding its maximum load, enabling it to disconnect from the main grid while continuing to supply local loads.

The concept of MGs has evolved over time. Initially, they were envisioned as broad power subsystems gathering both generation and loads. As time passed, they became more focused on distribution and showcased their islanding capabilities [34]. There is some regional variation in the perception of MGs; for instance, in the United States, MGs are often expected to provide both heat and power, whereas the European approach tends to emphasize power supply [32].

Microgrids can be implemented in various contexts and can assume different configurations. They can also be classified based on their internal voltage levels, whether Alternating Current (AC) or Direct Current (DC) or mixed, or by their ownership, which can be either public or private entities [35]. One of the most classic contexts is that of large-scale industrial plants. These facilities, in fact, start from a situation of geographically constrained, localized electrical grids with limited interaction with the distribution network. These types of plants have been in operation for many years and use an energy management system to control their internal operations. In recent years, we have witnessed the establishment of various types of MGs, such as university or research campuses, military installations, residential areas, commercial establishments, and industrial entities. Some of these typologies are, for example, defined and illustrated in [36], within the framework of the MERGE research project (Microgrids for Efficient, Reliable, and Greener Energy).

Microgrids offer a range of distinct and quantifiable advantages that shape their operation and functionality. These benefits make them a key technology for the development of modern active distribution systems. These advantages are:

1. Benefits related to Renewable Energy Sources (RES) integration:
    - Incorporating RESs situated in close proximity to the power demand.
    - Integrating RESs harnessing renewable energy resources (green power).
    - Mitigating aggregate power fluctuations on the distribution grid.
2. Benefits associated with distribution system configuration:
    - Enhancing the reliability and operational efficiency of existing distribution systems.

- Deploying new distribution systems, whether they are grid-connected or isolated.
- Enabling RESs installed within the MG to participate in energy markets.

3. Benefits related to end-users and the environment:
   - Empowering customers and end users.
   - Building a compelling business case for MG deployment based on:
     - Enhancing power supply reliability for end users.
     - Tailoring power quality to meet end-user requirements.
     - Offering ancillary services to the grid, including voltage and frequency-related services.
     - Reducing the carbon footprint.
     - Strengthening grid stability.
     - Bolstering energy security and the resilience of the distribution grid by leveraging local energy resources.

The disadvantages of using MG are mainly barriers, referring to the high initial cost of installation or the lack of regulation. Microgrids, in fact:

- require appropriate market regulation and incentives to make their implementation economically feasible and competitive.
- require a sophisticated control and management architecture to coordinate available resources and optimize operational decisions in real time.
- must address technical challenges related to the intermittency of renewable sources, transition between connected and isolated modes, and power protection and quality.
- must consider the conflicting interests of different stakeholders, such as consumers, producers, grid operators, and regulators.
- must consider long-term social impacts, such as the creation of new research and job opportunities, electrification of remote or underdeveloped areas, and active consumer participation.

1.2 Operation and control of microgrids

A MG control system encompasses the control functionalities that define the MG as a system capable of self-management. It can operate autonomously or remain connected to the main distribution grid while also having the ability to disconnect and exchange power with the distribution grid. As MG configurations vary based on their location and purpose, the requirements and functions of the MG and its controller can differ. In terms of implementation, a MG control system may involve software, hardware, or a combination of both. It can also be physically realized through different approaches, such as centralized or distributed control methods. Some of the key control system functions include:

- Coordinating operations in both grid-connected and islanded modes.
- Automatically transitioning from grid-connected to islanded mode to provide continuous power to MG loads during abnormal power system conditions, such as blackouts.
- Re-synchronizing and reconnecting from islanded mode to the grid-connected mode.
- Managing energy to optimize real and reactive power generation and consumption within the MG.
- Providing ancillary services, which may involve supporting the distribution grid and participating in energy markets or utility system operations as needed.

It is important to note that not all MGs may possess the capacity to perform all these tasks, such as enabling market participation. The extent of functionality can vary based on the specific characteristics and purpose of the MG.

The functions of the MG control system operate at various control levels and across different timeframes, addressing different components and assets within the MG. These functions span from the device-level operations, usually integrated into DERs, to the higher-level MG supervisory and grid-interactive functions.

Device-level functions operate on shorter timescales (from a few microseconds to some seconds), while management functions typically function on longer timescales (from seconds to several days). The functions responsible for managing transitions between connection and disconnection and for dispatching DERs assets operate on distinct timescales. In the case of unplanned disconnections, transition functions need to execute swiftly with

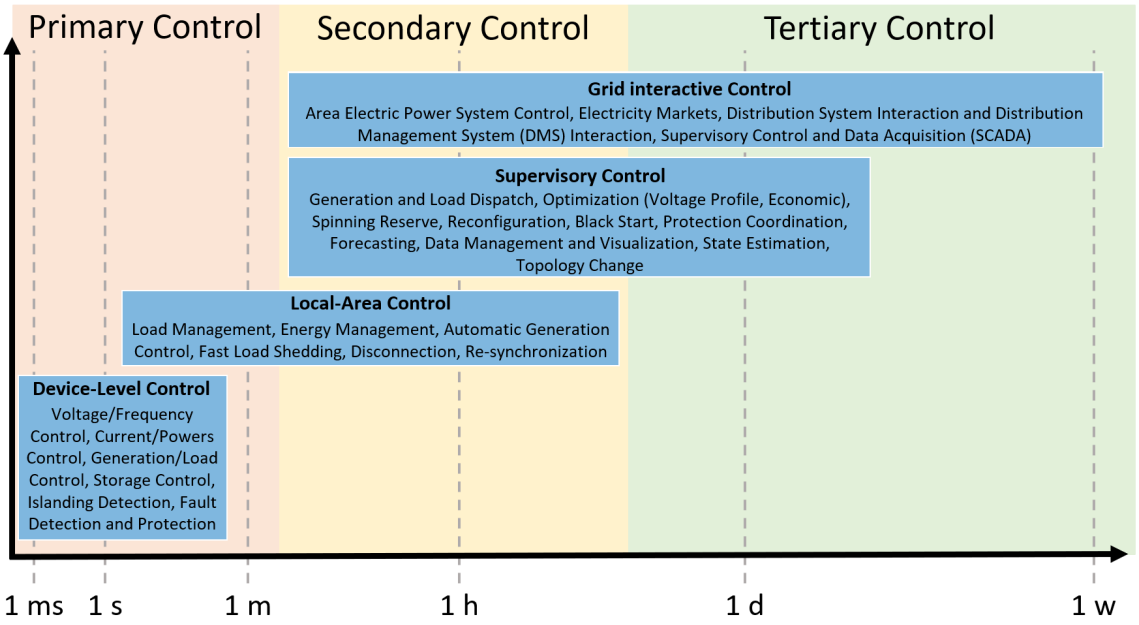


Figure 1.1: Timescales and classification of the MG control functions with hierarchical control structure

minimal delay, operating on a short timescale. On the other hand, dispatch functions are carried out at regular intervals and over a longer timescale, often within the range of minutes (typically 15 minutes or less).

Fig.1.1 outlines the specific timeframes in which these various MG control system functions come into play for a hierarchical control structure of a MG. In modern MGs, in fact, a hierarchical control system is mainly used, consisting of three levels of control:

- Primary control
- Secondary control
- Tertiary control

The primary control, known as the local or field level, is adopted to ensure reliable operation (i.e. in terms of security and operational reliability) of the MG, maintaining voltage and frequency stability, as well as offering plug-and-play capability to the various distributed resources (DERs). Typically, the techniques used for the primary level of control are based on local automation logic such as droop-control, applied to each connected distributed resource. The secondary control, or management level, is designed to restore the frequency and amplitude voltage of the MG, as well as manage communication between devices within it. The secondary control layer is usually developed according to two approaches: centralised and decentralised. Conventionally, the centralised control

structure is used, which requires a complex, high-speed communication network between the local controllers and the centralised controller. This adversely affects the reliability of the entire system, so much so that, according to many authors [37, 38] the decentralised approach of secondary control, either through gossip or consensus-based algorithms or through a multi-agent system, is desirable. The highest level of the grid control architecture is tertiary control, which is responsible for power management from an economic point of view, or economic dispatching. Centralised and decentralised approaches also exist for this level of control [37].

This same organization on three hierarchical levels is also envisaged in the IEEE 2030.7-2017 standard [34], with the simplest dispatching and transition control functions being assigned to the intermediate control level (Level 2), local automation and field device management functions to the lowest level (Level 1), and monitoring, control and optimization functions to the highest level (Level 3).

This standard has become a benchmark in the design of control architectures for MGs [11, 35]. It is supported by other standards: the IEEE Std. 2030.8-2018 [39] focuses on tests for evaluating controller performance, while the IEEE Std. 1547-2018 [40] establishes technical and test specifications for the interconnection and interoperability between DERs and the power grid.

However, the technical requirements may vary depending on location. In fact, the IEEE standards refer to the regulations in the US and an electrical system at 60 Hz frequency. The International Electrotechnical Commission (IEC) also defined a set of standards for MG control systems, covering both 50 Hz and 60 Hz power systems. The IEC 62898-1 [33] provides guidelines for MG project planning and specifications of components in it, including resource analysis, generation and load forecasting, DERs and MG power system planning, technical requirements for DERs, MG connection to the distribution network, and control, protection, and communication systems. The IEC 62898-2 [41], instead, is mostly focused in the operation and control of a MG, including operational modes and mode transition, Energy Management System (EMS) and MG control, communication and monitoring procedures, Energy Storage Systems (ESSs), protection principle covering principle for non-isolated MGs, isolated MGs, anti-islanding, synchronization and reconnection, power quality, commissioning, maintenance, and testing. The set of standards includes also the IEC 62898-3 [42], which provides general and specific technical requirements of fault protection and dynamic control in MGs. This standard focuses on stabilizing the frequency and voltage of MGs in AC using dispatchable loads that react autonomously to

frequency and voltage variations with a change in active power consumption.

In line with IEEE Std. 2030.7, IEC 62898-2 delves into the fundamental aspects of the control and operation of MGs. It thoroughly explores the core functions, dispatching strategies, and transient behaviors. However, it is important to note that the IEC 62898-2 standard treats the MG distinctly depending on whether it is a non-isolated grid-connected MG, a non-isolated islanded MG, or an isolated MG. According to the guidelines established in this standard, non-isolated MGs operate independently for a finite period. As a result, eventual reconnection to the power grid becomes a necessity. In contrast, isolated MGs do not have the ability to establish connections to a larger external grid [41]. The IEEE 2030.7, instead, just divides the MG states into grid-connected or islanded [34].

The two standards propose a quite similar control architecture for a generic MG. Anyway, they define somewhat different characteristics for the core functions, particularly for the dispatching functions that manage the MG during normal operation.

The IEEE 2030.7 [34] handles the case of connected or isolated MG in a very similar way, keeping the basic functions of dispatch the same. The dispatch of MG resources, in fact, remains the same under both operating conditions, except that in the case of islanded MG the power exchange at the POI of the dispatch control law must be set equal to zero.

The IEC 62898-2 [41] standard, on the other hand, remains less general and differentiates more sharply between the various MG operating conditions. For a non-isolated MG, the standard emphasizes that DER must comply with the connection rules defined by national grid codes, which is not required in an isolated MG. An unisolated, unconnected MG must always meet all the specifications of a connected MG, as it can connect to the grid, and it must constantly monitor the grid frequency and voltage to be ready for reconnection. For this reason, resource control functions must always be able to monitor and control the phase angle of the voltage during islanded operation.

Isolated grids are less constrained by grid connection rules, but their control functions must have higher capabilities than non-isolated grids. These capabilities include the ability to perform a black start, constant monitoring, management and load shedding for energy balancing, and significantly greater energy storage capacity.

1.3 Integration of microgrids into the power system framework

From the main grid point of view, a Microgrid refers to a collection of loads, Distributed Generations (DGs), and Energy Storage Systems (ESSs) operating at LV levels, that behaves as a single consumer/prosumer. This simplifies the inclusion of MGs in the power system framework and is a good opportunity for utilizing distributed Renewable Energy Sourcess (RESs), especially at the distribution level.

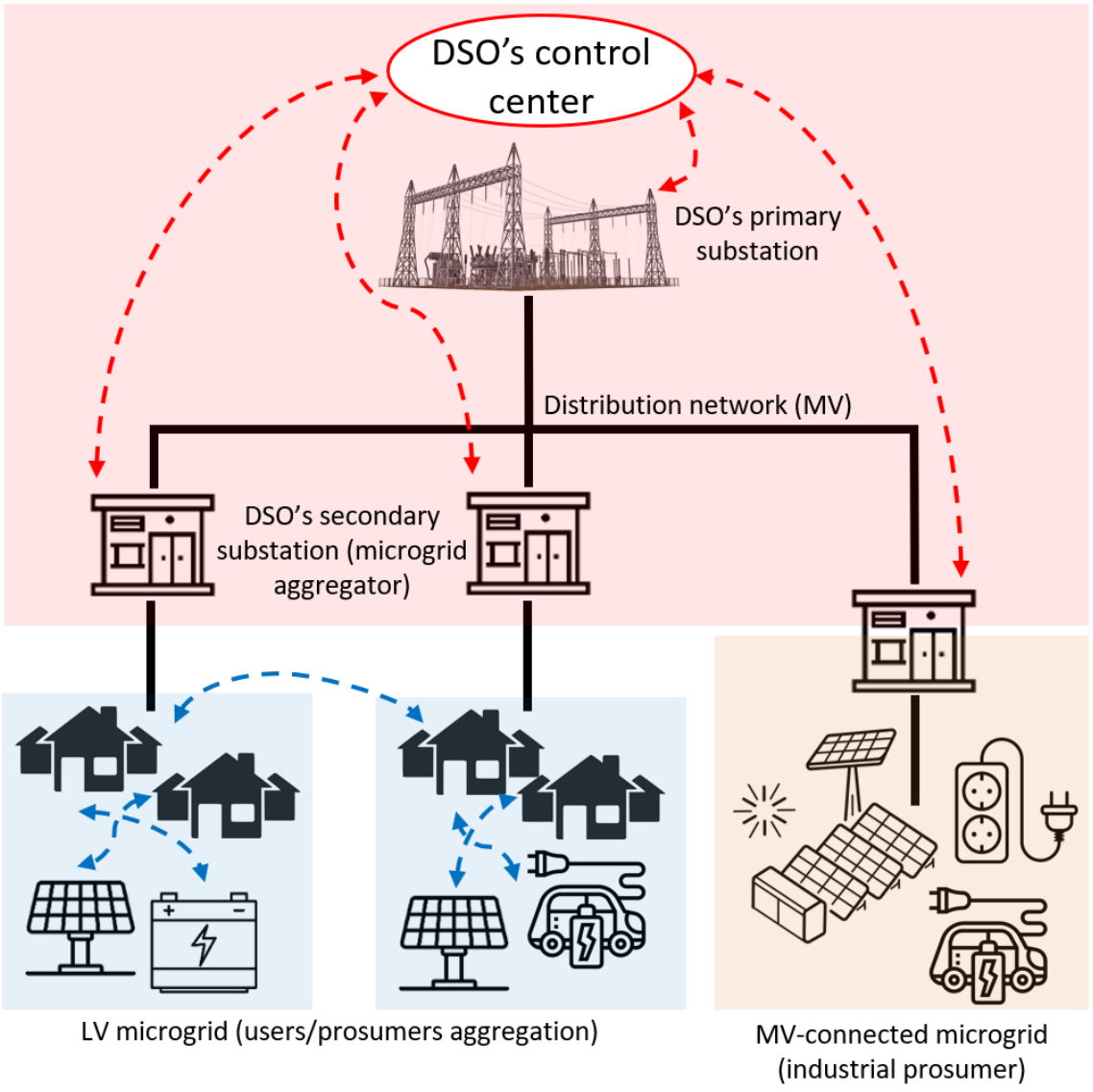


Figure 1.2: Interaction scheme between DSO and MGs

However, integrating MGs requires careful consideration of the variability and un-

predictability of RESs, affecting network stability, power supply quality, and power flow reversals [43–45]. This is particularly critical for isolated networks, such as those on small islands or weakly connected rural areas [11, 46].

In these cases, Distribution System Operators' (DSOs) interaction with dispatchable resources (DGs, ESSs, and loads) becomes crucial. A MG control architecture for isolated/weakly connected MGs is schematically represented in Fig. 1.2.

Microgrids made by aggregation of users and small prosumers operate at the LV level. Each MG may include various loads, DGs, ESSs, and vehicle charging stations. Even a MV-connected prosumer can be considered as a MG.

From the DSO's point of view, the MGs act as a single controllable entity. DSO exchanges information with the primary substation and the secondary substations (MG aggregators) and manages power flows on the distribution network and between the distribution network and MGs, even enabling functionalities of the various MGs, such as optimal MG operation or modulation/limitation of the exchanged power at Point of Interconnection (PoI) [13]. From the users' point of view, they can benefit from full utilization of distributed RESs, exchanging information with each other [46, 47].

Although MGs are designed primarily for the benefit of customers, it is critical to consider the perspective of DSOs, especially in isolated or weakly connected grid scenarios. In these scenarios, the DSO must interact with MG resources, trying to meet end-user wishes within the technical constraints of the network, ensuring the secure and stable operation of the system, through real-time algorithms or operational planning algorithms of the MV network.

Microgrid, if managed effectively, can also collaborate with DSOs for voltage and frequency regulation and maintaining power quality levels [17, 48]. For the integration of such MGs into distribution networks, advanced information and communication technologies are necessary to provide controllability and observability of the entire grid [11, 49].

Currently, DSOs have limited capabilities for monitoring and control of MV networks and almost no capabilities in LV networks. With these limited resources, DSOs cannot yet provide comprehensive network management solutions.

The general requirements include distributed measurement and control systems, a reliable communication infrastructure, and a supervisory center. Different solutions for distributed measurement systems are proposed in the literature, often based on using a limited number of MV measurement points and implementing state estimation and forecasting algorithms [50, 51].

In addition to a reliable monitoring algorithm, a control system is needed to remotely manage DGs and ESSs to prevent or mitigate over/under voltages or frequency variations. Current MV networks implement communication, control, and measurement infrastructures for Automatic Meter Reading (AMR) and MV network protection and supply restoration.

The AMR server in the DSO control center communicates via Global System for Mobile communication (GSM) or General Packet Radio Service (GPRS) with the aggregators at each secondary substation, which are connected to smart meters of both users and DGs. A supervisory control system for MV network protection is also installed in the DSO control center, directly controlling MV Breaker Controllers BCs via GSM or GPRS for protection, fault isolation, or supply restoration.

Various communication solutions are suggested in the literature to support smart grid applications, including wired, wireless, or hybrid solutions, which can be integrated into an Internet of Things (IoT) platform [52]. In managing heterogeneous communication networks, DSOs may encounter issues with limited resources offered by some existing communication links.

1.4 Capacity enhancement for monitoring and control of power grids in Italy

To improve monitoring and control capability in distribution networks in Italy and make them smarter, the Italian regulator *Comitato Elettrotecnico Italiano (CEI)* has published Annex "O" of the grid code CEI 0-16 [53]. Indeed, this annex represents the most up-to-date summary of the Italian regulations on the monitoring and control of electrical distribution networks.

In Annex "O" of the CEI 0-16 published in December 2020 [53], the *Controllore Centrale d'Impianto (CCI)* is discussed in detail. This controller must be present in every new connection to the MV grid for:

- Generation plants with a rated power of at least 1 MW, including all plants that have at least one generation and/or storage unit, with or without load
- Plants participating in the Italian ancillary services market, namely *Mercato dei Servizi di Dispacciamento (MSD)*

This controller's main purpose is to make the underlying plant "observable" by the

DSO. This is achieved by measuring relevant quantities and transmitting the data through a communication channel compliant with the IEC EN 61850 communication standard.

No less important purpose of the CCI is to coordinate the different elements of the subtended plant to meet the DSO's demands at the point of delivery (PdC). This ensures that the entire plant is perceived by the DSO as one equivalent generator. While optimal plant management might involve the control of controllable loads, it's important to note that such aspects are not covered in this annex.

In this section, an overview of the functionalities of the CCI has been discussed. This discussion aims to show the capabilities of this device already available in the Italian power system landscape. This device and its functionalities can always be considered in studies concerning the management of Italian distribution grids.

The Functional Performances (FP) of the CCI are divided into:

- FP1 (Mandatory): Information exchange with the DSO to achieve observability.
- FP2 (Optional): Voltage and power regulation at the PoD, services that, while not mandatory, must be implemented on the CCI.
- FP3 (Facultative): Performance related to (optimal) plant management and participation in the MSD. Functional services associated with plant management encompass activities such as start-up, re-start-up, connection, and disconnection from the grid, as well as optimized resource management. The MSD services considered in this performance include balancing services, and secondary and tertiary frequency regulation.

The CCI should not perform power protection and regulation functions in frequency transients (fast frequency regulation, primary regulation).

An indicative illustration of the correlation between the different interfaces with which the CCI must communicate, exchange information and transmit commands, is shown in Fig. 1.3. A GPS is observed in the figure, as the CCI must be equipped with a GPS receiver to acquire and maintain synchronized time. The time must be expressed with reference to Coordinated Universal Time (UTC), Greenwich time zone. The uncertainty of the time reference cannot be more than ± 100 ms. The General Protection (GP) and Interface Protection System (IPS) were illustrated separately in the scheme, but by performing similar tasks, they could coincide. The CCI must be equipped with a GSM/GPRS modem to receive commands from the TSO for the remote telecommissioning of a generating

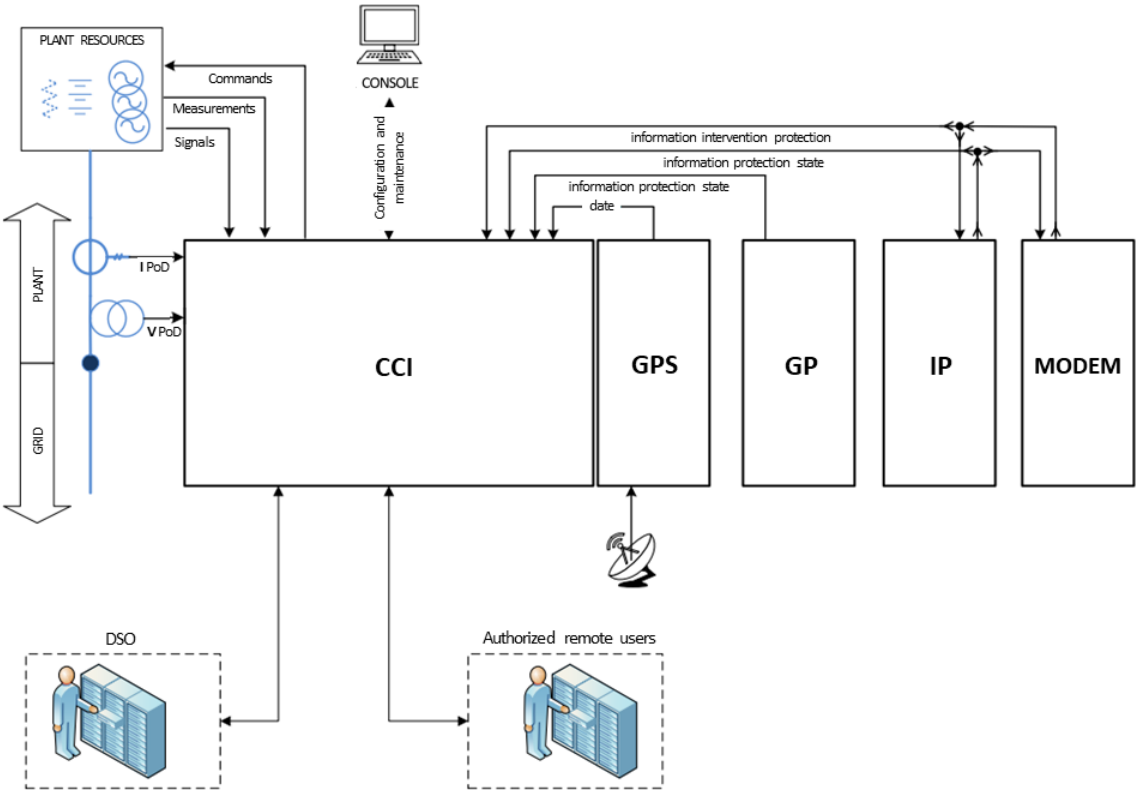


Figure 1.3: General scheme of the CCI system with related interfaces

unit. Moreover, the grid code stipulates that all generating plants must participate in the *National Power System Defense Plans* [54]. The CCI can limit or change the active power set-point of the units but cannot order their disconnection. Since this operation may be necessary for the *National Power System Defense Plans*, the installation of a GSM/GPRS modem specified in Annex "M" of the CEI 0-16 is mandatory, appropriately interfaced with the CCI in such a way that any disconnection is perceived as intentional, and automatic operations planned in the case of unintentional opening of the same switch are inhibited.

In Fig. 1.4, an indicative schematic of the logical functioning envisaged for the CCI is presented. This schematic highlights two regulation loops:

- Fast Regulation Loop: this loop establishes the operating point for each component of the plant coordinated by the CCI to reach the overall required operating point (also known as the "expected operating point" and corresponding to the "internal set-point" in Fig. 1.4) at the PoD. It corrects the deviation between the current and expected operating points by acting on the individual operating points of the plant components. The internal set-point can be input externally or calculated by the slow regulation loop. The fast regulation loop must ensure the achievement of the new

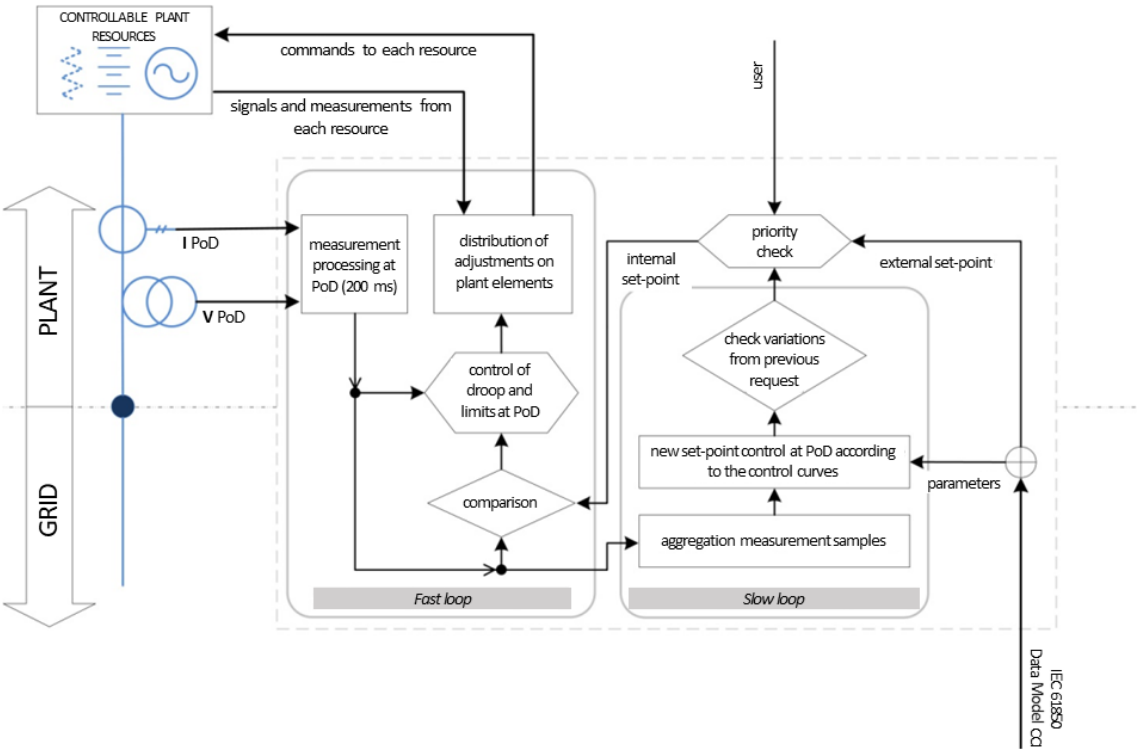


Figure 1.4: Block diagram of the control loops in the CCI

operating point for the controlled units within maximum settling times of: 1) 60 seconds for variations in the internal set-point of active power; 2) 10 seconds for variations in the internal set-point of reactive power.

- Slow Regulation Loop: in this loop, the operating point at the PoD is elaborated to meet the demands at the point of connection. This operating point is modified when the deviation of the requested quantities exceeds a certain dead-band and is defined through one of the following modes: 1) established by the user or sent externally by modifying an active power (P) or reactive power (Q) set-point; 2) calculated by the slow regulation loop according to functions such as Q = f(V) or cosφ = f(P).

The slow control loop operates with a cycle time (ΔT) between 10 and 600 seconds (default: 60 seconds), while set-points sent from outside must be sensed by the internal control loop within 3 seconds. Annex "O" does not specify a cycle time interval for the fast control loop. However, considering the information provided, it can be assumed that it should be between 200 milliseconds and 3 seconds. Measurements processed every 200 milliseconds, such as those on the magnitudes at the PoD, are the only measurements that the fast control loop can use. Similarly, the measurements processed every ΔT constitute the only measurements used by the slow control loop.

Annex "O" requires that the CCI must control the plant components through control signals transmitted through the user's internal communication network. These signals may be incremental or absolute, percentage or p.u. type. The communication network may be the same for all communications, but user monitoring and/or control of the CCI through the local terminal requires a communication network that is physically independent of that used for communication with external operators.

1.5 Isolated Distribution Grids

The aleatory nature of RES leads to unforeseen fluctuations in net-load profiles. Although robust systems, like continental interconnected ones, are less susceptible to such uncertainties thanks to the large inertia of rotating machines, smaller non-synchronous power systems could suffer for high level of RES integration due to their low rotational inertia, and could experience instability issues. Therefore, islanded distribution networks, like those on small islands, constitute an ideal test bed for testing the integration of innovative technological solutions deployed to face stability issues due to RES penetration.

All small islands globally share common characteristics, such as a small population, limited economic diversity, and relative remoteness, which poses challenges for trade and accessing essential services [55]. Despite these challenges, small islands boast unique biodiversity and cultural richness, making them attractive for tourism. Climate change, with its widespread effects, poses a significant threat to islands, particularly those in Europe, including the small Italian islands [56]. The Intergovernmental Panel on Climate Change (IPCC), in fact, predicts negative impacts related to temperature increases, extreme weather events, and changes in rainfall, intensifying pressure on water resources [57]. Small Italian islands, like many in the Mediterranean, grapple with issues such as fossil fuel dependency, challenges in electricity generation, high distribution costs, underutilization of renewable energy, seasonal human presence, water scarcity, waste management, and outdated mobility models [58]. Policies play a crucial role in preserving these islands, especially in the face of climate change. However, implementing effective policies is challenging for small islands, lacking easy access to expertise, data, and financial resources [59]. Recognizing the vulnerability of small islands, the 2015 Paris Agreement [60] acknowledges their susceptibility to climate change and highlights their potential as pioneers for new technologies. The EU has initiatives like NESOI [61] and the Clean Energy for EU Islands Secretariat [62], aiming to support clean energy transition. The

Clean Energy for EU Islands initiative focuses on reducing fossil fuel dependence by assisting islands in utilizing renewable energy sources [62]. Past initiatives, such as those in Bornholm and El Hierro, demonstrate successful strategies for achieving energy self-sufficiency [63, 64]. In [63], several projects for energy self-achievement on islands have been discussed, confirming that some of these attempts were successful, for example on the Canary Islands [64, 65].

The decarbonization path also involves waste management, the circular economy, water management, sustainable tourism, and mobility. Despite technical research on energy grids, there is a lack of extensive studies on small Mediterranean islands, hindering efforts to address their vulnerability to climate change [66]. Recent studies on waste in the Balearics and the Canary Islands, as well as evaluations of renewable electricity mix on Lampedusa Island, provide valuable insights [66, 67]. However, challenges persist in collecting data at a small island scale, especially regarding climate scenarios and spatial resolution of satellite data [68].

All this information has also been underlined in [69], with special emphasis on Italian small islands. That paper examined how islands worldwide have pursued sustainability, with particular emphasis on analyzing the achievements and shortcomings of current policies. These policies were evaluated concerning their environmental sustainability impact, as well as the identification of both technological and non-technological barriers.

The European Commission, in the report [70], defines wind energy as "a sustainable solution for islands, when used in conjunction with other energy sources, such as energy storage, mixed energy network or if access can be obtained to a large neighboring electricity network". Nevertheless, in Italy, the penetration of wind energy on the small island is still very low. Only a few small islands use this resource and only with micro-wind plants (Pantelleria, Sant'Antioco and Ventotene, with an installed power of 32 kW, 55 kW e 3.16 kW, respectively) [71]. There are many non-technological barriers that prevent adequate energy transition action from being put into practice in these areas, such as excessively rigid landscape constraints, complex connection requirements, intricate and often outdated permitting procedures, and a multiplicity of competent bodies on the subject that often do not communicate with each other [72].

These non-technological barriers also affect the development of PV power plants in the islands. Fortunately, the possibility of installing PV plants on existing buildings' rooftops allows better penetration of this kind of renewable energy on islands where land is protected or its use is limited. In spite of this, the installed PV power is still very low

Island	Isolated	Target 2020 [kW]	Target reached 2021 [%]	PV installed 2021 [kW]	PV installed/habitants 2021 [kW/habitant]	PV installed/habitants compared with national average 2021 [%]
Capraia	yes	180	19.73%	35.50	0.10	26%
Capri[a]	no	1000	20.63%	206.26	0.02	5%
Ischia	no	-	-	3960.40	0.06	16%
Giglio Island	yes	700	4.96%	34.74	0.03	8%
Elba Island	no	-	-	3623.80	0.12	32%
Aegadian Islands	yes	1060	142.68%	1512.44	0.34	90%
Aeolian Islands (Lipari)	yes	2860	17.79%	508.89	0.04	11%
Pelagie Islands	yes	2310	26.20%	605.12	0.09	24%
Tremiti Islands	yes	240	7.67%	18.40	0.04	11%
La Maddalena	no	-	-	990.50	0.09	24%
Pantelleria	yes	2720	30.89%	840.31	0.11	29%
Ponza	yes	720	40.18%	289.29	0.09	24%
Procida	no	-	-	339.78	0.03	8%
Salina	yes	580	43.10%	250.00	0.10	26%
San Pietro	no	-	-	1547.23	0.26	68%
Sant'Antioco	no	-	-	1934.61	0.14	37%
Ustica	yes	280	155.00%	432.64	0.33	87%
Ventotene	yes	170	77.48%	131.72	0.19	50%

Table 1.1: PV penetration in Italian islands in 2021 compared with 2020 targets

[a]Capri has a target because it was isolated in 2017 when the decree was issued and interconnected to the grid in 2019

compared to the same resource penetration in the peninsular area, and far from the national goals defined by the Italian Ministry for Economic Development for the past 2020 year[72]. The "*Ministerial Decree of 14 February 2017*" [73], in fact, had set renewable installation targets in 20 non-interconnected Italian small islands for a total of 12.820 kWp (of these, 1.000 kWp were allocated to the island of Capri, which was not interconnected in 2017 but is now). For example, in 2021, the Aeolian Islands were projected to reach a power output of 2,860 kWp, but they only managed to achieve 509 kWp. Pantelleria had a goal of 2,720 kWp, but it has only reached 872 kWp. The Pelagie archipelago has a power output of 605 kWp, falling short of the planned 2,310 kWp. Ustica stands out as the only one of the 27 islands to surpass its target, achieving 432 kWp of installed RES, which now fulfills 12 percent of its electricity needs. PV are found on all the smaller islands, although often in very small amounts, such as the Tremiti Islands (18.4 kWp) and Giglio Island (34.7 kWp). The largest installations are located on islands that are interconnected with the national power grid, specifically Ischia, Elba Island, and Sant'Antioco, with about 4,000, 3,700, and 2,000 kWp, respectively. Among the non-interconnected islands, Pantelleria has the most substantial PV installations, at 840 kWp, followed by Lampedusa and Linosa, at 605 kWp [72]. All information about PV penetration in the Italian small islands can be found in Table 1.1.

1.5.1 An example of a small Italian island: a benchmark

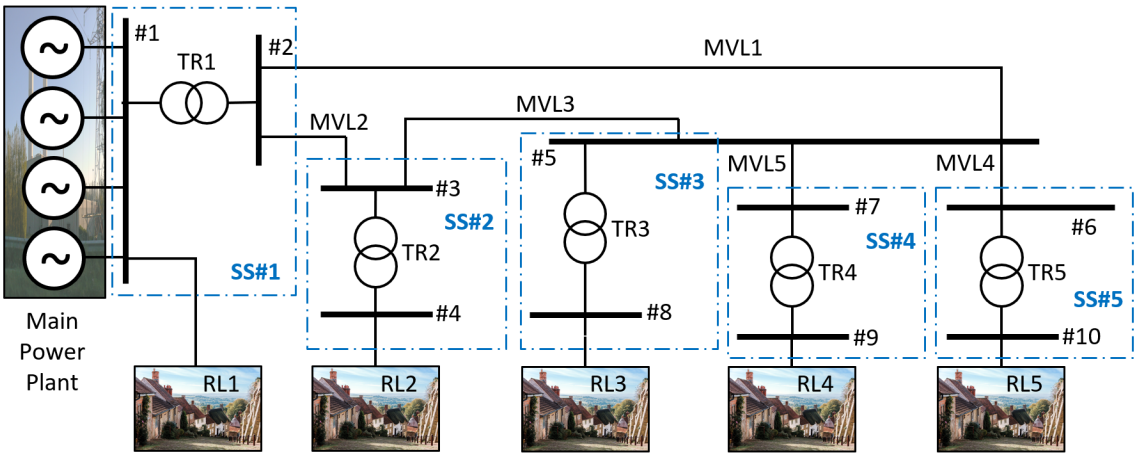


Figure 1.5: Representation of the small Italian island 10 kV distribution network under investigation

In this thesis work, the conducted studies have often focused on supporting isolated distribution networks on small islands. Primary objectives include improving network

stability and reducing operational costs associated with network management and fossil fuel use. In particular, many studies have focused on the structure of a typical small Italian island, for which comprehensive data on network structure and energy consumption in recent years have been made available. These data were provided by *e-Distribuzione*, the main DSO in Italy. Due to confidentiality obligations, the specific island cannot be disclosed, and changes have been made to the island scheme and some data. Therefore, the grid can be considered a good representation of a typical small Italian island, but it differs from the specific actual island. In the following chapters of the text, this model will be taken as a benchmark to test the proposed procedures.

The small Italian island under consideration has been schematically represented in Fig. 1.5 while in Table 1.2, the main characteristics of the grid have been reported.

Table 1.2: Main characteristics of the grid components

	TR1	**TR2**	**TR3**	**TR4**	**TR5**
S_n [kVA]	2000	400	630	250	630
V_{1n} [kV]	10.0	10.0	10.0	10.0	10.0
V_{2n} [kV]	0.4	0.4	0.4	0.4	0.4
P_{cc}%	0.91	1.15	1.04	1.15	1.04
V_{cc}%	6.0	4.0	4.0	4.0	4.0
P_{fe}%	0.14	0.21	0.18	0.25	0.18
I_0%	0.9	1.3	1.1	1.3	1.1
	RL1	**RL2**	**RL3**	**RL4**	**RL5**
P_n [kW]	1810	590	700	300	650
V_n [kV]	0.4	0.4	0.4	0.4	0.4
	MVL1	**MVL2**	**MVL3**	**MVL4**	**MVL5**
Length [km]	0.510	0.510	0.510	0.850	0.510
r_l [Ω/km]	0.387	0.387	0.387	0.253	0.387
x_l [Ω/km]	0.086	0.086	0.086	0.120	0.086

In the typical small Italian island under investigation, there is a Main Power Plant (MPP) responsible for supplying the entire island and regulating frequency and voltage. Therefore, the MPP must remain connected at all times and supply a minimum part of the island's load. The MPP consists of 4 diesel units with rated apparent power of 600 kVA (2.4 MVA for the entire plant) and no technical minimum. The MPP is privately owned and not directly controllable by the DSO that manages the island network. However, each producer must have a CCI installed, as described in Section 1.4. Therefore, the DSO has access to the states of the MPP's resources and the power outputs of each of

them. Moreover, the MPP's CCI can include additional features allowing the DSO to communicate with the MPP and exchange specific information or requests.

The distribution network operates at 10 kV and comprises five substations (from SS#1 to SS#5), as depicted in Fig. 1.5. Each substation supplies a portion of the island's residential load (from RL1 to RL5). The MV distribution comprises 5 MV distribution lines (from MVL1 to MVL5) connecting the substations in a loop. MVL1 is typically open during normal operations but ensures reclosure in case of faults or maintenance work.

The MPP is connected to SS#1, where the main load source (RL1) is connected. The MPP's diesel units operate at 400 V and directly feed the residential load RL1 without any transformation stage. The connection between the MPP and the island distribution grid is made by means of a MV/LV transformer with 2 MVA of rated power (TR1). The remaining residential loads (from RL2 to RL5) are also supplied at low voltage through a transformer in the corresponding substation (from TR2 to TR5).

As it is possible to note from the data visible in Table 1.2, the total installed power is about 4 MW, but the actual power absorbed by the island during operation is much less. In fact, the SS#1's transformer has a maximum power rating of 2 MVA because it was sized for the actual load absorbed by the island, which reaches a maximum (in the summer months) of 30 percent of the installed load. This is confirmed by looking at the load data recorded on the island and used in this thesis.

The data available for this island include:

- The monthly energy and fuel consumption recorded on the island during the year 2021;
- The maximum, average, and minimum hourly load obtained from measurements made on the island in the year 2019;
- The average quarter-hourly measures of the year 2021.

The monthly energy and fuel consumption data offer insights into the variation in monthly consumption throughout the year. Table 1.3 provides a breakdown of monthly fuel consumption on the island, categorized by diesel unit. The table illustrates that consumption is notably higher during the summer months, spanning from June to September. Particularly, August alone contributes to 18% of the annual fuel consumption, while the winter, fall, and spring months collectively account for approximately 5-6% of the total. The "Relative" consumption column depicts monthly consumption as a percentage of the

fuel consumed in August, the peak consumption month. Notably, consumption during the winter/autumn/spring months is around 30% of that observed in August, underscoring a substantial disparity in electricity demand during the summer compared to the rest of the year. This surge in demand is primarily attributed to tourism, a key driver of the economy in Italian islands.

For a comprehensive analysis, Table 1.4 presents a similar breakdown, this time focusing on energy consumption. While energy consumption aligns with fuel consumption, variations exist due to the operating conditions and efficiency of diesel units. Examining the "Relative" consumption column highlights a more pronounced difference between energy consumption in the summer months and that during the rest of the year. In most winter/autumn/spring months, the energy demand is less than 30% of the energy demand observed in August on the island.

The maximum, average, and minimum hourly data allow the generation of the load curves depicted in Fig. 1.6, obtained through linear interpolation. Such curves are crucial to understanding the variability of the load during one hour of the day. These data were also fundamental for calculating the minimum upward and downward reserves to be guaranteed for the operation algorithm discussed in Chapter 3.

As evident from the curves in Fig. 1.6, the electrical load pattern on the island is distinctly characterized by the day-night cycle. During this cycle, energy consumption varies significantly, with an increase during daylight hours and a decrease during nighttime hours, peaking in the evening. Despite this trend, differences between daytime and nighttime energy consumption are relatively more pronounced in small islands like the one under consideration, and nighttime load can reach extremely low levels.

The data reveal that the highest average load is consistently recorded between 8:00 pm and 10:00 pm, peaking at 9:00 pm in August at 924.71 kW. The lowest average load, on the other hand, consistently occurs during the nighttime hours, from 2:00 am to 6:00 am, with a minimum of 160.21 kW at 3:00 am in November. In August, a month characterized by the highest annual energy consumption, the minimum average load occurs at 6:00 am, totaling 463.21 kW, approximately half of the electrical load recorded at 9:00 pm. This clearly emphasizes the day-night cycle on the island.

Considering the recorded maximum and minimum values, the difference is even more pronounced. In August, the recorded minimum load was 373.81 kW at 5:00 am, while the recorded maximum load was 1122.93 kW at 9:00 pm, three times higher.

Table 1.5 illustrates the differences between the maximum and minimum values

Table 1.3: Diesel consumption of the island in the year 2021

	Diesel consumption (kg)				**Total (kg)**	**Percent**	**Relative**
	DG1	DG2	DG3	DG4			
Jan	16,640	-	9,833	20,170	**46,643**	**6%**	**34%**
Feb	17,413	-	14,050	9,187	**40,650**	**5%**	**30%**
Mar	17,146	-	12,460	11,853	**41,459**	**5%**	**30%**
Apr	5,410	11,296	12,485	13,793	**42,984**	**6%**	**31%**
May	2,366	3,069	30,819	13,300	**49,554**	**6%**	**36%**
Jun	31,097	5,826	19,164	24,779	**80,866**	**10%**	**59%**
Jul	31,840	28,656	26,953	27,989	**115,438**	**15%**	**84%**
Aug	24,497	31,037	48,312	33,379	**137,225**	**18%**	**100%**
Sep	16,414	32,679	6,985	32,979	**89,057**	**11%**	**65%**
Oct	392	1,470	12,691	31,458	**46,011**	**6%**	**34%**
Nov	8,950	10,350	5,550	13,750	**38,600**	**5%**	**28%**
Dec	6,959	16,509	23,721	-	**47,189**	**6%**	**34%**
Total	**179,124**	**140,892**	**223,023**	**232,637**	**775,676**		

Table 1.4: Energy consumption of the island in the year 2021

	Diesel consumption (MWh)				**Total (kg)**	**Percent**	**Relative**
	DG1	DG2	DG3	DG4			
Jan	59.50	-	35.16	72.12	**166.77**	**6%**	**31%**
Feb	62.26	-	50.24	32.85	**145.34**	**5%**	**27%**
Mar	61.30	-	44.55	42.38	**148.23**	**5%**	**28%**
Apr	19.34	40.39	44.64	49.32	**154.69**	**5%**	**29%**
May	8.46	10.97	114.61	47.55	**181.60**	**6%**	**34%**
Jun	117.49	20.83	68.52	88.60	**295.43**	**10%**	**55%**
Jul	119.89	103.38	96.37	100.07	**419.71**	**15%**	**79%**
Aug	87.59	115.74	203.23	127.82	**534.37**	**19%**	**100%**
Sep	58.69	125.63	24.97	127.17	**336.47**	**12%**	**63%**
Oct	1.40	5.26	45.38	117.91	**169.95**	**6%**	**32%**
Nov	32.00	37.01	19.84	49.16	**138.01**	**5%**	26%
Dec	24.88	59.03	84.81	-	**168.72**	**6%**	**32%**
Total	**652.80**	**518.23**	**832.31**	**854.95**	**2858.29**		

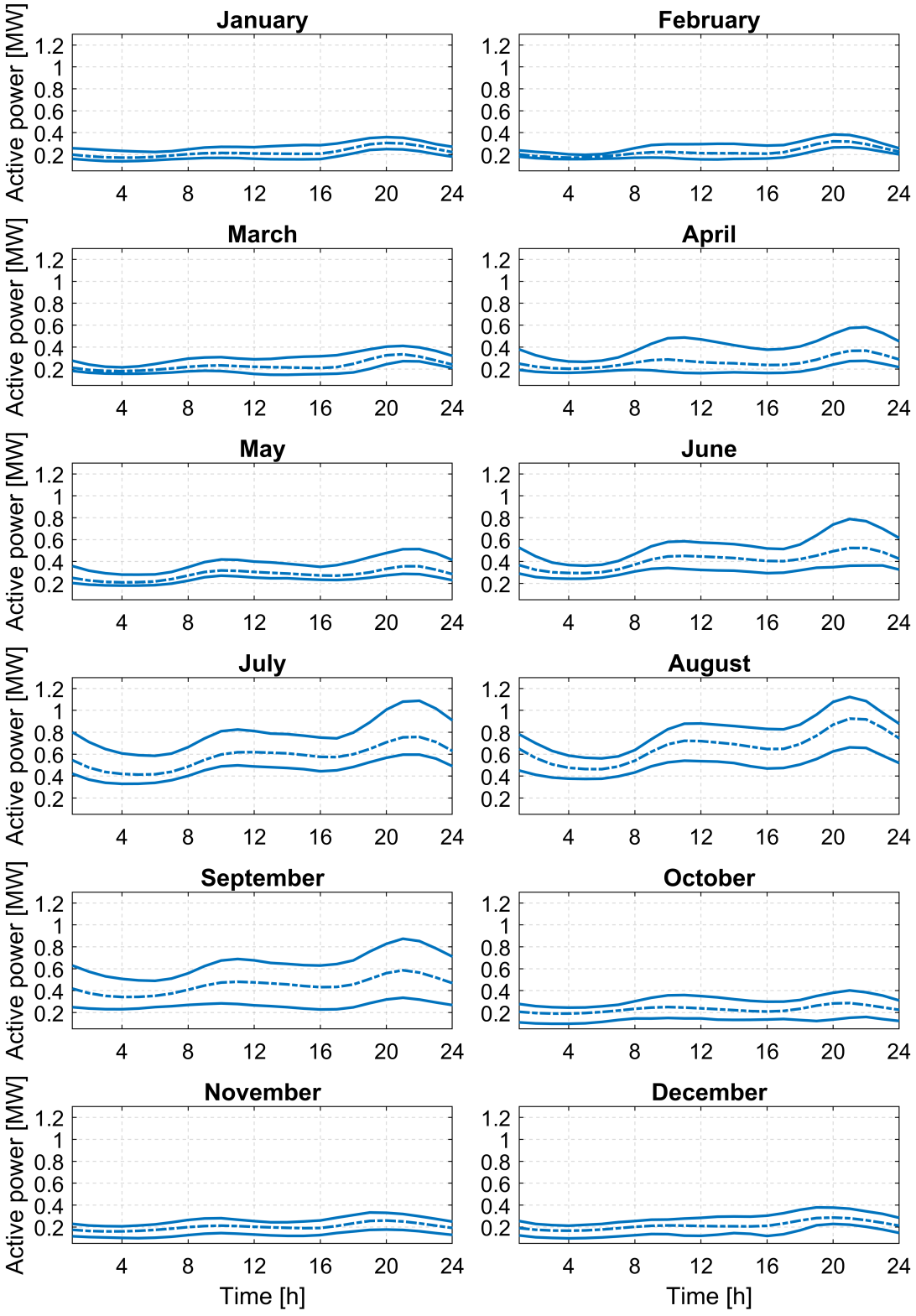


Figure 1.6: Maximum, average, and minimum hourly load profiles obtained from measurements made on the island in the year 2019

Table 1.5: Differences between maximum recorded load and minimum recorded load in kW, for each hour and for each month

	Month											
Hour	**Jan**	**Feb**	**Mar**	**Apr**	**May**	**Jun**	**Jul**	**Aug**	**Sep**	**Oct**	**Nov**	**Dec**
1	97	57	93	187	155	236	379	331	380	168	113	131
2	101	58	74	151	128	189	343	288	336	158	105	121
3	100	57	62	121	111	144	308	243	300	151	103	117
4	95	44	59	103	100	125	277	211	277	147	105	115
5	86	39	67	96	100	119	261	194	257	145	115	121
6	75	43	84	98	98	118	247	186	240	143	121	123
7	73	62	103	117	107	128	243	182	253	139	131	129
8	85	88	116	170	123	160	262	204	288	157	138	130
9	95	114	121	242	138	206	291	247	347	190	139	131
10	101	124	127	306	148	238	321	303	391	207	136	133
11	102	133	126	323	151	253	327	338	411	213	128	156
12	106	139	133	308	146	250	324	344	411	204	122	164
13	118	143	144	278	145	249	307	337	395	204	119	164
14	126	138	158	247	133	242	309	338	395	189	124	151
15	131	127	161	226	127	235	306	354	396	173	132	157
16	127	118	162	213	118	225	308	361	401	163	133	185
17	119	113	168	218	136	216	292	353	413	159	140	192
18	115	116	183	230	161	235	314	364	429	183	149	187
19	108	119	179	252	187	296	364	406	472	229	159	163
20	109	119	160	279	205	389	440	452	508	245	153	149
21	107	112	139	302	225	427	484	461	539	250	146	146
22	99	95	128	306	229	405	492	428	534	225	136	141
23	91	74	125	280	216	336	457	391	494	215	130	143
24	91	56	111	236	185	288	418	359	442	187	121	138

recorded for each hour of each month. The greatest differences occur in September, with a maximum of 538.76 kW at 9:00 pm, while the smallest differences are found in February, with a minimum of 39.12 kW at 5:00 am. This underscores the need for more substantial reserves to manage load fluctuations in the months from June to September, especially during the evening hours from 7:00 pm to midnight, while a lesser reserve will be required during nighttime hours, from 2:00 am to 7:00 am, and particularly in February and March.

In Table 1.6, the differences presented in Table 1.5 are expressed as a percentage of the average load for each hour. It is interesting to note that in the months of September and October, the expected variability is very high, often comparable to the load itself, remaining between 80% and 90% of the average load. This implies a greater need for diesel groups to be operational by the central station to ensure an adequate reserve compared to those strictly necessary to simply power the load. While in these two months, the ratio between load variability and the load itself is approximately constant, in April there is

Table 1.6: Differences between maximum recorded load and minimum recorded load for each hour and for each month, related to the average load for the hour

	Month											
Hour	**Jan**	**Feb**	**Mar**	**Apr**	**May**	**Jun**	**Jul**	**Aug**	**Sep**	**Oct**	**Nov**	**Dec**
1	49%	28%	44%	75%	62%	64%	70%	51%	91%	81%	64%	69%
2	55%	31%	39%	68%	56%	58%	72%	51%	89%	81%	64%	69%
3	57%	32%	34%	58%	52%	48%	70%	48%	85%	79%	64%	69%
4	55%	26%	33%	51%	48%	42%	66%	44%	81%	77%	66%	69%
5	50%	23%	36%	46%	47%	40%	63%	42%	75%	74%	70%	71%
6	42%	23%	43%	45%	45%	39%	59%	40%	68%	70%	70%	69%
7	38%	32%	50%	50%	45%	39%	55%	37%	68%	64%	71%	68%
8	42%	42%	53%	66%	45%	43%	54%	38%	71%	67%	69%	64%
9	45%	52%	53%	86%	45%	49%	53%	40%	78%	77%	66%	62%
10	47%	55%	54%	106%	46%	53%	54%	44%	83%	83%	64%	62%
11	48%	61%	56%	117%	48%	56%	53%	47%	86%	87%	61%	73%
12	50%	65%	60%	117%	48%	56%	52%	48%	86%	86%	60%	78%
13	57%	68%	66%	108%	49%	57%	50%	48%	85%	88%	61%	79%
14	61%	65%	73%	98%	46%	56%	51%	49%	86%	85%	64%	73%
15	64%	61%	76%	92%	45%	56%	52%	53%	90%	81%	69%	76%
16	61%	57%	77%	90%	43%	56%	53%	56%	93%	78%	70%	88%
17	52%	51%	77%	91%	50%	54%	51%	54%	95%	74%	67%	82%
18	44%	46%	74%	90%	57%	56%	52%	53%	94%	78%	64%	72%
19	37%	40%	61%	88%	62%	65%	56%	53%	93%	87%	62%	58%
20	36%	37%	49%	84%	61%	79%	62%	52%	91%	86%	59%	52%
21	35%	35%	42%	83%	63%	81%	64%	50%	92%	87%	58%	52%
22	35%	32%	41%	83%	64%	77%	65%	47%	94%	83%	58%	54%
23	36%	29%	45%	84%	66%	69%	64%	47%	95%	87%	61%	60%
24	41%	25%	46%	82%	65%	68%	66%	48%	94%	83%	63%	65%

significant variability ranging from 45% to 117% of the average load. This indicates that a deterministic reserve allocation, as currently implemented on the island, is not suitable for isolated networks like the one under consideration.

The quarter-hour load profiles recorded in 2021 provide insights into the variation in load profiles between days and demonstrate how the average load on the island changes from year to year. Fig. 1.7 illustrates the load trends on the island, categorized by month, for the year 2021. This figure reveals the fluctuations in the island's electrical load throughout the days of the same month.

In Fig. 1.9, a comparison is made between the maximum, average, and minimum trends of the year 2019, presented in Fig. 1.6, and the average quarter-hourly monthly load of the year 2021. It is evident that the average load in 2021 has changed compared to that of 2019, proving to be higher in the evening hours in all months, except for April, in which the average load in 2021 was much lower than that of 2019. This highlights the unpredictable nature of the load during that month.

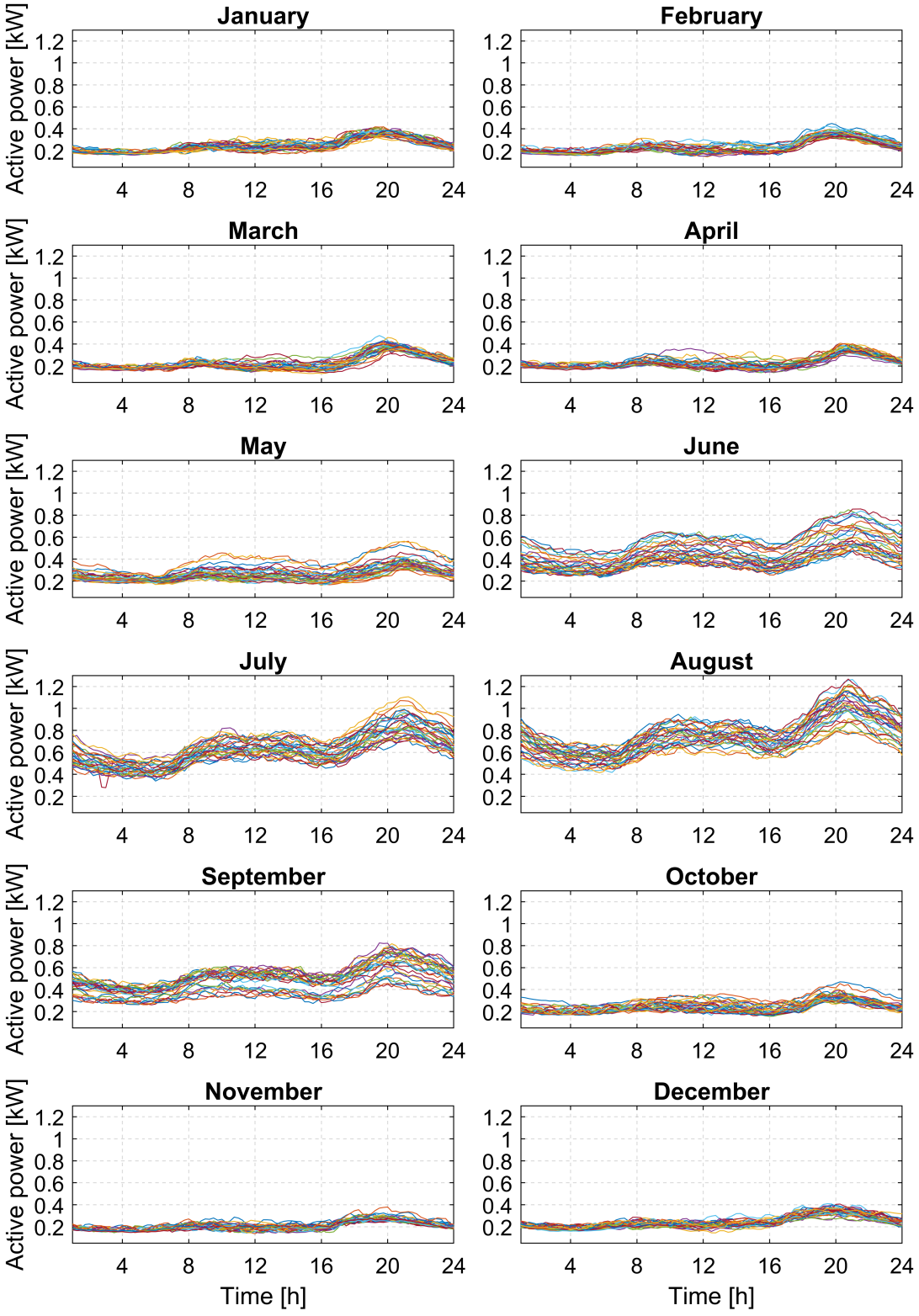


Figure 1.7: Average quarter-hourly load profiles of the year 2021

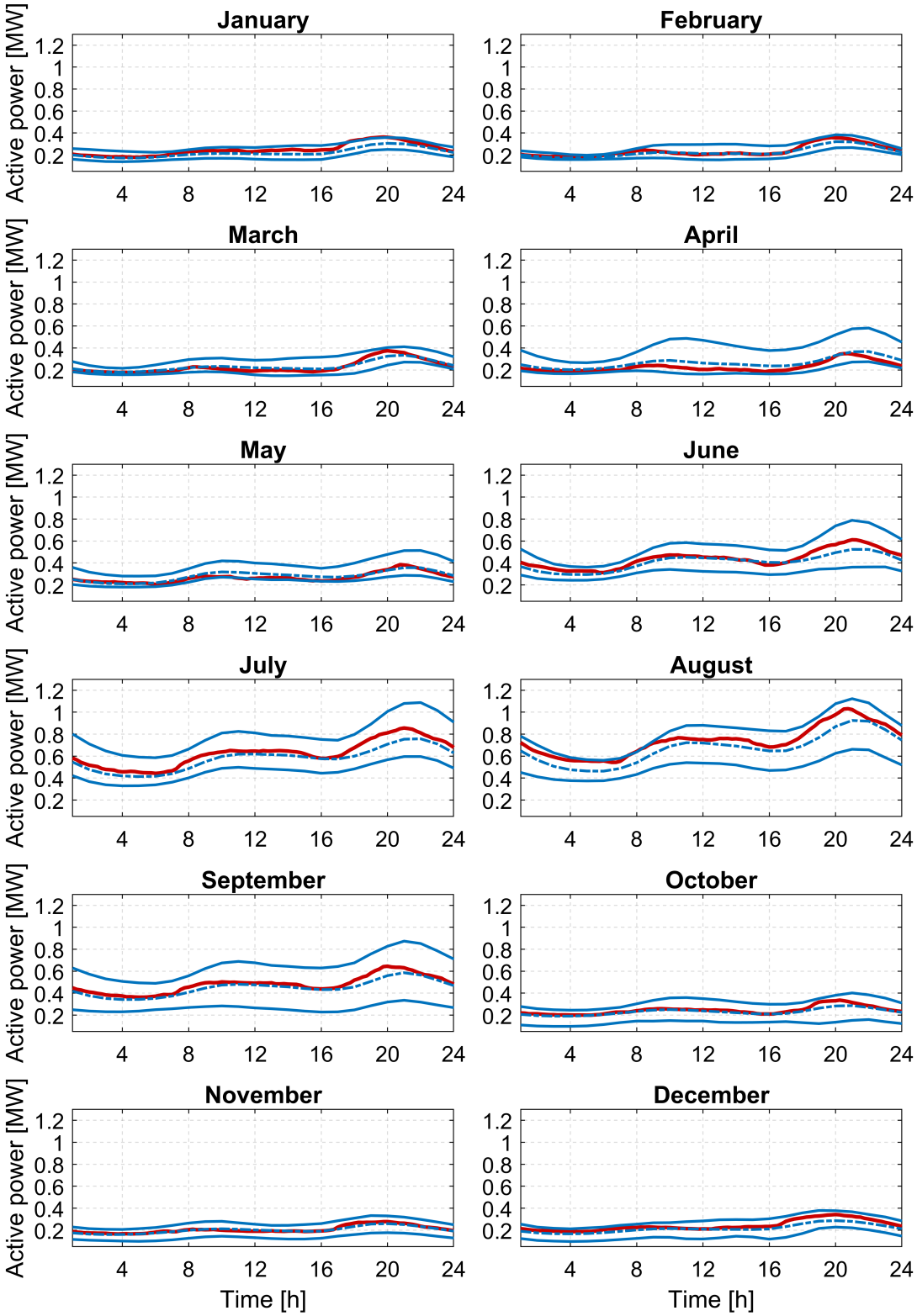


Figure 1.8: Average load trends in various months of the year 2021 compared with maximum-average trends 2019

In terms of distributed generation and renewable energy production facilities, the island currently has very few PV installations on residential rooftops, with a total installed capacity of just under 100 kWp. However, due to the targets set by the Italian Ministry for Economic Development [73], as discussed in the previous section, this capacity is set to increase.

Fig. 1.9 illustrates the power profiles that would be generated by a PV system installed on the island in the year 2020. These data were extracted from online databases containing measured irradiance information. In the studies conducted in this thesis, this PV profile was used as profile 2021 (unfortunately, 2021 data are not yet available).

Looking at the graphs, it can be seen that production is highly variable in the winter/autumn/spring months while it is less variable in the summer months. This is due to the weather, which is much more stable and sunny on the island in summer than in the rest of the year.

1.5.2 Operating reserve in small islands

As just seen, the net load on small islands varies greatly throughout the year, and the electrical load is always very low. In the case of the small Italian island under consideration, for example, a penetration of 200 kW PV would already bring the net load of the island almost to 0 in the middle hours of the day. it is therefore important to make sure that the operating reserve available on the island is such that it can cope with sudden variations in PV production by an amount equal to or slightly less than the island's electrical load.

As already discussed in Section 1.5, in conventional small non-synchronous systems, the power supply is based on the use of fossil-fueled generators. In small Italian islands, for example, diesel generators are mostly used since natural gas distribution does not reach the islands. In this kind of system, the operating reserve is managed through deterministic rule-based control strategies programmed in the control units of generators. Typically, these controllers are based on hysteresis control. They switch an additional generator on, whenever the active generators have approached with a sufficient and predetermined margin their capacity limit. Analogously a generation unit is switched off when the usage is below another fixed threshold. A hysteresis band is used to avoid continuous switching on and off of generators. However, in the presence of large net-load uncertainties caused by intermittent DG production, these deterministic methods may no longer be adequate to guarantee a reliable power supply.

The authors in [74] proposed to quantify the needs of operating reserve combining the

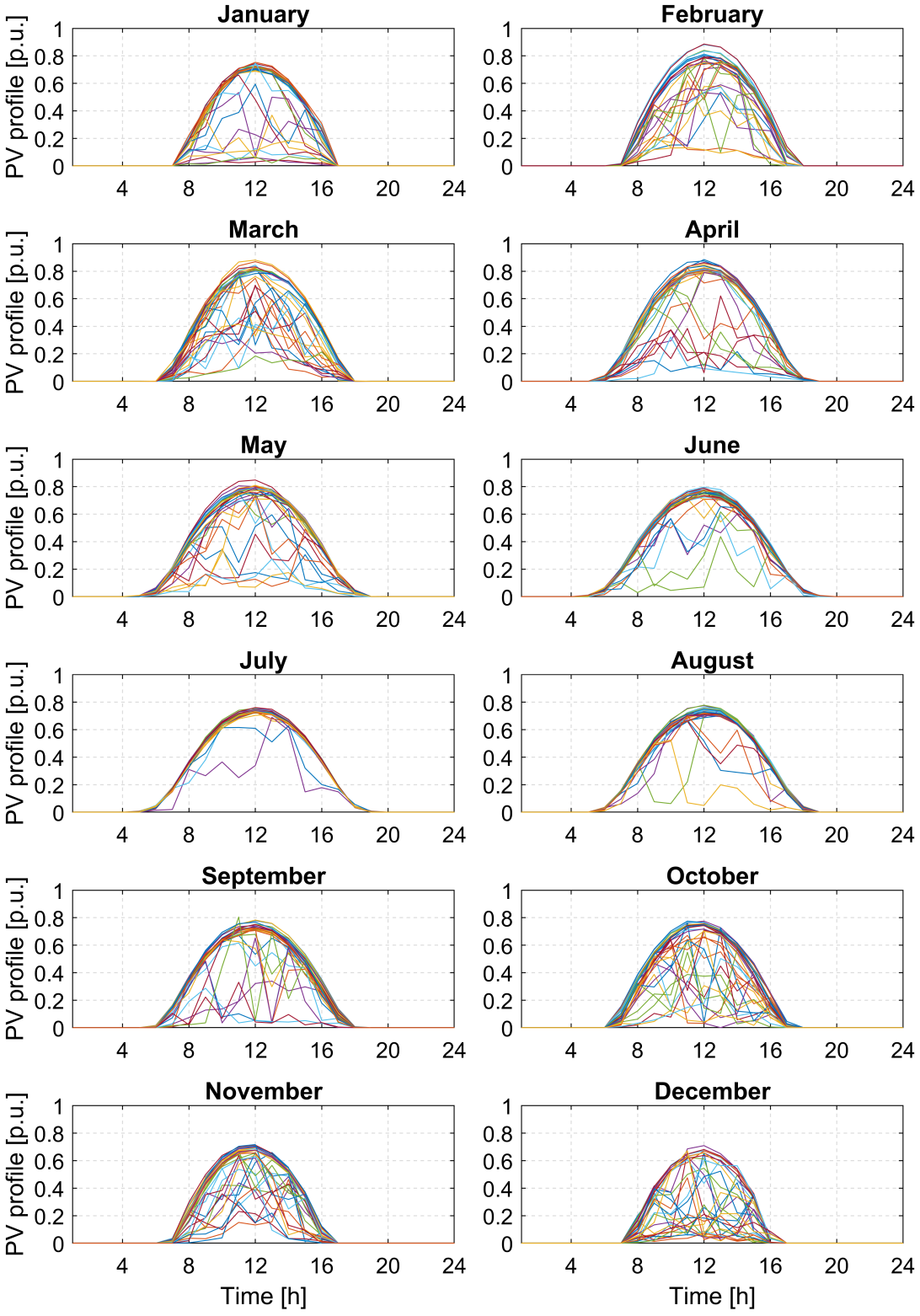


Figure 1.9: PV production trends in p.u. for the year 2020

contributions of two quantities calculated proportionally to the load and to the photovoltaic production. However, even if this method allows to calculate reserve according to the current system conditions, the proposed deterministic rule might fail in assessing the needed reserve in the presence of volatile RES generation or sudden system changes. In [75], instead, a risk evaluation approach is presented and a reserve management tool for operating reserve is proposed by setting acceptable risk thresholds. Analogously, in [76], an uncertainty analysis methodology was proposed to quantify the power reserve by taking into account PV power and load forecasting errors. Then, based on what was discussed in [76], in [77] a probabilistic model to calculate the required power reserve based on a probability distribution of both PV and load has been proposed.

These last methods showed that probabilistic approaches can be more suitable in the presence of high RES penetration. The authors in [78] compared different approaches showing how, with respect to rule-of-thumb methods, the use of probability- and risk-based methods permits to better balance reliability and reserve provision. Forecast errors were aggregated in cumulative curves which were then used to quantify reserve by fixing a probability or risk threshold. In [5], a similar probabilistic approach was proposed but, differently from [78], where a single cumulative curve of forecast errors is adopted, positive and negative errors were split into two different cumulative curves. The rationale in [5] is that positive forecast errors, experienced when the net-load is higher than the forecast, should be used to estimate upward reserve (vice versa negative errors to size downward reserve). The approach proposed in [5] appears to be more suitable to the case of small islanded systems with high RES penetration where, depending on the time of the day or season, both under- and overgeneration issues might be experienced.

Other works have based the sizing of operating reserve on the time-variability of net-load. For example, in [79] and [80], starting from a set of net-load measurements, obtained with a specific time resolution, the authors used the net-load variations between two successive measurements to build Probability Distribution Functions (PDFs) of net-load volatility. These PDFs were used to estimate the required operating reserve according to probabilistic [79] or statistical [80] functions. A methodology for sizing operating reserves based on the distribution of net-load variations is also recommended in [81]. Differently from [80], where statistical functions are evaluated, the report [81] suggests the adoption of risk- or probability-based methods according to the rationale that RES power variations do not usually follow normal probability distribution functions. In [81], the operating reserve is sized as the maximum relative step change that corresponds to a

fixed probability threshold, in the cumulative net-load variation distribution function. In operational planning, the absolute value of the operating reserves can be calculated using as basis of the latest load forecasts.

A drawback of these methodologies is that synchronous time series of historical load profiles and RES must be available [81], possibly with an adequate time resolution (10 to 15 minutes according to [81]). The works in [80] and [82] adopted even shorter time resolution (respectively 1 and 5 minutes). As pointed out in Section 1.5.1, unfortunately, in most realistic cases, the collection of historical data with such a short time resolution is difficult to achieve. In Italy, for example, distributors collect and use measurements with a very high resolution during real-time operation, but historical series are built on data obtained from smart meters on a 15-minutes average basis. Moreover, available measurements are usually related to net-load. According to the recent regulatory directions, transmission and distribution companies will be able in the next future to collect segmented data about generation and load from large aggregates of distributed energy resources [53]. These data will allow to achieve a better observability of the RES production below the substations, making also possible the application of methodologies such as the one described in [81].

Chapter 2

Operational Planning in Islanded Microgrids

This chapter shows an innovative operational planning algorithm for islanded Microgrids (MGs). Despite this algorithm being designed based on the general structure of islanded distribution grids, and especially on the structure of the small Italian island benchmark defined in the previous chapter, a sufficiently general formulation has been introduced that can be adopted in grid-connected MGs.

As already discussed in Section 1.5, the energy systems of non-interconnected (small) islands have been managed by allowing only negligible penetration of intermittent Renewable Energy Sources (RES), and all the various initiatives undertaken by the European Commission already discussed in Section 1.5 have both the goal of achieving sustainability and energy transition goals and of protecting islands from risks and fuel scarcity.

However, sometimes, these initiatives seem to neglect the technical issues and obstacles entailed with planning and operation of power systems with high RES penetration. Indeed, the presence of a relevant portion of non-programmable generation capacity in an islanded system requires careful planning [83] to ensure the availability of adequate quantity of operating reserve resources which can counterbalance the power generation uncertainties introduced by stochastic RES like wind and Photovoltaic (PV) [84]. The provision of operating reserve should not be based on the exploitation of conventional fossil fuel generation, since the choice would be in contrast with the same sustainability issues that drive RES penetration. Other flexible resources can be used to ensure operating reserve, such as Demand Response (DR) [9], flexible desalination units [85], biomass-fueled plants [83] or Battery Energy Storage Systems BESSs [6, 83]. Storage systems appear as the

most versatile resource of flexibility. However, due to the capital cost, which limits storage capacity, and to the stochastic nature of RES, the use of storage in operational planning and real-time operation must be supported by proper optimization and control tools [86].

Several studies propose methodologies for the optimal operational planning of energy and storage resources in isolated power systems, considering either geographically isolated systems like small islands and remote power systems, or MGs operating in stand-alone mode. Usually, these methodologies are based on the use of forecasts to find an optimal scheduling of resources that minimizes operative costs and ensures uninterrupted power supply and maximum exploitation of available renewable power [87–91].

However, in order to allow high penetration of non-programmable energy sources in islands (reducing the operating costs) and maintain, at the same time, satisfactory levels of system security and energy efficiency, the assessment of operating reserve must be included in the overall optimal management of system energy resources. With the increase in uncertain renewable resources, in small islands, where generation is mostly provided by conventional diesel-powered generating sets, the available rotating reserve may not be enough to accommodate large net load fluctuations.

The authors in [92] propose an algorithm for minimizing the operating costs of a MG taking into account constraints on operating reserve, without considering the possible errors on load and generation forecast that a small island MG may have, especially if inaccurate forecasting techniques are used. In [87], optimization is obtained using a three-stages approach where short-term forecasting is carried out by means of real-time field measurements and used to update the controlled resources set-points, that adopts forecasts ranging from one day to one month. In the short time optimization, short-term forecasting is carried out by means of real-time field measurements and used to calculates optimal set-points to be sent to the controlled micro-resources. In this approach, however, no minimum reserve margins are taken into account and the control relies on the accuracy of forecasts. The authors in [87] mention a large number of algorithms, which can lead to reliable forecasts. However, even if net load uncertainty can be reduced, some residual discrepancies between actual and forecasted net load will always remain [93]. This is especially true in very small sized systems where net load fluctuations cannot be averaged among several systems nodes [94]. Moreover, as shown in [95], PV generation forecasts can fail in the short-term under specific weather conditions.

In [88, 89], optimal control of competing storage resources in a hybrid isolated system is obtained through optimal predictive control. The impact of forecast error is minimized

through the application of a model predictive control technique that allows to update the optimal control law of all controlled units during actual system operation. A similar control technique is also adopted in [90], where upward spinning reserve constraints to deal with real-time power fluctuations are introduced. Spinning reserve constraints are deterministically sized according to a fixed percentage of PV generation and load.

The study conducted in this chapter aimed to explore how different methods for the evaluation of operating reserve affect the performance of the proposed control methodology, in the presence of different levels of RES penetration.

2.1 Operational planning algorithm

The proposed operational planning algorithm is based on a predictive optimal dispatch control scheme, depicted in Fig. 2.1. In that scheme, optimal day-ahead operational scheduling is obtained through the solution of a predictive control based on load and RES generation forecasts. As shown in Fig. 2.1, at the i-th time-step, a discrete optimal control algorithm minimizes operating costs, while satisfying technical limits and guaranteeing both Upward Operating Reserve (UOR) and Downward Operating Reserve (DOR), quantified through the procedure described in the previous section, for the remaining time-steps of the day (i.e. the time window $[t_i, t_{24 \cdot n}]$). Being n the number of time-steps in one hour, Δt is assumed to be the duration of each time-step. The optimal set-points are fed to the field. However, since real-time behavior could differ from expectations, the proposed operational planning algorithm relies on the use of an iterative *closed-loop* predictive control routine that permits to update the optimal set-points on an hourly base.

As in Fig. 2.1, the optimal set-points calculated through the predictive optimal dispatch are updated on an hourly basis to compensate the difference between the forecasted and the actual response of the system. In the tests, the response of the system during the n time-steps in an hour (time windows $[t_i, t_{i+n}]$) is simulated through the solution of a "greedy" optimization algorithm. A "greedy" algorithm, as defined by [96], is an algorithm that always takes the best immediate, or local, solution while finding an answer. During operation, the "greedy" control logic has been programmed to mimic the common control logic of the main island resources. At the same time, it aims to minimize deviations from the optimal set points defined by the operational planning algorithm while ensuring energy balance, even in the presence of unexpected fluctuations. In a system where also storage is present, these fluctuations will be mainly compensated by it, generating a mismatch

between the expected State of Charge (SoC) trajectory and the real one. SoC is therefore a relevant input to be fed back to the optimal control routine to update the control law set-points.

For the purpose of showing the effectiveness of the proposed Closed-Loop Routine (CLR), results can be compared to an Open-Loop Routine (OLR). This approach adopts the same formulation for calculating the optimal daily reserve dispatch, but it differs from the first one because the optimal control problem is solved only at the beginning of each day, without intra-day updates of the control law [89].

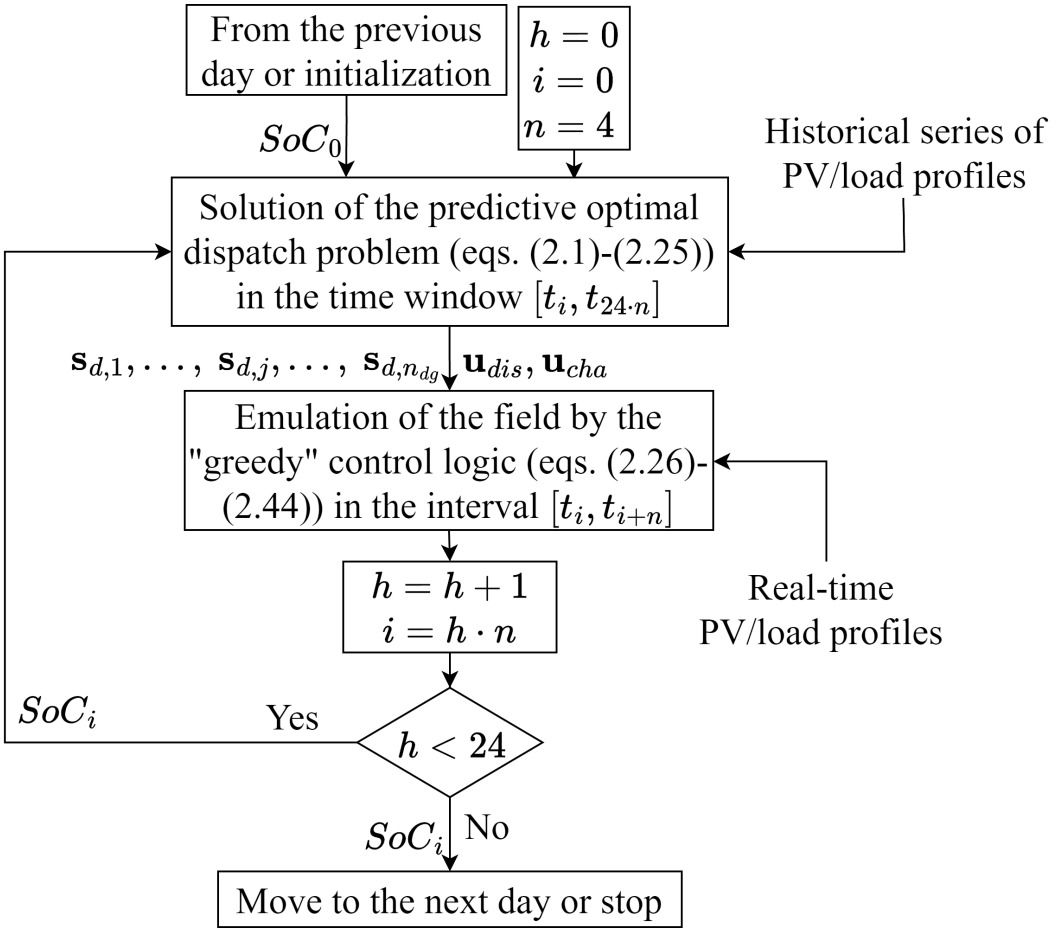


Figure 2.1: Proposed closed-loop optimization routine

2.1.1 Formulation of the predictive optimal dispatch problem

For each hour of the day ($\forall h = 0, 1, ..., 23$), the discretized optimal control algorithm can be formulated as a Mixed-Integer Quadratic Programming (MIQP) problem:

$$\min_{\boldsymbol{u},\boldsymbol{s}} \sum_{i=h\cdot n}^{24\cdot n-1} f_i(\boldsymbol{u}_i,\boldsymbol{s}_i,\boldsymbol{p}_i) \tag{2.1}$$

subject to equality and inequality constraints

$$\boldsymbol{g}_i(\boldsymbol{u}_i,\boldsymbol{p}_i) = 0; \tag{2.2}$$

$$\boldsymbol{h}_i(\boldsymbol{u}_i,\boldsymbol{s}_i,\boldsymbol{p}_i) \leq 0 \tag{2.3}$$

where, for each i-th time-step in the optimization time window $T = [t_{h\cdot n}, t_{24\cdot n}]$, $\boldsymbol{u}_i$ collects the value of all the control variables (i.e. the power output of all dispatchable resources); $\boldsymbol{p}_i$ contains the input forecasted profiles (i.e. load demand and RES production); $\boldsymbol{s}_i$ collects all the integer control variables used to handle with all the discontinuities in the system formulation. All power related variables are considered expressed in kW.

The set of continuous and integer control variables has been chosen considering a reasonable structure of isolated electrical distribution grids, which might include n_{dg} thermal units, distributed energy resources, and a Battery Energy Storage System (BESS). Thus, for each i-th time interval in the time window T, the set of continuous control variables is given by the vector:

$$\begin{aligned}\boldsymbol{u}_i = \Big[& u^i_{d,1}, ..., u^i_{d,j}, ..., u^i_{d,n_{dg}}, u^i_{dis}, u^i_{cha}, \\ & u^i_{dwn,na}, u^i_{up,na}, u^i_{slack}\Big]\end{aligned} \tag{2.4}$$

where $u^i_{d,j}$ is the generated power by the j-th thermal unit; u^i_{dis}, u^i_{cha} represent the BESS discharging and charging power, respectively; $u^i_{dwn,na}$ is the missing DOR; $u^i_{up,na}$ is the missing UOR; u^i_{slack} represents a slack variable that allows to reach a feasible solution even in the case of system inadequacy, as discussed in [5].

Integer control variables are used to represent elements that introduce discontinuities in the formulation of the objective function or constraints. In this problem, the integer variables for each i-th time-step in the time window T are:

$$\boldsymbol{s}_i = \left[s^i_{d,1}, ..., s^i_{d,j}, ... s^i_{d,n_{dg}}, s^i_{cha} \right] \tag{2.5}$$

where $s^i_{d,j}$ is 1 if the j-th thermal group is on, 0 when off; s^i_{cha} is 1 if the BESS is charging, 0 if discharging.

Finally, the non-dispatchable power inputs for each i-th time interval in T are:

$$\boldsymbol{p}_i = \left[p_L^i, p_{RES}^i\right] \tag{2.6}$$

where p_L^i is the forecasted total load power demand; p_{RES}^i is the forecasted total power generation by RES.

The Open-Loop Routine (OLR) used just for comparison in test results can be formulated similarly: the problem is solved only for $h = 0$, and the resulting optimal control law is applied to the entire day without any update.

2.1.1.1 Objective function

In the proposed optimal control problem, the energy resources are dispatched in order to minimize the overall management cost. The objective function is formulated as

$$\min_{\boldsymbol{u},\boldsymbol{s}} \sum_{i=h\cdot n}^{24\cdot n-1} \left(c_{dg}^i(\boldsymbol{u}_i,\boldsymbol{s}_i) + c_{bess}^i(\boldsymbol{u}_i) + c_{res,na}^i(\boldsymbol{u}_i) + c_{slack}^i(\boldsymbol{u}_i) \right) \tag{2.7}$$

where $c_{dg}^i(\boldsymbol{u}_i,\boldsymbol{s}_i)$, $c_{bess}^i(\boldsymbol{u}_i)$, $c_{res,na}^i(\boldsymbol{u}_i)$, $c_{slack}^i(\boldsymbol{u}_i)$ represent the costs related to thermal units, BESS, missing operating reserve, and the use of the slack variable.

The diesel generation cost for each time-step is given by the sum of the two contributes in (2.8). The first term associates a fixed cost λ (€) to the state variation and represents the cost of turning on and off a single generation unit. The second term expresses the diesel consumption as a quadratic function of the production level through the coefficients α_{dg}, β_{dg} and γ_{dg}. It is quantified in euro considering the diesel unit cost c_{dies} (€/l).

$$\begin{aligned} c_{dg}^i = {} & \lambda \cdot \sum_{j=1}^{n_{dg}} \left| s_{d,j}^i - s_{d,j}^{i-1} \right| + \\ & + \Delta t \cdot c_{dies} \cdot \sum_{j=1}^{n_{dg}} \left(\alpha_{dg} \cdot {u_{d,j}^i}^2 + \beta_{dg} \cdot u_{d,j}^i + \gamma_{dg} \cdot s_{d,j}^i \right) \end{aligned} \tag{2.8}$$

The BESS cost function appearing in (2.7) refers to wear cost, which is associated to the discharge phase only in the proposed model. In particular, the unit wear cost α_{bess} (€/kWh) is simply formulated as the ratio between the substitution cost of the battery and the energy throughput as proposed in [88].

$$c^i_{bess} = \alpha_{bess} \cdot u^i_{dis} \cdot \Delta t \tag{2.9}$$

Since lack of UOR might involve unsupplied loads, while lack of DOR might require RES production to be curtailed, the costs due to missing UOR and DOR in (2.7) have been assumed to depend on the unit cost of not served load β (€/kWh) and RES power curtailment γ (€/kWh), respectively.

$$c^i_{res,na} = \left(\beta \cdot u^i_{up,na} + \gamma \cdot u^i_{dwn,na}\right) \cdot \Delta t \tag{2.10}$$

As already mentioned, a slack variable has also been introduced so that the solver is always able to find a solution even if there are not enough forecasted resources to satisfy the energy balance. The cost function (2.11) adopts a suitably large weight M (€/kWh) to minimize the possible use of the slack variable.

$$c^i_{slack} = M \cdot u^i_{slack} \cdot \Delta t \tag{2.11}$$

2.1.1.2 Energy balance

The main equality constraint for each i-th time-step is given by the energy balance that, having assumed the injected power as positive, can be written as:

$$\sum_{j=1}^{n_{dg}} u^i_{d,j} + p^i_{RES} + u^i_{dis} - p^i_L - u^i_{cha} + u^i_{slack} = 0 \tag{2.12}$$

Note that the amount of power in the slack variable represents only a hypothetical corrective action, such as load shedding or generation curtailment, that might occur during real-time operation. These actions, therefore, are neglected in the operational planning problem. During the simulation of real-time operation, on the other hand, these corrective actions can actually be applied to ensure the power balance.

2.1.1.3 Diesel generators

At each i-th time-step, for each thermal unit, eq. (2.13) limits the power output between the minimum P^{min}_{dg} and the maximum P^{max}_{dg} power capability. eq. (2.14) defines a priority order among the diesel units for the turning on phase.

$$P^{min}_{dg} \cdot s^i_{d,j} \leq u^i_{d,j} \leq P^{max}_{dg} \cdot s^i_{d,j} \qquad \forall j = 1, ..., n_{dg} \tag{2.13}$$

$$s^i_{d,n_{dg}} \leq ... \leq s^i_{d,j} \leq ... \leq s^i_{d,1} \tag{2.14}$$

2.1.1.4 Battery energy storage system

BESS charging and discharging are modelled through

$$q^i_b(\boldsymbol{u}) = q^{h\cdot n}_b + \sum_{k=h\cdot n}^{i-1} \left(\frac{\eta_{cha} \cdot u^k_{cha}}{100} - \frac{u^k_{dis}}{\eta_{dis}} \cdot 100 \right) \cdot \Delta t \tag{2.15}$$

where $q^{n\cdot h}_b$ (kWh) is the energy stored at the beginning of the optimization time window T, q^i_b (kWh) is the stored energy at the beginning of the i-th time-step, η_{cha} (%) and η_{dis} (%) are respectively the charge and discharge efficiency. An additional equality constraint is also added to ensure that half of Q_n (kWh), that is the BESS rated capacity, is available at the beginning of the following day:

$$q^{24\cdot n}_b - \frac{Q_n}{2} = 0 \tag{2.16}$$

Inequality constraints are also included to take into account maximum charging and discharging power, and minimum and maximum capacity:

$$0 \leq u^i_{cha} \leq P^{max}_{bess} \cdot s^i_{cha} \tag{2.17}$$

$$0 \leq u^i_{dis} \leq P^{max}_{bess} \cdot \left(1 - s^i_{cha}\right) \tag{2.18}$$

$$Q_{b,min} \leq q^i_b(\boldsymbol{u}) \leq Q_{b,max} \tag{2.19}$$

with

$$Q_{b,min} = \frac{SoC_{min} \cdot Q_n}{100} \ , \ Q_{b,max} = \frac{SoC_{max} \cdot Q_n}{100} \tag{2.20}$$

and where P^{max}_{bess} is the BESS rated power, $Q_{b,min}$ (kWh) and $Q_{b,max}$ (kWh) are respectively the minimum and the maximum storable energy, corresponding to minimum, SoC_{min} (%), and maximum, SoC_{max} (%), SoC conditions.

2.1.1.5 Reserve requirements

Equations (2.21) and (2.22) represent the constraints on UOR and DOR, respectively. At each i-th time-step, the sum of available and missing reserve must be greater than the reserve requirements, $r^i_{up,min}$ and $r^i_{dwn,min}$, calculated through the procedures described in Section 2.2.

$$r^i_{up,a} + u^i_{up,na} \geq r^i_{up,min} \tag{2.21}$$

$$r^i_{dwn,a} + u^i_{dwn,na} \geq r^i_{dwn,min} \tag{2.22}$$

According to (2.23) and (2.24), for each i-th time-step, the available UOR $r^i_{up,a}$ and DOR $r^i_{dwn,a}$ are related to the operating point of the diesel groups:

$$r^i_{up,a} = \sum_{j=1}^{n_{dg}} \left(P^{max}_{dg} \cdot s^i_{d,j} - u^i_{d,j} \right) \tag{2.23}$$

$$r^i_{dwn,a} = \sum_{j=1}^{n_{dg}} \left(u^i_{d,j} - P^{min}_{dg} \cdot s^i_{d,j} \right) \tag{2.24}$$

Constraints in (2.25) limit missing operating reserve in each i-th time interval to be non-negative.

$$0 \leq u^i_{up,na};\ 0 \leq u^i_{dwn,na} \tag{2.25}$$

2.1.2 Formulation of the "greedy" control logic

As in Fig. 2.1, the optimal set-points calculated through the predictive optimal dispatch are updated on hourly basis to compensate the difference between the forecasted and the actual response of the system. In the tests, the response of the system during the n time-steps in an hour is simulated through the solution of a "greedy" optimization algorithm that aims to guarantee energy balance despite unexpected power fluctuations. For the sake of simplicity, no further cost optimization is performed at this stage and the state of each j-th diesel unit ($s^i_{d,j}$) is considered constant. Simultaneously, the algorithm aims to minimize the mismatch from the optimal BESS charging u^i_{cha} and discharging u^i_{dis} set-points defined by the optimal dispatch algorithm.

Therefore, for each time-step in the interval $[t_i, t_{i+n}]$, the "greedy" optimization algorithm is formulated as a Mixed-Integer Linear Programming (MILP) problem:

$$\min_{\boldsymbol{u},s} f(\boldsymbol{u},s) \tag{2.26}$$

subject to

$$\boldsymbol{g}(\overline{\boldsymbol{u}},\overline{\boldsymbol{s}},\boldsymbol{u},\boldsymbol{p}) = 0; \qquad \boldsymbol{h}(\overline{\boldsymbol{u}},\overline{\boldsymbol{s}},\boldsymbol{u},s,\boldsymbol{p}) \leq 0 \tag{2.27}$$

where $\overline{\boldsymbol{u}}$ collects the optimal set-points defined by the predictive algorithm (i.e. charge or discharge power of the BESS); $\overline{\boldsymbol{s}}$ contains the status of dispatchable units fixed by the predictive algorithm (i.e. the status of the diesel units); $\boldsymbol{u}$ collects all real-time control variables (i.e. the power output of dispatchable resources); s represents the real-time state of the BESS (1 for charge and 0 for discharge); $\boldsymbol{p}$ contains the input real-time profiles (i.e. load demand and RES production).

In this problem, the continuous and integer control variables, defined by the solution of the optimal dispatch problem, are used as fixed set-points for the interval $[t_i, t_{i+n}]$:

$$\overline{\boldsymbol{u}} = [\overline{u}_{dis}, \overline{u}_{cha}]\,;\; \overline{\boldsymbol{s}} = \left[\overline{s}_{d,1}, ..., \overline{s}_{d,j}, ...\overline{s}_{d,n_{dg}}\right] \tag{2.28}$$

where $\overline{u}_{dis}$ and $\overline{u}_{cha}$ are the BESS discharging and charging power set-points, respectively; $\overline{s}_{d,1}, ..., \overline{s}_{d,j}, ...\overline{s}_{d,n_{dg}}$ are the defined status (1 if on, 0 when off) of each diesel unit in the thermal plant.

The actual variables in the real-time problem are given by the integer variable s, just defined and representing the state of the BESS, and by the continuous variables $\boldsymbol{u}$:

$$\begin{aligned}\boldsymbol{u} = \Big[&u_{d,1}, ..., u_{d,j}, ..., u_{d,n_{dg}},\\ &u_{dis}, u_{cha}, u_{RES,curt}, u_{L,shed}\Big]\end{aligned} \tag{2.29}$$

where $u_{d,j}$ is the generated power by the j-th diesel group; u_{dis}, u_{cha} represent the BESS discharging and charging power, respectively; $u_{RES,curt}$ is the curtailed RES production; $u_{L,shed}$ is the electrical load shedding.

Non-varying parameters for each time-step represent real-time system behaviour:

$$\boldsymbol{p} = [p_{L,rt}, p_{RES,rt}] \tag{2.30}$$

where $p_{L,rt}$ is the actual total power demand; $p_{RES,rt}$ is the actual total RES production.

2.1.2.1 Objective function

The real-time management of the available resources aims to guarantee energy balance while minimizing the mismatch from the optimal set-points $\overline{\boldsymbol{u}}$. Thus, the objective function is formulated as

$$\min_{\boldsymbol{u},s} \left[c_{shed}(\boldsymbol{u}) + c_{\Delta b}(\overline{\boldsymbol{u}}, \boldsymbol{u}, s)\right] \cdot \Delta t \tag{2.31}$$

where c_{shed} and $c_{\Delta b}$ are penalty functions related to corrective actions and mismatches from BESS optimal set-points, respectively. The first term in (2.31) depends on load shedding and RES curtailment and it is weighted by a suitably large factor M_{rt}, so that emergency actions are enforced only in the presence of severe adequacy violations:

$$c_{shed} = M_{rt} \cdot \left(u_{L,shed} + u_{RES,curt}\right) \tag{2.32}$$

The second term in (2.31) allows to minimize variations in the use of BESS:

$$c_{\Delta b} = |\Delta u_{cha}| + |\Delta u_{dis}| \tag{2.33}$$

The variation from the scheduled charging and discharging power are called Δu_{cha} and Δu_{dis}, respectively, and are defined as:

$$\Delta u_{cha} = u_{cha} - s \cdot (\overline{u}_{cha} - \overline{u}_{dis}) \tag{2.34}$$

$$\Delta u_{dis} = u_{dis} - (1 - s) \cdot (\overline{u}_{dis} - \overline{u}_{cha}) \tag{2.35}$$

2.1.2.2 Energy balance

The greedy algorithm mainly guarantees energy balance through the constraint:

$$\begin{aligned} \sum_{j=1}^{n_{dg}} u_{d,j} + u_{dis} + (p_{RES,rt} - u_{RES,curt}) = \\ = u_{cha} + \left(p_{L,rt} - u_{L,shed}\right) \end{aligned} \tag{2.36}$$

2.1.2.3 Diesel generators

For each j-th activated thermal unit ($\bar{s}_{d,j} = 1$), eq. (2.37) limits the power output between P_{dg}^{min} and P_{dg}^{max} power capabilities. Eq. (2.38) forces the diesel groups to produce the same power.

$$P_{dg}^{min} \cdot \bar{s}_{d,j} \leq u_{d,j} \leq P_{dg}^{max} \cdot \bar{s}_{d,j} \qquad \forall j = 1, ..., n_{dg} \tag{2.37}$$

$$\bar{s}_{d,j} \cdot \left(u_{d,j} - u_{d,j-1}\right) = 0 \qquad \forall j = 2, ..., n_{dg} \tag{2.38}$$

2.1.2.4 Battery energy storage system

BESS charging and discharging are modelled through

$$q_b^{new}(\boldsymbol{u}) = q_b^{old} + \left(\frac{\eta_{cha} \cdot u_{cha}}{100} - \frac{u_{dis}}{\eta_{dis}} \cdot 100\right) \cdot \Delta t \tag{2.39}$$

where q_b^{new} and q_b^{old} (kWh) are the energy stored at the end and beginning of the time-step, respectively.

Technical limits of the energy storage have been considered through the following inequality constraints:

$$0 \leq u_{cha} \leq s \cdot P_{bess}^{max} \tag{2.40}$$

$$0 \leq u_{dis} \leq (1 - s) \cdot P_{bess}^{max} \tag{2.41}$$

$$Q_{b,min} \leq q_b^{new}(\boldsymbol{u}) \leq Q_{b,max} \tag{2.42}$$

2.1.2.5 Corrective actions

Further constraints, with eq. (2.43) and eq. (2.44) limit the load shedding and RES curtailment to the actual load demand and RES production, respectively:

$$0 \leq u_{L,shed} \leq p_{L,rt} \tag{2.43}$$

$$0 \leq u_{RES,curt} \leq p_{RES,rt} \tag{2.44}$$

2.2 Reserve evaluation methods for non-synchronous power systems

As discussed in Section 1.5.2, there are various methods to assess the operating reserve required during the operation of islanded distribution systems. Most of these methods use forecasting and historical data to evaluate the amount of both Upward Operating Reserve (UOR) and Downward Operating Reserve (DOR). However, as in this case, historical data availability is often limited, relying on hourly or, at most, fifteen-minute average measurements. For the conducted studies, in fact, we referred to data provided by the distributor concerning the reference small Italian island presented in Section 1.5.1.

Based on the available data, two different operating reserve valuation methods were considered and compared in this study:

- Method A, based on the use of absolute net-load forecasting errors and two separate cumulative curves for downward and upward reserve (as in [5]);
- Method B, based on the use of absolute net-load forecasting errors and a single cumulative curve (as in [78]).

These methods have been compared with different approaches, settings, and in relation to the increasing penetration level of RES generation.

The available time series contain one year of 30-minute average load measurement (for the year 2019) and one year of 15-minute average load measurement (for the year 2021). Since PV/RES data are not known, historical series were extracted from [97] for the two years under observation (since the data for the year 2021 are not available in [97], the 2020 data were used, as already anticipated in Section 1.5.1). The data from the first entire year of operation will be used to quantify UOR and UOR, according to the methods just defined. The data collected in the second year will be used to evaluate the actual response of the proposed control methodology over an entire year of system operation.

2.2.1 Method *A*

This is the method previously proposed by the authors in [5]. It employs historical time series to compare net-load measurements with forecasted ones. A simple naïve forecast method was assumed. In day-ahead scheduling, at each i-th time interval, cumulative

curves are built considering the forecasting error done at time-steps in a close interval (i.e. from i-2 to i+2), in all previous days of the same month.

The forecast error data set is used to build two different cumulative curves for each time-step, one for negative and one for positive errors. Having defined a confidence interval, the cumulative curves are used to quantify UOR and UOR. Considering separately positive and negative errors allows to obtain conservative estimations and suitable amounts of both UOR and UOR with any confidence interval. The example in Fig. 2.2 (up) shows how UOR is quantified at 12:00 of a generic summer day, using different confidence interval. The upper-right graph shows the difference between the maximum observed error and the selected reserve. In the same figure, an analogous approach is used to quantify the DOR needs (down).

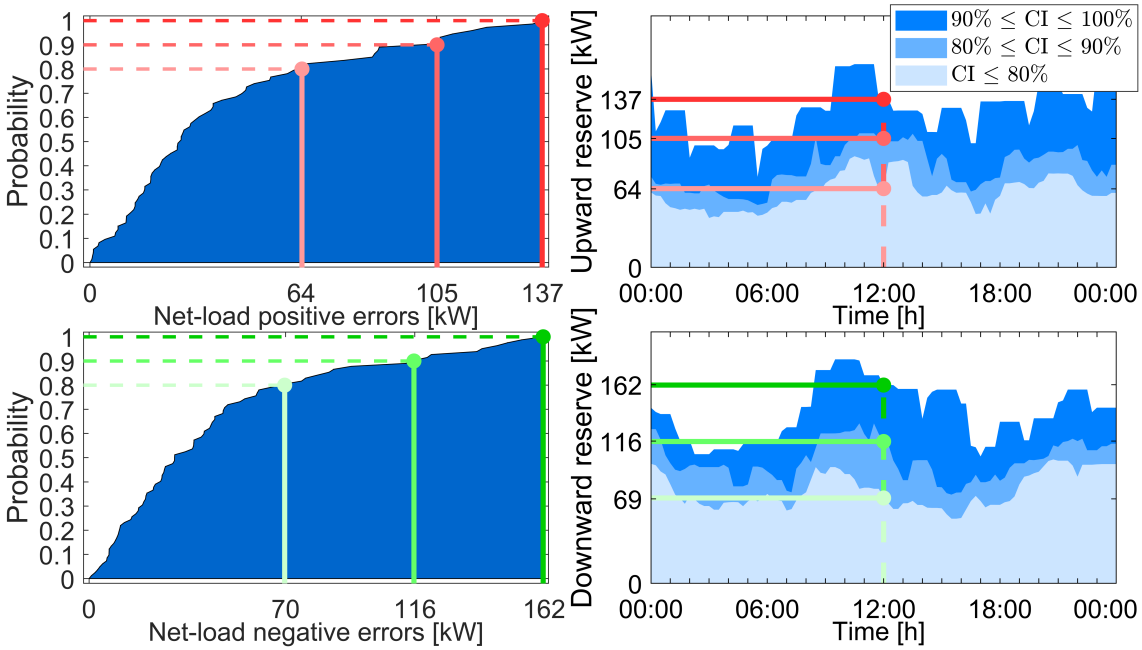


Figure 2.2: Method A. On the left: Cumulative curves of net-load positive (up) and negative (down) forecast errors; on the right: daily estimation of upward (up) and downward (down) operating reserve

2.2.2 Method *B*

This method, differently from the previous one, aggregates positive and negative forecasting errors in a single cumulative curve. As before, the cumulative curve at the i-th time-step is built considering the errors in the interval $[i\text{-}2, i\text{+}2]$, in all previous days of the same month.

Fig. 2.3 shows how UOR and UOR are quantified at 12:00 of a generic summer day,

using different confidence intervals. Having chosen for example a 90% confidence interval, the UOR is equal to the corresponding value in the cumulative distribution function. Analogously, DOR is given by the value corresponding to 10%. By comparing Fig. 2.3 and Fig. 2.2, it is clear how, adopting the same confidence interval, Method B will always be less conservative than Method A. A 100% confidence will generate the same results with both methods.

Since errors aggregated in the cumulative function are either positive or negative, Method B might fail in quantifying suitable amounts of reserve at all time intervals. For example, if RES forecast errors are predominant, the cumulative curve can result shifted towards the positive semi-axis. In this case the downward operating reserve can result largely underestimated or even null.

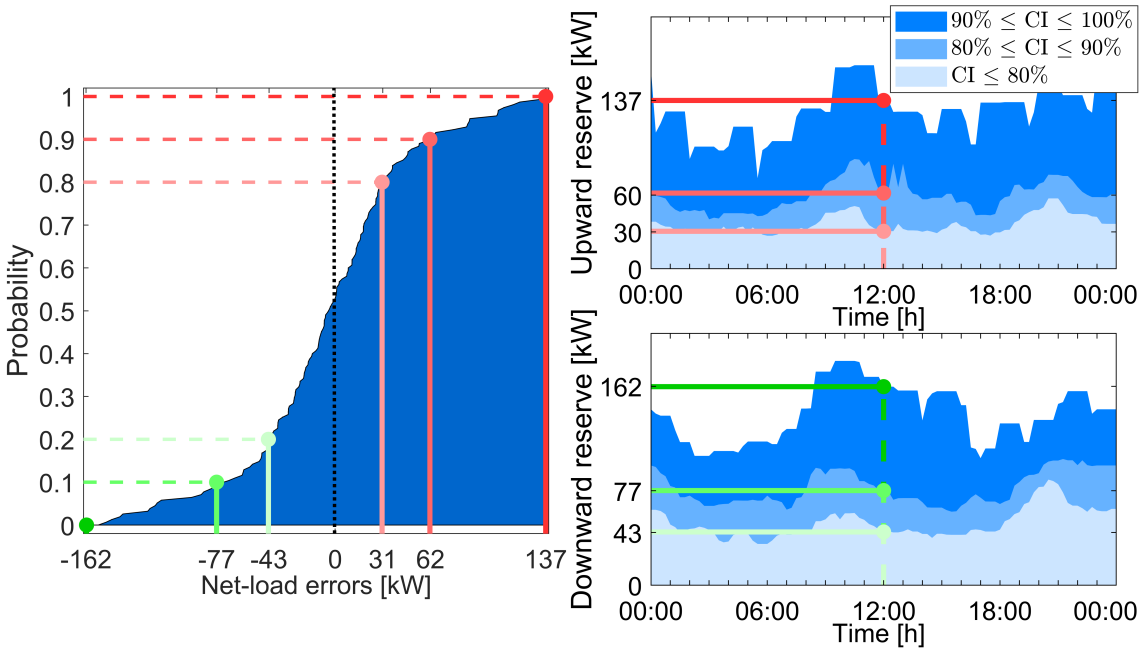


Figure 2.3: Method B. On the left: Cumulative curve of net-load forecast errors; on the right: daily estimation of upward (up) and downward (down) operating reserve

2.3 Testing the algorithm on a real case study

The predictive optimal dispatch algorithm described in Section 2.1 was applied to a single bus system that represents a simplified structure of the reference small Italian island discussed in Section 1.5.1. A representation of the network under investigation is shown in Fig. 2.4. As depicted in the figure, unlike the current state of the island described in

Section 1.5.1, to make the grid suitable for these studies, the inclusion of a PV system and a BESS plant was assumed.

It is recalled that the distribution network of the island is composed by 5-buses. Each bus supplies end-users through a MV/LV substation, whereas the whole island is powered by a Main Power Plant (MPP) composed by four 480 kW diesel units, with no technical minimum. From the load consumption data available, the total peak load is about 1.2 MW. The peak is reached in summer since the loads are strongly dependent on the tourist season. During summer months, indeed, the total load demand can reach 3 times the value of the winter months.

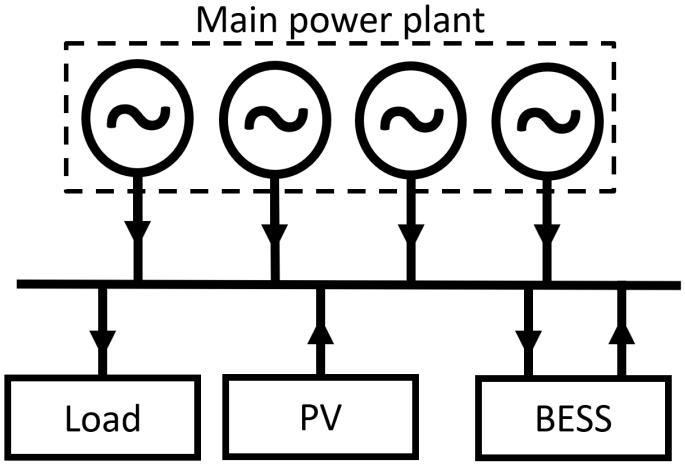


Figure 2.4: Single-bus representation of the reference small Italian island distribution network under investigation

In the following, test results obtained by the proposed methodologies are compared, considering different PV penetrations and different methods for operating reserve assessment. For the sake of simplicity, an equivalent PV unit was considered. Please note that wind generation can be neglected because of the environmental protection rules enforced in most Italian small islands.

The following assumptions were made. Since load measurements were recorded with a 15-minutes time resolution, n has been assumed equal to 4. Hence, the algorithm generates a control law with a 15 minutes resolution ($\Delta t = 0.25$). The cost factors α_{dg}, β_{dg} and γ_{dg} in (2.8) were calculated assuming a specific consumption of 0.202 kg/kWh at 100%, 0.203 kg/kWh at 75% and 0.210 kg/kWh at 50% of rated power. The assumed diesel cost was 1.055 €/l (as given in [98]) and a state variation cost equal to 7.50 €was considered.

Flexibility resources are ensured by a 250/500 kW/kWh BESS. A $\mathrm{SoC}_{\min}$ of 10% and a $\mathrm{SoC}_{\max}$ of 90%, a total number of 3000 life-cycles, a charging/discharging efficiency

of 90% and a substitution cost of about 250.00 €/kWh have been assumed. Under these assumptions, the wear cost α_{bess} is equal to 0.1042 €/kWh.

Interruption costs for loads and PV production have been set to 20.00 €/kWh and 0.27 €/kWh, respectively. Load shedding cost was estimated considering the value of lost load in [99], whereas generation curtailment was assumed equal to the incentive given to PV producers in small Italian islands [98].

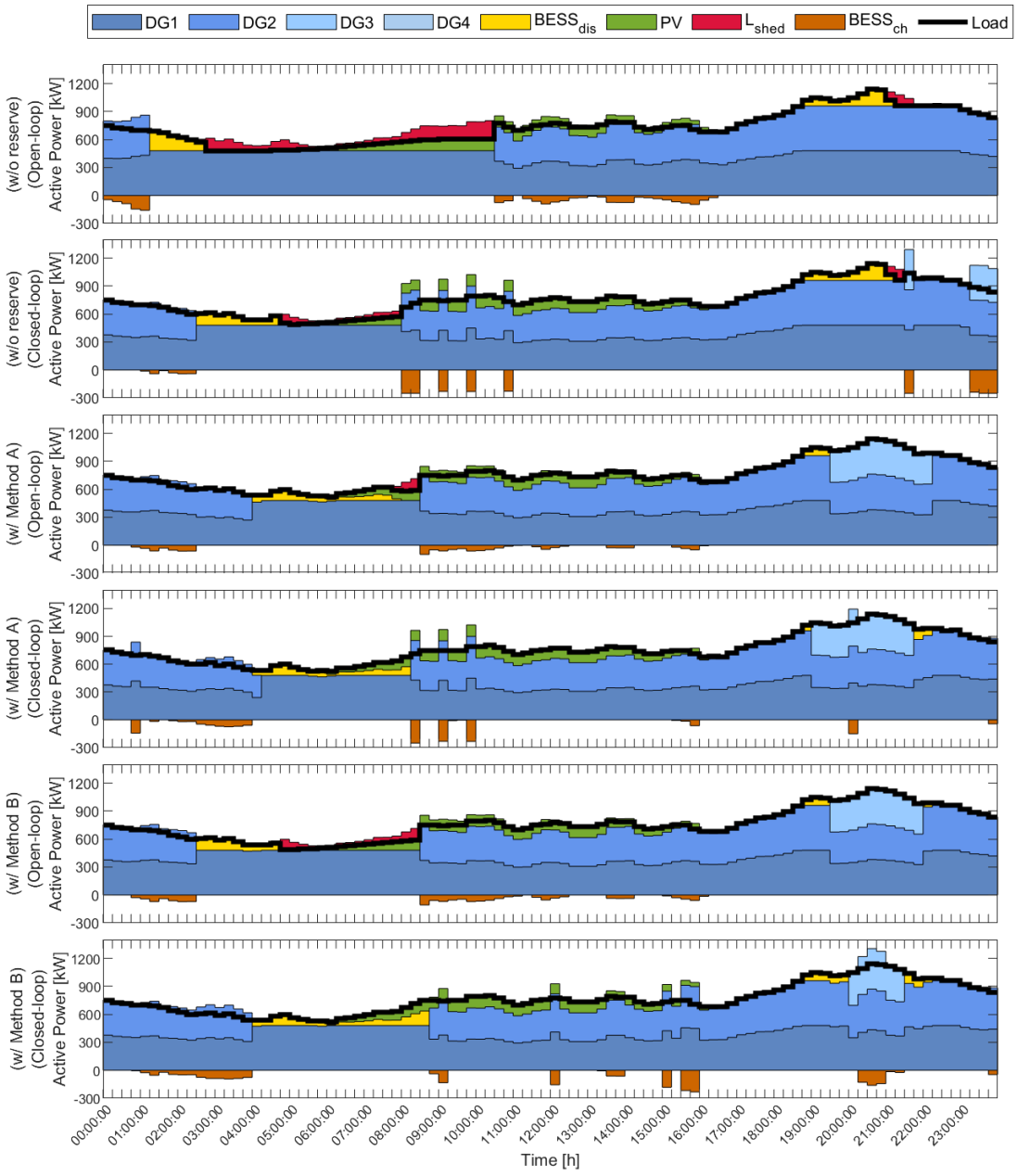


Figure 2.5: Comparison between different control methodologies on August 8 - Active power

A preliminary test has been carried out considering 200 kWp of PV penetration and a

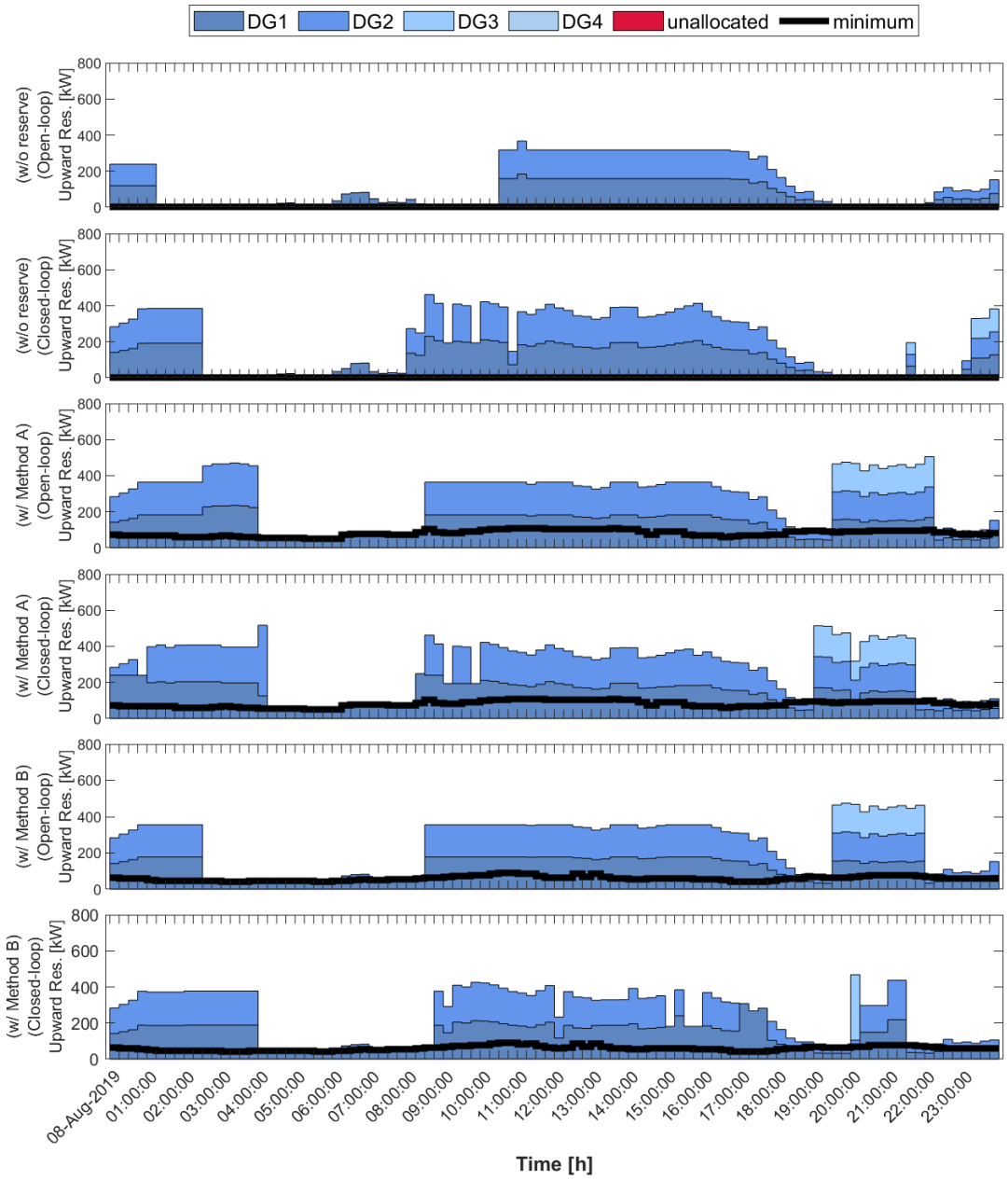


Figure 2.6: Comparison between different control methodologies on August 8 - Planned upward operating reserve

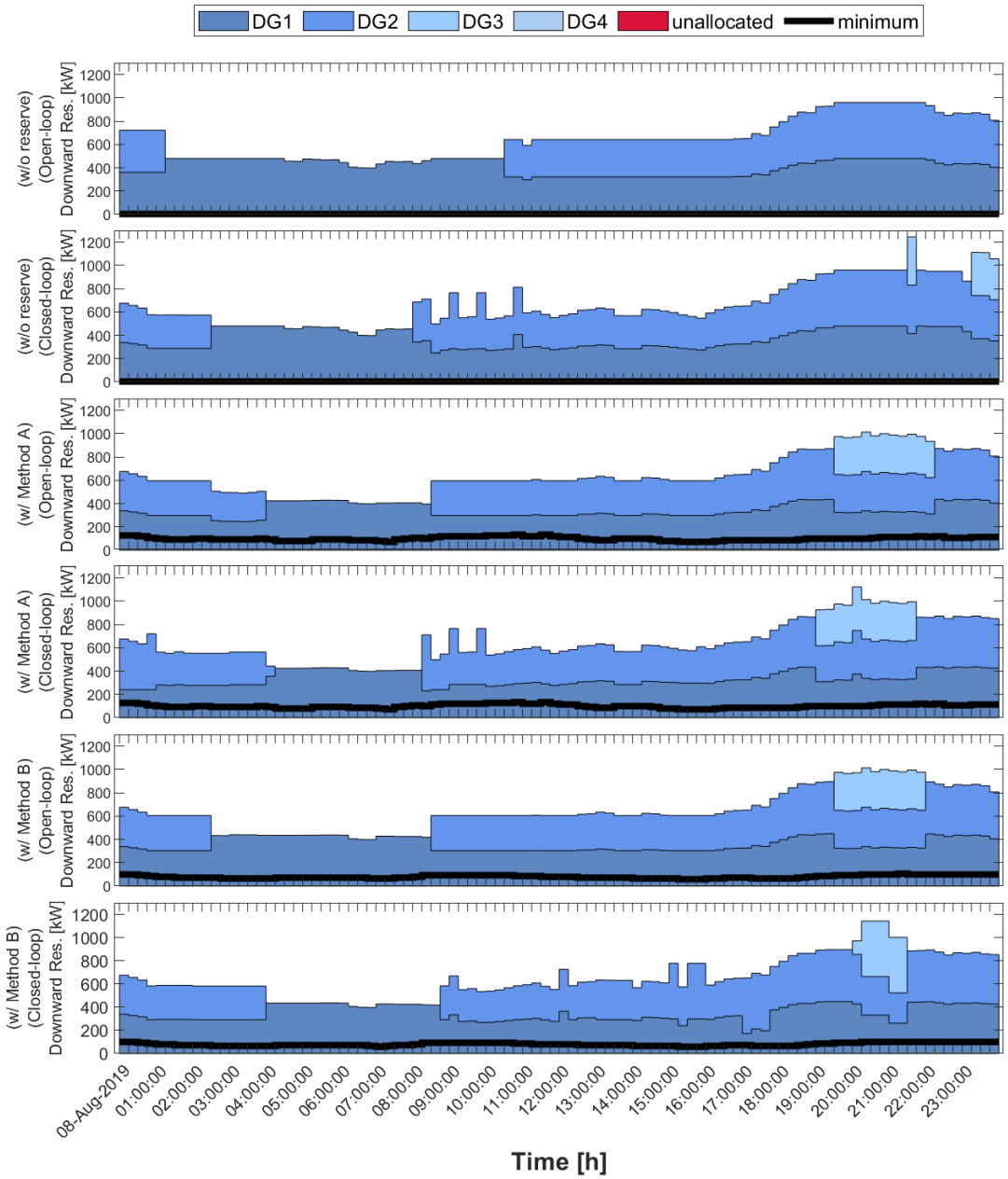


Figure 2.7: Comparison between different control methodologies on August 8 - Planned Downward operating reserve

90% confidence interval for reserve estimation. Fig. 2.5 shows the results obtained in a significant day in August. Reserve requirements in that day are the ones shown in Fig. 2.2 and Fig. 2.3 for a 90% confidence interval. The day is characterized by unforeseen shortage of PV generation.

When no reserve is considered and an Open-Loop Routine (OLR) is followed (first plot), the forecast error causes significant load shedding due to the unavailability of more than one diesel generator. This scheduling error can be soon solved if a Closed-Loop Routine (CLR) is used (second plot). In general, by comparing OLR and CLR there is evidence of the higher effectiveness of CLR with respect to OLR. The intra-day adjustments permit, in fact, not only to correct the number of scheduled diesel generators, but also to better exploit storage resources.

Finally, it can be observed that a more conservative estimation of reserve (third plot, Method *A*) allows to mitigate load shedding actions when an OLR is followed. Similar deductions are drawn in the following subsections where annual test results are obtained considering increasing PV penetration and different confidence intervals.

In Fig. 2.6, graphs illustrate the profiles of the UOR allocated during the planning phase for the various methodologies examined on August 8. It is evident that the algorithm consistently adhered to the operating reserve constraints (dark line), ensuring that there was never a deficiency in UOR. However, the allocated reserve did not always prove sufficient to prevent load shedding in cases where a OLR was adopted (refer to the third and fifth graphs in Figure 2.6). At the beginning of the day, the load level was significantly higher than expected and the algorithm was unable to adjust its decisions, unlike the CLR case. For completeness, the DOR allocated is also presented in Fig. 2.7.

2.3.1 Influence of PV penetration

Four different case studies with increasing penetration of installed PV were assumed:

1. no PV, in order to consider only load uncertainty;
2. 100 kWp PV capacity, which is about the current installed power;
3. 200 kWp PV capacity, roughly equal to the RES penetration target at year 2020 set by the Italian Ministry of Economic Development [73];
4. 500 kWp PV capacity, target at year 2030 [73].

Table 2.1: Annual operating costs for different PV penetration levels (€)

		w/o reserve		Method *A*		Method *B*	
		Closed-loop	Open-loop	Closed-loop	Open-loop	Closed-loop	Open-loop
0 kWp	on/off DGs	2003	1613	1628	1688	1658	1673
	DG Prod.	826307	822632	830369	828804	829323	827875
	BESS usage	1963	2423	1376	1962	1400	1833
	Load/PV curt.	11272	149481	118	2832	0	11344
	Overall cost	**841545**	**976149**	**833490**	**835285**	**832380**	**842724**
100 kWp	on/off DGs	1988	1523	1733	1613	1733	1553
	DG Prod.	789288	785766	794027	792524	792775	791303
	BESS usage	1948	2498	1597	2135	1654	2070
	Load/PV curt.	17381	150623	273	7404	1167	18921
	Overall cost	**810604**	**940409**	**797630**	**803676**	**797328**	**813847**
200 kWp	on/off DGs	2857	2317	1642	1657	1672	1672
	DG prod.	749707	744973	758755	757358	757097	755470
	BESS usage	3995	3938	4435	5010	3051	3599
	Load/PV curt.	42290	279758	39	7970	260	16347
	Overall cost	**798851**	**1030987**	**764872**	**771996**	**762082**	**777089**
500 kWp	on/off DGs	10222	6307	4432	2257	4387	2302
	DG prod.	630307	620162	665786	664629	663418	662452
	BESS usage	9370	9731	11596	11751	11281	11397
	Load/PV curt.	577115	1064040	16771	21286	15688	30562
	Overall cost	**1227015**	**1700241**	**698586**	**699924**	**694774**	**706714**

In Table 2.1, test results for the four cases are shown. Tests results have been obtained considering an entire year of operation and adopting different approaches in terms of operating reserve provision (no reserve, reserve with Method *A* and Method *B*) and optimal control scheme (CLR vs. OLR). For operating reserve evaluation a 90% confidence interval has been considered since, as shown in the next subsections, it is a value that offers a good comprise in the performances of both OLR and CLR.

As expected, generation costs are lower when operating reserve constraints are neglected, since the dispatch aimed only to satisfy the forecasted net-load at a minimum cost. However, during real-time operation, due to the forecasting errors, the lack of operating reserve resulted in several load and generation curtailment events. If reserve requirements are neglected the installation of PV can ensure a minimization of operating costs only up to a certain capacity (100 kW adopting a OLR and 200 kW adopting a CLR). After that, operating costs increase with the RES penetration due to the adequacy problems. The introduction of operating reserve constraints allows instead to minimize costs, independently from the adopted control approach.

In general, the CLR permitted always to mitigate the impacts of forecasting errors on yearly operating costs, since it allowed to update the system state and optimal trajectories during real-time operation. Nevertheless, it can be noticed that the adoption of CLR was not secure enough if reserve constraints are neglected with relevant level of RES penetration. Indeed, for 200 kWp and 500 kWp of PV penetration, costs of CLR without

reserve were even higher than costs obtained by an OLR schemes including the operating reserve constraints. Conversely, when operating reserve constraints were introduced, the results obtained with the CLR and OLR were very close. Actually, according to results in Table 2.1, CLR appeared to be always a little more efficient than the OLR. In particular, it can be noticed that the first routine resulted in higher generation costs, whereas, the second one led to relevant costs due to load/PV curtailment.

With regard to the methodology adopted in operating reserve quantification, it can be observed that the expected results were very close. However, since OLR does not update set-points throughout the day, such a control scheme performed better when a more conservative method for reserve provision was adopted (Method *A*). On the contrary, a less conservative method (Method *B*) appeared to be preferable when a CLR is adopted. In general, it is evident that the introduction of operating reserve constraints in the formulation is the most critical aspect, independently from the method adopted to estimate them.

2.3.2 Influence of the confidence interval

This section investigates the influence of the confidence interval choice. Test results were obtained by fixing the PV capacity (i.e. 200 kWp which seems to be the capacity that could be easily reached in a next future) and changing the confidence interval used in Methods *A* and *B*.

Table 2.2 shows the costs obtained in one year of operation, adopting confidence intervals in the range 80-100%. Test results confirm the deductions drawn in the previous subsection. In addition, it can be observed that, when a CLR is adopted, a reduction of the confidence interval can help in reducing operating costs. Allocating too much reserve can be, in fact, counterproductive with CLR. However, confidence intervals too small can lead to higher costs even with CLR. On the other hand, with an OLR, the adoption of a higher confidence interval allows to reduce operating costs by increasing the amount of reserve. However, test results show that a 95% confidence interval is probably the most suitable choice for OLR, confirming the recommendations in [81].

Costs obtained with low confidence intervals (CI= 80%) are the lowest only if the more conservative Method *A* is adopted. With larger confidence intervals, Method *A* brings advantages only using an OLR. In the CLR, Method *B* performs better with lower confidence intervals. The choice of method for reserve evaluation is irrelevant at 100%, since the two methods yield the same results, as previously also shown in Fig. 2.2 and Fig. 2.3.

Table 2.2: Annual operating costs with different confidence intervals (€)

		Method *A*		Method *B*	
		Closed-loop	Open-loop	Closed-loop	Open-loop
CI= 100%	on/off DGs	1703	1763	1703	1763
	DG Prod.	763815	762204	763815	762204
	BESS usage	6622	7411	6622	7411
	Load/PV curt.	0	19	0	19
	Overall cost	**772139**	**771397**	**772139**	**771397**
CI= 95%	on/off DGs	1687	1672	2272	1657
	DG Prod.	760327	758855	757678	757552
	BESS usage	5359	6009	5662	5040
	Load/PV curt.	0	3783	525	5523
	Overall cost	**767374**	**770321**	**766138**	**769773**
CI= 90%	on/off DGs	1642	1657	1672	1672
	DG Prod.	758755	757358	757097	755470
	BESS usage	4435	5010	3051	3599
	Load/PV curt.	39	7970	260	16347
	Overall cost	**764872**	**771996**	**762082**	**777089**
CI= 85%	on/off DGs	1612	1657	2182	1642
	DG Prod.	757821	756339	754849	754307
	BESS usage	3658	4267	3360	2966
	Load/PV curt.	30	11196	1073	22467
	Overall cost	**763122**	**773460**	**761465**	**781384**
CI= 80%	on/off DGs	1732	1672	2167	1567
	DG Prod.	756814	755378	754205	753487
	BESS usage	3075	3570	3088	2654
	Load/PV curt.	365	15688	2770	29962
	Overall cost	**761988**	**776309**	**762232**	**787671**

2.4 Inclusion of energy stored by BESSs in operating reserve constraints

The operating reserve available for any kind of resource is closely linked to its capacity, the operating point, and the actual availability of the primary energy source. Unlike diesel-powered generating plants, whose fuel reserve is replenished through long-term planning so that they can be considered as unlimited resources during the short-term operation, the energy reserve stored in a BESS can be rapidly depleted during short-term operation [3]. The operating reserve that a storage system can provide is closely linked not only to its rated power and capacity, but also to its SoC, which varies over time. Since charging or discharging power capacity of BESS is in general not known in advance, the formulation of the proposed daily optimal dispatch control problem discussed in Section 2.2, did not

include storage in the operating reserve constraints. Although the BESS operating reserve was not considered in the operational planning problem, the real-time optimization problem could control the island's BESS to cope with generation shortfalls or excesses and meet the energy balance by trying to avoid load/PV curtailments. Thus, the BESS' operating reserve was always present but considered only as a reserve of last resort.

In this section, a new approach to evaluating the available operating reserve is proposed and compared with the previous one. This new approach is based on the recursivity of the proposed Closed-Loop Routine (CLR), which permits to define with sufficient precision the amount of BESS capacity actually available in the time interval between two successive optimizations. This approach allows to include the reserve capacity of storage systems, without the risk of overestimating their capabilities in the whole controlled time window. If the BESS reserve should ever be depleted because of the results of real-time operation, the Closed-Loop Routine (CLR) will include this condition when updating the control law.

The two approaches to operating reserve assessments which will be compared in this section can be summarized as follows:

- *Approach #1*: it represents the approach discussed in Section 2.2, where the operating reserve constraints are satisfied only by the operating reserve available from diesel generation, and load or generation curtailment.
- *Approach #2*: it represents the approach proposed in this section, where the operating reserve constraints are satisfied taking into account all the resources in Approach #1, plus the operating reserve available from the BESS.

In the *Approach #1*, the overall upward and downward operating reserves were the sum of two contributions: the first related to the operating point of the diesel units, eqs. (2.23) and (2.24), and the second related to the operating reserve that has not been allocated. In *Approach #2*, however, the overall upward and downward operating reserves also depend on a third contribution, which depends on the energy stored in the BESS.

The operating reserve constraints of *Approach #1*, eqs. (2.21) and (2.22), in the *Approach #2* are formulated including BESS capacity terms $r^i_{b,up}$ and $r^i_{b,down}$.

$$r^i_{dg,up} + r^i_{b,up} + u^i_{l,shed} \geq r^i_{up,min} \tag{2.45}$$

$$r^i_{dg,down} + r^i_{b,down} + u^i_{res,curt} \geq r^i_{down,min} \tag{2.46}$$

with (2.45), (2.46), and

$$r^i_{b,up} = \max\left\{0, P^i_{up}\right\} \tag{2.47}$$

$$r^i_{b,down} = \max\left\{0, P^i_{down}\right\} \tag{2.48}$$

$$P^i_{up} = \min\left\{P^{max}_{bess}, \frac{q^i_b - Q_{b,min}}{n \cdot \Delta t} \cdot \eta_{dis}\right\} - u^i_{dis} + u^i_{cha} \tag{2.49}$$

$$P^i_{down} = \min\left\{P^{max}_{bess}, \frac{Q_{b,max} - q^i_b}{n \cdot \Delta t} \cdot \frac{1}{\eta_{cha}}\right\} - u^i_{cha} + u^i_{dis} \tag{2.50}$$

Equations (2.47)-(2.50) are new constraints that have to be added in the *Approach #2*, compared to the *Approach #1*, allowing to take into account SoC in the formulation of BESS reserve. BESS reserve is limited to the maximum charging or discharging power that can be kept continuously for an entire hour. The total available reserve must be greater than the reserve requirements, $r^i_{up,min}$ (kW) and $r^i_{down,min}$ (kW), sized as described in Section 2.2.

2.4.1 Influence of the BESS' operating reserve

The comparison of the two approaches has been done using the same assumptions made in Section 2.3, with a PV installed capacity of 200 kWp and a CIinterval of 90%.

As in the previous analysis, trends in active powers during August 8 are shown, this time using *Approach #2* described in this section (Fig. 2.8). Moreover, in this analysis, the Upward Operating Reserve (UOR) trends have been shown in Fig. 2.9, to show how on that specific day, several times the minimum UOR requirement was satisfied by considering the BESS' operating reserve without turning on a new diesel generator. For the sake of completeness, in Fig. 2.10, the Downward Operating Reserve (DOR) trends have also been shown.

It is important to underline how the operating reserve made available by the BESS during the adoption of OLR is very low, almost negligible, compared to the case of adopting CLR. This is because the operating reserve of the BESS is calculated based on the time between two subsequent optimizations. While with CLR, optimization occurs every hour, with OLR, optimization occurs every 24 hours. Therefore, in the case of OLR, the reserve of the BESS is calculated equal to the power that can be reliably provided for 24 hours,

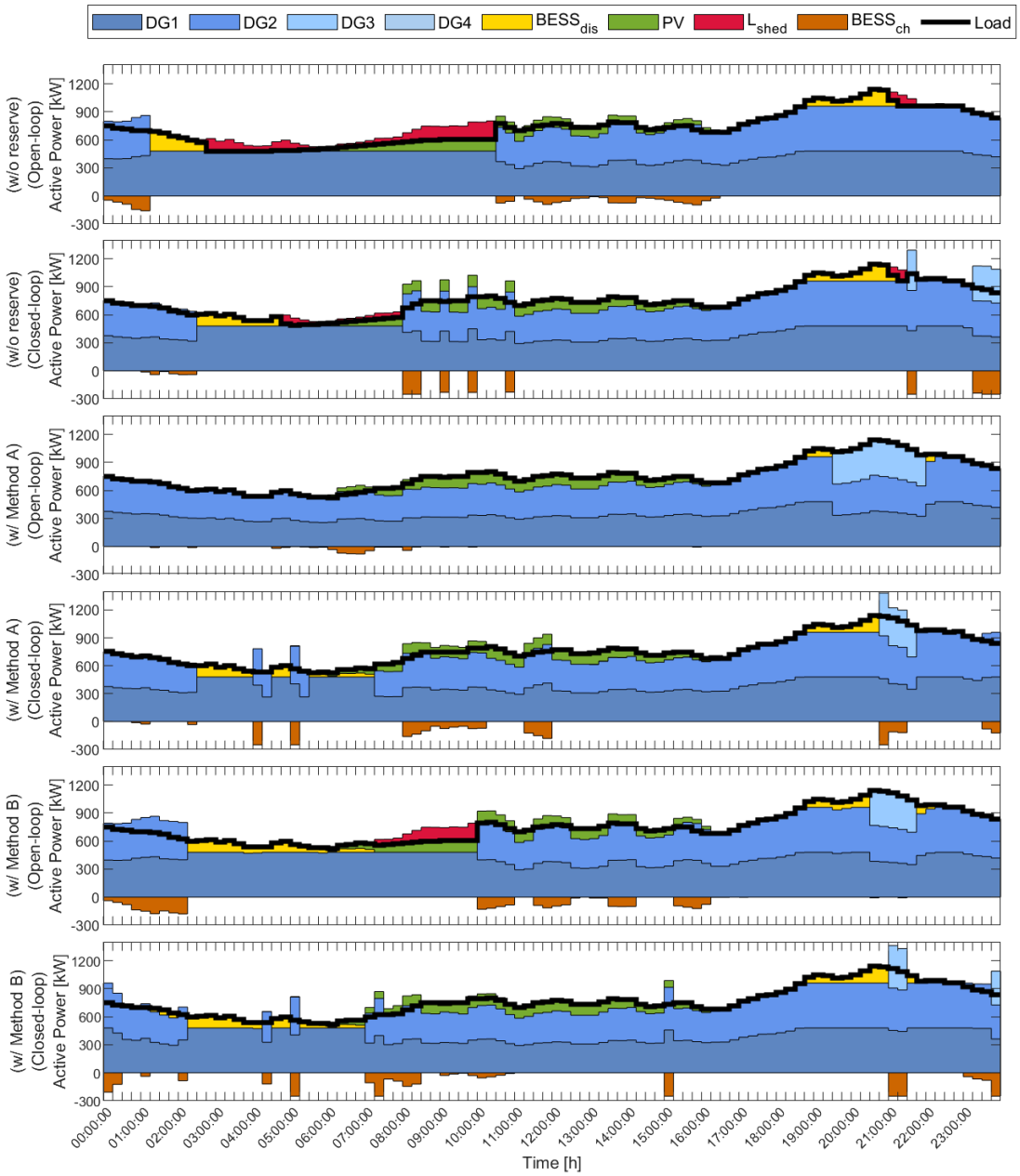


Figure 2.8: Comparison between different control methodologies on August 8 considering BESS' operating reserve in the operating reserve constraints (*Approach #2*) - Active power

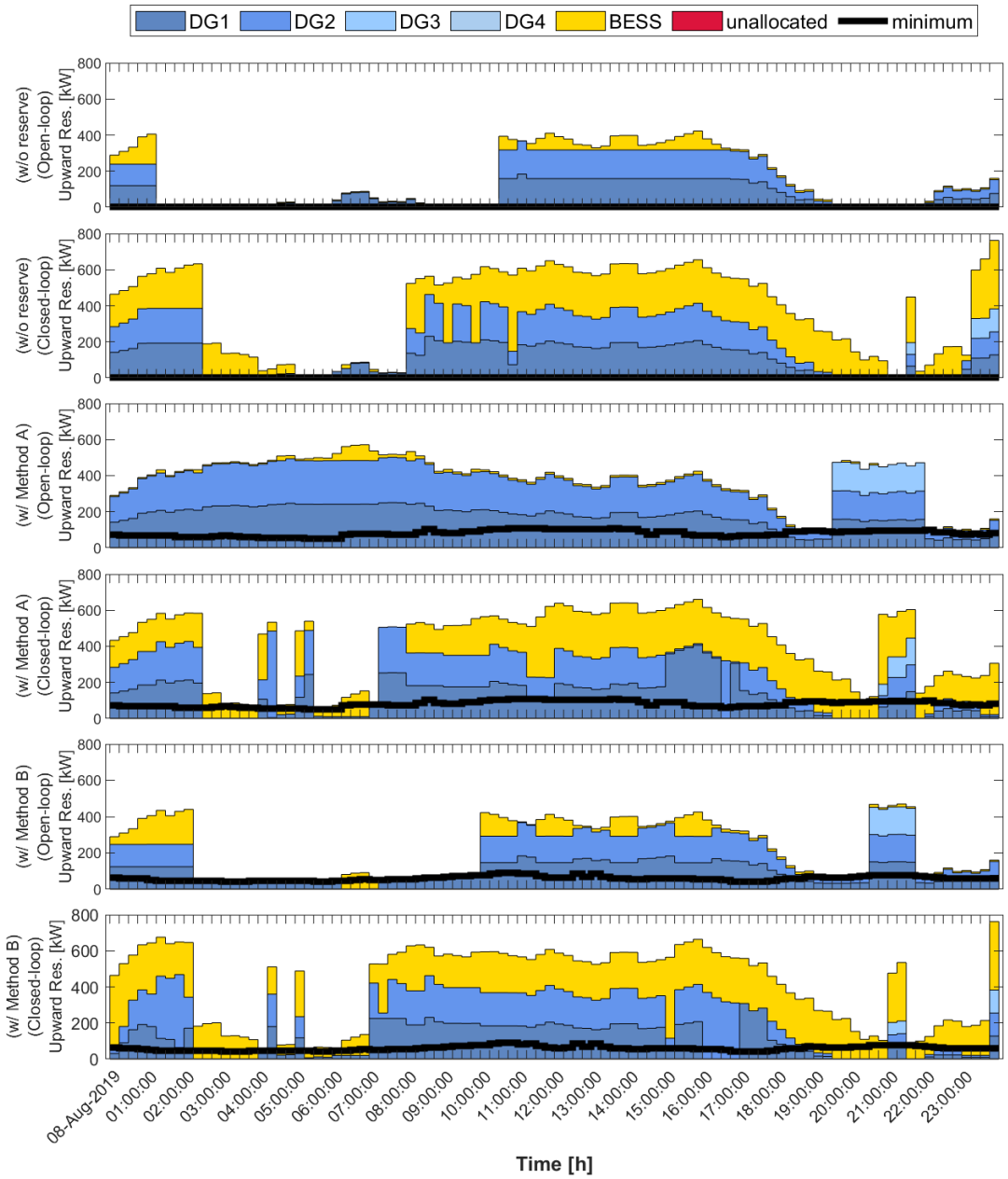


Figure 2.9: Comparison between different control methodologies on August 8 considering BESS' operating reserve in the operating reserve constraints (*Approach #2*) - Upward operating reserve

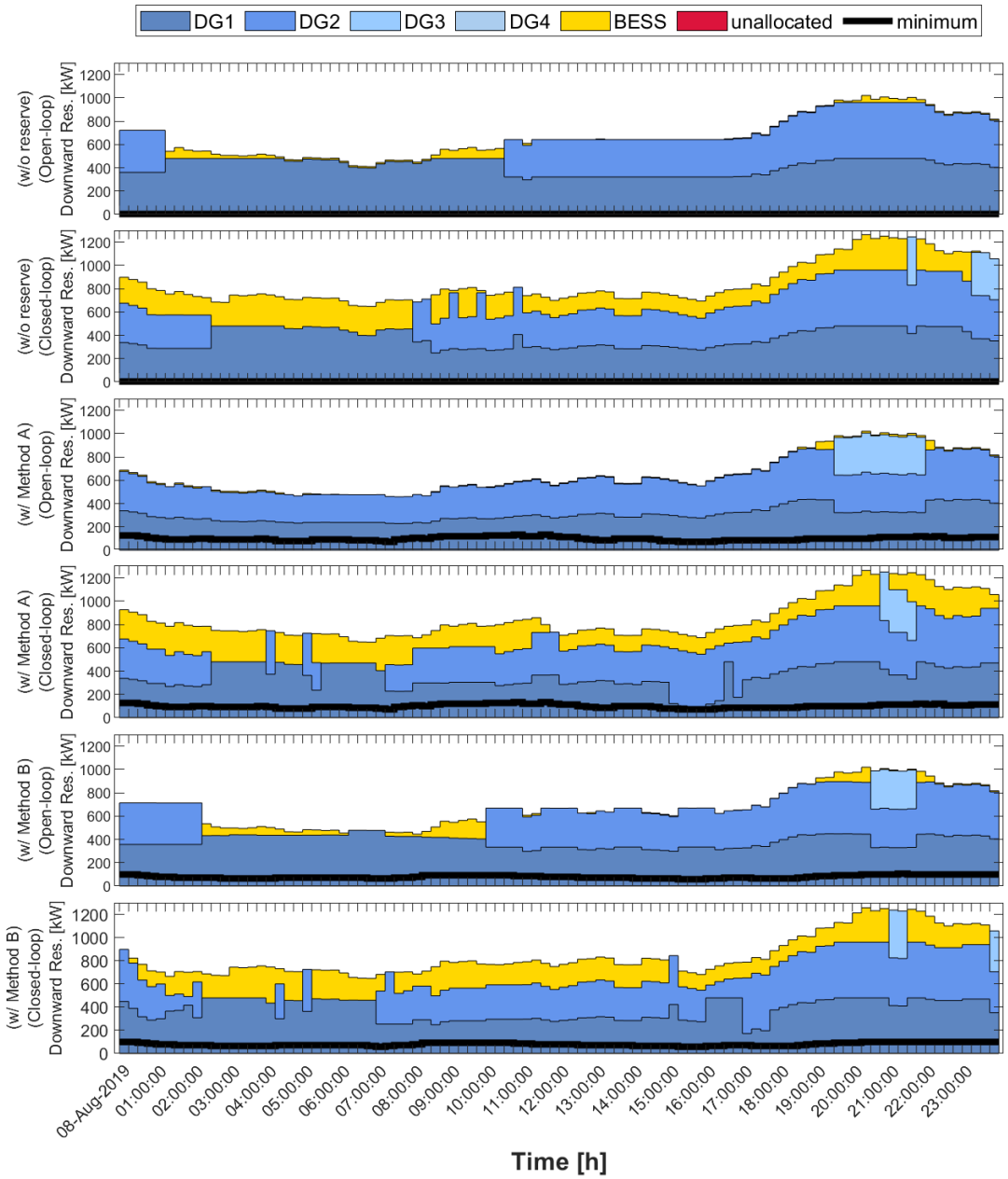


Figure 2.10: Comparison between different control methodologies on August 8 considering BESS' operating reserve in the operating reserve constraints (*Approach #2*) - Downward operating reserve

which is extremely smaller compared to what can be provided for 1 hour, as in the case of CLR. This makes the effect of the BESS operating reserve constraints consideration very small in the case of OLR adoption.

Leaving out this aspect, all the considerations made in the previous section using the *Approach #1* remain true using the *Approach #2*. The CLR produced better results by mitigating load shedding. Taking operational reserve constraints into account in the operational planning problem significantly decreased the curtailment of load. In particular, the conservative nature of reserve Method *A*, compared to reserve Method *B*, proved advantageous on the specific day shown, allowing a reduction in load shedding during August 8. In contrast to the use of *Approach #1*, in the case of Open-Loop Routine (OLR) with reserve Method *A*, *Approach #2* presented an even better result, managing to totally avoid load shedding during the day. The algorithm decided to keep the second diesel generator running during those hours, demonstrating a better ability to manage the network when it has more resources with operating reserve to manage.

By examining the UOR allocated throughout the day, as depicted in Fig. 2.9, it becomes evident that the avoided load shedding was successfully managed, meeting the minimum reserve requirement through the BESS operating reserve. This highlights how *Approach #2* proved cost-effective on that particular day, concurrently reducing load shedding and diesel consumption.

Also, using *Approach #1*, the third diesel group is turned on for a longer time during the evening than when *Approach #2* was used (comparing Figs. 2.8 and 2.5). To allow for this, in the CLR cases, the algorithm turns on a second diesel unit for 30 to 60 minutes (using Method *B* and Method *A*, respectively) in the early morning hours to charge the BESS and allow it to have enough reserve to limit the turning on of the third diesel unit during the evening.

In Tables 2.3 and 2.4, the annual operating costs using the two approaches can be compared for different PV penetration, in case of adopting the CLR or OLR, respectively. The approaches can also be compared for different confidence intervals with the Tables 2.5 and 2.6.

Comparing the operational costs of *Approach #2* with the case without reserve constraints (Table 2.1), all the considerations discussed in the analysis using *Approach #1* remain valid. Generation costs are lower when reserve constraints are neglected, since the dispatch aimed only to satisfy the forecasted net-load at a minimum cost. However, during real-time operation, due to the forecasting errors, the lack of reserve resulted in

Table 2.3: Comparison of annual operating costs between *Approach #1* and *Approach #2* with closed-loop routine, for different levels of PV penetration (€)

Closed-loop		Method *A*		Method *B*	
		Appr. #1	*Appr. #2*	*Appr. #1*	*Appr. #2*
0 kWp	on/off DGs	1628	2213	1658	2288
	DG Prod.	830369	826386	829323	826101
	BESS usage	1376	2255	1400	2371
	Load/PV curt.	118	520	0	7675
	Overall cost	**833490**	**831373**	**832380**	**838435**
100 kWp	on/off DGs	1733	2213	1733	2258
	DG Prod.	794027	789431	792775	789331
	BESS usage	1597	2301	1654	2292
	Load/PV curt.	273	636	1167	2707
	Overall cost	**797690**	**794580**	**797328**	**796588**
200 kWp	on/off DGs	1642	3203	1672	3023
	DG prod.	758755	751400	757097	750967
	BESS usage	4435	3324	3051	3402
	Load/PV curt.	39	1497	260	2778
	Overall cost	**764872**	**759423**	**762082**	**760169**
500 kWp	on/off DGs	4432	7373	4387	8123
	DG prod.	665786	651928	663418	648571
	BESS usage	11596	9433	11281	9530
	Load/PV curt.	16771	25548	15688	55898
	Overall cost	**698586**	**694281**	**694774**	**722122**

several load and generation curtailment events. The introduction of reserve constraints allows instead to minimize costs, independently from the adopted control approach.

Comparing the results using *Approach #2* with CLR (Table 2.3 and 2.5) and OLR (Table 2.4 and 2.6), precisely the same considerations can be made as when dealing with *Approach #1* in Section 2.3.

The CLR permits always to mitigate the impacts of forecasting errors on yearly operating costs, since it allows to update the system state and optimal trajectories during real-time operation. In particular, it can be noticed that the CLR results in higher generation costs, whereas, the OLR leads to relevant costs due to load/PV curtailment. In general, the CLR appears to be always a little more efficient than the OLR, except for the case with a PV penetration of 500 kWp and operating reserve evaluated by Method *B*.

The CLR generally appears to be consistently more efficient than the OLR, except for the scenario with a PV penetration of 500,kWp and an operating reserve evaluated by Method *B*.

Approach #2, being less conservative than *Approach #1*, is more vulnerable to fore-

Table 2.4: Comparison of annual operating costs between *Approach #1* and *Approach #2* with open-loop routine, for different levels of PV penetration (€)

	Open-loop	Method *A*		Method *B*	
		Appr. #1	*Appr. #2*	*Appr. #1*	*Appr. #2*
0 kWp	on/off DGs	1688	1897	1673	1897
	DG prod.	828804	829670	827875	828348
	BESS usage	1962	1921	1833	1957
	Load/PV curt.	2832	1780	11344	17553
	Overall cost	**835285**	**835269**	**842724**	**849756**
100 kWp	on/off DGs	1613	1972	1553	2047
	DG prod.	792524	792952	791303	791591
	BESS usage	2135	2440	2070	2439
	Load/PV curt.	7404	7798	18921	16406
	Overall cost	**803676**	**805162**	**813847**	**812484**
200 kWp	on/off DGs	1657	2302	1672	2017
	DG prod.	757358	757784	755470	755782
	BESS usage	5010	4858	3599	3523
	Load/PV curt.	7970	6588	16347	17842
	Overall cost	**771996**	**771534**	**777089**	**779166**
500 kWp	on/off DGs	2257	3202	2302	3562
	DG prod.	664629	664981	662452	661663
	BESS usage	11751	13256	11397	12529
	Load/PV curt.	21286	794924	30562	793638
	Overall cost	**699924**	**708264**	**706714**	**715797**

casting errors. High penetration of renewable sources (500 kWp) necessitates a greater operating reserve but also introduces a higher susceptibility to forecasting errors. In the case of OLR, the quantified operating reserve of the BESS was very low, forcing the optimal planning algorithm to meet operating reserve requirements almost always only through the operating reserve of diesel generators.

In instances where the BESS reserve was sufficient, the CLR resulted in keeping one more diesel generator offline compared to the OLR. This choice, observed multiple times during the analyzed year, proved to be counterproductive when adopting the less conservative reserve evaluation method (Method *B*). Ultimately, the adoption of a CLR was not enough to compensate for the less conservative nature of the *Approach #2*.

Comparing the two approaches, it can be seen that *Approach #2* results in a greater number of generator state changes, but a reduction in the actual fuel cost, which also saves CO_2 emissions. For a high CI, the usage of BESS is reduced because it is used more frequently to ensure reserve capacity. However, its use increases when the CI is lower, mainly to reduce the cost of production from diesel sources.

Table 2.5: Comparison of annual operating costs between *Approach #1* and *Approach #2* with closed-loop routine, for different confidence intervals (€)

	Closed-loop	Method *A*		Method *B*	
		Appr. #1	*Appr. #2*	*Appr. #1*	*Appr. #2*
CI=100%	on/off DGs	1703	2888	1703	2933
	DG Prod.	763815	752761	763815	752230
	BESS usage	6622	2499	6622	2725
	Load/PV curt.	0	65	0	0
	Overall cost	**772139**	**758213**	**772139**	**757888**
CI=95%	on/off DGs	1687	2858	2272	3083
	DG Prod.	760327	752030	757678	751374
	BESS usage	5359	2774	5662	3299
	Load/PV curt.	0	179	525	1176
	Overall cost	**767374**	**757840**	**766138**	**758931**
CI=90%	on/off DGs	1642	3203	1672	3023
	DG Prod.	758755	751400	757097	750967
	BESS usage	4435	3324	3051	3402
	Load/PV curt.	39	1497	260	2778
	Overall cost	**764872**	**759423**	**762082**	**760169**
CI=85%	on/off DGs	1612	2918	2182	3323
	DG Prod.	757821	751224	754849	751005
	BESS usage	3658	3387	3360	3692
	Load/PV curt.	30	2930	1073	3559
	Overall cost	**763122**	**760458**	**761465**	**761579**
CI=80%	on/off DGs	1732	3128	2167	3083
	DG Prod.	756814	751025	754205	750748
	BESS usage	3075	3512	3088	3802
	Load/PV curt.	365	1843	2770	7035
	Overall cost	**761988**	**759508**	**762232**	**764667**

Approach #2, in general, almost always leads to a lower overall operating cost, especially for a high CI and adopting a CLR. This is because the OLR pays less attention to the behavior of the BESS during the current day, and the reserve provided by this resource may be consumed in cases where load conditions deviate significantly from forecasts. Although *Approach #2* achieves overall savings, more load and PV generation outages occur. This approach, therefore, has a higher risk of curtailments, which have almost always proven to be cost-effective.

As PV penetration varies, there is no clear dominance between the two approaches. *Approach #2* always proves advantageous when using the Method *A* for reserve evaluation and with the adoption of the proposed CLR. In other cases, the two approaches give similar results. It seems too conservative to consider BESS' operating reserve in operating reserve constraints when the penetration of the PV is very high. For example, in the case of a PV

Table 2.6: Comparison of annual operating costs between *Approach #1* and *Approach #2* with closed-loop routine, for different confidence intervals (€)

	Open-loop	Method *A*		Method *B*	
		Appr. #1	*Appr. #2*	*Appr. #1*	*Appr. #2*
CI=100%	on/off DGs	1763	2153	1763	2108
	DG Prod.	762204	763547	762204	761225
	BESS usage	7411	7351	7411	2398
	Load/PV curt.	19	1460	19	0
	Overall cost	**771397**	**774510**	**771397**	**765730**
CI=95%	on/off DGs	1672	2093	1657	2093
	DG Prod.	758855	759629	757552	758006
	BESS usage	6009	5972	5040	4958
	Load/PV curt.	3783	2974	5523	3522
	Overall cost	**770321**	**770667**	**769773**	**768579**
CI=90%	on/off DGs	1657	2303	1672	2018
	DG Prod.	757358	757785	755470	755782
	BESS usage	5010	4859	3599	3523
	Load/PV curt.	7970	6589	16347	17843
	Overall cost	**771996**	**771535**	**777089**	**779166**
CI=85%	on/off DGs	1657	1958	1642	2063
	DG Prod.	756339	756625	754307	754648
	BESS usage	4267	4167	2966	2990
	Load/PV curt.	11196	8348	22467	15363
	Overall cost	**773460**	**771097**	**781384**	**775064**
CI=80%	on/off DGs	1672	1988	1567	2033
	DG Prod.	755378	755767	753487	753832
	BESS usage	3570	3528	2654	2745
	Load/PV curt.	15688	11713	29962	23759
	Overall cost	**776309**	**772995**	**787671**	**782368**

of 500 kWp, the savings due to lower diesel consumption of the main power plant is not sufficient to cover the costs associated with the higher number of generator state changes and load and generation curtailments. For lower values of PV, however, considering the less conservative approach (*Approach #2*) often leads to a saving, but overall the two approaches can be considered equivalent.

Table 2.7: Annual operating costs variation considering the BESS' operating reserve in the operating reserve constraints (*Approach #2* vs *Approach #1*) for different PV penetration levels (€)

	Closed-loop		Open-loop	
	Method *A*	Method *B*	Method *A*	Method *B*
0 kWp	**-0.25%**	**+0.73%**	**-0.00%**	**+0.83%**
100 kWp	**-0.38%**	**-0.09%**	**+0.18%**	**-0.17%**
200 kWp	**-0.71%**	**-0.25%**	**-0.06%**	**+0.27%**
500 kWp	**-0.62%**	**+3.94%**	**+1.19%**	**+1.29%**

Table 2.8: Annual operating costs variation considering the BESS' operating reserve in the operating reserve constraints (*Approach #2* vs *Approach #1*) for different confidence interval (€)

	Closed-Loop		Open-Loop	
	Method *A*	Method *B*	Method *A*	Method *B*
CI=100%	**-1.80%**	**-1.85%**	**+0.40%**	**-0.73%**
CI=95%	**-1.24%**	**-0.94%**	**+0.04%**	**-0.16%**
CI=90%	**-0.71%**	**-0.25%**	**-0.06%**	**+0.27%**
CI=85%	**-0.35%**	**+0.01%**	**-0.31%**	**-0.81%**
CI=80%	**-0.33%**	**+0.32%**	**-0.43%**	**-0.67%**

The relative percentage variation of the overall operating costs using *Approach #2* compared to *Approach #1* are shown in Tables 2.7 and 2.8. The previously discussed statements can be further highlighted by the data presented in these tables.

Examining the data in Tables 2.7, it is noted that adopting Method *A* and CLR, *Approach #2* is always advantageous compared to *Approach #1*. Furthermore, it is observed that this advantage increases as the PV size increases. However, this improvement gradually diminishes as the PV size exceeds a certain value, as highlighted by the fact that with a size of 500 kWp, the improvement is lower than the case with 200 kWp. Reducing the conservativeness of the adopted methods leads to a decrease in the advantage of *Approach #2* over *Approach #1*.

This relationship between conservativeness and economic effectiveness of *Approach #2* is also evident in Table 2.8. Changes in CI, using CLR, show how the advantage of *Approach #2* over *Approach #1* decreases with decreasing CI, both with Method *A* and Method *B* for operating reserve evaluation. However, with the adoption of OLR, this relationship is lost, suggesting a reversal of the trend (observing data related to OLR with Method *A*). It is important to note that in OLR, the BESS operating reserve is spread over all 24 hours of the day, often proving to be very small. In these cases, differences in overall costs between the two approaches arise from small decisions that, depending on the circumstances, can prove advantageous or disadvantageous.

2.5 Conclusion

Accommodating increasing shares of RES generation in non-synchronous power system requires the adoption of suitable control schemes. In some small Italian islands, during off-season days, RES generation can easily exceed load, even at low levels of RES penetration, thus either limiting hosting capacity or introducing threats to system adequacy and security.

Storage systems can provide support to compensate generation/load imbalance, although the adoption of predictive control schemes is suggested to optimize their use.

Test results, obtained using historical load data of a benchmark of an actual small island in Italy, showed that the provision of suitable amounts of reserve and the inclusion of reserve constraints in the formulation of the control problem constitute the most relevant aspect for energy resource dispatch. In the presence of high RES penetrations, unforeseen net-load fluctuation can generate high operating costs in terms of curtailed load or generation, if no reserve has been ensured. The proposed closed-loop operational planning algorithm allowed to obtain the best results, independently from RES capacity and from the method adopted to estimate reserve requirements. Also, an open-loop control can guarantee satisfactory results, although in this case the adoption of a more conservative approach to estimate reserve is suggested.

Results obtained with two different methods to estimate upward and downward reserves, both based on a probabilistic approach, have also been discussed. The adoption of the most conservative method (Method *A*) allowed to obtain always good results, independently from the control scheme and from the share of PV generation. Further tests have shown how the choice of a confidence interval while quantifying reserve can impact on final results. In general, a lower confidence interval (around 80-85%) can be adopted together with a Closed-Loop Routine (CLR). Higher confidence (95%) is instead necessary when Open-Loop Routine (OLR) is used.

When BESS power capacity is neglected from formulation (*Approach #1*), the control scheme leads to more conservative solutions. Conventional generation units (in this case small-sized diesel generators) are dispatched more often, with increasing production costs due to more frequent on/off cycles and less efficient operating points. Moreover, the BESS unit is dispatched more often because its capacity is not set aside as a reserve, resulting in higher wear costs.

The inclusion of BESS capacity in operating reserve constraints allows instead to decrease generation costs and minimize the use of BESS. In facts, the solution found with this approach (*Approach #2*) allows to avoid the switching on of extra generators just to satisfy operating reserve requirements. Also BESS is activated less often because its capacity is reserved. Thanks to the recursive CLR, BESS operating reserve is updated at each cycle of the control loop, permitting to estimate very accurately the actual BESS capability in the next hour of operation. However, this approach has the drawback of overestimating the capabilities of the battery along the rest of the optimization window. In

certain cases, when higher net-load fluctuations or forecasting errors are experienced, the solutions found might be not conservative enough and lead to undesirable curtailments. This approach might not be suggested when load shedding costs are particularly high or forecasts are not very accurate.

In small isolated power systems where the load varies greatly depending on the season, as in the case examined in this chapter, it may be more convenient to switch between the two approaches depending on the period of the year.

Chapter 3

Real-Time Operating Reserve Assessment and Allocation

The previous chapter discussed a new operational planning algorithm for islanded Microgrid (MG)s, based on an optimal predictive dispatch algorithm with a closed-loop routine. This algorithm aimed to optimally schedule the diesel generators and manage the Battery Energy Storage System (BESS) State of Charge (SoC) and charge and discharge power, in order to reduce the quantity of load not served or renewable production curtailed, and save money. The time frame of operation of this algorithm, because of concerning the operational planning of the resources, was on the order of hours. Moreover, the previous study was considered only theoretically, without considering the optimization program in a more practical framework, i.e. included in a control architecture.

In this chapter, a Real-Time Algorithm (RTA) for operating reserve assessment and allocation is presented. Differently from the previous study, this control algorithm has been realized in order to be implemented in an actual control architecture for isolated MGs. The control algorithm monitors and manages the security and secure grid operation, assessing the available operating reserve and sending requests to the controllable resources in order to ensure the minimum operating reserve allocation. The time frame of operation of this RTA is faster than the algorithms described in the previous chapter, being in the range of 1 minute to 15 minutes.

As in the previous chapter, also this RTA (as well as the control architecture in which it is to be implemented) has been developed based on the general structure of a small Italian island, namely the reference small Italian island introduced in Section 1.5.1.

The control architecture considered in this chapter was introduced in [11] and represents

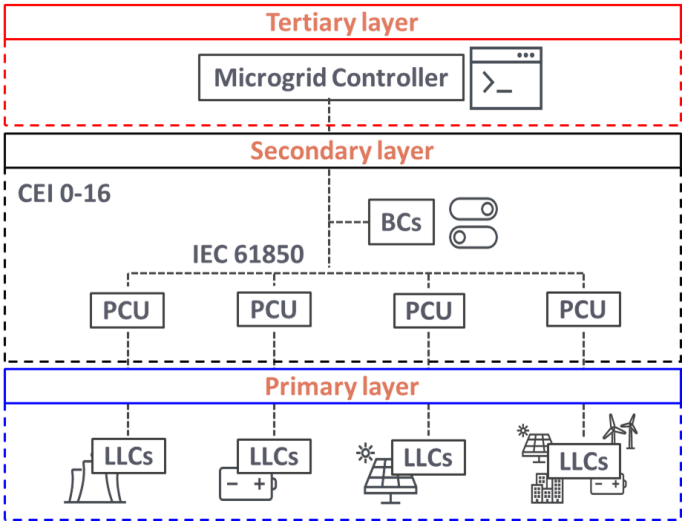


Figure 3.1: Hierarchical scheme of the proposed control architecture

one of the key points of a national research project, namely *ISMI (Integrated Storage and Microgrid Innovation)*. The ISMI project, in fact, aimed to realize a unified architecture capable of ensuring efficient and stable control of isolated networks (MGs such as small Italian islands), consisting of the integration of a high-level control logic (Microgrid Controller) and local control logic of generation and storage resources. The control architecture developed in that project aimed not only at ensuring the correct and secure operation of the MG but also at being simple and immediately implementable in islanded distribution networks. This control architecture, in fact, has been conceived by including in it devices and components already present in the Italian national landscape, installed in today's networks, or otherwise provided for by current regulations.

As discussed extensively in Chapter 1, the physical and functional grouping of the control system functionalities can be defined in several ways. That said, in the considered control architecture, the functionalities of the three control layers are integrated and operated according to the hierarchy depicted in Fig. 3.1, in a way that is suitable for various islanded MG configurations.

The considered control architecture is derived from the structure of the IEEE 2030 standard for Microgrid Controller (MGC)s [34], which is based on three control layers, namely, primary, secondary, and tertiary. In such control architecture, the primary control layer comprises all the functionalities operated by the Local Level Controllers (LLCs), such as speed governors and excitation current regulators of thermal units, as well as droop techniques required to share power contributions for voltage and frequency regulation.

The secondary layer of the architecture is decentralized and can be identified in Breaker

Controllers (BCs) and Plant Control Units (PCUs). In this specific control architecture, the BCs can provide measuring and protection functionalities, while the PCUs, which are associated to each generation and storage plant, collect measures and states from single generating units or aggregation of different ones. This assumption is consistent with the specifications set by the Italian grid code CEI 0-16 [53] which makes devices with monitoring capabilities to be mandatory for plants with relevant production (with rated power greater than 1 MW). The PCU introduced by the Italian grid code CEI 0-16 is called *Controllore Centrale d'Impianto (CCI)*, discussed in Section 1.4. As already discussed in Section 1.4, grid code also specifies the availability of several controlling functionalities for the CCI, i.e. (a) active power limitation, (b) modulation of the imported/exported active power, (c) voltage regulation by supplying inductive/capacitive reactive power, (d) power factor setpoint, (e) reactive power regulation as a function of the voltage, (f) power factor regulation as function of active power.

In the specified control architecture, the implementation of some of the available functionalities is made mandatory (i.e., active power limitation). Further functions, currently not considered in the abovementioned grid code, like spinning reserve regulation, were also considered. BCs are considered present in correspondence of secondary substation MV feeders, where specialized devices are already diffused in the Italian grids, and along LV lines, where remote monitoring and controlling capabilities are still an innovation proposal.

Finally, on the tertiary layer a central Microgrid Controller (MGC) gathers all the information received by the lower level and uses them to elaborate operative decisions. These decisions are then explicated by commanding operations and sending set-points to the abovementioned plant and breaker controllers. In particular, the functionalities implemented in the MGC are: (a) collecting measures and status from the plant and breaker controllers, (b) processing, through a dedicated algorithm (described in the following section), the input status and measurements to determine the control actions, namely, (c) dispatching activation/deactivation commands and set-points to the plant controllers, (d) commanding the operation commands of circuit breakers.

3.1 Control algorithm of microgrid controllers for isolated microgrids

In the previous chapter, the operational planning algorithm and the evaluation of the minimum operating reserve to be guaranteed were based on the use of historical forecasts and forecasting errors, but in industrial applications, this information is often lacking. In developing this Real-Time Algorithm (RTA), an attempt was made to adopt approaches that were as simple and implementable as possible in industrial devices commonly used in today's distribution networks. Most often, these devices are Programmable Logic Controller (PLC)s, which only allow the implementation of rule-based algorithms and the management of measurements and time series of data. Accordingly, the RTA proposed in this chapter is rule-based, and designed for easy implementation on modern industrial PLCs.

In the industrial context, it is common to have difficulty in finding time series of data with good temporal resolution. The available time series are often hourly or, at most, quarter-hourly. Therefore, in the reserve analysis, this RTA uses time series of monthly maximum, average, and minimum island load on an hourly basis. In addition, industrial devices used today do not always have the capabilities to estimate reserve through probability-based methodologies as in the case of the methods proposed in Section 2.2. The operating reserve required in the island calculated by the assessment RTA presented in this chapter is based on these time series and instantaneous measurements of power absorbed by loads and generated by energy resources in the island during operation.

The main purpose of the proposed RTA is to verify the adequacy of the isolated system by assessing the operating reserve provided by the available resources. The RTA verifies that the available reserve is sufficient to withstand any major loss of generation from intermittent renewable sources or sudden load variations. Whenever system reserve is not enough, the RTA pre-emptively procures the needed extra operating reserve or evaluates preventive/corrective control actions.

The algorithm is also able to deal with resources which reject the required control action or are non-responding. The RTA is also programmed to shed load or limit the power produced by intermittent generating units in cases of excessive load or production. These additional functions are enabled even without the control of operating reserves and make it possible to inhibit unnecessary controls, solve problematic grid situations that could not be avoided in advance, and prevent the generation plant from reaching unfeasible operating

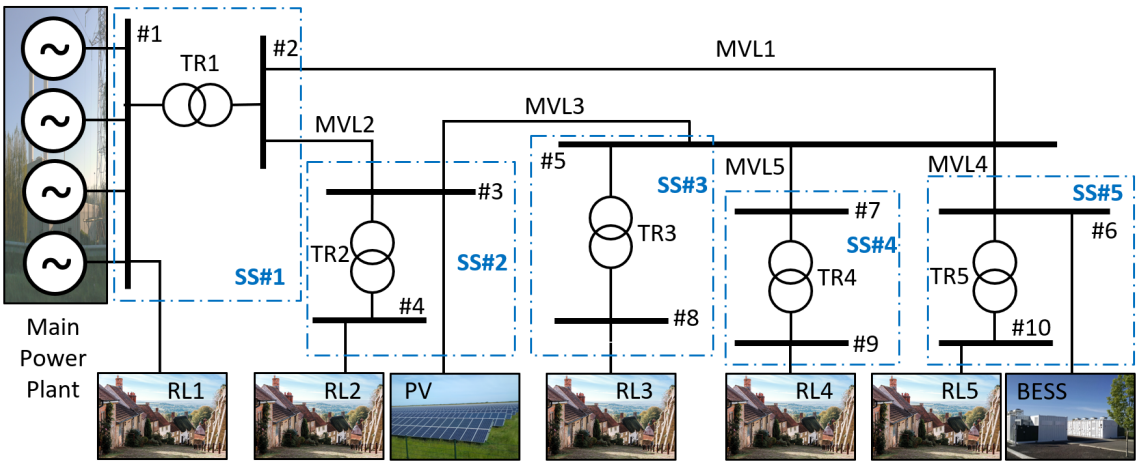


Figure 3.2: Representation of the small Italian island distribution network under investigation

points (negative net load or net-load greater than the plant's maximum power output).

The RTA, which is to be deployable in a commercial PLC, is programmed using finite state-based logic that can be implemented in a finite-state machine. In each operating state, the adequacy of the system is checked under specific conditions. If the conditions in the current operating state are not satisfied, a transition to a different operating state takes place. Each operating state transition results in a different grid condition and different actions by the RTA. The adequacy of the system is verified by assessing both the available Upward Operating Reserve (UOR) and Downward Operating Reserve (DOR), at the same time. These verifications are carried out simultaneously and affect different operating states of the RTA.

As already said, the RTA is based on the reference small Italian island discussed in Section 1.5.1. As in the previous chapter, to fit the grid for the study, a PV system and a BESS were assumed to be present on the island. These resources were assumed to be connected directly to the MV distribution grid at substations SS#2 and SS#5, respectively. The distribution network scheme of the small Italian island under consideration, with the modifications just mentioned, has been represented in Fig. 3.2.

Thus, the assumptions taken into account for the RTA development have been listed below:

- The proposed RTA is assumed to be implemented within a Microgrid Controller (MGC) that is responsible for supervising and controlling the entire Microgrid (MG);
- The controlled network represents the typical distribution network of a small Italian island, where there is a Main Power Plant (MPP) responsible for supplying the

entire island and regulating frequency and voltage. Therefore, the MPP must remain connected at all times;

- It was assumed that the MPP consists of 4 diesel units with rated apparent power of 600 kVA (2400 kVA for the entire plant) and no technical minimum;
- Given the small size of the island, it was assumed that the frequency and voltage would be the same at all nodes in the network;
- The MGC was assumed to be responsible for active power operating reserve assessment and allocation, while it is left to the MPP to ensure adequate reactive power reserve;
- To allow the MPP to regulate the voltage and provide the reactive power required by the island, a minimum amount of apparent power of the diesel units has been left available for reactive power balancing and voltage regulation. This amount is determined based on the average power factor recorded on the island which is 0.8. A rated active power of diesel units was then defined and set equal to 480 kW;
- The power plant is privately owned and not directly controllable by a MGC. However, it was assumed that requests can be sent to the MPP;
- Each producer must have a CCI installed, as described in Section 1.4. Therefore, the MGC has access to the states of the MPP's resources and the power outputs of each resource;
- As in the Chapter 2, a 250/300 kW/kWh BESS owned by the DSO managing the island distribution network was assumed to be present on the island;
- As specified in the CEI 0-16 network code, the BESS must be equipped with a CCI. Therefore, power exchange measurements from the BESS are available, and it is possible to modulate the exchanged power;
- Like any BESS connected to the distribution network, according to the CEI 0-16 network code, the "*Active Power Regulation of a Storage System for Over- and Under-Frequency Transients Originating on the Grid*" must be implemented. To make the text more readable, it has been called *CEI-Storage Frequency Power Regulation (CEI-SFPR)* in this document and it has been described in Section 3.2.1.3.

The BESS must always be able to adjust its exchanged power as the frequency varies. However, the activation thresholds for this control could be varied;

- It was assumed that the MGC can vary the activation thresholds of active power regulation for frequency transients, transitioning from "wide" regulation thresholds where the BESS can be assumed to be "disabled" for frequency regulation, to "narrow" regulation thresholds where the BESS can be assumed to be "enabled" for frequency regulation;
- The upward/downward reserve made available by BESS was calculated as the instantaneous active power that can be continuously delivered/absorbed for a specific time, default set to 30 minutes. The time can be varied by setting a time greater or less than 30 minutes, choosing to be more or less conservative, respectively;
- As in the Chapter 2, a 200 kW PV system was assumed to be installed on the island;
- Like any non-rotating production system, as indicated in the CEI 0-16 network code, "*Active Power Limitation for Over-frequency Transients Originating in the Grid*" must be implemented for the PV system. To make the text more readable, it has been called *CEI-Over-Frequency Power Limitation (CEI-OFPL)* in this document and it has been described in Section 3.2.1.4;
- As specified in the CEI 0-16 network code, the PV system must be equipped with a CCI. Therefore, measurements of power produced by the PV system are available, and it is possible to limit the power produced by it;
- The presence of a prosumer on the island was assumed, also equipped with a CCI, as indicated by the CEI 0-16 network code. The prosumer's role was solely to facilitate testing of the proposed control algorithm;
- It was assumed that each substation in the network is equipped with a CCI and a BC, allowing for load measurements and the ability to disconnect loads upon the MGC's request;
- Furthermore, it was assumed that BCs are present in low-voltage networks, controllable by the MGC, enabling actions for load shedding of small load portions.

The logical scheme of the RTA is shown in Fig. 3.3. The algorithm performs three different simultaneous checks, referred to as macro-states:

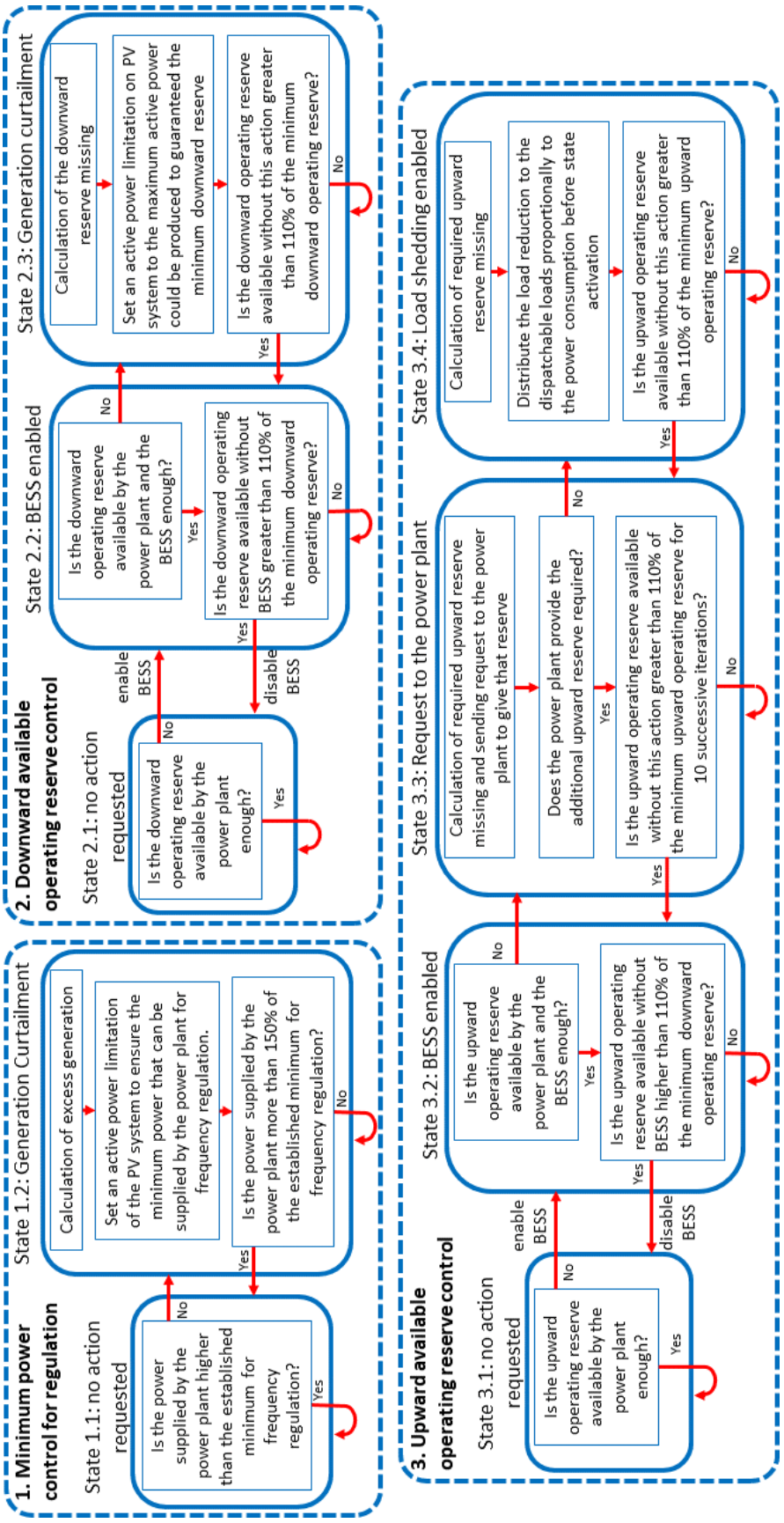


Figure 3.3: Flowchart of the proposed RTA for MGCs for isolated MGs

- Macro-state 1: Minimum power control for regulation (ensures the island's central unit a Minimum Downward Regulation Bandwidth (MDRB) to adjust the frequency)
- Macro-state 2: Downward available operating reserve control
- Macro-state 3: Upward available operating reserve control

To avoid conflicts among the three macro-states, a priority order has been established, reflecting the sequence in which they were listed. Each macro-state includes operational states of the algorithm, starting from the initial state where the MGC in which the algorithm is implemented takes no action, to the most critical state where generation or load curtailment is made to ensure the secure operation of the MG.

3.1.1 Macro-state 1: Minimum power control for regulation

The first control is designed to ensure a minimum amount of power to be delivered by the power plant during island operation. This allows the power plant to have a MDRB that allows it to smoothly adjust the frequency and adapt to rapid changes in net load during the day. This condition is crucial and not always guaranteed by the other two controls, since the down operating reserve provided by a BESS on the island may, in some cases, be sufficient to completely cover the minimum required DOR, even if the power plant were to have no downward control bandwidth. In this case, since the power plant is responsible for frequency regulation and does not have downward regulation capability, the grid could be exposed to the risk of blackout.

In state 1.1, the algorithm verifies that the power currently delivered by the power plant is above a predetermined minimum threshold (MDRB). In the event that this condition is not met, the algorithm switches to state 1.2, where the excess power generated on the island is calculated, and a request is issued to limit the power generated by the island's generating facilities, mainly photovoltaic plants. At each cycle, the algorithm verifies the need for this action by assessing whether the power produced by the plant exceeds a specific hysteresis threshold (to avoid sudden changes in state), predefined at 1.5 times the minimum power value set for frequency regulation. In case this condition occurs, it is changed from state 1.2 to state 1.1.

3.1.2 Macro-state 2: Downward available operating reserve control

This control is designed to ensure a minimum DOR during MG operation, preventing a rapid increase in renewable generation (mainly due to a resumption of production following cloud cover over PV systems) or the loss of a significant portion of the island's load. In each cycle, it is checked whether the DOR provided by the island's MPP is sufficient to cover the minimum required DOR.

If this condition is not met, the algorithm transitions from state 2.1 to state 2.2, where the BESS on the island is enabled. If configured for primary frequency regulation, the BESS can contribute its charging capacity to support the power plant during load or renewable source imbalances.

In state 2.2, it is verified that the reserve available between the MPP and the BESS is sufficient to cover the minimum required. If, even with the enabled BESS, the available reserve is insufficient to cover the minimum required, the algorithm transitions from state 2.2 to state 2.3, where a limitation of power produced by renewable sources is applied to increase the DOR available from the MPP (similar to the action taken in the state 1.2). It is important to define that, in the event of a downward load deviation, the PV power plant should self-limit its power production through the control "Active Power Limitation for Over-Frequency Transients Originated on the Grid" (i.e. CEI-OFPL). As will be discussed in Section 4.2, the response time of this control is not fully defined and it is insecure to tie the security of the island network to this control. Therefore, this control is considered as a control of last resort, not taken into account in the MGC logic. In addition, the intervention of this control leads to the establishment of a frequency above 50.2 Hz for an indefinite time, a condition that is desired to be avoided to ensure better quality of electrical service. To avoid this and ensure grid security, the power produced by the PV power plant is preemptively limited.

Similar to state 1.2, in state 2.3, it is verified whether the generation curtailment action is necessary, checking if the available DOR without the cut action is greater than the minimum required reserve with a certain hysteresis threshold, set by default at 10%. If this condition is met, the transition from state 2.3 to state 2.2 occurs.

In state 2.2, at each cycle in which this state is active, the need to keep the BESS enabled for frequency regulation is checked, ensuring that the reserve provided by the MPP alone exceeds the minimum required reserve, with a hysteresis threshold, also set as default at 10%. If this condition is met, the algorithm returns to state 2.1, where no action related to the DOR control is taken.

The transition from state 2.3 to state 2.1 can also take place without necessarily going through state 2.2. For this purpose, it is sufficient to check in state 2.3 whether the DOR of the MPP alone is sufficient. Similarly, the transition from state 2.1 to state 2.3 without going through state 2.2 can be implemented by checking already in state 2.1 whether the BESS enabling is sufficient or not. These state transitions are not represented in Figure 1, which illustrates the basic logic of the operating algorithm, but they were considered in the finite-state machine in which the algorithm was implemented, described in Section 3.1.4, and with which the tests were conducted.

3.1.3 Macro-state 3: Upward available operating reserve control

This control is designed to ensure that there is enough UOR available on the island to cope with reductions in generation from non-programmable sources (e.g., due to cloud cover on PV installations) or a sudden increase in electric load on the island. In this macro-state, the RTA verifies that the UOR available of the MPP is sufficient to meet the minimum UOR to be guaranteed. In case it is not sufficient, similar to the DOR control, the BESS is enabled for frequency regulation, transitioning from state 3.1 to state 3.2. Every cycle, the need to remain in state 3.2 is checked by comparing the reserve provided by the MPP alone with the minimum required UOR, with a default hysteresis set at 10%. If enabling the BESS is no longer deemed necessary, there is a return to state 3.1. In state 3.2, each cycle also checks that the UOR available, that of the MPP plus the enabled BESS, is sufficient; otherwise, it transitions to state 3.3.

In state 3.3, the MGC implementing the algorithm calculates the missing UOR and sends a request to the MPP, asking for a greater reserve than it currently provides. The MPP is not obligated to accept or may refuse the request (for example, if it lacks resources to meet the requested reserve). If the MPP accepts the request, the algorithm remains in state 3.3 for a minimum number of cycles, by default set to 10. Afterwards, if the available reserve is greater than the required reserve plus a hysteresis value, also set at 10%, it exits state 3.3 and returns to state 3.2. This decision was made for the same reasons discussed for exit from state 2.3. In addition, to avoid making too short requests to the MPP, which may have to turn on an additional diesel unit to meet the request, the minimum hysteresis time was set somewhat larger than that for exit from state 2.3. Maintaining the demand when it is no longer needed should not be considered a problem and does not result in higher operating costs, as it would then be lower than what the MPP would have available without any request, requiring no effort from the MPP.

If the MPP does not consent to the request or can no longer meet the reserve value requested by the MGC, it transitions from state 3.3 to state 3.4, where load shedding occurs. In state 3.4, the missing UOR is calculated and distributed to various controllable loads based on proportionality coefficients. These coefficients can be calculated in various ways; in this chapter, they are computed as the percentage of power absorbed by each controllable load relative to the total power absorbed by controllable loads. These coefficients are calculated based on measurements taken at the moment of the transition to state 3.4 and remain constant throughout the time in the state. When load shedding is no longer necessary, i.e., when the total UOR exceeds the minimum required reserve plus a hysteresis percentage, again set at 10% by default, it transitions to state 3.3 and then to state 3.2. The transition through state 3.3 is not necessary and could be skipped to expedite the move to state 3.2. However, the forced transition to state 3.3 allows for a more orderly process, considering scenarios where the MPP has only partially accepted the request rather than refusing it outright. The continued presence in state 3.3, when unnecessary, is not problematic, as the reserve set-point sent to the MPP would be lower than the reserve it is currently providing, effectively requiring no action from the MPP.

In the recently described macro-state, load shedding is preemptively applied by commanding the low-voltage BCs. An alternative method can be employed in which the BCs are not initially activated but are enabled to intervene in the event of under-frequency events. This method, not detailed in this thesis, has been introduced in [11]. Upon entering state 3.4, the algorithm calculates the minimum number of BCs to enable in the case of over-frequency events. The enabled BCs will only intervene if the contingency actually occurs, without preemptively disconnecting the load. In that scenario, the BCs will disconnect only the minimum load necessary to ensure the secure operation of the network, ensuring electrical service for the maximum number of users possible.

In this macro-state as well, as macro-state 2, the transition from state 3.3 to state 3.1 and vice versa can occur without necessarily passing through state 3.2. Although these state transitions are not depicted in the basic logic of the algorithm shown in Fig. 3.3, they have been implemented in the finite-state machine model described in Section 3.1.4.

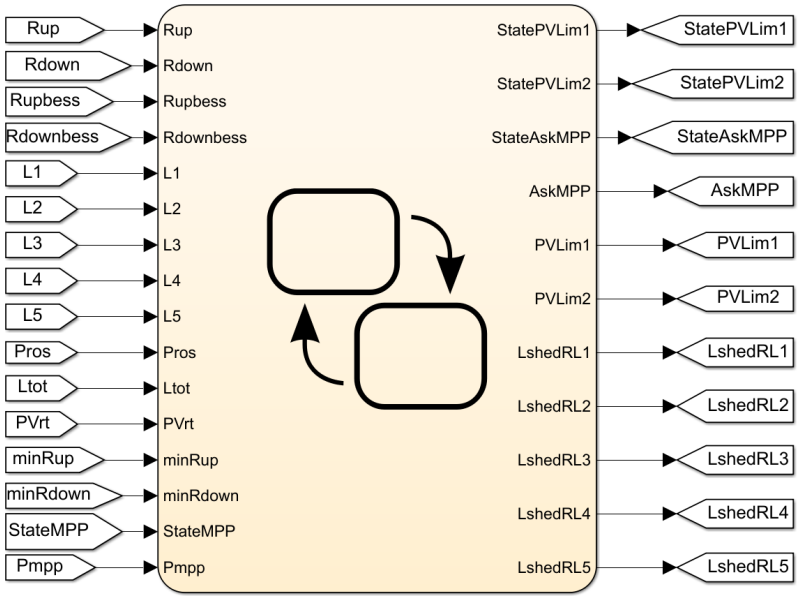


Figure 3.4: Finite-state machine model of the MGC

3.1.4 Real-time algorithm implementation in a finite-state machine model

Shown in Fig. 3.4 is the finite-state machine model of the MGC, with its inputs and outputs, in which the RTA described in Section 3.1 has been implemented. The internal structure of the model, shown in Fig. 3.5, mirrors the schematic of the RTA visible in Fig. 3.3. The MGC is composed of the 3 macro-states defined in Section 3.1: macro-state 1 which is intended to provide the Main Power Plant (MPP) with an Minimum Downward Regulation Bandwidth (MDRB) for frequency regulation, the macro-state 2 for Downward Operating Reserve (DOR) control, and the macro-state 3 for Upward Operating Reserve (UOR) control. All the variables used in the model have been defined in the following bullet points:
Input variables:

- R_{UP}: UOR of the MPP;
- R_{DOWN}: DOR of the MPP;
- R_{UPBESS}: UOR of the island's BESS;
- $R_{DOWNBESS}$: DOR of the island's BESS;
- L_1 to L_5: active power consumption of the 5 residential loads of the island (from RL1 to RL5, respectively).

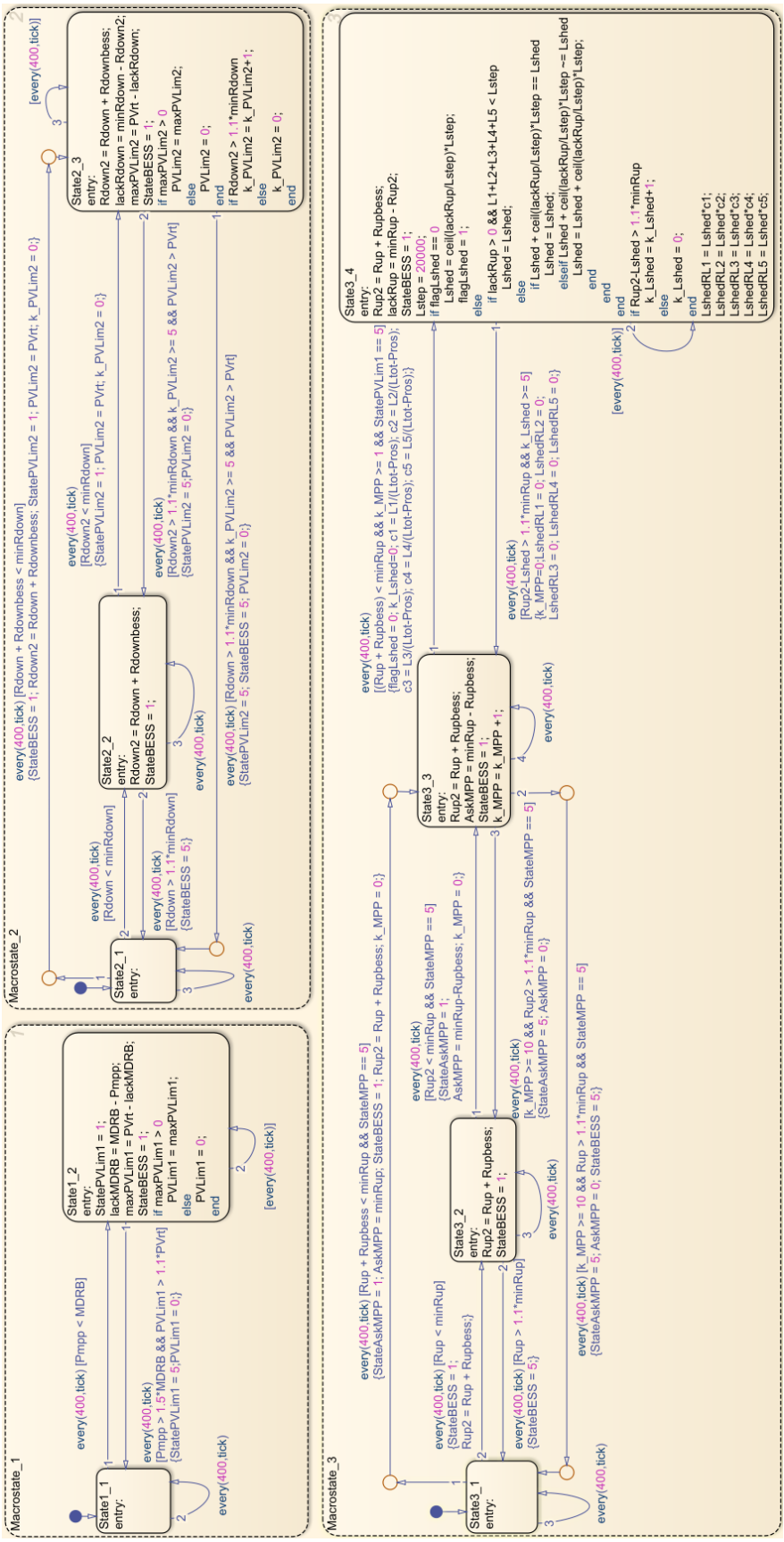


Figure 3.5: MGC implemented algorithm

- *Pros*: active power exchanged by the island's prosumer;
- L_{TOT}: total active power absorbed by the island load;
- PV_{rt}: active power produced by the island's PV power plant;
- $minR_{UP}$: minimum UOR to be guaranteed (calculated as described in Section 3.1.5);
- $minR_{DOWN}$: minimum DOR to be guaranteed (calculated as described in Section 3.1.5);
- *StateMPP*: operational state of the MPP (1 if the MPP is taking actions following a request sent by the MGC, 5 if no actions related to MGC logic are being performed).;
- P_{MPP}: active power supplied by the MPP;

Output variables:

- *StatePVLim*1: operational state of active power limitation to the PV power plant of the island related to macro-state 1 (1 if the limitation is active, 5 if it is not active);
- *StatePVLim*2: operational state of active power limitation to the PV power plant of the island related to macro-state 2 (1 if the limitation is active, 5 if it is not active);
- *StateAskMPP*: operational state of the UOR request function related to the logic of state 3.3 (1 if the MGC is sending a request to the MPP, 5 if the MGC is not sending any request to the MPP);
- *AskMPP*: Value of the UOR request sent by the MGC to the MPP;
- *PVLim*1: Active power limit sent to the island's PV power plant for logic related to macro-state 1;
- *PVLim*2: Active power limit sent to the island's PV power plant for logic related to macro-state 2.
- *LshedRL*1 to *LshedRL*5: the amount of active power to be shed to a residential load (from RL1 to RL5, respectively), calculated by the MGC and sent to the low-voltage BCs;

Local variables:

- *MDRB*: minimum downward reserve bandwidth to be guaranteed to the MPP for frequency regulation;
- *StateBESS*: operational state of the BESS (1 if the BESS is enabled for frequency regulation, 5 if it is not enabled);
- R_{UP2}: UOR after BESS activation, equal to the sum of the MPP's UOR and the BESS's UOR;
- R_{DOWN2}: DOR after BESS activation, equal to the sum of the MPP's DOR and the BESS's DOR;
- *lackMDRB*: quantity of lacking DOR of the MPP to guarantee the MDRB;
- $lackR_{UP}$: lack of UOR;
- $lackR_{DOWN}$: lack of DOR;
- *maxPVLim*1: represents the active power at which to limit the island's PV power plant to guarantee the MPP the MDRB;
- *maxPVLim*2: represents the active power at which to limit the island's PV power plant to guarantee the minimum DOR ($minR_{DOWN}$);
- k_{PVLim2}: counter for the exit condition from state 2.3;
- k_{MPP}: counter for the exit condition from state 3.3;
- k_{Lshed}: counter for the exit condition from state 3.4;
- $flag_{Lshed}$: variable useful for the logic of state 3.4 (its value is 0 at the entry into state 3.4 and becomes 1 after the first cycle in that state);
- L_{STEP}: represents the discrete amount of load shedding with which the total amount of load shedding is calculated in state 3.4;
- L_{SHED}: the total amount of load shedding to be performed to guarantee the minimum UOR ($minR_{UP}$);
- $c1$ to $c5$: proportionality coefficients for the distribution of load shedding on the various residential loads (from RL1 to RL2, respectively).

In each state, the first line represents the name of the state and the second line contains a condition "*entry*". This condition causes the code within the state to be executed when entering the state. The following bullet points describe the logic within each operational state of the MGC. Within the macro-state 1 there are 2 states:

- State 1.1 indicates the normal power delivery situation where the MPP's active power output exceeds the MDRB.
- State 1.2 indicates a scenario where the net-load that the MPP should supply is lower than the set MDRB. This occurs due to excess production from the PV power plant on the island, necessitating a limitation of solar power. In this state, the maximum PV production is limited iteratively to ensure the MPP can supply the minimum power threshold. The power difference between the MPP's actual output (P_{MPP}) and the MDRB, defined as $lackMDRB$, is calculated. This value is subtracted from the power currently generated by the MV-connected PV power plant ($PVrt$), determining the quantity of active power that has to be curtailed ($maxPVLim1$). An "*if*" condition is introduced to prevent negative limit values, and the actual limit value sent to the PV power plant's CCI is $PVLim1$.

Within the macro-state 2, for DOR control, 3 states are present:

- State 2.1 indicates a situation where the DOR available of the MPP (R_{DOWN}) exceeds the required DOR ($minR_{DOWN}$), satisfying security constraints.
- State 2.2 indicates a scenario where enabling the BESS is necessary to increase the reserve by activating it to the frequency regulation. Within this state, the new available DOR ($R_{DOWN}2$) is defined by adding the reserve provided by the MPP to the reserve provided by the BESS: $R_{DOWN}2 = R_{DOWN} + R_{DOWNBESS}$. The $StateBESS$ variable, initially equal to 5 (BESS disabled) is set equal to 1 (BESS enabled);
- State 2.3 indicates a situation where the BESS alone cannot provide sufficient reserve levels. In this state, to ensure grid security in case of downward net-load variation, the power produced by the PV power plant is preemptively limited. The calculation and the action of the limitation are analogous to the state 1.2: The power difference between the minimum DOR $minR_{DOWN}$ and the DOR available $R_{DOWN}2$ is calculated ($lackR_{DOWN}$). This value is subtracted from the power currently generated by the MV-connected PV power plant ($PVrt$), determining the value with which the PV

active power has to be limited ($maxPVLim2$). An "*if*" condition is introduced to prevent negative limit values, and the actual limit value sent to the PV power plant's CCI is $PVLim2$. The counter k_{PVLim2} is incremented each cycle in which $R_{DOWN}2$ is higher than 110% of the required $minR_{DOWN}$ and is used to impose a temporal hysteresis for state exit.

Within the macro-state 3, for UOR control, 4 states are present:

- State 3.1 indicates a situation where the normal UOR of the MPP (R_{UP}) exceeds the required UOR ($minR_{UP}$), satisfying security constraints.
- State 3.2 indicates a scenario where enabling the BESS is necessary to increase the UOR by activating frequency regulation service. Within this state, the new available UOR ($R_{UP}2$) is defined by adding the UOR provided by the MPP to the UOR provided by the BESS: $R_{UP}2 = R_{UP} + R_{UPBESS}$. The $StateBESS$ variable, initially equal to 5 (BESS disabled) is set equal to 1 (BESS enabled);
- State 3.3 indicates a situation where, even with the BESS enabled, the available UOR would not be able to withstand the maximum expected upward load deviation. A request is then sent to the MPP to make a higher level of UOR available. Within this state, the actions performed by the MGC include updating the UOR value as seen in state 3.3 and calculating the $AskMPP$ variable. This variable represents the set-point of UOR that the MPP must achieve and is calculated as the required UOR value decreased by the UOR provided by the BESS: $AskMPP = minR_{UP} - R_{UPBESS}$. The $StateBESS$ variable, in this working state, is kept equal to 1. The counter k_{MPP} is incremented each cycle and is used to impose a temporal hysteresis for state exit.
- State 3.4 indicates a situation where all previous resources cannot guarantee an adequate UOR level. Therefore, a quantity of load that would need to be shed to maintain UOR levels at security values is calculated using the equation: $lackR_{UP} = minR_{UP} - R_{UP}2$. The amount of load to be shed is calculated discretely as a multiple of L_{STEP}, set at 20 kW. Upon first entry into the state ($flag_{Lshed}$=0), when the need for load shedding actions arises, the amount of load to be shed (L_{SHED}) is immediately set to the minimum multiple of L_{STEP} greater than the minimum power that would return the system to security UOR levels, using the equation: $L_{SHED} = ceil(lackR_{UP}/L_{SHED}) \cdot L_{SHED}$. The "ceil" function approximates to the nearest integer rounding up. In subsequent iterations ($flag_{Lshed}$=1), the amount of

load shedding to be applied is updated by summing the value determined in the previous state with the additional amount needed. This procedure was performed through the following verification process: It checks whether the amount of load to be shed matches with the same multiple of L_{STEP} observed in the previous cycle. If this condition is true, the shedding remains the same amount. Conversely, if the condition is false, shedding of the newly calculated multiple of L_{SHED} required is performed. For the calculation of the amount of load shedding, an additional control was considered: in the hypothetical scenario where no more dispatchable load is available, the implemented algorithm would continue to increase the value of L_{SHED} but would not be able to apply it. To prevent this from happening, in case additional load needs to be shed ($lackR_{UP} > 0$), if the amount of dispatchable load still available (in this case $L1 + L2 + L3 + L4 + L5$) is less than the value of L_{STEP}, this additional amount of load to be shed is neglected, imposing L_{SHED} equal to that of the previous interaction. The total load to be cut is divided among the various nodes using a weighting coefficient "c" calculated based on the power consumption of each residential load at the moment of state entrance. For the residential load 1, for example, the load shedding amount is $LshedRL1 = L_{SHED} \cdot c1$. Furthermore, a counter k_{Lshed} has been introduced that allows exiting these states only if these actions are no longer necessary for a predetermined number of consecutive iterations.

Having described the logic within each operational state of the MGC, the logic for the transition between the various states is now described. The various states of the finite state machine model are connected by arrows to which conditions are assigned. The transition from one state to another occurs when those conditions are met. The following tables show, in order of priority, all conditions and actions performed during transitions between states within macro-state 1 (Table 3.1), macro-state 2 (Table 3.2), and macro-state 3 (Table 3.3).

Table 3.1: All conditions and actions performed, in order of priority, during transitions between states within macro-state 1

from	**to**	**conditions**	**actions**
1.1	1.2	$P_{MPP} < MDRB$	$StatePVLim1 = 1;$ $PVLim1 = PVrt;$
1.1	1.1	-	-
1.2	1.1	$P_{MPP} > 1.5 \cdot MDRB$ $PVlim1 > 1.1 \cdot PVrt$	$StatePVLim1 = 5;$ $PVLim1 = 0;$
1.2	1.2	-	-

Table 3.2: All conditions and actions performed, in order of priority, during transitions between states within macro-state 2

from	**to**	**conditions**	**actions**
2.1	2.3	$R_{DOWN} + R_{DOWNBESS} < minR_{DOWN}$	$StateBESS = 1;$ $R_{DOWN}2 = R_{DOWN} + R_{DOWNBESS};$ $StatePVLim2 = 1;$ $PVLim2 = PVrt;$ $k_{PVLim2} = 0;$
2.1	2.2	$R_{DOWN} + R_{DOWNBESS} < minR_{DOWN}$	$StateBESS = 1;$ $R_{DOWN}2 = R_{DOWN} + R_{DOWNBESS}$
2.1	2.1	-	-
2.2	2.3	$R_{DOWN}2 < minR_{DOWN}$	$StatePVLim2 = 1;$ $PVLim2 = PVrt;$ $k_{PVLim2} = 0;$
2.2	2.1	$R_{DOWN} > 1.1 \cdot minR_{DOWN}$	$StateBESS = 5;$
2.2	2.2	-	-
2.3	2.1	$R_{DOWN} > 1.1 \cdot minR_{DOWN}$ $k_{PVLim2} \geq 5$ $PVLim2 > PVrt$	$StatePVLim2 = 5;$ $StateBESS = 5;$ $PVLim2 = 0;$
2.3	2.2	$R_{DOWN}2 > 1.1 \cdot minR_{DOWN}$ $k_{PVLim2} \geq 5$ $PVLim2 > PVrt$	$StatePVLim2 = 5;$ $PVLim2 = 0;$
2.3	2.3	-	-

As an example, it can be noted that from state 2.1, three arrows lead either to state 2.2 or state 2.3. Conditions that must be met to transition from one state to another are enclosed in square brackets, and the actions that the finite-state machine must perform when transitioning from one state to another are enclosed in curly braces. It is also important to note the number placed on each arrow (near the state 1.1), indicating the priority order in which the model checks the conditions for transitioning between states. In this example, the exit condition to state 2.2 is checked first, and if this is not met, the condition for transitioning to state 2.3 is checked. If none of the conditions are met, the system will remain within the starting state.

As can be observed in Fig. 3.5 and Tables 3.1, 3.2, and 3.3, during the transition between states, certain variables are initialized. For instance, the upward and downward operaring reserves available after the BESS enabling ($R_{UP}2$ and $R_{DOWN}2$) or the operating reserve set-point requested from the MPP (*AskMPP*). This is done to achieve a quicker and more efficient response from the MGC.

In addition, a condition for the transition to state 3.4, in which load shedding occurs, is that the variable *StateLim*1 equals 5. This condition ensures that the system is not in

Table 3.3: All conditions and actions performed, in order of priority, during transitions between states within macro-state 3

from	to	conditions	actions
3.1	3.3	$R_{UP} + R_{UPBESS} < minR_{UP}$ $StateMPP == 5$	$StateAskMPP = 1;$ $AskMPP = minR_{UP};$ $StateBESS = 1;$ $R_{UP}2 = R_{UP} + R_{UPBESS};$ $k_{MPP} = 0;$
3.1	3.2	$R_{UP} < minR_{UP}$	$StateBESS = 1;$ $R_{UP}2 = R_{UP} + R_{UPBESS}$
3.1	3.1	-	-
3.2	3.3	$R_{UP}2 < minR_{UP}$ $StateMPP == 5;$	$StateAskMPP = 1;$ $AskMPP = minR_{UP} - R_{UPBESS};$ $k_{MPP} = 0;$
3.2	3.1	$R_{UP} > 1.1 \cdot minR_{UP}$	$StateBESS = 5;$
3.2	3.2	-	-
3.3	3.4	$(R_{UP} + R_{UPBESS}) < minR_{UP}$ $k_{MPP} \geq 1$ $StatePVLim1 == 5$	$flag_{Lshed} = 0;$ $k_{Lshed} = 0;$ $c1 = L1/(L_{TOT} - Pros)$ $c2 = L2/(L_{TOT} - Pros)$ $c3 = L3/(L_{TOT} - Pros)$ $c4 = L4/(L_{TOT} - Pros)$ $c5 = L5/(L_{TOT} - Pros)$
3.3	3.1	$R_{UP} > 1.1 \cdot minR_{UP}$ $k_{MPP} \geq 10$ $StateMPP == 5;$	$StateAskMPP = 5;$ $AskMPP = 0;$ $StateBESS = 5;$
3.3	3.2	$R_{UP}2 > 1.1 \cdot minR_{DOWN}$ $k_{MPP} \geq 10$ $StateMPP == 5$	$StateAskMPP = 5;$ $AskMPP = 0;$
3.3	3.3	-	-
3.4	3.3	$(R_{UP}2 - L_{SHED}) > 1.1 \cdot minR_{UP}$ $k_{Lshed} \geq 5$	$k_{MPP} = 0;$ $LshedRL1 = 0;$ $LshedRL2 = 0;$ $LshedRL3 = 0;$ $LshedRL4 = 0;$ $LshedRL5 = 0;$
3.4	3.4	-	-

state 1.2, in which PV limitation occurs due to an excessively low net load. It would be an absurdity to perform load-shedding when the net load is already extremely low.

Finally, some arrows return to the same starting state. These transitions are necessary to repeat the instructions contained in these states at predetermined intervals. In fact, for all transition conditions from one state to another in the finite-state machine, the "*every(400,tick)*" function is present. This condition allows the MGC to check the operational

status of the island network every 400 time steps, corresponding to 0.05 seconds of simulation time, i.e. 3 minutes of simulated time. The relation between "simulation time" and "simulated time" will be discussed in Section 3.2.2.

It is deemed that the operation update of the control action should align with the temporal framework of reserve management functions within the SCADA/EMS functions of transmission electrical systems. As delineated by [100], reserve management typically interfaces with security analysis and contingency analysis procedures, which, within the SCADA/EMS domain, are within a temporal range from minutes to tens of minutes. These temporal frameworks are further substantiated by the organizational schemes of security functions in a SCADA system, as outlined in [101], identifying a time frame of 1-5 minutes for recognizing the system's operational state and 1-10 minutes for contingency analysis.

To harmonize with the aforementioned SCADA/EMS systems, a refresh time for the algorithm that is aligned with these intervals has been proposed. Considering the isolated nature of the examined system, its limited control resources, and the faster dynamics compared to those of large interconnected systems, it is judicious to refer to the 1-5 minute time interval. For the studies conducted, a refresh time of 3 minutes has been chosen, positioned as an intermediate value within this interval.

3.1.5 Operating reserve requirement evaluation method for isolated microgrids

To cope with the variability of load and generation on the island and ensure service continuity with the increasing penetration of renewable energy installations, it is crucial to appropriately assess the minimum UOR and DOR to be guaranteed throughout the various days of the year. As observed in the previous chapters, the load variability on the island is substantial, and evaluating the reserve deterministically, as currently done on the island, is not an optimal choice. The allocated quantity might be insufficient in some months and excessive in others, leading to increased disruptions and operational costs for the island.

This section describes the reserve evaluation method used in this work, which will be implemented and utilized in the tests presented in Section 3.4. Starting from the historical profiles of maximum-average-minimum load recorded on the island (shown and described in Section 1.5.1), a quantity of reserve both upward and downward, that depends on the net load measurements during the network's operation, is defined. This method also ensures a minimum reserve both upward and downward at all times.

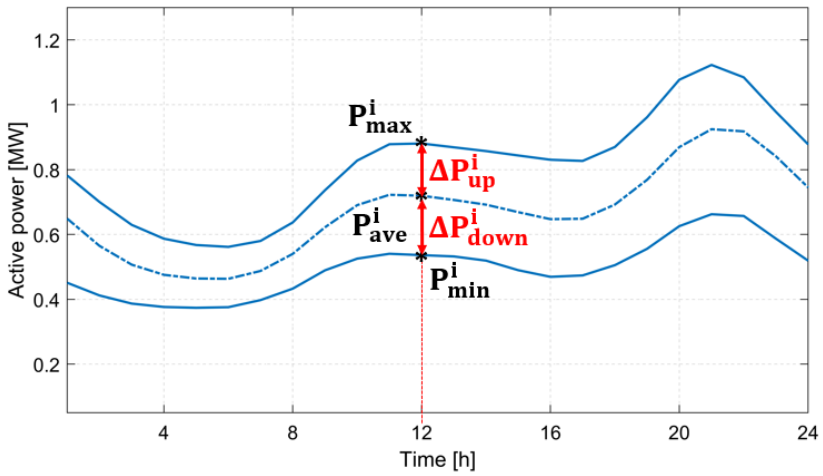


Figure 3.6: Graphical representation of the calculation of the maximum historical upward deviation

During the simulations performed and subsequently shown in this chapter, the historical load profiles used by the minimum reserve calculation method are the load curves for the years 2018-2019 (Fig. 1.6). As the actual load on the island during operation, the load curves for the year 2021 were used (Fig. 1.7).

Starting from the maximum-medium-minimum load profiles observed in Fig. 1.6, at each i-th iteration of the MGC, in which the RTA must be implemented, the maximum historical upward deviation ΔP^i_{up} (kW) is calculated. This is the difference between the historical maximum load P^i_{max} (kW) and the historical average load P^i_{ave} (kW):

$$\Delta P^i_{up} = P^i_{max} - P^i_{ave} \tag{3.1}$$

For the calculation of the DOR, the procedure is analogous. At each iteration of the MGC, the maximum historical downward deviation ΔP^i_{down} (kW) is calculated:

$$\Delta P^i_{down} = P^i_{ave} - P^i_{min} \tag{3.2}$$

A graphical representation of the calculation of the maximum historical upward and downward deviations is shown in Fig. 3.6, using as an example the month of August at midday.

Through the values of maximum, average, and minimum historical loads (P^i_{max}, P^i_{ave}, and P^i_{min}, respectively), a characteristic is generated that relates the relative UOR to be guaranteed r^i_{up} (p.u.) and the measured electrical load P^i (kW). This characteristic is shown in Fig. 3.7.

The obtained value r^i_{up} represents the amount of UOR to be guaranteed relative to the

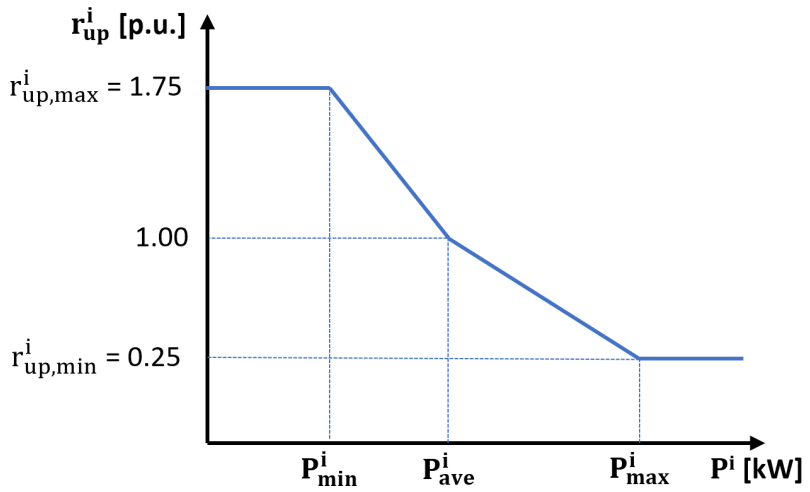


Figure 3.7: Characteristic relative upward operating reserve - measured load

maximum historical upward deviation ΔP^i_{up} (kW). The absolute UOR to be guaranteed based on the historical data $R^i_{h,up}$ (kW) is then given by the following product:

$$R^i_{h,up} = r^i_{up} \cdot \Delta P^i_{up} \tag{3.3}$$

Setting a minimum relative UOR value $r^i_{up,min}$ (p.u.) greater than zero ensures that a minimum UOR is always guaranteed. This value has been set to 25% of the maximum historical upward deviation. When the island load is close to the minimum value P^i_{min} (kW), one might imagine having to guarantee an UOR equal to the deviation between the maximum and minimum historical loads. This deviation, as discussed in Section 1.5.1, can be very high, even exceeding the current net-load. To prevent this, a maximum relative UOR value $r^i_{up,max}$ (p.u.) has also been defined, limiting the maximum UOR that the method can request. This value has been set to 175% of the maximum historical upward deviation. The absolute UOR to be guaranteed based on the historical data $R^i_{h,up}$ (kW) obtained through this method is finally compared with the hypothetical loss of renewable generation due to cloud cover P^i_{pv} (kW), and the actual minimum UOR to be guaranteed $minR^i_{up}$ (kW) is the maximum of these two values:

$$minR^i_{up} = \max\{R^i_{h,up}, P^i_{pv}\} \tag{3.4}$$

For determining the actual DOR to be guaranteed, the procedure is analogous. Through the values of maximum, average, and minimum historical loads (P^i_{max}, P^i_{ave}, and P^i_{min}, respectively), a characteristic is generated that relates the relative DOR to be guaranteed r^i_{down} (p.u.) and the measured load P^i (kW). This characteristic is shown in Fig. 3.8.

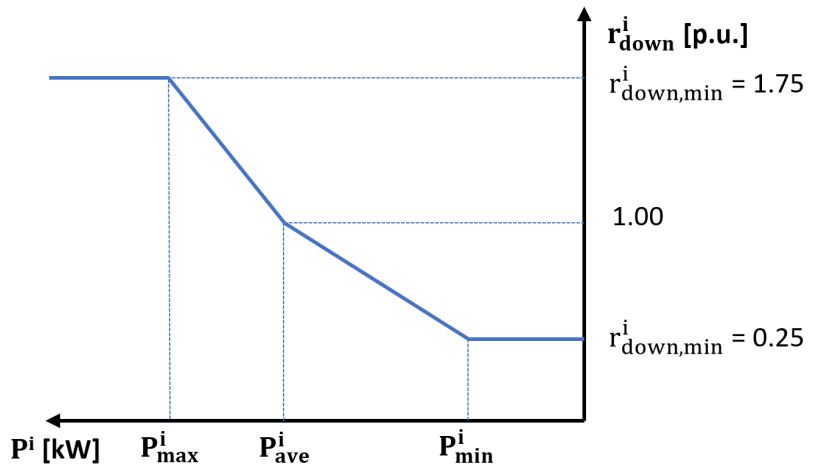


Figure 3.8: Characteristic relative downward operating reserve - measured load

The value r^i_{down} obtained represents the amount of DOR to be guaranteed relative to the maximum historical downward deviation ΔP^i_{down} (kW). The absolute DOR to be guaranteed based on the historical data $R^i_{h,down}$ (kW) is then given by the following product:

$$R^i_{h,down} = r^i_{down} \cdot \Delta P^i_{down} \tag{3.5}$$

The minimum and maximum relative DOR values $r^i_{down,min}$ (p.u.) and $r^i_{down,max}$ (p.u.) have been set to 175% and 25% of the maximum historical downward deviation, respectively, similarly to the case of UOR. The absolute DOR to be guaranteed based on the historical data $R^i_{h,down}$ (kW) obtained through this method is finally compared with the hypothetical loss of the local load that is absorbing the most power at that moment $P^i_{loadmax}$ (kW), for example, due to the opening of the protection switch located in the substation as a result of a fault. The actual minimum DOR to be guaranteed $minR^i_{down}$ (kW) is the maximum of these two values:

$$minR^i_{down} = \max\{R^i_{h,down}, P^i_{loadmax}\} \tag{3.6}$$

3.2 Modelling of a small island for real-time algorithms tests

During the development of the proposed Real-Time Algorithm (RTA), it was assumed that, under acknowledged system vulnerability conditions, additional controls could be activated on specific devices (particularly the storage system owned by the distributor) to

provide support for system stability. This support is typically delivered through automatic regulation actions implemented on network resources, such as those mandated by the CEI 0-16 grid code (introduced in Section 3.1). To evaluate the impact of the decisions made by the proposed RTA, taking into account all the dynamics present on the network, and to determine the benefits on the frequency transients in terms of Rate of Change of Frequency (RoCoF), minimum under-frequency (nadir), settling time and stability, a dynamic model of the distribution network of the reference small Italian island under investigation was developed to simulate electromechanical transients.

This initial model required defining the dynamic model of the machines in the Main Power Plant (MPP) and describing the frequency response of the operational features of the main distributed generation units (primarily BESS and PV), including the control actions imposed by the CEI 0-16 grid code. The dynamic network model was created to be integrated into a real-time Power Hardware-in-the-Loop (PHIL) simulation. Given that electromechanical oscillations have dynamics that unfold within a few seconds of simulation, this initial model was characterized by the presence of constant loads.

A second model was constructed to test the proper functioning of the proposed RTA. The use of non-programmable sources for production leads to increased net-load volatility due to potential production variations from weather conditions or ramps introduced by PV shutdown in the minutes before sunset. Moreover, in the face of increased (net) load volatility, the possible reduction in the number of synchronous machines connected to the system also results in a decrease in available Upward Operating Reserve (UOR) or Downward Operating Reserve (DOR) for system balancing. The second developed network model was designed to reproduce the behavior of the isolated system over a longer time interval (e.g., the entire day) following a quasi-static model. The quasi-static analysis aimed to capture time-dependent aspects of power flow, including the interaction between daily load variations, PV production, and control actions of the generation units. Unlike the first model, the MPP did not require a dynamic representation and was modeled using an ideal generator. Instead, the model allowed simulating the behavior of the control system present in the MPP, studying the influence of charge and discharge cycles of BESS on operating reserve availabilities, and determining potential fluctuations in active power exchanged on the system. The model included modeling loads and renewable generation using chronological curves to represent expected variations in net-load on the network throughout the day.

3.2.1 Dynamic grid model of a reference small Italian island

The small Italian island under study, described in Section 3.1, was modeled in the Matlab/Simulink environment. This choice has been taken to make this dynamic model usable for real-time simulations through a real-time simulator from the OPAL-RT company [102]. The grid model is depicted in Fig. 2.4. The RES and loads have been modeled using a *three-phase p-q theory-based dynamic load*, proposed by the authors in [12, 16], characterized by a less computation burden than the *three-phase dynamic load* available in the Simulink's library. Adopting this load model allowed resources to be modeled more accurately, without incurring overruns. In Fig. 3.9 the overall grid model has been shown.

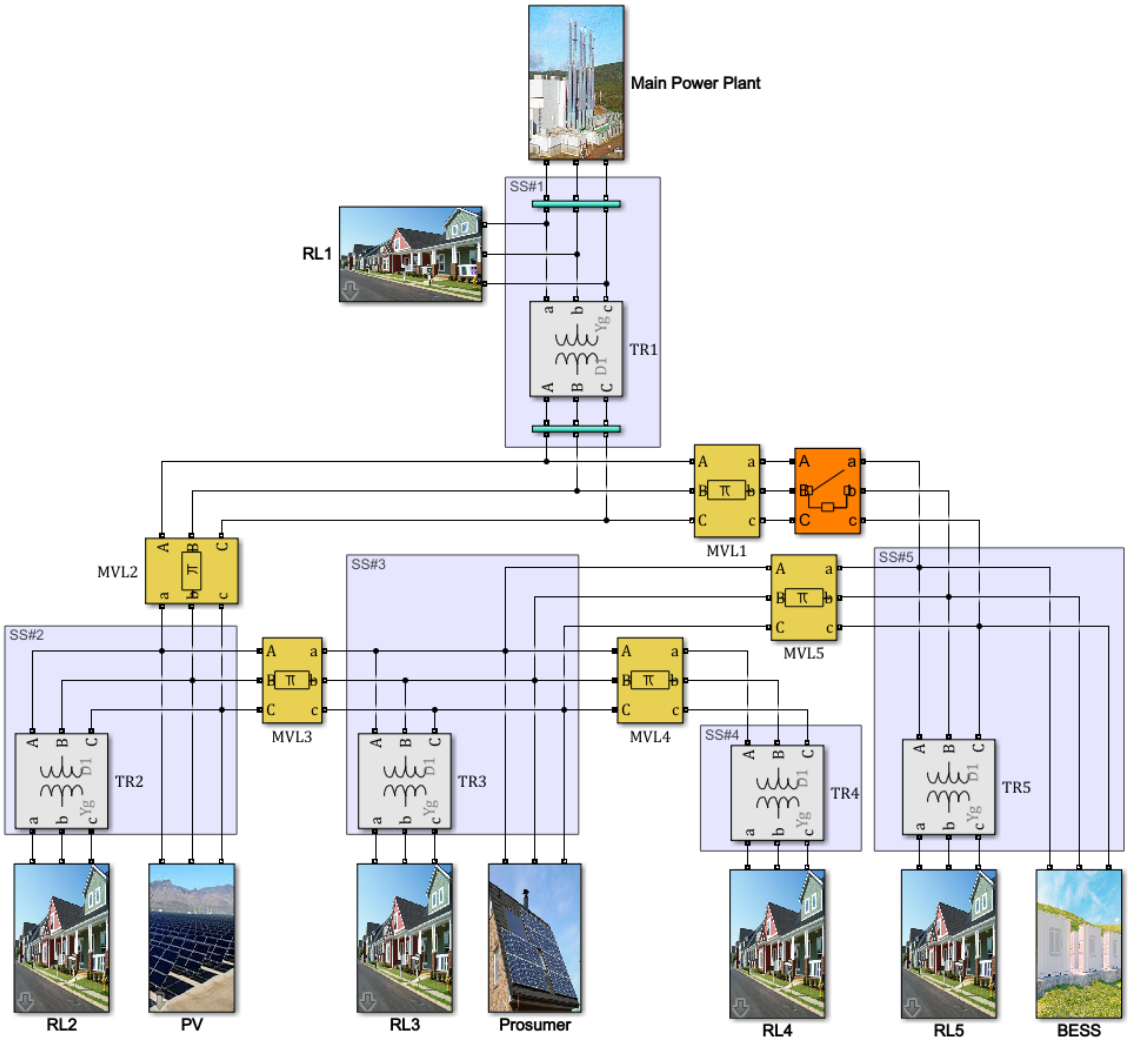


Figure 3.9: Dynamic model of the small Italian island under study

The distribution network operates at 10 kV and comprises five substations (from SS#1 to SS#5). Each substation supplies a portion of the island's residential load (from RL1 to

RL5). The Main Power Plant (MPP) is connected to SS#1, where the main load source (RL1) is connected.

The MPP consists of 4 diesel units operating at 400 V with a maximum power capacity of 480/600 kW/kVA (1920/2400 kW/kVA for the entire plant) and no technical minimum. In this model, for simplification and to enable real-time simulation, the MPP has been represented by an equivalent diesel generator. The MPP directly feeds RL1 and connects to the MV distribution grid through an LV/MV transformer (TR1).

The MV distribution comprises 5 MV distribution lines (from MVL1 to MVL5) connecting the substations in a loop. MVL1 is typically open during normal operation but ensures reclosure in case of faults or maintenance work. Each distribution line has been modelled using the Simulink three-phase PI model (*Three-Phase PI Section Line*). Positive-sequence characteristics have been set accordingly to the actual data received by the distributor.

As in Chapter 2, SS#2 was assumed to host an MV PV plant, with an installed capacity of 200 kWp (PV capacity used as a reference in the studies in Section 2.3.2, roughly equivalent to the Renewable Energy Sources (RES) penetration target set by the Italian Ministry of Economic Development [73] for the small Italian island under study by the year 2020). SS#5, instead, was assumed to host a 250/300 kW/kWh BESS owned by the DSO. Additionally, as introduced earlier, a generic prosumer was assumed to be connected to SS#3 for the purpose of testing the RTA.

3.2.1.1 Main power plant dynamic model

The diesel generation plant has been modelled as an equivalent synchronous generator, connected to the MV grid via a 0.4/10 kV equivalent step-up transformer. The equivalent model of the diesel generation plant is shown in Fig. 3.10.

Exciter and governor were modeled according to typical schemes that can be found in the simulation software libraries. As the presented model aims to simulate the behaviour of the diesel plant in a specific operating point, controllers and the synchronous generator model have been adapted for an overall equivalent rated power that depends on the number of active diesel units. Total inertia was set to a value of 0.3 s, according to the technical specifications of the actual diesel generators used by the MPP of the island under study. The equivalent step-up transformer shown in Fig. 4.8 has been sized according to the total rated power of the MPP.

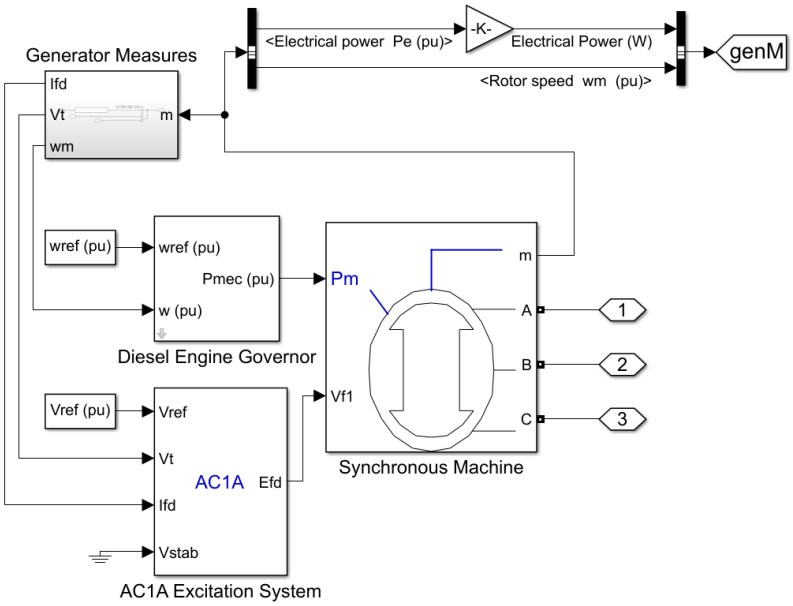


Figure 3.10: Equivalent diesel generator model for the MPP

3.2.1.2 Residential load and interface protection system dynamic models

As an example, the dynamic model of the residential load RL1 has been depicted in Fig. 3.11.

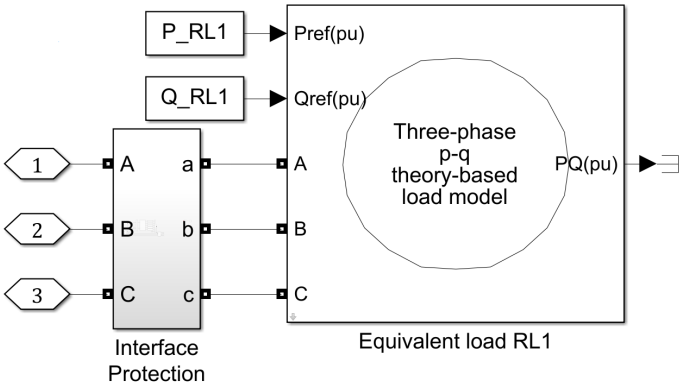


Figure 3.11: Residential load dynamic model

As already said, the equivalent residential loads have been modeled using a *three-phase p-q theory-based dynamic load*, proposed by the authors in [12, 16]. As input of these models, the active and reactive power set-point have been sent. The prosumer, included in the network model for testing purposes, was modeled in the same way. These values change every simulation in accordance with the case study considered. As depicted in Fig. 3.11, each residential load has been equipped with an Interface Protection System (IPS) model, shown in Fig. 3.12. This IPS takes into account all the specifications mandated by

the Italian grid code CEI 0-16.

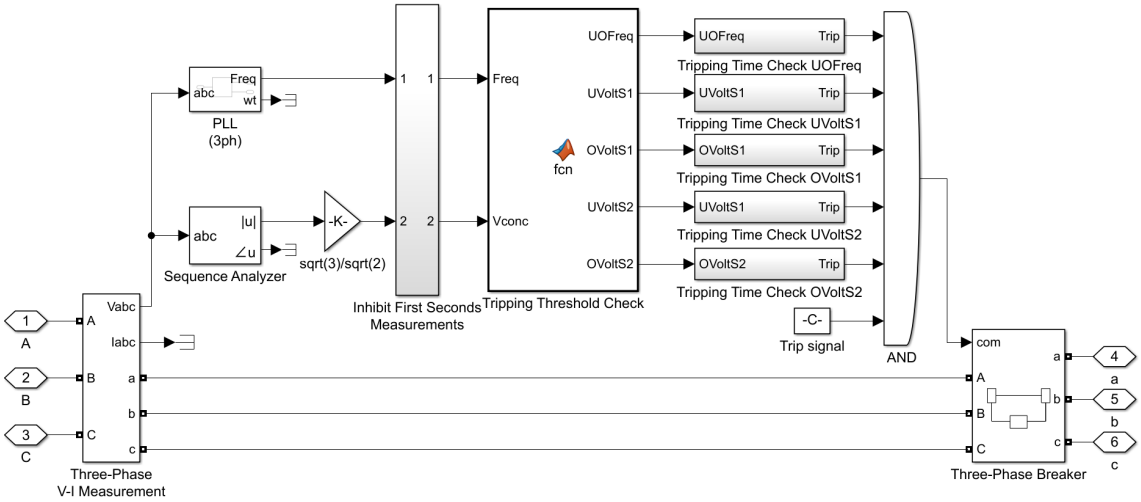


Figure 3.12: Interface protection system dynamic model

Through a measurement block ("Three-Phase V-I Measurement") the waveforms of the three-phase voltages are made available. From these, through a "Phase-locked loop (PLL)" block it is possible to get the grid frequency and from a "Sequence Analyzer" block the amplitude of the three-phase star voltage. Wanting to get the effective value of the concatenated voltage, that value was multiplied by $\sqrt{3}/\sqrt{2}$. At the beginning of the simulation, the network may start from unbalanced conditions and need a few seconds to stabilize. This basically depends on slight model differences in the calculation of initial conditions obtained through a steady-state Load Flow analysis and the model adopted for the electromechanical transient simulation (e.g., a generator in the Load flow is treated as a power injection to a MV bus while the electromechanical simulator takes into account internal generator impedances, small losses, non-symmetrical impedances etc.). To prevent protection from intervening in the first moments of simulation, before the system reaches its equilibrium point, voltage and frequency measurements are inhibited in the first seconds by passing through the subsystem called "Inhibit First Seconds Measurements".

Within the block, simply the nominal value of frequency (50 Hz) and voltage (10 kV) is imposed for the first 3 seconds of simulation. From repeated tests, it has been observed that the system was able to stabilize within that time. The voltage and frequency values go through a *MATLAB function* block, called "*Tripping thresholds check*" in which the instants when the frequency and voltage exceed certain thresholds are detected. The block is structured into five parallel "if" checks. Specifically, the block has the following operation:

- UOFreq is 1 if the frequency is between 47.5 Hz and 51.5 Hz, otherwise it is 0;

- UVoltS1 is 1 if the voltage is greater than 0.85 Vn, otherwise it is 0;
- OVoltS1 is 1 if the voltage is less than 1.1 Vn, otherwise it is 0;
- UVoltS2 is 1 if the voltage is greater than 0.15 Vn, otherwise it is 0;
- OVoltS2 is 1 if the voltage is less than 1.2 Vn, otherwise it is 0.

These checks were made separately because the grid code CEI 0-16 indicates different tripping times for exceeding these thresholds. To account for the tripping times of the protections, the outputs of the "*Tripping Threshold Check*" block go through "*Tripping Time Check*" subsystems that count the time for which the individual threshold has been exceeded and, if that time exceeds the set tripping time, sends a "0" signal to the output. The tripping times set for the various thresholds, and meeting those specified in CEI 0-16 [53], are as follows:

- for UOFreq: 4 seconds;
- for UVoltS1: 1.5 seconds;
- for OVoltS1: 600 seconds;
- for UVoltS2: 0.2 seconds;
- for OVoltS2: 0.6 seconds.

In this way, through an "AND" logic operator, when even one of the thresholds is exceeded for a time longer than the tripping time set for that threshold, a value of "0" will be sent as an input to the "Three-Phase Breaker" block, changing its state from "closed" to "open," disconnecting the generic system from the grid. This block, in fact, represents a three-phase breaker that maintains its initial state (set as closed) as long as "1" is sent to it as input and changes its state when "0" is sent to it instead. In addition, an external tripping signal was considered to manually force the tripping of the protection during testing.

3.2.1.3 Battery energy storage system dynamic model

The island's BESS dynamic model has been illustrated in Fig. 3.13. As can be seen in the figure, there is both a block that accounts for the dynamics of the component (called "*Energy Storage*"), based on applications and examples on the official Mathworks website

[103], and the control system that determines the reference active and reactive power values to be imposed on the device. In addition to these, as can be seen in Fig. 3.13, the BESS has also been equipped with the IPS previously discussed.

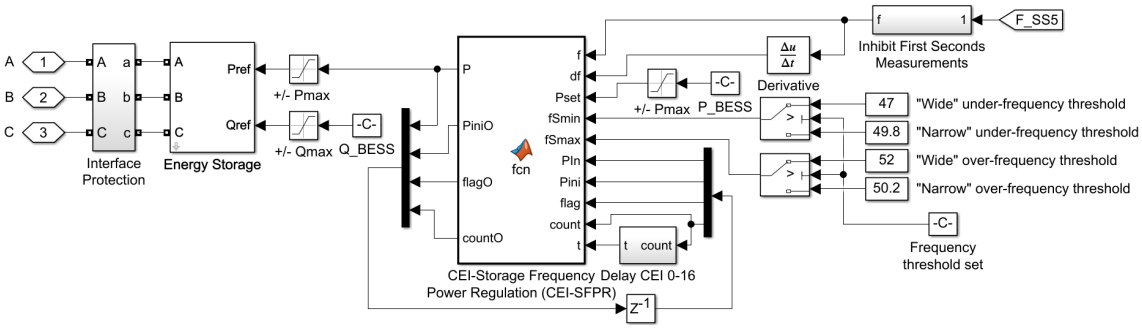


Figure 3.13: Battery energy storage system dynamic model

The parameters of the dynamic storage model were set based on literature and commercial datasheets, including a nominal active power of 250 kW, a nominal capacity of 300 kWh, and an overall efficiency of 80%. Since the grid model is made in such a way that transient stability studies can be carried out, the control system of the device was made taking into account the requirements mandated by the CEI 0-16 Italian grid code regarding the "*Active Power Regulation of a Storage System for Over- and Under-Frequency Transients Originating on the Grid*", i.e. the already mentioned CEI-SFPR.

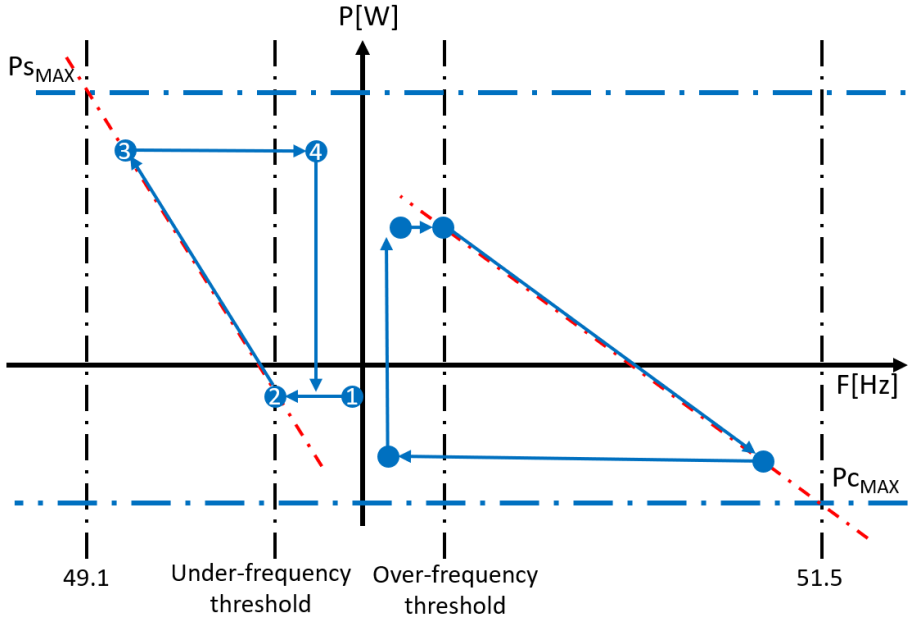


Figure 3.14: Graphical illustration of the CEI-SFPR control law

The CEI-SFPR control law has been depicted in Fig. 3.14. Regardless of the storage operating point (point 1 in the figure), it must not vary the exchanged power as long as the

frequency remains within the user-settable under-frequency and over-frequency thresholds. If the frequency drops below the under-frequency threshold (point 2 in the figure), the storage system must gradually reduce the absorbed power (if it was in absorption) and then start discharging along a line passing through the power being exchanged at the time of reaching the under-frequency threshold and the maximum power that the device can absorb, until the frequency nadir is reached (point 3 in the figure). When the frequency begins to rise, the power exchanged by the device must no longer follow the line it followed while the frequency was decreasing, but it must remain constant for a minimum period of 300 seconds (point 4 in the figure). After this time, the device can gradually return to the pre-event operating point, linearly with a transient duration of not less than 300 seconds to avoid re-exciting the system from a dynamic point of view. The control law is identical for over-frequency events.

As can be seen in Fig. 3.14, according to what is imposed by the grid code, the maximum output power must be reached for a frequency value of 49.1 Hz while the maximum absorption power must be reached for a frequency value of 51.5 Hz. The CEI-SFPR control law has been implemented in the Matlab function block visible in Fig. 3.13.

As previously highlighted in this chapter, the BESS is required to continuously adjust its exchanged power based on the CEI-SFPR control, as mandated by the grid code. However, in the proposed control architecture of this chapter, the island's MGC can influence the CEI-SFPR control trip thresholds. This allows for a transition between a set of "narrow" thresholds and a set of "wide" thresholds, and vice versa.

In the implementation of this control system, the default values (49.8 Hz and 50.2 Hz) were employed as the threshold values corresponding to the "narrow" thresholds. During this setting, the BESS is considered "enabled" for frequency regulation. On the other hand, the "wide" thresholds were established at frequency values requiring the storage system to exchange the maximum power (49.1 Hz and 51.5 Hz). These threshold values are considered extreme, designating the BESS as "disabled" for frequency regulation.

3.2.1.4 Photovoltaic power plant dynamic model

The island's MV-connected PV power plant dynamic model has been illustrated in Fig. 3.15.

The PV power plant is modeled by means of a three-phase p-q theory-based load model. The amount of active and reactive generation can be set as an external input to the

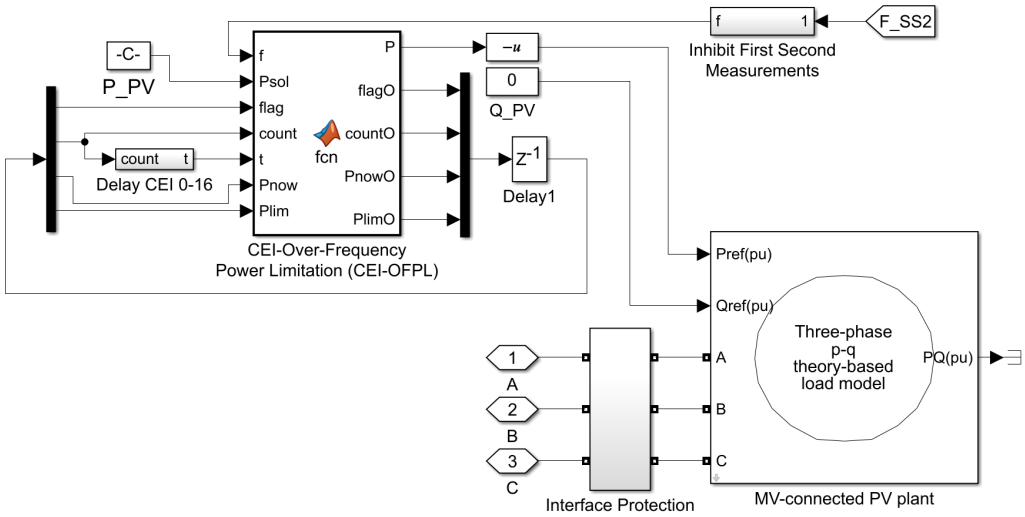


Figure 3.15: Photovoltaic power plant dynamic model

dynamic load. Usually, the amount of PV production is imposed by a constant value (P_{PV}) depending on the case study considered. However, as required by the Italian grid code CEI 0-16 [53], the power generation can be curtailed for the purpose of primary frequency regulation. Accordingly to CEI 0-16, the reduction of the generated power follows a droop characteristics that depend on the frequency deviation from the 50 Hz nominal value. This control is called "Active Power Limitation for Over-frequency Transients Originating in the Grid" by the national grid code CEI 0-16. As mentioned at the beginning of the chapter, to make the text more readable, it was called *CEI-Over-Frequency Power Limitation (CEI-OFPL)* in this document. In particular, for values of frequency between 50.3 Hz and 51.5 Hz, a droop between 2% and 5% must be adopted. Typically droop is set to 2.4% so that the PV production is completely curtailed when the maximum over-frequency limit (51.5 Hz) is reached. PV power plants are not required to vary the generated power for values of frequency between 47.5 Hz and 50.3 Hz. As with the other components of the grid model, except for the MPP which must always be connected, the PV power plant was also coupled by an IPS, shown in Fig. 3.12.

3.2.2 Quasi-static grid model for the real-time algorithm testing

The overall model of the network, along with all its components, developed for the study of electromechanical transients, has been modified to allow for studies on the adequacy and availability of operating reserve over longer time intervals. This section describes the modifications made to simulate the behavior of slower dynamics that can describe

the system's evolution over a broader time window (e.g. an entire day). This quasi-static model was built with the goal of matching 1 second of simulation to 1 hour of simulated time (a 24-hour day is solved in 24 seconds of simulation). The simulation step (Ts) of the model, as well as that of the dynamic model, is 0.125 milliseconds, and each Ts corresponds to 0.45 seconds of simulated time (every 8000 Ts results in 3600 seconds of the day simulated). The ratio of simulated time (in hours) to the simulation time (in seconds) is defined as "time ratio" (Tr) and is equal to 1. Before describing how the model of each component in the network has been modified, it is worth noting that it is not necessary to model interface protections in this analysis, resulting in a reduction in simulation times.

3.2.2.1 Modification of the main power plant model and consideration of its operating reserve

Long-term simulations do not require modeling fast dynamics like electromechanical transients, allowing for a simplification of the plant model. Unlike the first model, the Main Power Plant (MPP) does not require a dynamic representation but was modeled using an ideal infinite power source generator. Specifically, the entire diesel production plant (consisting of the 4 units) has been modeled using the "Three-Phase Source" block in Simulink. This modeled plant is responsible for the entire power demand net of contributions from MV-connected PV power plant and BESS. However, using this model does not preclude analyzing the reserve provided by the production plant. Fig. 3.16 shows the quasi-static model of the MPP with the logic regarding the calculation of the number of active diesel units, the available operating reserve, and the assessment of its operating status.

Based on the total active power supplied by the plant P_{MPP} and the nominal active power of a diesel unit (P_N = 480 kW), the number of active generators N_{GEN} can be calculated with eq. (3.7).

$$N_{GEN}(t) = ceil(\frac{P_{MPP}(t)}{P_N}) \tag{3.7}$$

This is supplemented by the control logic that manages the MPP's diesel units, described in [104]. This logic has been implemented in the *Matlab function* block "Control Unit's Logic".

The logic implemented, if the control unit's logic is enabled (variable *enable* = 0 visible in Fig. 3.16), checks if the available upward reserve R_{UPMPP} is less than a minimum

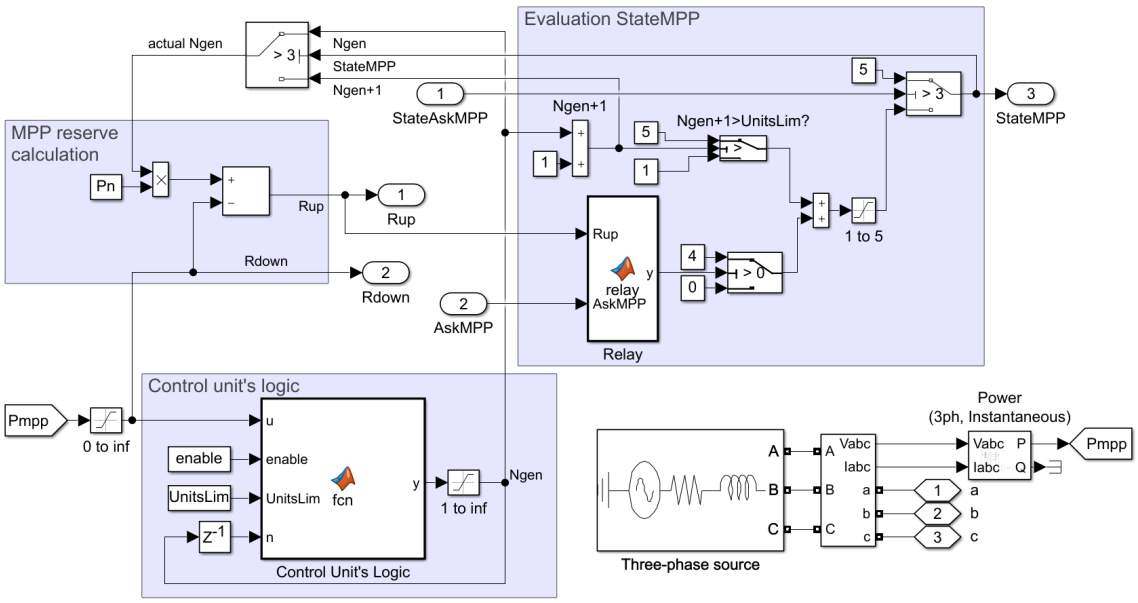


Figure 3.16: Quasi-static model of the Main Power Plant with the attached logic

value set in the control unit (called "P1201" in [104]). If this value is indeed lower, then the previously calculated minimum number of generators will be increased by one. On the contrary, if, by turning off the last unit just activated, the available upward reserve R_{UPMPP} should be greater than another threshold "P1202", necessarily greater than the value of "P1201" to ensure a certain hysteresis to the control system, the logic turn off one diesel generator. If the control unit's logic is not enabled ($enable = 0$), the number of active generators will always be the minimum number of units needed to satisfy the load calculated using eq. (3.7), without utilizing the thresholds "P1201" and "P1202". The number of generators calculated was finally limited to the maximum number of available generators "$UnitsLim$", normally set to the number of diesel units in the MPP but can be reduced to emulate some diesel units in maintenance.

In the "Evaluation StateMPP" model section in Fig. 3.16, the system processes the request sent by the MGC. Given the presence of only diesel units in the MPP, the additional UOR required can only be provided by turning on an additional diesel unit in addition to the one that the MPP would normally turn on to power the load (or for the control unit's logic). For the purpose of these tests, it is assumed that the MPP always accepts the request sent by the MGC, turning on an additional diesel unit whenever possible.

In Fig. 3.16, it can be seen that, thanks to the switch on the right, as long as the value of the variable *StateAskMPP* is equal to 5 (indicating that the MGC is not in state 3.3), the variable *StateMPP* also remains at 5 (indicating that the MPP is not taking

actions to accommodate the requests of the MGC). However, when *StateAskMPP* equals 1 (indicating that the MGC is in state 3.3), the variable *StateMPP* depends on the number of diesel units that are both turned on and available in the MPP.

Firstly, it is checked whether the number of active diesel units is less than or equal to the number of available diesel units (*UnitsLim*). If this condition is not met, implying that the MPP cannot start an additional unit, the operational state of the MPP (*StateMPP*) is set to 5. In the scenario where the MPP has available diesel units that can be turned on, the variable *StateMPP* is set to 1.

The MPP might fulfill the request from the MGC without having to force the activation of an additional diesel unit. For example, if, due to load variations throughout the day, the available UOR without the additional diesel unit turned on would be sufficient to meet the reserve set-point requested by the MGC. For this reason, it has been deemed appropriate to allow the MPP to change its operational state when it can meet the request without forcing the activation of diesel units.

The "Relay" block compares the MPP's UOR (R_{UP}) with the UOR set-point sent by the MGC (*AskMPP*). If *AskMPP* is greater than R_{UP}, the output of the "Relay" block (y) is set to 0, and *StateMPP* is set to 1. On the contrary, if R_{UP} exceeds 110% of the request *AskMPP* (to introduce hysteresis, similar to the conditions for exiting the states of the MGC described in Section 3.1), the output y is set to 1, and the operational state of the MPP (*StateMPP*) is set to 5, indicating that the MPP is not taking any action to meet the request of the MGC.

The *StateMPP*, moreover, indicates the number of diesel units turned on. In fact, if *StateMPP* is equal to 5, the number of turned on diesel units is determined by the control unit's logic or the minimum specified by eq. (3.7) (N_{GEN}). On the other hand, if the MPP is forcing the activation of an additional diesel unit to meet the MGC's request, and therefore *StateMPP* = 1, then an extra diesel unit will be turned on, resulting in a total of $N_{GEN}+1$ turned on units.

Knowing the number of diesel units turned on, the available upward operating reserve of the plant R_{UP} (3.8) and downward operating reserve R_{DOWN} (3.9) can be defined. In particular, R_{DOWN} is set equal to the total active power delivered by the MPP since, from the information about the diesel units used on the island, they do not have a technical minimum and can reduce their power output to 0.

$$R_{UP}(t) = (N_{GEN}(t) \cdot P_N) - P_{MPP}(t) \tag{3.8}$$

$$R_{DOWN}(t) = P_{MPP}(t) \tag{3.9}$$

3.2.2.2 Partitioning of island load profiles and implementation of load shedding actions

The island load profiles used to carry out the OP tests, provided by the DSO, refer to the total power consumption of the island. These profiles have been proportionally distributed among residential loads based on the declared installed power under each substation. The utilization coefficient K_u was defined as the ratio of the total power absorbed by the island, at every moment, to the total installed power (3.10). This coefficient is then multiplied by the installed power of the individual substation and used as the load profile for the residential loads connected to that substation (3.11).

$$K_u(t) = \frac{P_{load}(t)}{P_{Nload}} \tag{3.10}$$

$$P_{loadRL1}(t) = K_u(t) \cdot P_{NloadRL1} \tag{3.11a}$$

$$P_{loadRL2}(t) = K_u(t) \cdot P_{NloadRL2} \tag{3.11b}$$

$$P_{loadRL3}(t) = K_u(t) \cdot P_{NloadRL3} \tag{3.11c}$$

$$P_{loadRL4}(t) = K_u(t) \cdot P_{NloadRL4} \tag{3.11d}$$

$$P_{loadRL5}(t) = K_u(t) \cdot P_{NloadRL5} \tag{3.11e}$$

The reactive power, for which data was not available, has been computed using a fixed power factor PF set at 0.8. This value corresponds to the ratio of the rated active power of MPP diesel units (480 kW) to their rated apparent power (600 kW).

The model employed for representing residential loads differs significantly from the one used in the dynamic grid model. For instance, the model of the residential load RL1 is illustrated in Fig. 3.17.

First, the dynamics of the Interface Protection System (IPS) was ignored, as it is no longer applicable given the adoption of an ideal constant-frequency generator, as discussed earlier. At the same time, the logic governing the low voltage Breaker Controllers BCs at the local level was incorporated to implement the load shedding commands given by the MGC.

Subsequently, in this quasi-static network model, the three-phase p-q theory-based

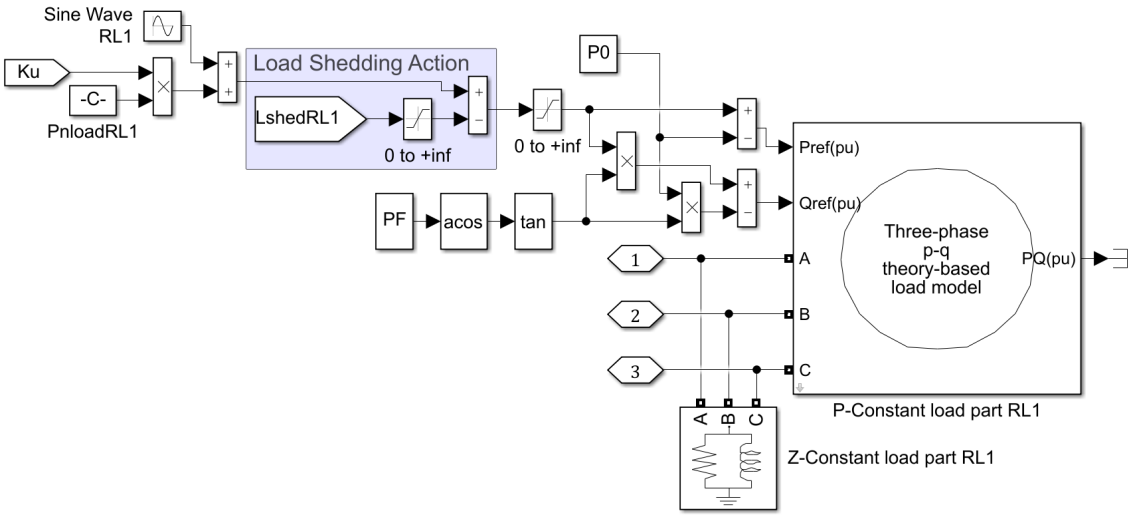


Figure 3.17: Quasi-static model of the residential load 1

dynamic load model was supplemented by a *Three-phase RLC load* block, which functions as a Z-constant load. Unlike the dynamic network model presented in the Section 3.2.1, which was designed for the analysis of short simulations in which the behavior of the load is considered constant and independent of voltage and frequency fluctuations, in the quasi-static network model it was deemed more appropriate to subdivide the load into 2 parts. This subdivision includes a component where power consumption is affected by grid conditions ("Z-constant" load model part) and another component where power consumption is not affected by these grid conditions ("P-constant" load model part).

The nominal active power assigned to the Z-Constant load part ($P0$) has been established by considering the average K_u of each residential load. Similarly, the nominal reactive power has been determined by adhering to the previously mentioned fixed PF for defining the reactive power profile.

The active and reactive power set-points imposed to the P-Constant load model part have been defined as the active and reactive power profiles discussed earlier, adjusted by subtracting the nominal active and reactive power of the Z-Constant load model part. This approach ensures an overall power consumption equivalent to the active and reactive power profiles, with variations around these values influenced by the grid's frequency and voltage during the simulations.

To differentiate the load profiles under the various substations and ensure that they do not all follow the same pattern, the load profile of each residential load was refined by adding a sinusoidally varying load profile. To keep the overall island load aligned with the load profile provided by the DSO, each added sinusoidal profile was configured with the

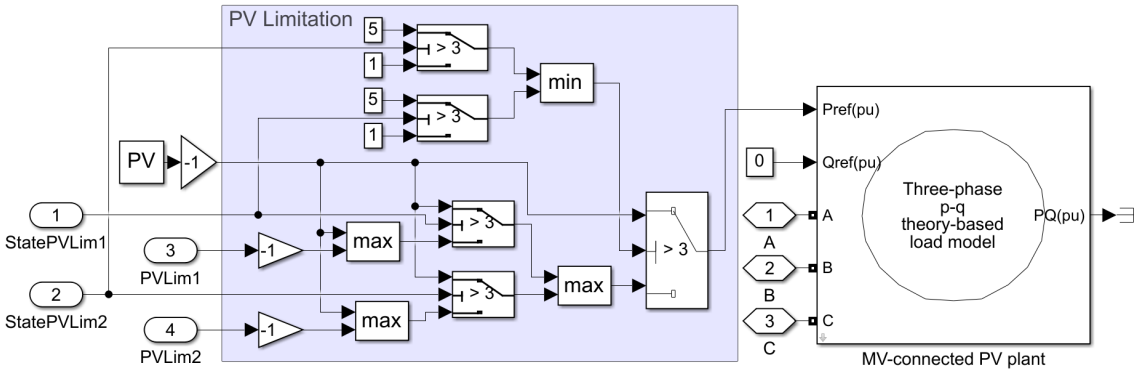


Figure 3.18: Quasi-static model of the PV power plant

same amplitude (10 kW) and each was offset by $1/5$ of a round angle from the others.

The "Load Shedding Action" section of the model, visible in Fig. 3.17, emulates the actions of BCs on the low-voltage grid. In fact, when the MGC enters state 3.4, it sends each residential load model an amount of load shedding ($LshedRL1$). This quantity is subtracted from the input load profile.

3.2.2.3 PV power plant behavior and implementation of the active power limitation actions

The model used to represent the PV system has not changed compared to the dynamic grid model presented in Section 3.2.1, as the three-phase p-q theory-based dynamic load model is sufficiently lightweight and accurate, requiring no modifications. However, the dynamics of the IPS and CEI-OFPL control, related to frequency dynamics, have been neglected since they are no longer applicable following the adoption of the ideal generator, as indicated above. Meanwhile, the logic of the local level controllers/CCIs was implemented to enable the PV system to interact with the MGC and apply its commands.

The PV generation profiles of the island under study were obtained from online databases [97], the same profiles used on the planning algorithm analysis proposed in Chapter 2. Having modeled a single PV system, these profiles were imposed directly without making any subdivisions.

Fig. 3.18 illustrates the PV system model and how the active power limitation actions sent by the MGC are applied. In the diagram shown in the "PV Limitation" section of the model, the limitation is imposed only if at least one of $StatePVLim1$ or $StatePVLim2$ is set to 1 (indicating that the MGC is in state 1.2 or state 2.3). The model emulating the PV system will follow the lower value between the limitation sent by the MGC and the input

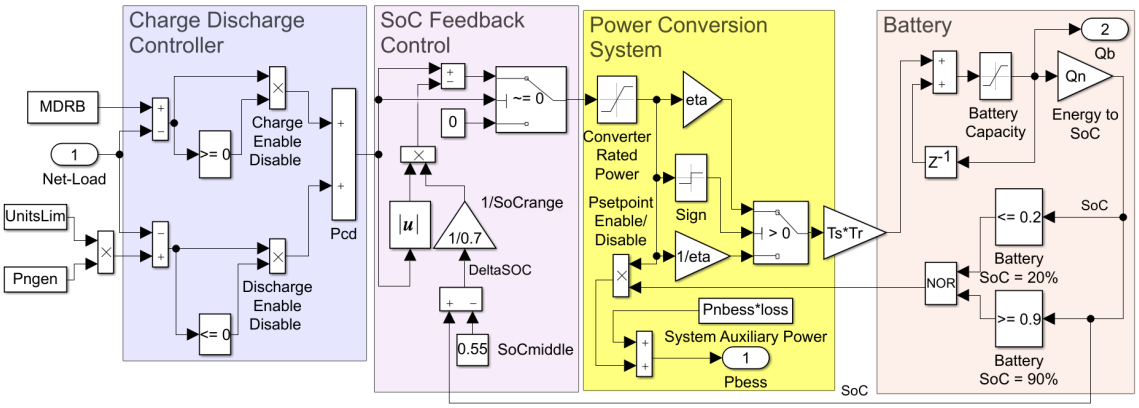


Figure 3.19: BESS logic-mathematical model and local level control systems

generation profile.

Both the input generation profile and the power limitation values sent by the MGC are positive, so they are multiplied by -1 and made negative. This is because the dynamic load model must receive negative set-point values to behave as a generation element.

3.2.2.4 BESS logic-mathematical model and local level control systems

In this quasi-static model, as residential loads and the PV power plant, even the BESS has been connected to the grid by a three-phase p-q theory-based dynamic load. As the BESS can both absorb and supply power, positive values indicate a charging phase (load behavior), while negative values indicate a discharging phase (generation behavior). The reactive power is consistently set to 0 vars, while the active power exchanged with the grid depends on a BESS logic-mathematical model and its local level control system, depicted in Fig. 3.19.

This model has been presented for the first time by the authors in [105] which included the model sections "Charge Discharge Controller", "Power Conversion System", and "Battery" visible in Fig. 3.19. In this model, the model section "SoC Feedback Control" has also been considered. Moreover, the "Charge Discharge Controller" was given a different purpose than that presented by [105], and has been used to adapt the BESS model to the case studies presented in this chapter.

Power Plant Support Controller: This control is based on the same logic of the "Charge Discharge Controller" presented by [105]. This control allows the BESS to support the grid at times of excess generation or load.

The controller is based on the definition of two power quantities, "charge_pwr" and

"discharge_pwr," which, depending on their value, determine different behaviors of the BESS.

Specifically, when the grid load is below the set "charge_pwr" value, the conversion system enables battery charging from the grid. The charging power is equal to the difference between "charge_pwr" and the net-load level, limited by the BESS's nominal power. If this difference is negative, charging is disabled. Similarly, if the net-load level exceeds the "discharge_pwr" value, the discharging phase is enabled, with negative power (limited by the nominal power) equal to the difference between the load value and "discharge_pwr."

From this controller, a positive or negative power set-point P_{cd} is defined. This value is calculated as follows:

$$\begin{aligned} P_{cd}(t) = (charge_pwr - Net\text{-}load)(t) \cdot C_{en}(t) + \\ + (discharge_pwr - Net\text{-}load(t)) \cdot D_{en}(t) \end{aligned} \tag{3.12}$$

where C_{en} represents the logical value enabling battery charging by the controller, and D_{en} represents the logical value enabling its discharging.

In this control, the "charge_pwr" value has been set equal to the Minimum Downward Regulation Bandwidth (MDRB) (introduced in Section 3.1). In this way, the control enables the BESS to charge when the net load is too low, trying to prevent the power delivered by the MPP from falling below the MDRB. Thereby, it tries to avoid the RTA going to state 1.2 and limiting the power produced by the island's PV, or at least try to reduce this cut-off.

The value "discharge_pwr", on the other hand, was set equal to the maximum power that can be delivered by the MPP (i.e., the number of diesel units available in the MPP "$UnitsLim$" multiplied by the rated power of a diesel unit "P_{NGEN}"). In this way, the control tries not to overload the MPP.

SoC Feedback Control: The set-points generated by the controller just discussed should be sent to the "Power Conversion System". In this work, anyway, another control has been taken into account. This control is based on the SoC feedback method that will be discussed in detail in Section 4.4. This control aims to reduce the exchanged power by the BESS if near reaching the SoC limits. This prevents the BESS from suddenly stopping delivering/absorbing energy causing a large and dangerous net-load change. In fact, the power output of the BESS is about half the active power output of a single MPP diesel unit (250 kW and 480 kW respectively). The MPP may not have enough reserve to compensate

for a supply/absorption interruption of this amount. With this control, the actual active power set-point sent to the BESS is equal to:

$$P_{set\,point}(t) = P_{cd}(t) \cdot (1 + \frac{SoC(t) - SoC_{middle}}{SoC_{max} - SoC_{min}}) \tag{3.13}$$

where SoC_{middle} represents the midpoint of SoC between the maximum (SoC_{max}) and the minimum (SoC_{min}) limits. The set values are SoC_{max} equal to 90%, SoC_{min} equal to 20%, resulting in SoC_{middle} equal to 55%. Consequently, the available range of SoC is 70%.

Moreover, the switch in this model section, visible in Fig. 3.19, allows canceling the effect of the SoC feedback control when the set-point provided by the controller is zero.

Power Conversion System and Battery: In this model section, the active power set-point value is pre-saturated to the maximum allowable value by the power converter (typically equal to the maximum charge and discharge power of the battery). By analyzing the sign of the power set-point, it is possible to determine whether the BESS is in a charging or discharging phase.

Once defined, it is possible to determine the amount of power that contributes to increasing or decreasing the state of charge of the BESS, by taking into account the respective efficiency for charging and discharging phases. If the charging phase is enabled, the charging power, net of inefficiencies, can be calculated as follows:

$$P_{batt}(t) = \eta \cdot P_{set\,point}(t) \tag{3.14}$$

While if the discharging phase is enabled, the power supplied by the battery is calculated as:

$$P_{batt}(t) = \frac{P_{set\,point}(t)}{\eta} \tag{3.15}$$

The efficiency η (called "eta" in the model shown in Fig. 3.19) has been set equal to 96%.

The battery is modeled in the right section highlighted in pink in Fig. 3.19. It receives, as input, the charging/discharging power from the previously analyzed model section (P_{batt}). The loop downstream of the initial summing node is necessary to implement an integral behavior related to accumulation and energy supply associated with power P_{batt}. This is done by multiplying the calculated power by the time sampling interval "Ts" and "Tr" (the ratio between the simulated time and the simulation time, defined at the beginning of the Section 3.2.2), considering that every second of simulation has to

be considered 1 hour of simulated time. The calculated stored energy is limited between 20% and 90% of the nominal BESS capacity (Q_N). Consequently, regarding SoC, when it reaches the aforementioned limits, the power contribution P_{BESS} to/from the grid in the yellow section is canceled. Conversely, the power component related to the auxiliary services of the conversion system, represented by the "System Auxiliary Power" block, is always considered to account for power consumption by conditioning and lighting systems. The "loss" parameter was set equal to 6%.

The variable "Qb", corresponding to the amount of energy stored in the BESS, was used to calculate the BESS upward (R_{UPBESS}) and downward ($R_{DOWNBESS}$) operating reserve:

$$R_{UPBESS}(t) = min(P_{NBESS}; \frac{Qb(t) - 0.2Q_N}{ReserveTime}) \tag{3.16}$$

$$R_{DOWNBESS}(t) = min(P_{NBESS}; \frac{0.9Q_N - Qb(t)}{ReserveTime}) \tag{3.17}$$

As already indicated in the assumptions in Section 3.1, the BESS upward/down-ward reserve made available by BESS was calculated as the instantaneous active power that can be continuously delivered/absorbed for a specific time range (*ReserveTime*). This time has been set to 30 minutes. This power, anyway, has to be limited to the maximum power exchangeable by the device. Due to that, the R_{UPBESS}/$R_{DOWNBESS}$ has been calculated as the minimum between these 2 quantities. The BESS operating reserve calculations are shown in Fig. 3.20, along with the complete BESS model for quasi-static simulations. As can be seen, *ReserveTime* was set to 0.5 seconds of simulation time, corresponding to half an hour of simulated time in the quasi-static model.

3.3 Finite-state machine model testing

In this section, the modeled finite-state machine and the implemented algorithms will be tested under purely theoretical operating conditions to consider all possible circumstances of the control system and verify its correct functioning. In these tests, in order to better observe the behavior of the Microgrid Controller (MGC) modeled, load and generation trends were imposed constant except for those that were made to vary specifically to stress the system. The control unit's logic of the Main Power Plant (MPP), discussed in Section 3.2.2, was disabled. This was done to remove some variables and thus make the test results more easily interpretable.

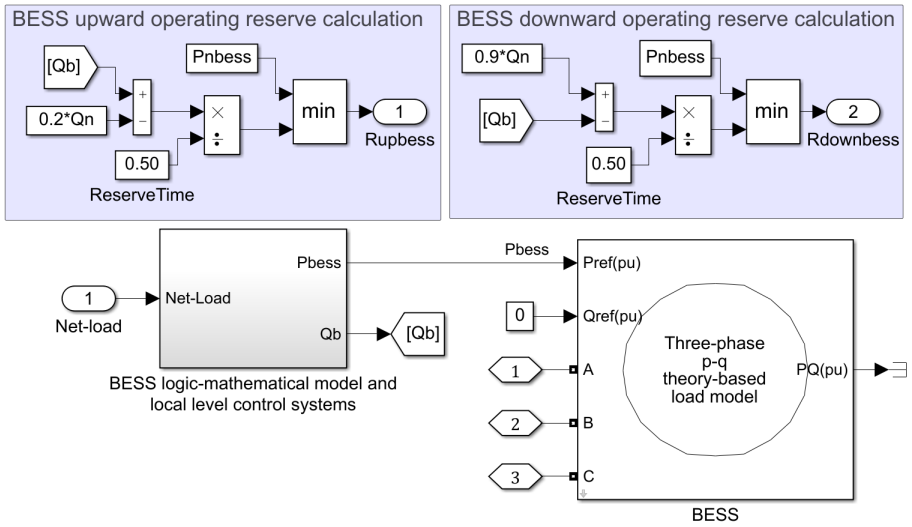


Figure 3.20: Complete BESS model for quasi-static simulations and operating reserve calculation

3.3.1 Validation of the MGC model assuming an extreme load behavior

During this test, the operating condition chosen refers to the early morning hours of a typical winter day, characterized by non-critical operating conditions. The MGC was in its initial state in each macro-state. The Photovoltaic (PV) system generates about 21.1 kW, and the Battery Energy Storage System (BESS), with a State of Charge (SoC) of 50%, was uncontrolled, exchanging only 12.5 kW with the grid for auxiliary services consumption. The active power absorbed by loads was approximately 307.1 kW, while the active power generated by the MPP was about 303.1 kW. The discrepancy between these powers includes the power absorbed by the BESS's auxiliary services, the PV production, and network losses, amounting to approximately 1.5%. The operating reserves to be ensured were held constant for all the day since the goal of these tests was to verify the proper functioning of the RTA and the MGC model built. Having a variable reserve would only make it more complex to verify this operation and perform the tests. The Upward Operating Reserve (UOR) to be ensured was set to 338.6 kW, while the Downward Operating Reserve (DOR) was set to 307.8 kW. These values are derived from the reserve valuation method described in Section 3.1.5.

In this test, step variations in load consumption were imposed successively. The load changes were simulated within the prosumer model, which, for this very purpose, has been considered non-dispatchable by the MGC. As mentioned in Section 3.2.1, a prosumer was considered in this network for testing purposes only. The prosumer model is the

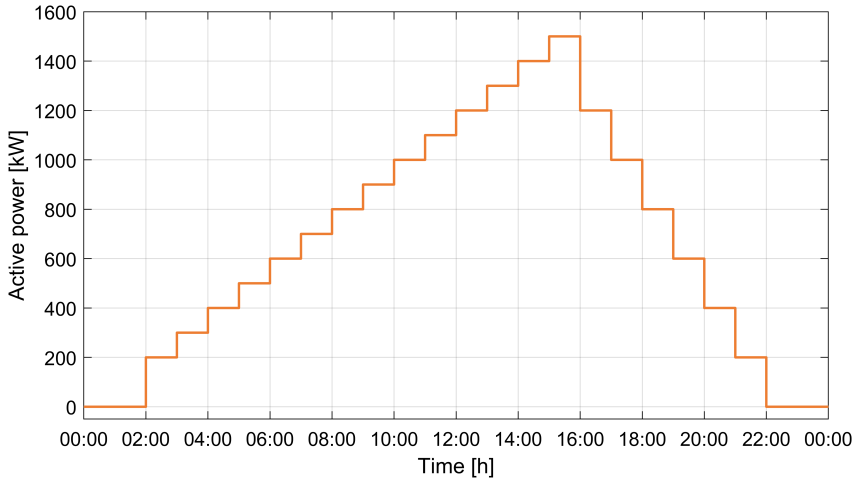


Figure 3.21: Change in the active power consumption imposed on the prosumer

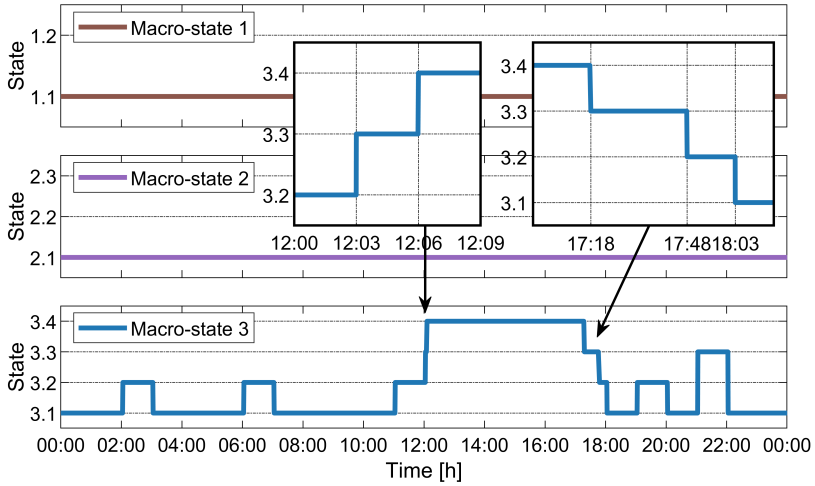


Figure 3.22: Operational states of the MGC following the extreme load behavior

same as a residential load in the dynamic grid model, shown in Fig. 3.11. The imposed increase in load consumption for the prosumer during this test is depicted in Fig. 3.21. This trend of load consumption permits verification of the proper functioning of the algorithms implemented in the MGC model of all affected operating states.

At 02:00 the load is increased by 200 kW, then instead it is increased by 100 kW until 15:00. At 16:00 the prosumer load is reduced by 300 kW, and in the following hours it is reduced by 200 kW until 22:00 when it returns to zero. All the state transitions that occurred during the test can be examined in Fig. 3.22. As can be seen in the figure, only macro-state 2 related to the control of the upward operating reserve was affected.

Fig. 3.23 shows the energy balance during the test while Fig. 3.24 and Fig. 3.25 show the upward and downward reserve trends, respectively. Specifically, enlargements are also

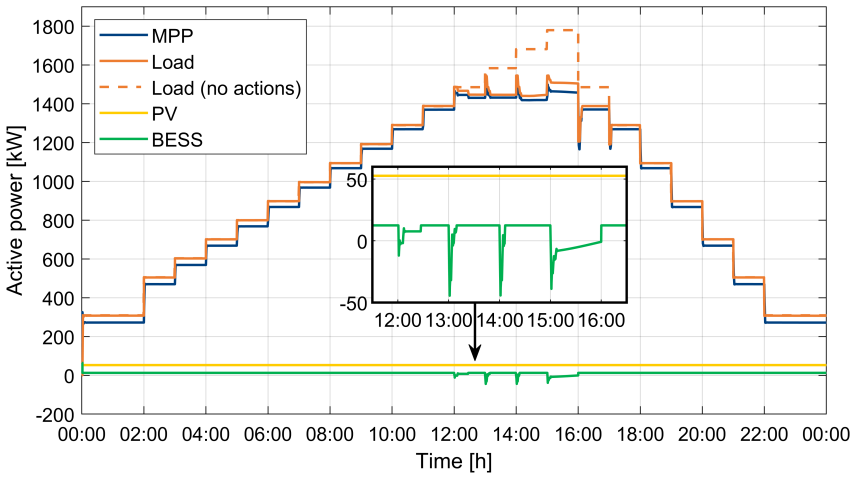


Figure 3.23: Active power balance following the extreme load behavior

shown in Fig. 3.24 to better show what happens during the hours when the prosumer load was at its peak. In these figures, the available operating reserve is equal to the reserve made available by the MPP when the BESS is not enabled (R_{UP}, R_{DOWN}), while it is equal to the sum of the reserve of the MPP and the operating reserve of the BESS when the latter is enabled by the MGC ($R_{UP}2$, $R_{DOWN}2$). In this test, the limit of MPP's diesel units was set to 3, assuming a unit under maintenance.

At 2:00, after the load increase, the UOR provided by the MPP is no longer sufficient to ensure the minimum required value. As shown in Fig. 3.24, the MPP's UOR drops almost to zero as the total available UOR. After one iteration, the MGC activated the BESS for primary frequency regulation and, taking into account the BESS, the available UOR returned above the minimum required value. After the load increase at 3:00, the MPP turned on a second diesel unit to supply the island's load, and the MGC verified that the activation of the BESS was no longer necessary, returning to state 3.1 at 04:03 (to the succeeding iteration).

A similar process was repeated for subsequent load increases until the load increase at 12:00. Since the MPP had no more available diesel units, it operated in overload condition, and simultaneously, the BESS started to discharge. This is evident in both Fig. 3.24, which shows the variation in power exchanged by the BESS, and Fig. 3.24, where the BESS's UOR started to decrease. A consequent increase in BESS's DOR can be seen in Fig. 3.25.

As can be seen in the small enlargement of Fig. 3.24, the available UOR fell below the requirement by about 12:08. The MGC detected this lack of UOR at 12:09 and sent a request to the MPP to increase its UOR available. Since the MPP had no more available diesel units, the request was rejected, and after a few minutes, the MGC moved to state 3.4.

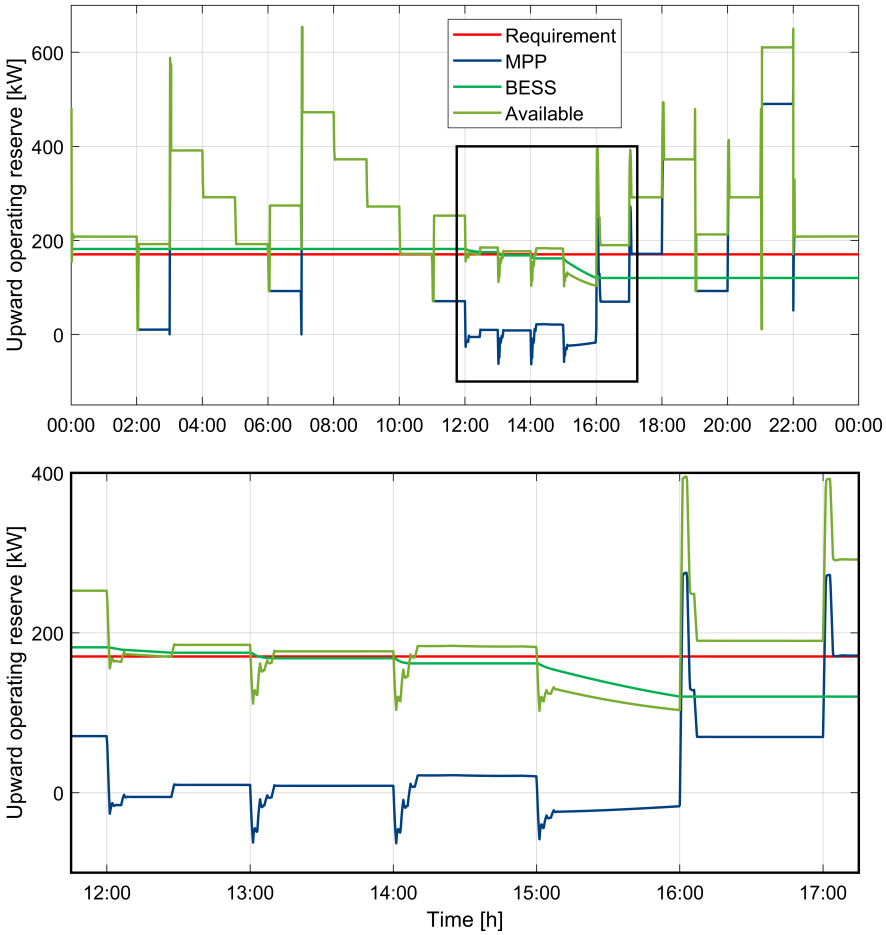


Figure 3.24: Upward operating reserves following the extreme load behavior

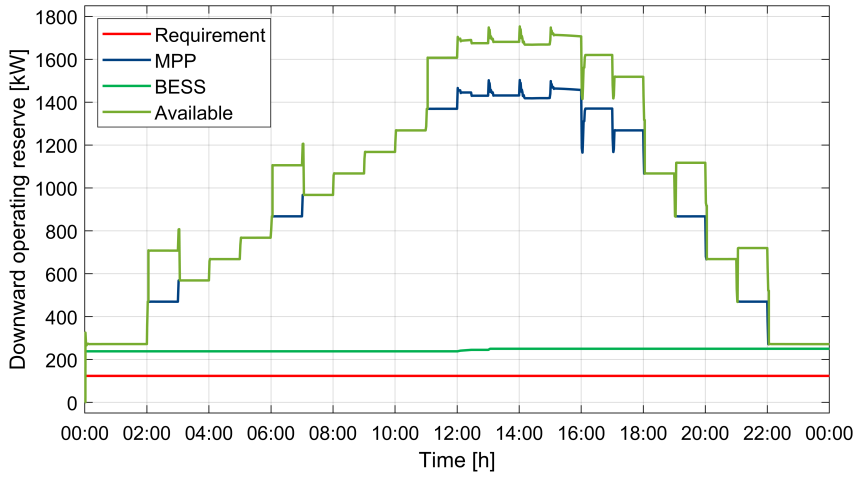


Figure 3.25: Downward operating reserves following the extreme load behavior

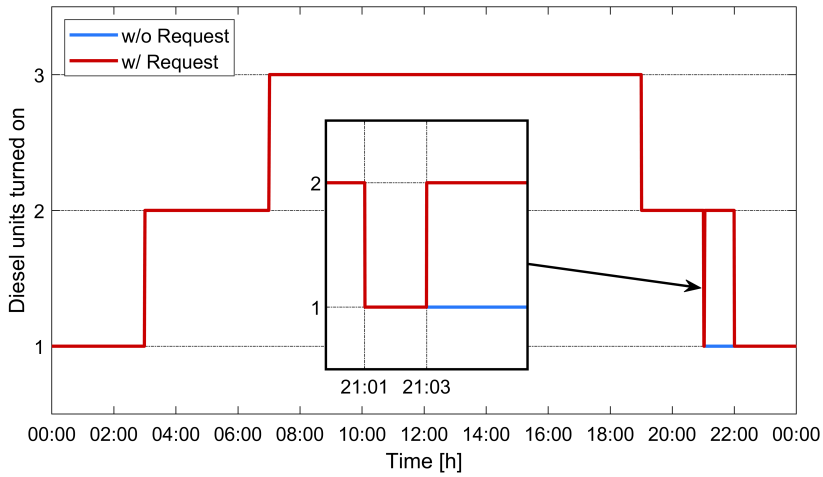


Figure 3.26: Diesel unit commitment following the extreme load behavior

This sequence of actions can be observed in Fig. 3.22, where an enlargement shows these state changes related to macro-state 3.

Observing Fig. 3.24, it can be noted that the UOR made available by MPP was negative in the middle hours of the day. The reserve actually made available by MPP in those cases was 0, but the MPP's UOR calculation allows considering a negative UOR when MPP diesel units are providing beyond the set rated active power (480 kW). This enables MGC to perform more precise load shedding actions and restore the stable operating condition of the system more quickly.

In this state, the MGC calculated a value multiple of "$Lstep$" (20 kW), sufficient to bring the total UOR above the minimum required value. On the other hand, the load reduction was not enough to disable the control imposed on the BESS, which continues, even if in a reduced manner, to discharge. This happens because the active power delivered by the MPP is still higher than its rated active power ($3 \cdot 480$ kW=1440 kW), working in overload condition. It is important to specify that the MPP does not really work in overload, since the apparent power of a diesel unit is 600 kW. As mentioned in the introduction of this chapter, voltage regulation has been given to the MPP, as well as reactive power control, and the MGC should only be responsible for the assessment and allocation of the operating reserve of active power. Therefore, a minimum amount of apparent power of the diesel units was left available for reactive power balancing and voltage regulation. Each diesel unit, in this case, provided more than the defined rated active power of 480 kw, with less reactive power capacity.

Due to the reduction of the UOR of the BESS, the total UOR available felt below the minimum required value again, and an additional load shedding was applied at 12:57 to

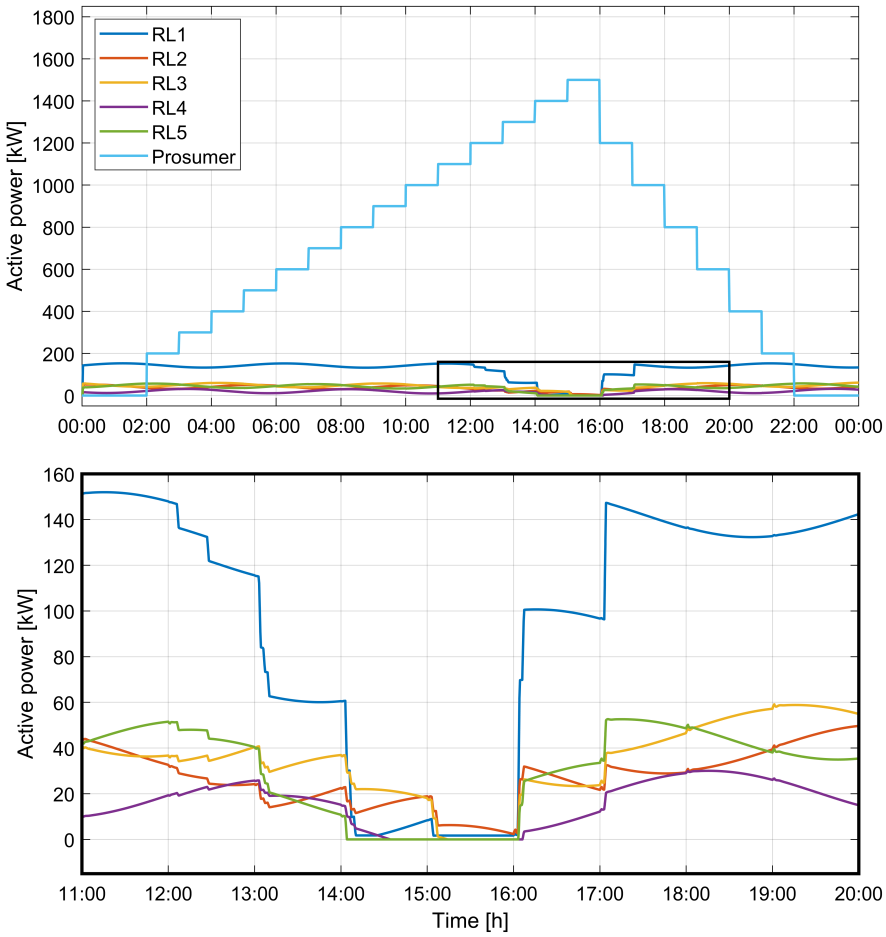


Figure 3.27: Active power consumption of residential loads following the extreme load behavior

meet the reserve constraint.

Shortly thereafter, at 13:00, the next load increase was applied at the prosumer. From this event and for subsequent events, each time a load change was applied, the total available UOR fell below the required minimum, leading the MPP to produce more than its rated active power and to the discharge of the BESS until the MGC returned the available UOR above the imposed limit.

At 15:00, the last load increase occurs at the prosumer, prompting the MGC to request a further load shedding. However, all dispatchable loads were already reduced to the minimum, resulting in a lower load shedding than that requested by the MGC for that hour. The trend of island loads during the day is illustrated in Fig. 3.27. In particular, in the specified hour, all loads on the island were reduced to zero and only the prosumer absorbed active power from the grid. The figure also shows the sinusoidal trends that were introduced to differentiate the profiles of the residential loads from each other, as discussed

in Section 3.2.2.

Examining Fig.3.23, it is evident that the BESS experienced significant discharge during that hour to support the MPP. This, in turn, led to the rapid decrease in the operating reserve of the BESS that can be seen in Fig.3.24.

It is important to note that this network operating condition in which dispatchable loads are no longer available is purely theoretical and artificially created to stress the MGC model. In the intended operation of the MGC, the prosumer load should also be dispatchable by the MGC and the condition observed during this test would not occur.

At 16:00, the load starts to decrease, and gradually, the MGC requested the reconnection of the loads it had disconnected. This reconnection was simulated to be instantaneous, but it is essential to emphasize that in reality, the reconnected load would likely differ from the exactly cut value. In that case, the RTA will evaluate whether the connected load is greater or less than the calculated load and decide accordingly.

At 17:00, state 3.3 became unnecessary because, with BESS activation alone, the available UOR exceeded the minimum value to be guaranteed (Fig. 3.24). As clarified in the Section 3.1.4, this state is held for 30 minutes. Therefore, the state persists until 17:48, at which time the transition to state 3.2 occurred. Although the MPP's UOR alone was also higher than the required UOR, the MPP's reserve alone was not 110% higher than the required reserve (a necessary condition for returning to state 3.1). For this reason, there was no direct transition from state 3.3 to state 3.1, nor transition from 3.2 to 3.1. At 18:00, however, that condition was verified and at the next iteration (18:03) the transition to state 3.1 occurred.

The BESS activation was required from 19:00 to 20:00 as, due to the load reduction, the MPP turned off one of its diesel units, reducing its available UOR. At 21:00, the MPP turned off another diesel unit as it is no longer needed to meet the net load, but this shutdown leads to another reduction in the available UOR. In this case, differently from what happened at 19:00, the activation of the BESS was not sufficient to ensure the minimum required UOR and the MGC moved directly to the state 3.3. In this case, the power plant had available diesel units and accepted the request to increase its UOR by turning on the diesel unit it had just turned off.

At 22:00, the load profile imposed on the prosumer returned to 0, the MGC moved directly from state 3.3 to state 3.1, and the MPP turned off the additional diesel unit that was required of it. The MGC remained in state 3.3 from 21:03 to 22:03, thus more than the minimum 30 minutes imposed as a condition for leaving the state. Therefore, as soon

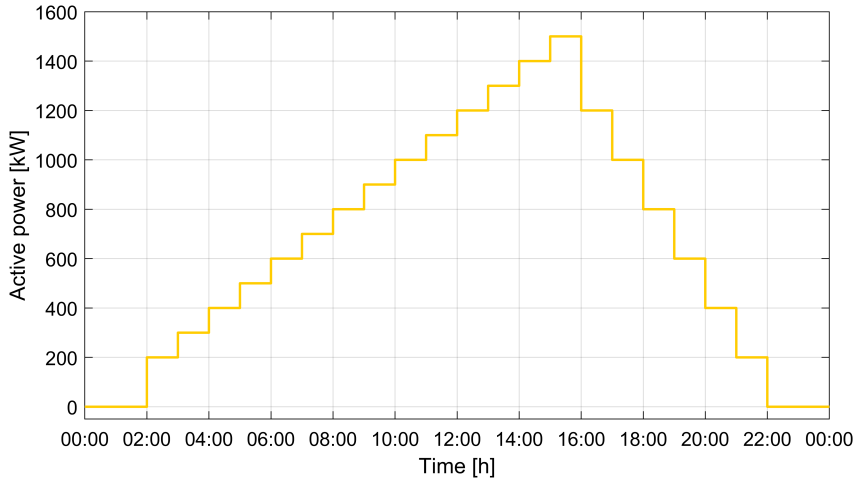


Figure 3.28: Change in the generated power imposed on the PV power plant

as the demand was no longer needed there was the exit from the state.

3.3.2 Validation of the MGC model assuming an extreme PV generation

During this test, the chosen operating condition represents the peak evening load of a typical summer day, characterized by non-critical operating conditions. The MGC was in its initial state in each macro-state. The PV system started with no generated power, and the BESS, with a SoC of 50%, was uncontrolled, exchanging only 12.5 kW with the grid for auxiliary services consumption. The active power absorbed by loads was approximately 960.7 kW, while the active power generated by the MPP was about 984.1 kW. The discrepancy between these powers includes the power absorbed by the BESS's auxiliary services and network losses, amounting to approximately 1%. The operating reserves to be ensured were held constant for all the day. The upward operating reserve to be ensured was set to 338.6 kW, while the downward operating reserve was set to 307.8 kW. These values are derived from the reserve valuation method described in Section 3.1.5.

In this test, step variations in active power produced by the PV plant were imposed successively. The active power variations were applied to the PV plant, which, in this case, can be constrained by the MGC. The imposed increase in production for the PV plant during this test is illustrated in Fig. 3.28.

Starting from 2:00, the power produced by the PV plant was incrementally increased every hour, first by 200 kW followed by steps of 100 kW until 15:00. From 16:00, the produced power was reduced by 300 kW first, then by 200 kW every hour until 22:00

when it returned to zero. The operational states of the MGC during the test are shown in Fig. 3.29.

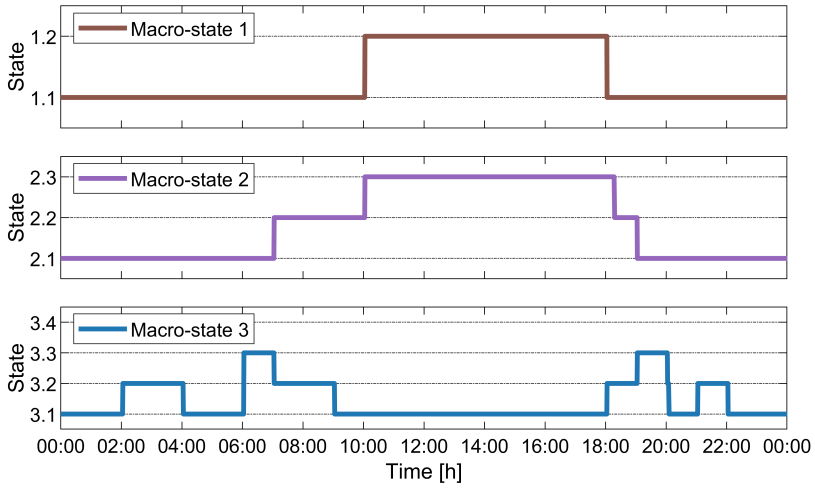


Figure 3.29: Operational states of the MGC following the extreme PV generation

In Fig. 3.30, the active power balance during the test is observed, while Figs. 3.31 and 3.32 depict the trends of upward and downward operating reserves of the island's resources, respectively.

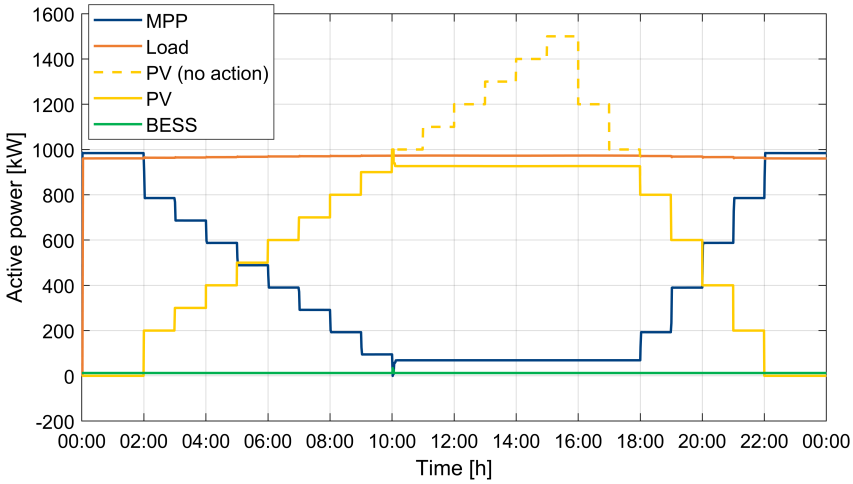


Figure 3.30: Active power balance following the extreme PV generation

In these figures, as already specified in the previous scenario, the available operating reserve is equal to the reserve made available by the MPP when the BESS is not enabled (R_{UP}, R_{DOWN}), while it is equal to the sum of the reserve of the MPP and the operating reserve of the BESS when the latter is enabled by the MGC ($R_{UP}2$, $R_{DOWN}2$).

After the increase in PV production by 200 kW at 2:00, the significant reduction in net load created a problem with UOR as the MPP shut down one of its groups, no longer

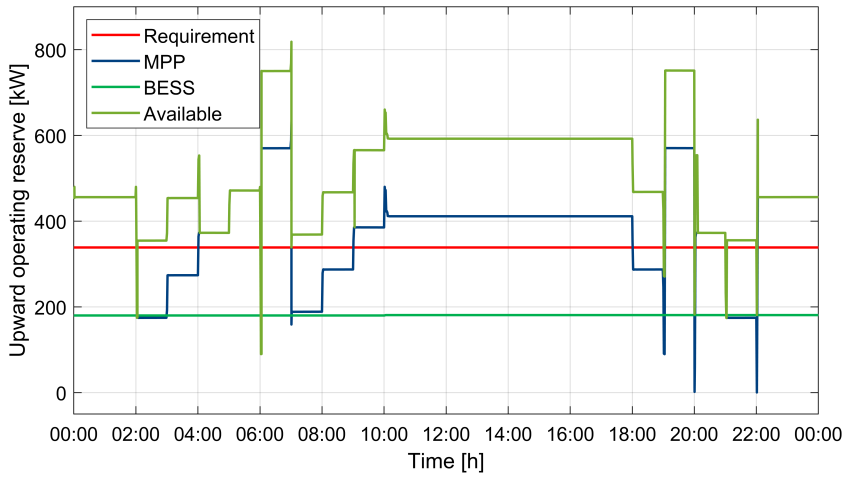


Figure 3.31: Upward operating reservesfollowing the extreme PV generation

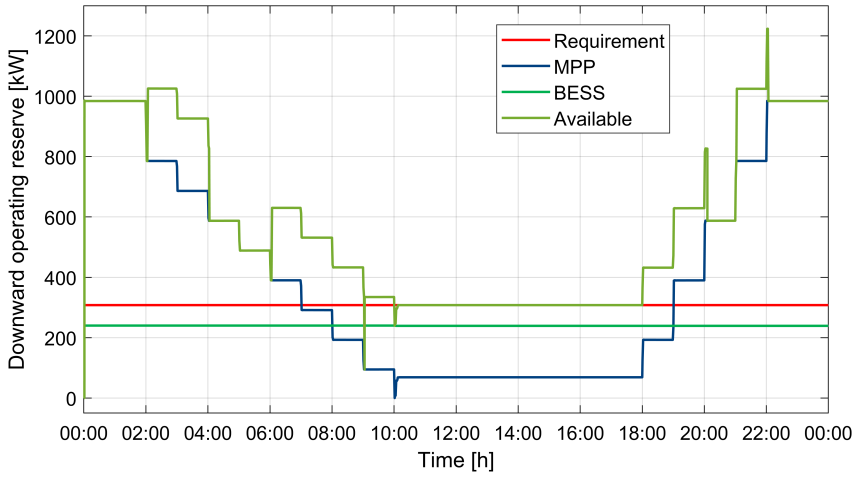


Figure 3.32: Downward operating reserves following the extreme PV generation

necessary to meet the load, visibly reducing the available upward reserve. Consequently, the MGC enabled the BESS for primary frequency regulation to bring the available UOR above the preset limit.

The production change at 6:00 caused another diesel unit to shut down, bringing the MPP units turned on to 1. This recreated the same situation as at 2:00, but in this case, the BESS alone would not be sufficient to ensure the minimum UOR. Therefore, the MGC transitioned directly from state 2.1 to state 2.3. The MPP accepted the request for an increase in UOR from the MGC by restarting a diesel unit and bringing the available UOR above the minimum required. This situation is more clear by looking at the number of diesel units turned on during the simulation, depicted in Fig. 3.33. It can be seen in the enlargement that at 6:00 the MPP turned off the second diesel unit, but this was turned on

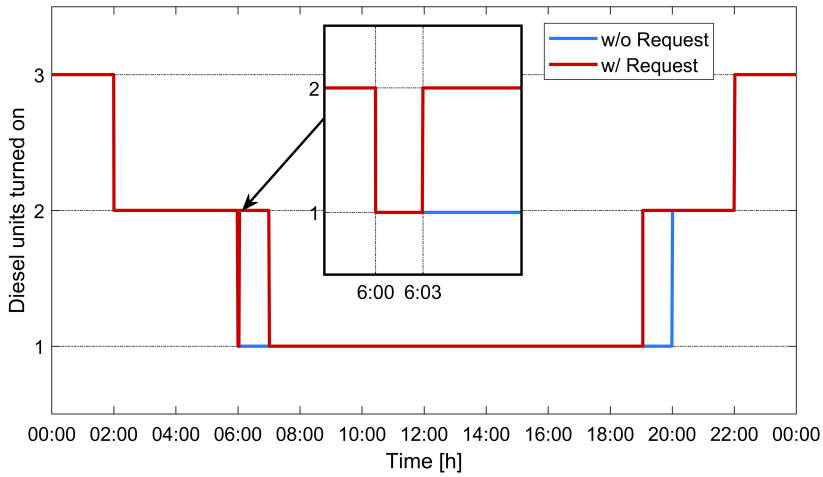


Figure 3.33: Diesel unit commitment following the extreme PV generation

again after 3 minutes (an iteration of the MGC), fulfilling the MGC's request.

The PV power plant continued to increase its production, and at 7:00, the request for reserve to the MPP was no longer necessary, transitioning to state 2.2 until 9:00, and then returning to state 2.1.

The BESS, however, remained enabled because, at 7:00, the shutdown of the MPP diesel unit made it necessary to enable the BESS to ensure the minimum DOR. The MGC, exiting state 2.2, set the variable $StateBESS = 5$, but it was set back to 1 by state 3.2 at the next iteration. This is evident in Figs. 3.31 and 3.32, where the reserve provided by the BESS was no longer considered at 9:00, and after one iteration, it returned to being considered in the total available reserve.

At 10:00, the PV power became too high, causing the MPP to deliver less than the MDRB, in this case, set to 10% of a diesel unit (48 kW). In macro-state 2, at the same moment, the MGC moved to state 2.3. The limitation required by this state, calculated to guarantee the minimum DOR, was greater than the limitation required by state 1.2, calculated to guarantee the MDRB. Thus, the limitation carried out was referred to state 2.3, and state 1.2 was no longer needed. However, the MGC remained in state 1.2 because the exit condition was not satisfied. The P_{MPP}, in fact, was about 68.7 kW, which was less than 110% of the MDRB (72 kW) imposed as a constraint for state exit. In any case, as discussed above, this has no impact on grid behavior.

In the first moments after this last load change, the BESS, programmed to respond when the output power of the MPP falls below the MDRB value, absorbed power until the MGC restored the active power output of the MPP above the set minimum.

The PV power was limited to the maximum acceptable to ensure an available DOR

greater than the requirement until the PV power dropped below that limitation. This happened at 18:00 and, after a waiting time of 15 minutes ($k_{PVLim2} \geq 5$), there was a transition to state 2.2. At 18:00, state 1.2 is also no longer necessary. Unlike macro-state 2, however, the transition from state 1.2 to state 1.1 can occur immediately without waiting 15 minutes, since it was not deemed appropriate to impose a time hysteresis on this transition as well.

At 19:00, the BESS was no longer needed to ensure the minimum DOR but was necessary to ensure the minimum UOR. Analogously to what happened previously, the BESS was first disabled, exiting state 2.2 in macro-state 2, and then re-enabled, transitioning to state 3.3 in macro-state 3. Since the BESS alone would not be sufficient to ensure the required minimum UOR, the MPP accepted the request and turned on a new diesel unit, bringing the available UOR above the minimum required.

At 20:00, neither the request to the MPP nor the enabling of the BESS was necessary, and the MGC moved from state 3.3 to state 3.2, and after one iteration, to state 3.1. Then, the BESS was enabled again from 21:00 to 22:00 to ensure the minimum UOR, after which everything returned to the initial operating conditions as the imposed PV power variation returned to zero (Fig. 3.28).

3.4 Testing the real-time algorithm on real test scenarios

In this chapter, various scenarios are presented to demonstrate the situations in which the Microgrid Controller (MGC) may find itself, allowing for the verification of its correct operation. The model was tested using the 2021 load and photovoltaic production profiles presented in Section 1.5.1. These simulations revealed several challenges in both Upward Operating Reserve (UOR) and Downward Operating Reserve (DOR), enabling the verification of the correct functioning of the states and the conditions for transitioning between them.

The algorithm underwent testing by simulating typical winter and summer months, from which two specific days were chosen for detailed analysis. The decision to consider one summer month and one winter month is grounded in the seasonal dependence of the island's electrical load, extensively discussed in Section 1.5.1. In summer months, due to the high load, a lack of UOR is more likely to occur, allowing for the observation of the activation of MGC states related to the macro-state 3, concerning the UOR assessment and allocation. In winter months, when the island's electrical load is very low, a deficiency in DOR is

more probable. This allows for the observation of the MGC's behavior when activating states related to the macro-state 1, concerning the DOR assessment and allocation, and macro-state 2, concerning the Minimum Downward Regulation Bandwidth (MDRB) to be guaranteed to the Main Power Plant (MPP) of the island.

3.4.1 Test case of a typical summer day

The control algorithm was tested by simulating the entire month of July 2021. From these simulations, a typical summer day, specifically July 28, was chosen for detailed analysis. On this day, all states of the macro-state 3 related to UOR assessment and allocation were activated.

For the simulation of the entire month, a PV penetration of 200 kWp was assumed, close to the Italian Ministry for Economic Development's target for 2025 [73]. The number of available diesel units in the MPP was set to 2, assuming the other two units were under maintenance. Simulating the entire month from July 1, starting with the BESS at 50% of State of Charge (SoC), the simulation reached the beginning of the specified day (July 28) with a slightly lower charge level, around 47%. This decrease was due to the BESS activation in the preceding days of the month, triggered by excessive or insufficient net-load conditions. These conditions go beyond simple peak load or PV production: as already introduced in Section 3.19, the BESS exchanges power in cases where load demand exceeds the MPP's maximum deliverable capacity or when the net-load falls below the MPP's Minimum Downward Regulation Bandwidth (MDRB) (48 kW).

The state trends during the day are visible in Fig. 3.34. Specifically, 10 "*key moments*" during the day, representing MGC state changes, are identified and listed in Table 3.4.

During this day, the UOR to be guaranteed ($minR_{UP}$), calculated by eq. (3.4), was mostly equal to the UOR to be guaranteed based on historical data ($R_{h,up}$), as it was mostly greater than the active power generated by the PV (P_{pv}). From about 09:58 to 10:55 and from about 11:27 to 14:26, however, the active power generated by the PV (P_{pv}) was greater than $R_{h,up}$. In the middle part of the day, therefore, $minR_{UP}$ was mostly equal to the active power produced by the PV P_{pv}. The DOR to be guaranteed ($minR_{DOWN}$), on the other hand, calculated through eq. (3.6), was always equal to the active power absorbed by load RL1 (which, during the day, was always the load that absorbed the most active power, $P_{loadmax}$), because it was always greater than the minimum DOR to be guaranteed based on historical data ($R_{h,down}$).

While, for the examined case study, there were no issues regarding the DOR assessment,

meeting the minimum UOR required various actions throughout the day. The MGC had to activate all states related to macro-state 3.

Table 3.4: Key moments during July 28

Time	Observed action
5:18	Macro-state 3: transition from state 3.1 to state 3.2
7:15	Macro-state 3: transition from state 3.2 to state 3.1
7:42	Macro-state 3: transition from state 3.1 to state 3.3
8:09	Macro-state 3: transition from state 3.3 to state 3.1
18:15	Macro-state 3: transition from state 3.1 to state 3.2
19:51	Macro-state 3: transition from state 3.2 to state 3.3 but rejects
19:54	Macro-state 3: transition from state 3.3 to state 3.4
21:54	Macro-state 3: transition from state 3.4 to state 3.3
22:18	Macro-state 3: transition from state 3.3 to state 3.2
23:21	Macro-state 3: transition from state 3.2 to state 3.1

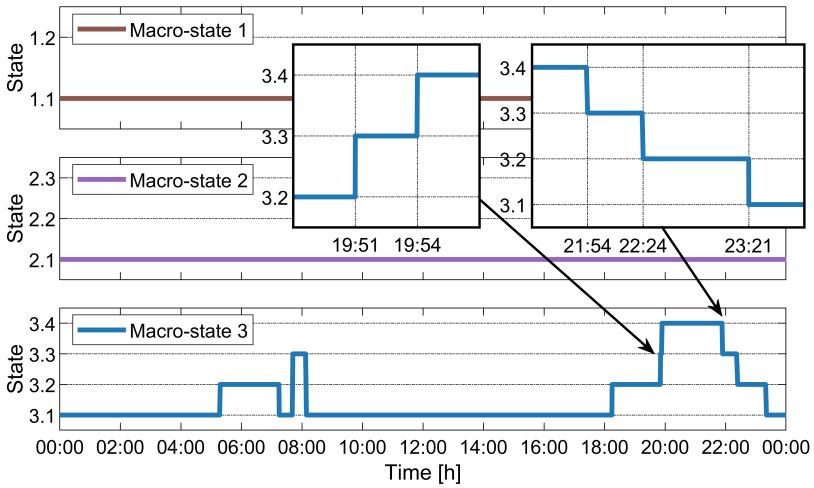


Figure 3.34: MGC states during July 28

The active power generation and absorption trends on July 28 are shown in Fig. 3.35, while the upward and downward operating reserve trends during the day are depicted in Fig. 3.36 and Fig. 3.37, respectively.Furthermore, in Fig. 3.38 it is possible to observe the number of MPP diesel generators turned on during the day, with and without considering the requests of the MGC during the period of being in state 3.3.

Analyzing the events during the day (Table 3.4), at 5:18, the MGC moved from state 2.1 to state 2.2 as the shutdown of a diesel unit by the MPP (Fig. 3.38) lowered the total available UOR below the required minimum UOR (dull green curve and red curve in Fig. 3.36, respectively). With the activation of the BESS, setting the power regulation thresholds based on the CEI 0-16 frequency from "wide" thresholds to "narrow" thresholds,

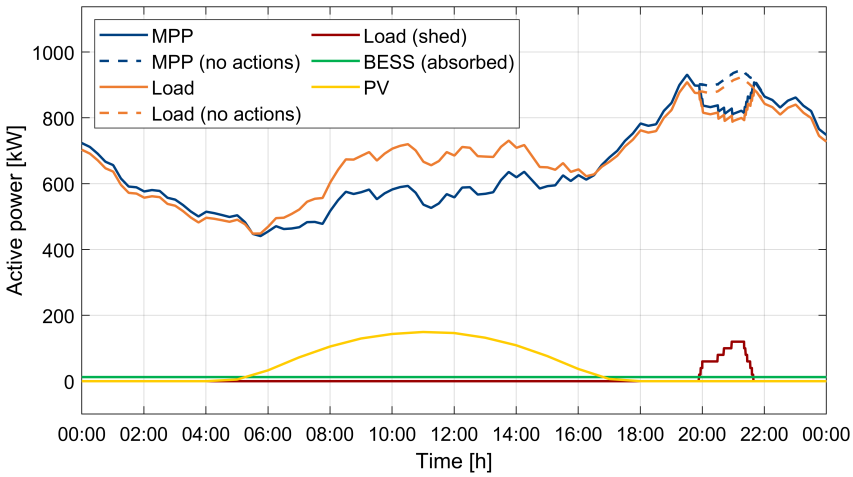


Figure 3.35: Energy balance during July 28

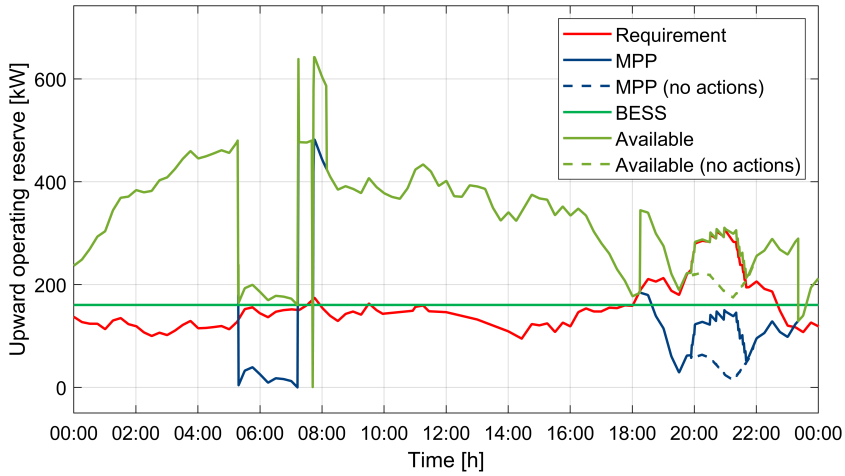


Figure 3.36: Upward operating reserves during July 28

the total available UOR rose again above the required UOR. In Figs. 3.36 and 3.37, the total available UOR is the sum of the UOR provided by the MPP (blue curve) and that of the BESS (bright green curve, when enabled).

As shown in Fig. 3.38, around 7:15, the MPP autonomously turned on a second diesel unit, and consequently, the MGC no longer deemed it necessary to keep the BESS enabled, returning to state 3.1 Fig. 3.34.

Around 7:40, however, the MPP decided to turn off that second unit, and precisely at that moment, the UOR to be guaranteed was too high to be satisfied by enabling only the BESS. Therefore, at the next interaction at 7:42, the MGC directly moved from state 3.1 to state 3.3 and asked the MPP to turn back on the unit just shut down, bringing the available reserve back above the minimum.

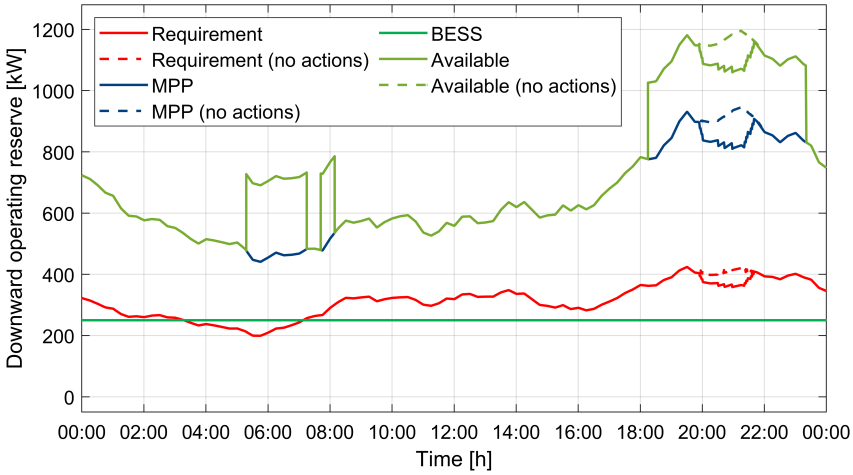


Figure 3.37: Downward operating reserves during July 28

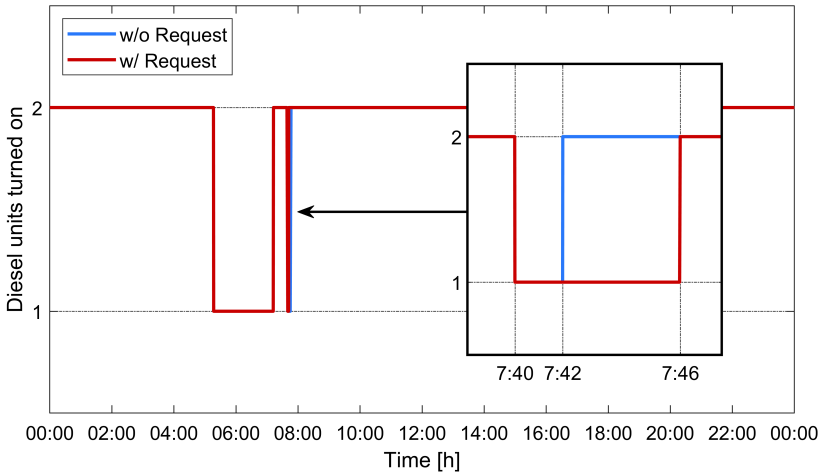


Figure 3.38: Main power plant diesel units active during July 28, with or without MGC actions

As shown in Figure 16, especially in the highlighted detail, around 7:46, the MPP considered the second unit necessary not only to ensure the reserve required by the MGC but also to supply the island's load. However, only at 8:09, after the k_{MPP} variable reached the value of 10, did the MGC exit state 3.3 and return to state 3.1. It is worth recalling that the k_{MPP} variable was introduced to prevent MPP requests from being made for a few moments and exiting and re-entering the state multiple times when the required reserve is only slightly higher than what can be obtained by BESS activation only.

Moreover, it is crucial to remember that the request made to the MPP by the MGC is a minimum set-point of operating reserve to be provided. Therefore, even though still present in the state, the additional reserve requested from the MPP is 0 in moments when waiting for the k_{MPP} variable to reach 10. Thus, staying in state 3.3 in these cases does not

cause discomfort to the MPP.

At 18:15, the BESS was re-enabled, and its contribution was sufficient until 19:51 when the MGC again requested additional reserve from the MPP. In this case, however, the MPP had no available units, so it rejected the request received. At the next iteration at 19:54, the MGC moved to state 3.4 and began load shedding on the network.

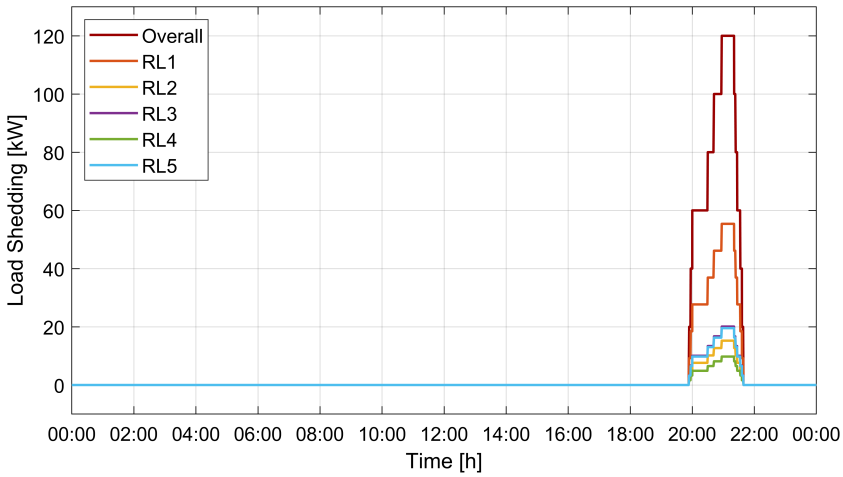


Figure 3.39: Load shedding during July 28

Fig. 3.39 shows the load shedding performed during the day. Load shedding was carried out in increments of 20 kW, as set in the MGC, reaching a total of 120 kW around 21:00 and canceling a few minutes before 21:54. In Fig. 3.37, it can be seen that load shedding also reduced the DOR requirement, as it was equal to the power absorbed by load RL1.

At 21:54, the MGC moved from state 3.4 to state 3.3, requesting 0 kW reserve from the MPP, and then moved to state 3.2 at 22:18 and state 3.1 at 23:21. It is important to note that, as designed in the MGC model, it was not possible to transition directly from state 3.4 to state 3.1 without first passing through state 3.3. However, since no additional reserve was needed during the stay in state 3.3, the MGC requested 0 kW from the MPP without causing it any inconvenience.

3.4.2 Test case of a typical winter day

The control algorithm was tested by simulating the behavior of the entire month of February 2021. From these simulations, a typical winter day was chosen for detailed analysis: February 5, when macro-states 1 and 2 were mostly involved.

In these simulations, a PV penetration on the island of 200 kWp was assumed, close to the Italian Ministry for Economic Development's target for 2025 [73]. The number of diesel units available in the MPP was set to 2, assuming the other two units were under maintenance. The SoC of the BESS was set to 50% at the beginning of February, and its SoC variation was linked to the activation of control rules aimed at supporting the MPP in cases of excessively high or low net-load (as in the previous test case). In the first days of the simulated month, there were no events requiring intervention from the BESS. For this reason, the SoC remained unchanged (50%) until February 5, the day chosen for detailed analysis.

During this day, the UOR to be guaranteed ($minR_{UP}$), calculated by eq. (3.4), was mostly equal to the UOR to be guaranteed based on historical data ($R_{h,up}$), as it was mostly greater than the active power generated by the PV (P_{pv}). From about 06:07 to 13:26, however, the active power generated by the PV (P_{pv}) was greater than $R_{h,up}$. In the middle part of the day, therefore, $minR_{UP}$ was equal to the active power produced by the PV P_{pv}. The DOR to be guaranteed ($minR_{DOWN}$), on the other hand, calculated through eq. (3.6), was always equal to the active power absorbed by load RL1 (which, during the day, was always the load that absorbed the most active power, $P_{loadmax}$), because it was always greater than the minimum DOR to be guaranteed based on historical data ($R_{h,down}$).

While, for the examined case study, there were no problems regarding the UOR assessment, to satisfy the minimum DOR to be guaranteed, the MGC had to enable the BESS for frequency regulation, but it never had to activate state 2.3. This state was not activated on any day in February. The trend of states during the day is visible in Fig. 3.40. Specifically, four key moments of the day can be identified, representing changes in the state of the MGC, listed in Table 3.5. Furthermore, throughout the examined day, the MPP was always able to supply the load and guarantee the minimum UOR using only one diesel unit.

Table 3.5: Key moments during February 5

Time	**Observed action**
8:51	Macro-state 2: transition from state 2.1 to state 2.2
10:09	Macro-state 1: transition from state 1.1 to state 1.2
13:06	Macro-state 1: transition from state 1.2 to state 1.1
13:15	Macro-state 2: transition from state 2.2 to state 2.1

The trends of the generated and absorbed powers on February 5 are shown in Fig. 3.41, while the amount of upward and downward operating reserves during the day are shown in

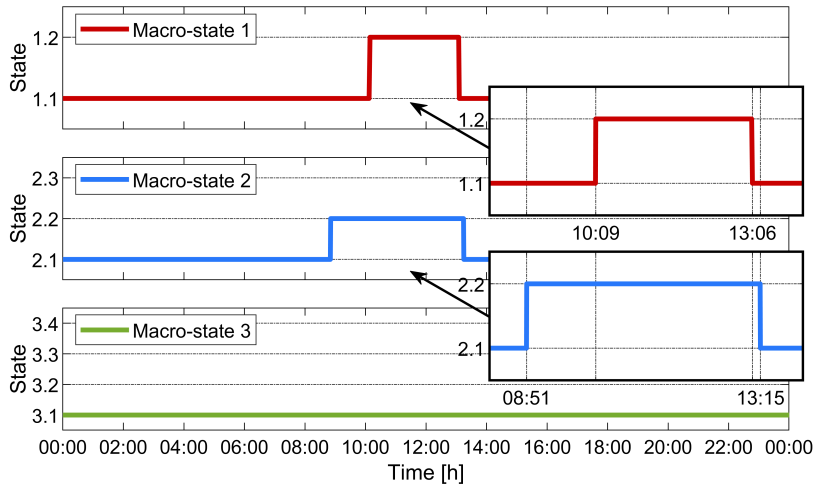


Figure 3.40: MGC states during during February 5

Figs. 3.42 and 3.43, respectively.

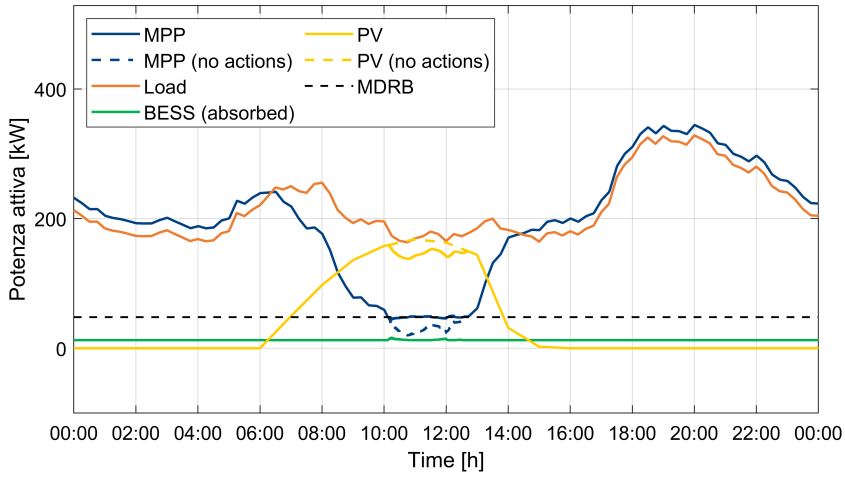


Figure 3.41: Energy balance during February 5

Analyzing the day in detail, at 8:51, the MGC determined a lack of DOR and moved from state 2.1 to state 2.2. By enabling the BESS for primary frequency regulation, the available DOR of the grid (dull green curve), given by the sum of the DOR provided by the MPP (blue curve) and that of the BESS (bright green curve, if enabled), returned above the minimum DOR to be guaranteed (red curve).

At 10:09, the net-load fell below 48 kW, the Minimum Downward Regulation Bandwidth (MDRB) set in macro-state 1. The power supplied by the MPP must not fall below this threshold to allow the diesel units to have a minimum DOR and thus regulate the frequency and support the voltage. This power value was set equal to 10% of the rated active power of a diesel unit (480 kW). Once this value was reached, the MGC moved from

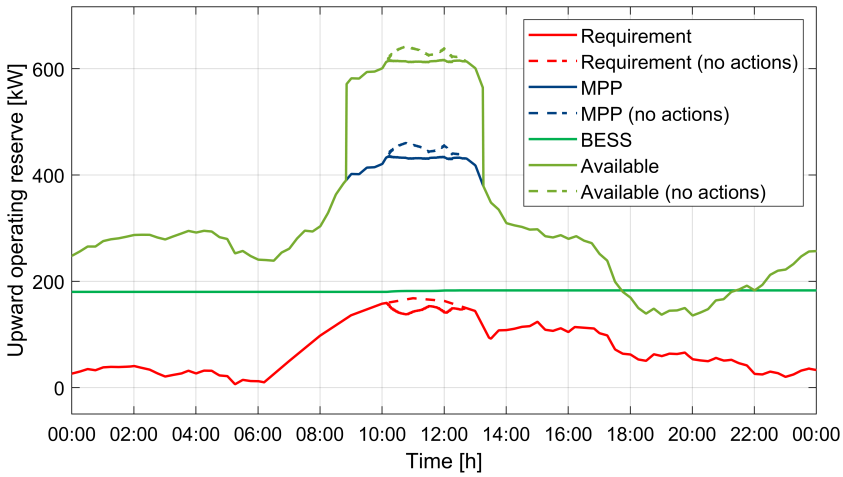


Figure 3.42: Upward operating reserves during February 5

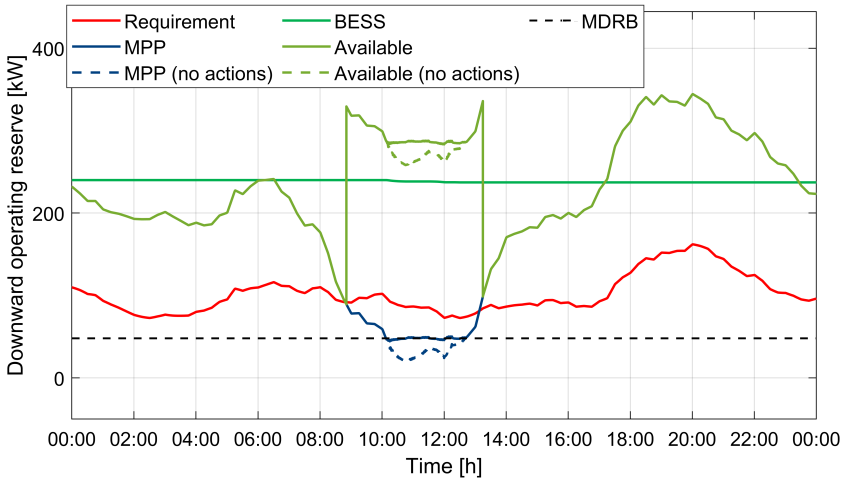


Figure 3.43: Downward operating reserves during February 5

state 1.1 to state 1.2 and applied a limitation to the power generated by the PV system to keep the net-load above the Minimum Downward Regulation Bandwidth (MDRB). The difference between the power that would ideally be produced by the PV without this action (dashed yellow curve) and the power actually produced by it during the day (yellow curve) can be observed in Fig.63.41.

In Fig. 3.42, it can be observed that the limitation of PV production also reduced the UOR requirement. This occured because, as mentioned earlier, the UOR to be guaranteed corresponded to the PV production during the central hours of the day.

Around 12:30, state 1.2 stopped limiting the PV, but only at 13:06 did the conditions occur to exit this state and return to the state 1.1. At 13:15, the DOR available from the MPP alone became sufficient to cover the minimum DOR to be guaranteed, and the MGC

moved from state 2.2 to state 2.1.

3.5 Verification of the effectiveness of actions processed by the microgrid controller

In this section, the actual effectiveness and necessity of the actions devised by the Real-Time Algorithm (RTA), validated in the previous section, are verified. Taking specific conditions from the cases examined in Section 3.4, these conditions have been imposed on the dynamic model described in Section 3.2.1. The necessity and utility of the controls required by the MGC will be examined.

3.5.1 Dynamic analysis of key moments of the typical summer day test case

In this section, reference is made to the typical summer day discussed in Section 3.4.1. Not all key moments of the day listed in Table 3.4 have been examined in detail, but only those that are fundamental and sufficient to verify the effectiveness of the algorithm's choices. In the studied case, assuming a 200 kWp PV system, the actions performed by the MGC to be examined are listed in Table 3.6. The network conditions for the various cases are reported in Table 3.7.

Table 3.6: MGC actions of the typical summer day analyzed in Section 3.4.1 that have been chosen to be examined dynamically

Case	Time	Action
1	5:18	Moving to "narrow" thresholds of the BESS
2	7:42	MPP request accepted
3	19:54	Load shedding due to MPP request rejected

Table 3.7: Grid operating conditions during the MGC actions of the typical summer day analyzed in Section 3.4.1 that have been chosen to be examined dynamically

			Active power [kW]							
			Generated		Absorbed					min
Case	SoC	N_{GEN}	MPP	PV	RL1	RL2	RL3	RL4	RL5	UOR
1	47	1	477	13	212	58	83	44	76	131
2	47	2	479	95	266	96	92	30	83	171
3	47	2	897	0	404	111	146	71	142	229

3.5.1.1 Key moment of 05:18: Moving to "narrow" thresholds of the BESS

In Case 1, as reported in Table 3.7, there was a total load consumption on the island of approximately 473 kW, distributed across 5 residential loads, with an additional 12.5 kW from the auxiliary services of BESS. The PV source produces about 13 kW and, according to the BESS control logic implemented and described in Section 3.2.2.4, the BESS' SoC had reached 47%.

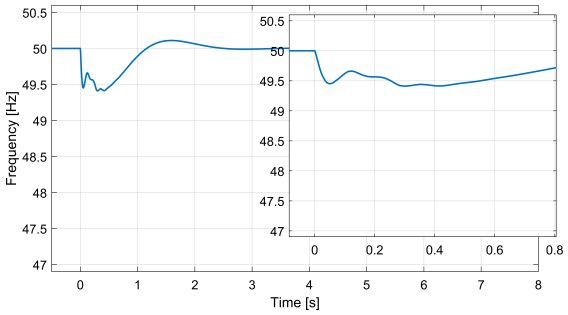
During those hours of the day, the MPP was able to supply the required load with only one diesel unit turned on (N_{GEN} in Table 3.7). The minimum Upward Operating Reserve (UOR) to be guaranteed was 131 kW and was related to the absolute Upward Operating Reserve (UOR) to be guaranteed based on the historical data at that moment on that day.

After setting the values of active power absorbed by various loads, the power supplied to the PV system, the number of diesel units turned on, and the BESS' SoC, a load increase equal to the minimum UOR to be guaranteed identified by the MGC was set to the prosumer. This setting was used to determine whether, with the occurrence of such a load variation, the network was indeed in a condition of potential danger to the system's stability, and it was indeed necessary to implement the action requested by the MGC, i.e. the transition to "narrow" thresholds of the frequency regulation of BESS.

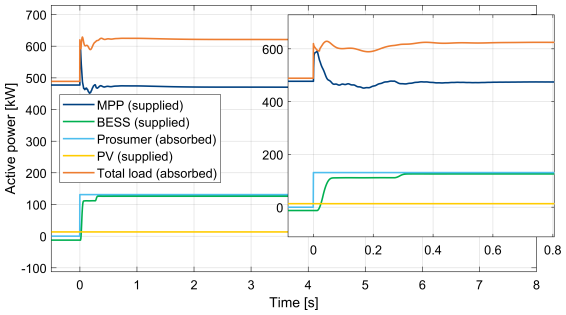
Fig. 3.44 shows the frequency and active power trends during the transient, with and without enabling the BESS to frequency regulation. These two tests were conducted to observe how the choice of enabling the BESS to frequency regulation by the MGC was right and necessary for the secure operation of the island's power grid. The figures show 8 seconds of transient to observe the complete behavior of frequency and powers. However, in most cases, the transient can be considered finished in 3-4 seconds. An enlargement of the first 800 ms of the behaviors was shown in order to better observe the first instants after the contingencies.

Figs. 3.44a and 3.44b show the trends of frequency and power following the imposed power variation on the prosumer, with the f-P regulation of BESS set to "narrow" thresholds after the MGC action. In Fig. 3.44a, it can be observed that the frequency underwent a variation, reaching a nadir of approximately 49.4 Hz before completely recovering after about 2 seconds. Fig. 3.44b demonstrates how the electrical power supplied by the MPP instantly followed the power requested by the grid, while the power supplied by BESS followed the CEI-SFPR logic. Due to the CEI-SFPR logic, after the frequency reached the "narrow" under-frequency threshold of 49.8 Hz, the BESS started to supply power to the network, causing a rise in frequency. After the first increase, the frequency dropped

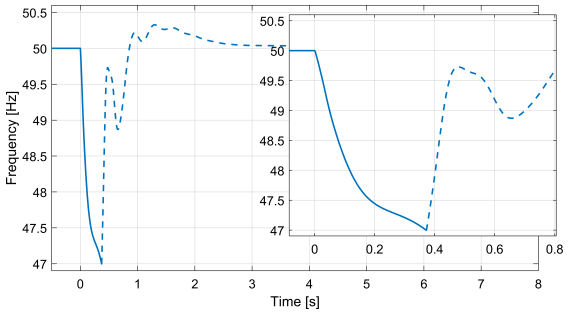
again to below the previous lower peak, causing another increase in power delivered by the BESS (for this reason, in Fig. 3.44b, a second increase in power delivered by the BESS is visible).



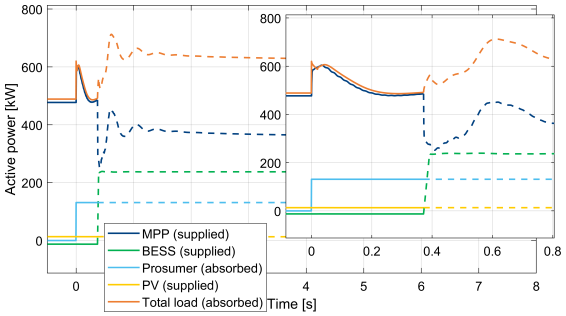
(a) BESS enabled



(b) BESS enabled



(c) BESS disabled



(d) BESS disabled

Figure 3.44: Case 1 - 5:18 event on July 28: frequency (left) and active power balance (right)

In Figs. 3.44c and 3.44d, the frequency and power trends were reported in the case where the "narrow" thresholds of the CEI-SFPR control of BESS were not set, remaining on "wide" thresholds. In this way, it is possible to demonstrate that, without the MGC action, the network would have reached a frequency of 47 Hz. At that point, BESS supplied its maximum active power since the lower limit of its "wide" thresholds was reached, avoiding a blackout.

However, this activation is considered a last resort action and was therefore not taken into account in the MGC logic. When those frequency values are reached, it is not possible to assert with certainty that BESS provides its contribution in time before the network is completely lost. Delays due to frequency measurement and control are unknown and may not guarantee a sufficiently timely response from the device. This aspect will be widely discussed in Section 4.2.

This condition can be considered unacceptable, and for this reason, it can be stated that the transition to "narrow" thresholds of the BESS CEI-SFPR requested by the MGC has indeed proven to be necessary. Frequency and power trends beyond the 47 Hz limit

have been reported, but with a dashed line, indicating that such trends are no longer to be considered.

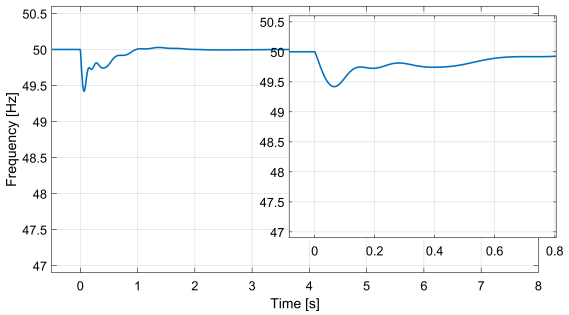
3.5.1.2 Key moment of 07:42: MPP request accepted

In Case 2, as reported in Table 3.6, there was a total load consumption on the island of approximately 567 kW, distributed across the 5 residential loads, in addition to the 12.5 kW related to the auxiliary services of BESS. The PV system, during that hour, was producing 95 kW of active power, and BESS was at 47% of its SoC. The MPP was able, thanks to the power produced by the PV system, to supply the load while keeping only one of its diesel units in operation. The UOR to be ensured, calculated using the method described in Section 3.1.5, was 171 kW (related to the absolute Upward Operating Reserve (UOR) to be guaranteed based on the historical data at that moment on that day). This reserve was not covered by the reserve made available by the MPP and BESS. For this reason, the MGC sent a request to the MPP to increase its available UOR. The MPP had one diesel unit available to turn on to accommodate the request expressed by the MGC.

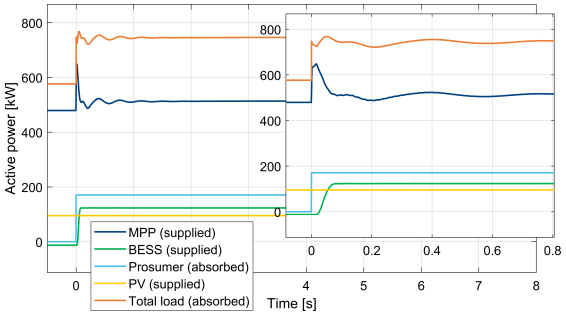
After setting the values in the model as reported in Table 3.6 for Case 2, simulations were carried out to verify the actual need for the MGC to send the request to increase the UOR to the MPP. To do this, simulations with and without the increase in reserve by the MPP were performed. Frequency and active power trends during the transient have been shown in Fig. 3.45. Particularly, an additional condition has been considered to better validate the MGC's decision in this specific case.

Figs. 3.45a and 3.45b show the trends of frequency and active power supplied by the components of the island grid in the event of a load variation equal to the UOR to be ensured, under the network conditions determined by the MGC. Obviously, with the MGC actions, the network had enough UOR to meet the instantaneous load variation imposed. Turning on an additional diesel units, the MPP had a quantity of UOR much higher than the requirement and the frequency transient was very mild: the transient could be considered terminated in less than 2 seconds, with a frequency nadir of about 49.5 Hz.

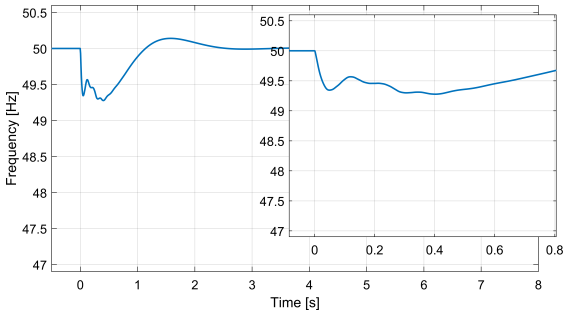
In Figs. 3.45c and 3.45d, on the other hand, the frequency and power trends are shown in the case where the MPP did not accept the request sent by the MGC. Due to the significant frequency variation that occurred on the network, BESS, following its CEI-SFPR control, supplied more power than the UOR available calculated for it from the MGC. In fact, following the assumptions and settings described in Section 3.1 and 3.2.2.4, respectively, the upward/downward reserve made available by BESS was calculated as the



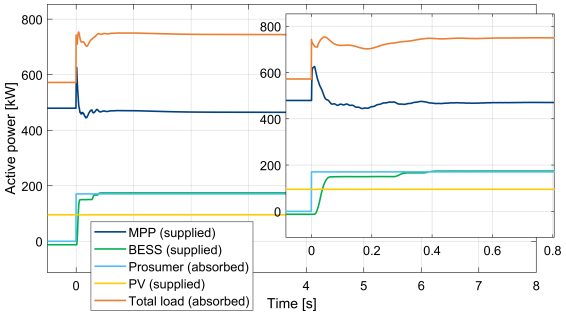
(a) MGC request accepted



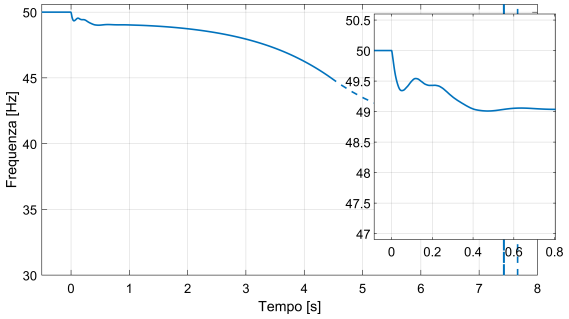
(b) MGC request accepted



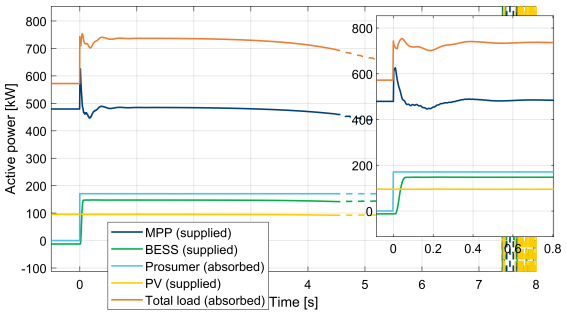
(c) MGC request not accepted



(d) MGC request not accepted



(e) MGC request not accepted and BESS power exchange limited to the calculated reserve



(f) MGC request not accepted and BESS power exchange limited to the calculated reserve

Figure 3.45: Case 2 - 07:42 event on July 28: frequency (left) and active power balance (right)

instantaneous power that can be continuously delivered/absorbed for 30 minutes.

Starting with a SOC of 47% and remaining within the limits of 20%-90%, the UOR available was 180 kW ($50\% - 20\% = 27\%$ of available discharge $=> 0.27 * 300 = 81$ kW of UOR for 1 hour $=>$ 162 kW for 30 minutes), while the DOR would be 258 kW ($90\% - 47\% = 43\%$ of available charge $=> 0.43 * 300 = 129$ kW of DOR for 1 hour => 258 kW for 30 minutes) but is limited to the nominal power of 250 kW. The time for which it is desired that the BESS can deliver power continuously can be varied by setting a time greater or less than 30 minutes, choosing to be more or less conservative, respectively.

For the sole purpose of observing what would happen if BESS could deliver only the UOR calculated for it, Figs. 3.45e and 3.45f show the same case just described (the plant

has rejected the request from the MGC and BESS CEI-SFPR thresholds set to "narrow") but limiting the maximum power deliverable by BESS to the instantaneous power deliverable continuously for 30 minutes.

By limiting the BESS to this power value, in fact, the network was not able to cope with the imposed load variation. It is specified that from the moment the frequency reached approximately 45 Hz, the trends shown in Figs. 3.45e and 3.45f lose their validity. From that moment on, the frequency and power trends have still been reported but with a dashed line, indicating that such trends are no longer to be considered.

3.5.1.3 Key moment of 19:54: Load shedding due to MPP request rejected

In Case 3, as reported in Table 3.6, after the load shedding action performed by the MGC of a total of 20 kW, there was a total load consumption on the island of approximately 874 kW, distributed across the 5 residential loads (in addition to the 12.5 kW related to the auxiliary services of BESS). The load shedding performed for each of the 5 residential loads was as follows:

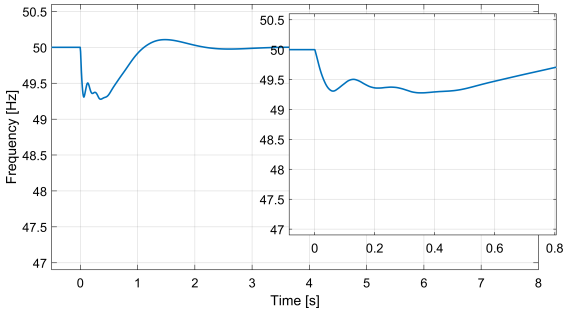
	RL1	RL2	RL3	RL4	RL5
Load shedding (kW)	9.2	2.5	3.4	1.6	3.3

Table 3.8: Load shedding performed during the key moment of 19:54 of July 28

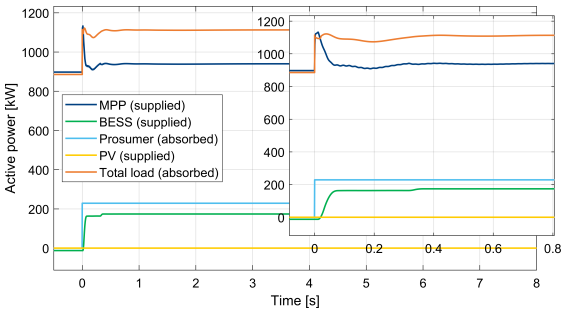
The PV system, during that hour, no longer produced energy, and BESS remained at 47% of its SoC. The MPP could not, even considering BESS, meet the minimum UOR to be ensured, amounting to 229 kW without the load reduction performed. The MGC had sent a request to the MPP in the previous iteration to increase its available UOR. However, the MPP, having no more diesel units available, rejected the request made to it, and for this reason, the MGC began to perform load shedding on the network. After setting the values in the dynamic model described in Section 3.2.1 as reported in Table 3.6 for Case 3, simulations were carried out to verify the actual need for the MGC to perform load shedding. To do this, simulations with and without this action were performed. Frequency and active power trends during the transient have been shown in Fig. 3.46. Particularly, an additional condition has been considered to better validate the MGC's decision in this specific case.

In Figs. 3.46a and 3.46b, it can be observed the trends of frequency and power after imposing a load variation on the network equal to the UOR to be ensured, in the network conditions as a result of the MGC actions. It is noted how the network was able to cope

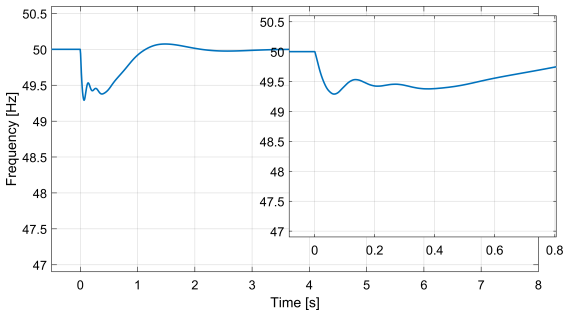
with the abrupt load variation imposed. Despite the two diesel units turned on by the MPP, to cope with the imposed load variation, the BESS provided about 173 kW of active power, which was higher than the calculated available reserve that was 163 kW (as previously discussed) because of the nadir of about 49.3 Hz reached by the frequency during the transient.



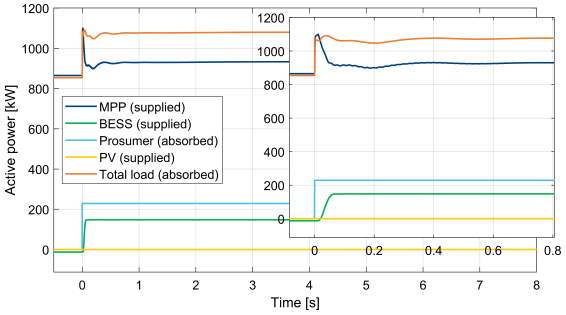
(a) Load shedding performed



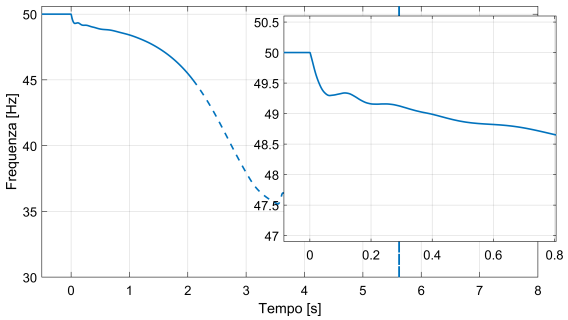
(b) Load shedding performed



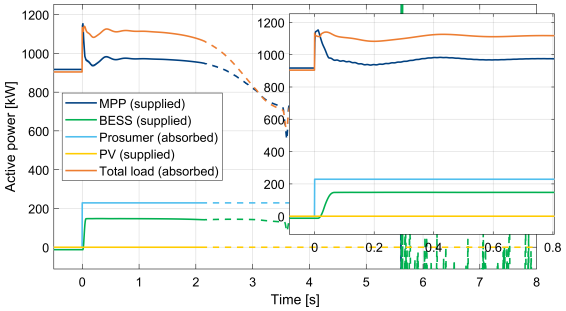
(c) Load shedding performed and BESS power exchange limited



(d) Load shedding performed and BESS power exchange limited



(e) Load shedding not performed and BESS power exchange limited



(f) Load shedding not performed and BESS power exchange limited

Figure 3.46: Case 3 - 19:54 event on July 28: frequency (left) and active power balance (right)

In the Figs. 3.46c and 3.46d, the same case has been reported in which, however, the instantaneous power deliverable by the BESS has been limited to the instantaneous power deliverable continuously for 30 minutes, i.e., the available reserve calculated for the BESS at that time by the MGC. This is to verify that, the amount of load shedding carried out

(20 kW), represented the minimum necessary to enable the grid to cope with the imposed load variation.

In Figs. 3.46c and 3.46d, on the other hand, it can be observed the trends of frequency and powers if the load shedding action had not been performed and with the power deliverable by BESS limited to its available UOR deliverable continuously for 30 minutes. This represented the point of view of the MGC without acting the load shedding. Also in this case, from the moment the frequency reaches values of about 45 Hz, the trends are no longer to be considered and have been reported with a dashed line.

3.5.2 Dynamic analysis of key moments of the typical winter day test case

In this section, reference is made to the typical winter day discussed in Section 3.4.2. Not all the key moments of the day listed in Table 3.5 have been examined in detail, but only those essential and sufficient to verify the effectiveness of the algorithm's choices. The actions carried out by the MGC to be examined are reported in Table 3.9. For the various cases, the conditions of the network are reported in Table 3.10.

Table 3.9: Actions of the MGC dynamically examined for the typical winter day

Case	Time	Action
4	8:51	Moving to "narrow" thresholds of the BESS
5	13:15	Moving to "wide" thresholds of the BESS

Table 3.10: Grid situation during MGC actions for the typical winter day

			Active power [kW]							
			Generated		Absorbed					min
Case	SoC	N_{GEN}	MPP	PV	RL1	RL2	RL3	RL4	RL5	UOR
4	50	1	89	130	92	37	42	10	22	92
5	50	1	99	116	84	31	44	17	23	84

As can be seen from Table 3.9, only the key moments related to the activation and deactivation of the "narrow" thresholds of the BESS have been considered. This is because, in the remaining two key moments of the day, there was no action related to a lack of reserve, but only an action to keep the net-load above the MDRB of 48 kW set. In summary, the reserve provided was always higher than the minimum to be guaranteed, so it is not necessary to verify it through additional tests.

3.5.2.1 Key moment of 08:51: Moving to "narrow" thresholds of the BESS

In Case 4, as reported in Table 3.10, there was a total load consumption on the island of about 203 kW divided among the 5 residential loads and 12.5 kW of auxiliary services from the BESS. At 8:51, the active power generated by the PV power plant was about 130 kW, and the BESS, according to the control logic implemented and described in Section 3.2.2.4, had a SOC of 50%. The MPP, for those hours of the day, manages to feed the required load with only one diesel unit turned on. The minimum DOR to be guaranteed was 92 kW, referred to the loss of the load that was absorbing more active power at that moment (RL1).

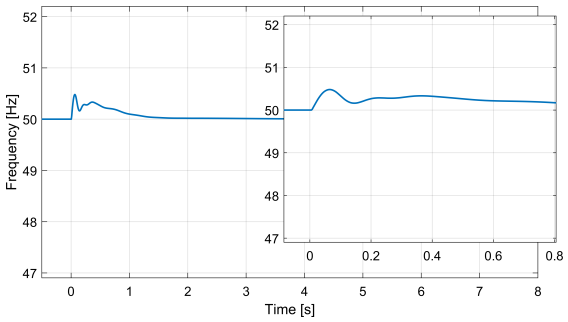
After setting the values of active power absorbed by the various residential loads, the power supplied to the PV system, the number of diesel units of the MPP turned on, and the SoC of the BESS, the disconnection of the residential load absorbing more power (RL1) was simulated. This setting was useful to determine if, in the occurrence of such an event, the network was actually in a condition of possible danger to the system's stability, and it was indeed necessary to implement the action required by the MGC, namely the transition to the "narrow" thresholds of the BESS' CEI-SFPR control.

Frequency and active power trends during the transient have been shown in Fig. 3.47. Particularly, an additional condition has been considered to better validate the MGC's decision in this specific case.

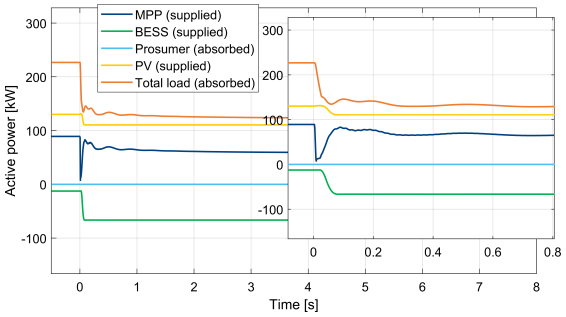
Figs. 3.47a and 3.47b show the trends of frequency and powers following the disconnection of RL1, with the BESS enabled after the MGC's action. In Fig.3.47a, it can be observed that the frequency underwent a variation, reaching a zenith of about 50.5 Hz, and then completely stabilizing after about 1.2 seconds.

In Fig. 3.47b, it is observed how the total load of the island was reduced following the imposed load disconnection and how the electrical power supplied by the MPP instantly followed the active power required by the network. The power supplied by the BESS, on the other hand, followed the logic of its CEI-SFPR with "narrow" thresholds, with a variation of active power absorption of about 60 kW (passing from the 12.5 kW absorbed by the auxiliary services of the BESS to about 72 kW). Another fact that can be noted is the reduction in the power produced by the PV system due to CEI-OFPL control. The power produced by the PV was limited by about 15%, from 130 kW to about 111 kW.

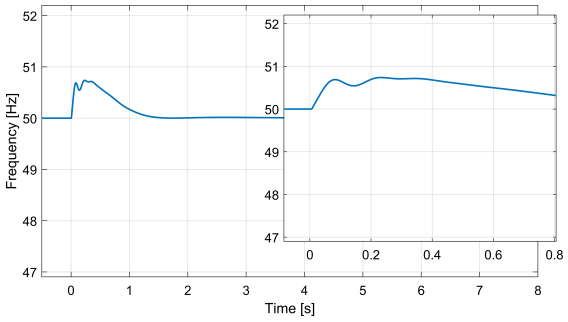
Figs. 3.47c and 3.47d show the trends of frequency and powers in the case where the thresholds of the CEI-SFPR of the BESS remained set to "wide". As can be seen from the figures, the network managed to cope with the imposed load disconnection without any intervention from the BESS because the set "wide" thresholds have not been reached. This



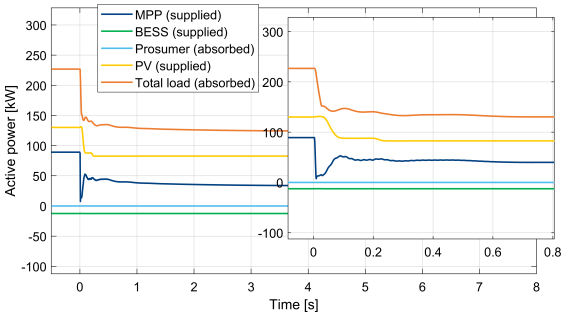
(a) BESS enabled



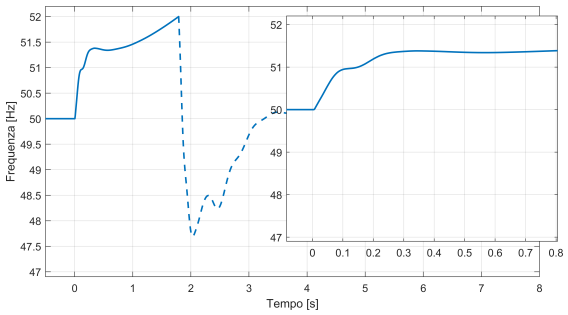
(b) BESS enabled



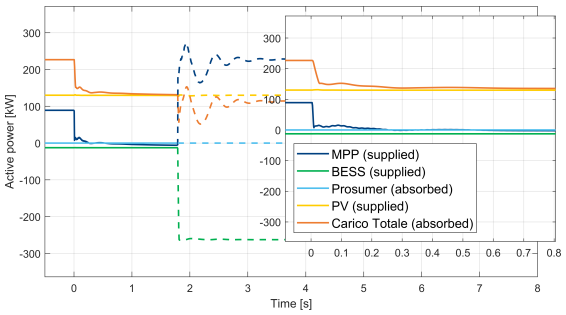
(c) BESS disabled



(d) BESS disabled



(e) BESS disabled and PV's CEI-OFPL control neglected



(f) BESS disabled and PV's CEI-OFPL control neglected

Figure 3.47: Case 4 - 08:51 event on February 5: frequency (left) and active power balance (right)

was due to the CEI-OFPL control that allowed the PV to reduce its active power produced.

As already discussed in Section 3.1, the response time of this control is not fully defined and it is insecure to tie the security of the island network to this control (this topic will be widely discussed in Section 4.2). In addition, the intervention of this control leads to the establishment of a frequency above 50.2 Hz for an indefinite time, a condition that is desired to be avoided to ensure better quality of electrical service. Therefore, this regulation has been considered a last resort action and was not taken into consideration in the control algorithm implemented in the MGC. For this reason, to verify the correct choice of the MGC, this regulation should not be considered in these tests.

Figs. 3.47e and 3.47f show the trends of frequency and powers disabling this control,

and it can be immediately noticed how the frequency reached 52 Hz, the upper limit of the "wide" thresholds of the BESS' CEI-SFPR. At that point, the BESS provided its maximum contribution, absorbing its 250 kW of rated power. Since this is also a last resort contribution, the condition just reached has to be considered unacceptable, validating the choice of the MGC.

3.5.2.2 Key moment of 13:15: Moving to "wide" thresholds of the BESS

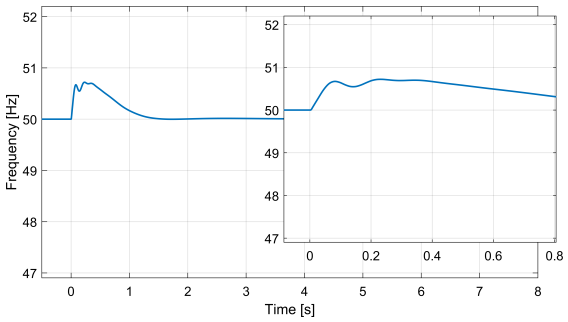
In Case 5, as reported in Table 3.10, there was a total load consumption on the island of about 199 kW divided among the 5 residential loads, and 12.5 kW consumed by the BESS for its auxiliary services. At 13:15, the production from the PV source was about 116 kW, and the BESS, according to the control logic implemented and described in Section 3.2.2.4, had a SoC of 50%. The MPP, for those hours of the day, was able to feed the required load with only one diesel unit turned on. The minimum DOR to be guaranteed was 84 kW, referred to the loss of the load that was absorbing more active power at that moment (RL1).

According to the evaluation by the MGC, at that moment, the reserve made available by the MPP was sufficient to guarantee the minimum DOR, and for this reason, the MGC disabled the BESS, switching the CEI-SFPR control thresholds of the BESS from "narrow" to "wide".

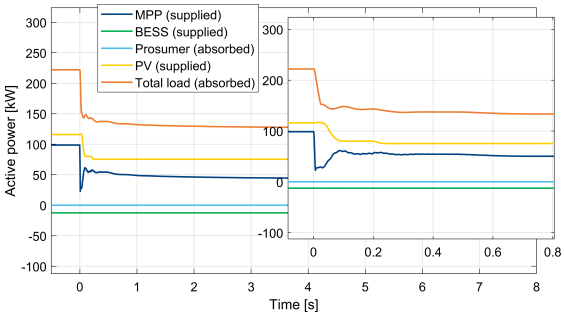
After setting the values of active power absorbed by the various residential loads, the power supplied to the PV system, the number of running MPP diesel units, and the SoC of the BESS, the disconnection of the load absorbing more power (RL1) was simulated. This setting was useful to determine if, in the event of such an occurrence, the network was actually in a secure condition for the stability of the system, and it was indeed no longer necessary to enable the BESS.

Frequency and active power trends during the transient have been shown in Fig. 3.48. Particularly, an additional condition has been considered to better validate the MGC's decision in this specific case.

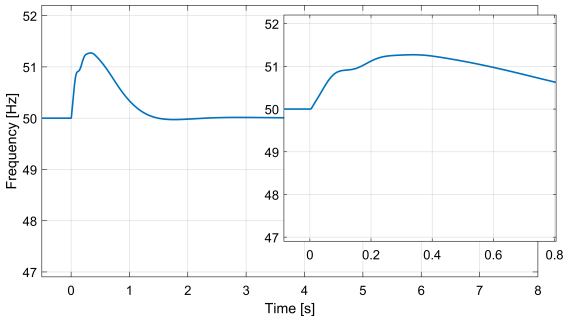
Figs. 3.48a and 3.48b show the trends of frequency and active powers following the disconnection of RL1, with the BESS no longer enabled after the MGC's action. From the figures, it can be observed that the load disconnection caused an over-frequency event with a peak of about 50.7 Hz, limited also by the action of the PV plant's CEI-OFPL, which limited its active power production to cope with the transient condition of excess generation on the grid. The power produced by the PV, in this case, was reduced from the initial 116 kW to about 70 kW.



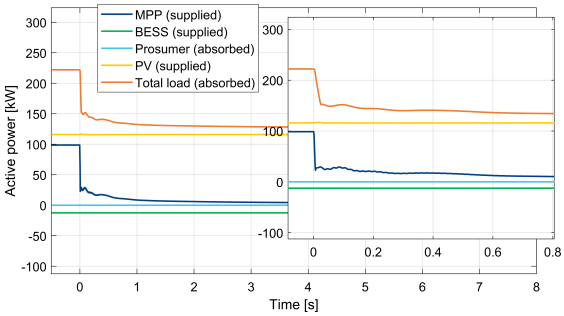
(a) BESS disabled



(b) BESS disabled



(c) BESS disabled and PV's CEI-OFPL control neglected



(d) BESS disabled and PV's CEI-OFPL control neglected

Figure 3.48: Case 5 - 13:15 event on February 5: frequency (left) and active power balance (right)

As discussed in the previous case, this action is considered a last resort action, not taken into consideration in the logic of the MGC. Although it was present in the dynamic model to consider all possible actions in play on the network, this action should not be considered when judging the decisions made by the MGC. Figs. 3.48c and 3.48d show the trends of frequency and power in the conditions considered by the MGC during its analysis, without the self-regulation action of the PV. It can be seen that the frequency reached a zenith of about 51.4 Hz, which was much larger than when considering the self-regulating action of the PV (50.7 Hz), but it did not reach the upper limit of 52 Hz that would trigger the last resort action of the BESS. Therefore, it is possible to denote that, under the conditions in which the network was at that time, the enabling of the BESS was indeed unnecessary.

3.6 Conclusion

In this chapter, a Real-Time Algorithm (RTA) for operating reserve assessment and allocation has been presented. This control algorithm, developed to be implemented in an actual control architecture for isolated distribution grids, monitors and manages the security and secure grid operation, assessing the available operating reserve and sending requests to the

controllable resources in order to ensure the minimum operating reserve allocation. First, all the assumptions taken into account for the development of the proposed RTA and its base logic have been discussed. Then, the proposed RTA was implemented in a finite-state machine model that represented the model of a Microgrid Controller (MGC) of a generic isolated Microgrid.

This RTA was tested through simulations on the electrical model of the small Italian island benchmark introduced in Section 1.5.1. To test an operational algorithm, it is necessary to consider the dynamic behaviors of the components connected to the network during its operation. However, testing an operational algorithm on real-time dynamic model simulations is very complex and hardly applicable. To observe the results of one day's operation, at least one day's simulation is required. For this reason, two different models have been developed: the first represented a dynamic model of the test network, in which all dynamics of the network components have been implemented, allowing observation of the impact of operational algorithm decisions on network stability. The second represented a quasi-static model of the test network, in which electromechanical dynamics have been neglected, providing a more agile testing environment for the operational algorithm.

Using the quasi-static grid model, after verifying the correct implementation of the RTA on the MGC model, the RTA was tested by going to simulate two months of grid operation, a summer month (July) and a winter month (February). From these simulations, one day of each month was taken to analyze the behavior of the RTA.

From these analyses, it was observed that the RTA always ensures the required minimum level of operational reserve, both upward and downward. However, from analysis, it can be said that during winter days the network is less likely to fall into insecure conditions in which the MGC is forced to intervene to restore it.

Both the winter and summer cases examined, however, resulted in generation or load shedding, respectively. The fewer operating state changes observed in the winter cases are due to a simpler control, which does not have the state in which additional reserve is required from the MPP. While macro-state 3 (which is tasked with ensuring adequate operational reserve to go up the island) reaches to perform the most extreme action (load shedding) after performing 3 state transitions, the generation curtailment action of renewable sources can occur just after 1 state transition (the one related to macro-state 1, which is tasked with ensuring MDRB to the MPP).

Even though the lower risk during winter days compared to summer days cannot be attributed to the state changes that have occurred, it is true that the downward reserve to be

ensured has always been low, and there has never been a case where generation curtailment was necessary due to a lack of downward reserve. This is because the capacity of the PV is significantly smaller than that of the BESS. Enabling the BESS never leads to situations where the PV needs to be limited to ensure reserve. In the event of considering a larger PV capacity, for instance, approaching a size close to 500 kW as the Italian Ministry of Economic Development target for 2050 [73], this condition can be expected to occur more frequently. This is because a higher PV capacity increases the downward operating reserve to be ensured. Of course, the limitation of the PV to prevent the net-load from falling below the MDRB will always be present and will limit the power produced by the PV up to a certain point, regardless of the size of the installed PV. Therefore, even for very large PV capacities, if the electrical load is very low, the limitation condition due to downward operating reserve issues is unlikely to occur. Despite everything, the state of limiting the PV for downward operating reserve issues ensures the secure operation of the network even in cases of unexpected and different network conditions, making the algorithm more general and applicable in various network scenarios.

It is worth noting that, thanks to the MGC's preventive curtailment actions, the hosting capacity of the smaller islands is significantly increased, enabling greater Renewable Energy Sources (RES) penetration in these highly fragile systems. Moreover, this benefit could also be extended to small portions of the mainland MV (or LV) distribution network, for example, if weakly interconnected, by managing these systems through the proposed operating algorithm.

Chapter 4

Innovative Solutions for the Provision of Fast Frequency Support Ancillary Services

Due to the penetration of renewable sources, in a small islanded system, new problems may occur in the operation of power grids related to both dynamic (system security and stability) and static (congestion and adequacy) issues [106, 107].

The stability and reliability of power systems depend on the system's ability to hold frequency excursions within a narrow range around the nominal value, particularly following significant disturbances that alter the balance between power generation and demand [108]. Conventional control methods, such as Frequency Containment Reserve (FCR), are used by conventional generators to regulate the response of the electrical system. The ability of the system to maintain a stable frequency after a grid outage, even before the manifestation of FCR, is referred to as system "inertia". As pointed out in [109], this parameter plays a critical role in the stability of the power system, as its value affects the RoCoF following abrupt changes in the load and generation balance.

While conventional power plants inherently contribute to the inertia of the system because it is associated with the kinetic energy stored by the rotating masses of synchronous generators, distributed resources, on the other hand, are usually interfaced with the power grid through power converters that mechanically decouple them from the grid and do not allow them to contribute to the inertia of the system. Distributed resources are usually generation facilities from renewable energy sources, at present, participating in the zero-cost energy market. For this reason, such resources tend to leave conventional units out of

economic dispatch, and electric systems begin to be characterized by low rotational inertia [110].

The main consequence of reduced system inertia is the acceleration and amplification of frequency transients, leading to risks such as improper operation of protections, unintentional opening of power lines, load shedding, and, in the most severe cases, a blackout [14]. These problems pose a significant threat to both interconnected systems and small isolated networks. Larger interconnected systems, for example, are susceptible to this problem because of the heterogeneous distribution of rotational inertia that can lead in many cases to instability of some parts of the network and their disconnection [111].

Many electric system operators have recognized the need to increase inertia, as highlighted in [112]. Italy, in accordance with Regulation 300/2017/R/EEL [113], has commissioned pilot projects to demonstrate the feasibility of providing DR services for fast load shedding and FCR services for generation units integrated with storage systems.

An alternative approach, discussed in [114], involves installing additional synchronous condensers to improve system inertia and mitigate frequency excursions. However, this method has the disadvantage of increasing the cost and complexity of the system. Another avenue explored in the literature, called Virtual Synchronous Machines, suggests controlling existing inverter-based resources to emulate the behavior of a synchronous generator and provide additional inertia [114, 115].

In addition, recent studies have explored the prospect of deriving additional inertia from controllable devices such as generators, storage devices, and loads [3, 15, 116, 117].

To enhance the electrical grid's inertia and mitigate frequency and RoCoF excursions, it is crucial to implement control actions such as Synthetic Inertia (SI) and Fast Frequency Response (FFR) on DERs and controllable devices. While some studies do not distinctly address the differences between Synthetic Inertia and Fast Frequency Response [118], each can be described separately.

As per the SI definition provided by ENTSO-E in [119]:

> *"**Synthetic Inertia** is defined as the controlled contribution of electrical torque from a unit that is proportional to the rate of change of frequency measured at the terminals of the unit".*

Despite the absence of a unified definition in the literature [118], SI can be interpreted as a control law proportional to the measured frequency derivative (RoCoF) [1, 120, 121].

Considering the description in [118], FFR is defined as:

> *"**Fast Frequency Response** is the controlled contribution of electrical torque from a unit which responds quickly to changes in frequency [...]".*

The definition of FFR is more general than that of SI and may encompass the latter within its scope. Therefore, the term FFR can refer to both a contribution simply proportional to the frequency deviation (as a primary frequency regulation with an high droop) and more sophisticated controllers that include mixed contributions, potentially dependent on the RoCoF, as in the case of SI. Anyway, Fast Frequency Response usually refers to a control law proportional to the frequency excursion that aims to provide inertial support through units capable of varying their exchanged power very rapidly. Various examples of FFR controls serving this purpose have been proposed in the literature [122], [123]. Most studies indicate that both Synthetic Inertia and Fast Frequency Response effectively enhance frequency excursions and the frequency nadir post-disturbance [118].

In this chapter, innovative solutions for the provision of Fast Frequency Support (FFS) ancillary services have been presented. Specifically, these methodologies aim to improve the effectiveness of such services over traditional FFS controls such as SI and FFR. The improvements focus mainly on increasing system stability with respect to the increased penetration of distributed energy resources interfaced through grid-following inverters, as well as safeguarding these resources during the delivery of such services.

In detail, an improved SI control is presented, aimed at reducing frequency oscillations during transients, reducing the settling time, and improving system stability in such situations. This facilitates greater penetration of distributed resources empowered to provide frequency regulation services. Regarding this additional SI control, two applications are shown in this chapter: the former concerning the provision of Fast Frequency Support (FFS) through V2G EVs on the island of *Favignana*, the latter concerning the provision of FFS through street lighting systems on the same reference small Italian island described in 1.5.1

Then, a State of Charge (SoC)-feedback-based control of distributed storage devices is illustrated. This control limits the action of such resources to preserve their health and extend their lifetime. In addition, it is shown how, through an optimization algorithm, it is possible to find the best trade-off between rapidity of response and component preservation, tailoring it to the needs of the end user who owns the resource.

4.1 Improved Synthetic Inertia Control Law for Distributed Grid-Following Inverter-Based Energy Resources

In this section, an improvement of the classical synthetic inertia control law is proposed. The proposed improved control law always achieves a better system frequency response than using the classical SI control law; moreover, it becomes critically important when delays in the control loop of the resources providing this service come into play. Distributed energy resources are often interfaced to the grid via grid-following inverters.

To provide fast frequency support service, such as synthetic inertia, these inverters require a frequency measurement system (e.g., Phase-Locked-Loop - PLL), which necessarily introduces errors and delays into the control loop. In the specific case of synthetic inertia, moreover, the control system must measure the derivative of frequency (RoCoF), which requires more computational complexity. The measurement of RoCoF, in any case, is more prone to errors and delays. In the case of high penetration of devices providing these services, errors and delays can lead to instability. This limits the maximum penetration of these services on the power grid.

In this section, the concept behind this improved synthetic inertia control law is first described. Next, the improvement of the frequency trend is shown compared with cases where the classical SI control law is used under ideal conditions, with no delays or disturbances in the measurement. In Section 4.2, related to the BLORIN research project, a real-world application of this method is shown, demonstrating how this improved SI control law allows for greater penetration of the distributed resources that provide this service. The BLORIN (BLOckchain for Renewables INtegration) research project [124], which will be further discussed in Section 4.2, focused on the creation of a blockchain platform for the management of solar Smart Communities able to facilitate interactions between small producers, consumers, and prosumers and enable them to provide network services. Finally, a second real application of the method is shown in Section 4.3, in which the method was used to demonstrate how street lighting systems can make an important contribution to frequency support.

4.1.1 Concept of the Proposed Synthetic Inertia Control Law

As just said, synthetic inertia is obtained by applying a control law proportional to the frequency derivative (RoCoF). However, a control law that follows continuously the RoCoF

trajectory can lead to an increase of the frequency settling time, because of the inertial support given after having reached the *nadir* point. Such a drawback can be overcome by adopting the solution proposed in [125] where the SI control is applied only when RoCoF and frequency deviations have the same sign.

The authors of [125] focused exclusively on primary frequency control because it is in the first moments after a contingency that synthetic inertia plays a significant role in power systems. After a major contingency, restoring the nominal frequency can take tens of seconds, and the approach proposed by [125] could be counterproductive, reducing the impact of inertial support provided by the controlled resource. To implement the control proposed by [125], it is therefore essential to know the steady-state frequency after the disturbance, information that is often challenging to obtain. In the context of non-synchronous distribution systems, such as small Italian islands primarily powered by small-scale diesel plants, the distinction between primary and secondary frequency regulation is less clear-cut. This is because frequency regulation occurs through a proportional-integral control implemented in the control systems of diesel generation units. Unlike the case analyzed in [125], in this scenario, it is easier to apply such control since the steady-state frequency can be considered consistently equal to the nominal frequency of the system.

To demonstrate the effectiveness of the proposed additional control, a simple single-bus model of an isolated power grid was built in the Matlab/Simulink environment. The model is shown in Fig. 4.1. The frequency dynamics is modeled through a first-order transfer function in which H represents the inertia of the system and D represents the damping, that is, the frequency dependence of the island load. This transfer function receives as input the power imbalance of the network and returns the resulting frequency change (in p.u.). It, compared with the nominal frequency, goes as input to the block that simulates the behavior of a diesel engine.

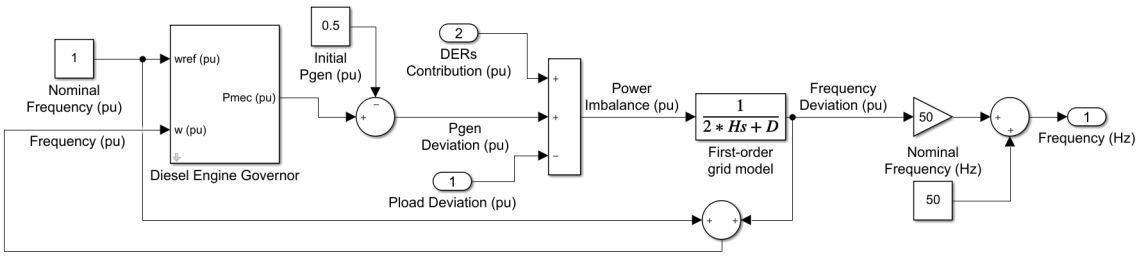


Figure 4.1: A single-bus grid model for frequency transient analysis

Figs. 4.2 and 4.3 graphically describe the concept behind the proposed additional SI control. In these figures, a standard frequency and RoCoF trend is shown during a transient,

which occurred by imposing a step load change of 0.3 p.u. on the model shown in Fig. 4.1. The graph has been divided into sectors marked by red or green letters. In the sectors marked by the letters in red, the inertial contribution is counterproductive, as it opposes the effect of the frequency regulation implemented by the speed controller of the diesel units. By neglecting the frequency measurement when it is not in accordance with the frequency deviation, an inverter-based distributed resource would provide the inertial contribution only at useful times (i.e. the sectors marked by the letters in green).

The concept behind the proposed additional SI control can be summarized in a simple *if statement*:

$$\begin{cases} if \quad F * dF/dt > 0 \\ \quad SI\ control\ ON \\ else \\ \quad SI\ control\ OFF \end{cases}$$

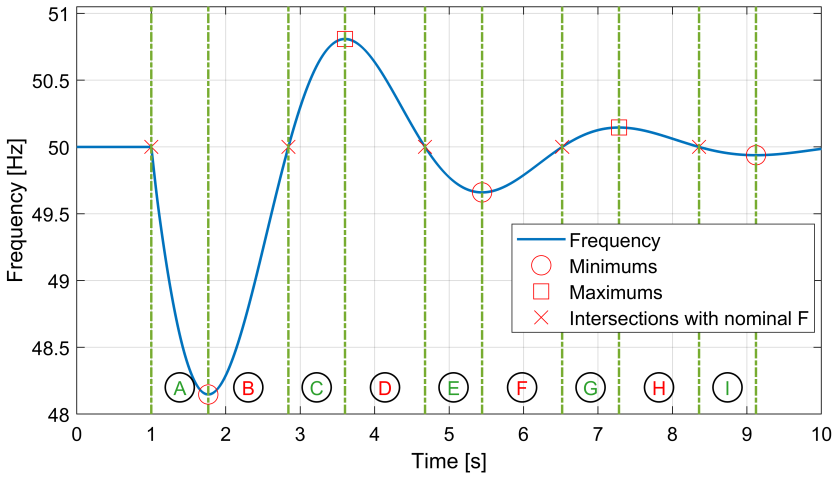


Figure 4.2: Example of frequency behaviour and definition of areas where the SI contribution is useful

As can be seen in Fig. 4.3, a good portion of the RoCoF can be ignored, and as a result, a good portion of the energy exchanged by the resource can be saved. In this way, the resource is less stressed during these types of events and, in the case of storage systems, its useful life is safeguarded more.

The proposed SI control is illustrated in Fig. 4.4. It is represented in relative values as a function of the penetration of DERs. The control set-point is constrained within ± 1 pu, which represents the maximum variation, increasing and decreasing, of the power exchanged by the individual controlled resource. Next, the set-point is multiplied by the

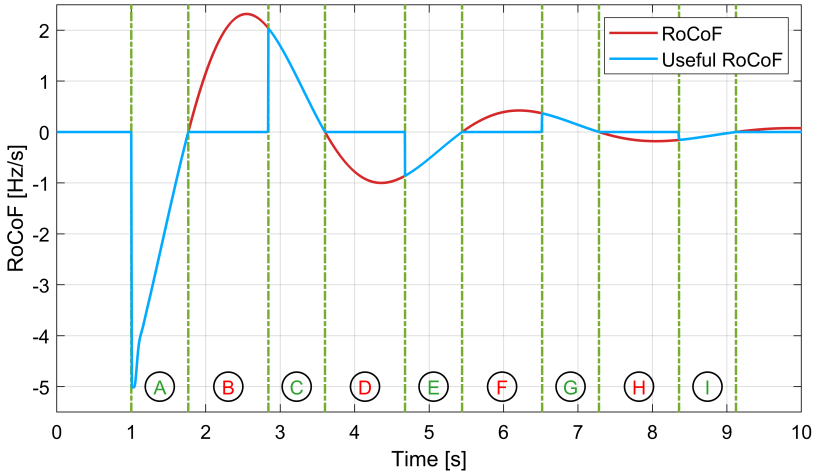


Figure 4.3: Comparison between the useful RoCoF results of acting the proposed concept with the actual RoCoF

penetration of DERs, defined as the amount of resources hypothetically connected and active on the network (assumed to be 0.2 pu), in order to simulate the impact of this amount of resources on the network.

As shown in Fig. 4.4, the proposed control incorporates the classical SI control. For the classical SI control, a gain K_{IR} of 6 was adopted, which corresponds to a virtual inertia of 3 s. In order to prevent the control from responding even to very small frequency changes, a dead band of 100 mHz (0.2% in pu) was implemented. The additional control introduced in the proposed SI controller generates a signal that takes the value of 1 when the RoCoF and frequency deviation are concordant, and 0 when they are discordant. This signal, multiplied by the output of the classical SI controller, sets the SI set-point to 0 when it is not needed. Finally, a first-order low-pass filter, with time constant T_{SI} equal to 40 ms, was integrated in order to mitigate abrupt variations in the control signal sent to the controlled resources.

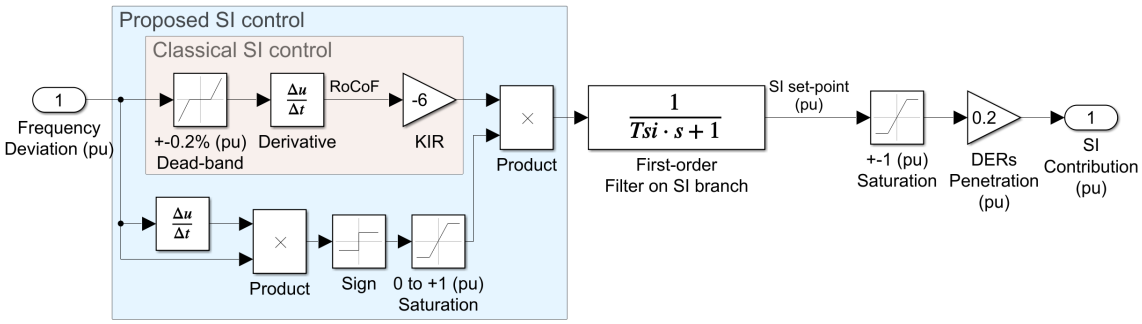


Figure 4.4: Model of the proposed SI control law

In Fig. 4.5, the frequency trends with and without the inclusion of the proposed

additional contribution are shown. A significant improvement over the case without the SI contribution is observed for both SI controls analyzed. However, the inertial contribution provided by the classical SI control, compared with that of the proposed SI control, does not significantly reduce the frequency overshoot and slows down the settling time.

Table 4.1 shows the characteristics of the frequency response in the 3 cases observed in Fig. 4.5. The proposed SI control shows no difference from the classical SI control in the first instants after the contingency until the nadir is reached. Both controls contributed to reducing the average RoCoF in the first instants after contingency by 21%, from 4.25 Hz/s to 3.30 Hz/s. The average RoCoF was calculated by considering the portion of the frequency characteristic from the instant of the load change to the moment when the frequency reached half of the maximum excursion (nadir). The maximum frequency excursion was reduced by 11% with both controls, from 1.85 Hz (nadir of 48.15 Hz) to 1.64,Hz (nadir of 48.36 Hz). An improvement was also observed in the time required to reach the nadir: thanks to the SI controls, the nadir is reached after 0.9 s instead of 0.77 s, indicating a slowdown in frequency dynamics of 17%.

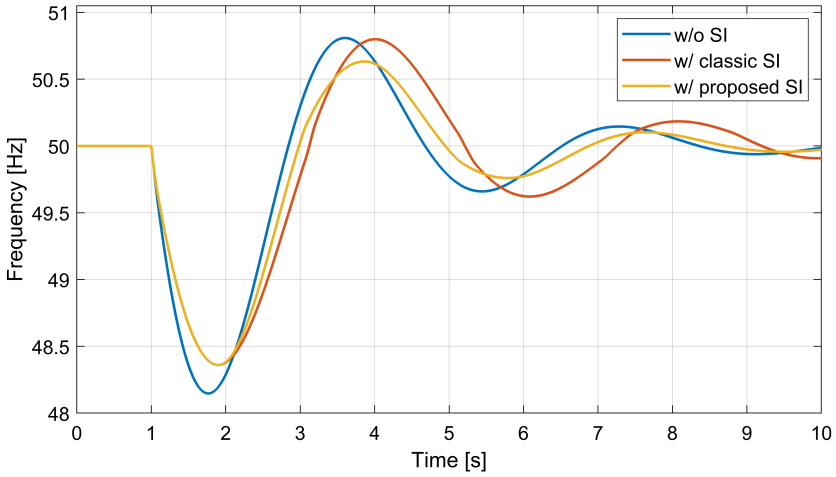


Figure 4.5: Frequency behaviour without SI, with classical SI and with proposed SI control

The differences between the two controls can be observed after reaching the nadir: the percentage overshoot obtained with the classical SI control decreased negligibly compared to the case without SI control, only by 0.02%, going from a maximum frequency value during the transient of 50.81 Hz to 50.80 Hz. With the proposed SI control, on the other hand, the reduction in percentage overshoot was 0.4%, falling from 50.81 Hz to 50.63 Hz. If only the frequency excursion during overshoot is considered, the improvement is significantly more noticeable. In fact, with the proposed SI control, the maximum excursion during overshoot went from 0.81 Hz to 0.63 Hz, reducing by 22%. By contrast,

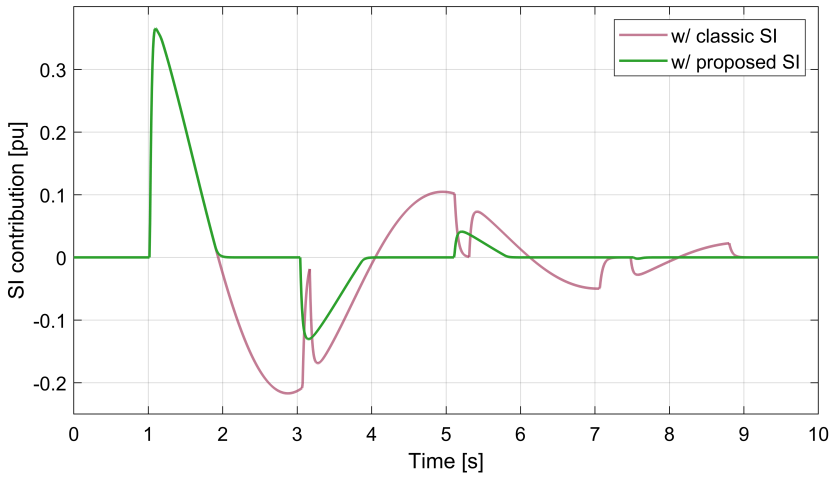


Figure 4.6: Comparison between SI set-point behaviour with classical SI and with proposed SI control

Table 4.1: Frequency characteristics during the transient without SI, with classical SI and proposed SI control

		w/o SI	w/ classical SI	w/ proposed SI
average RoCoF	Hz/s	4.25	3.30 (-21%)	3.30 (-21%)
nadir	[Hz]	48.15	45.36	45.36
max ΔF	[Hz]	1.85	1.64 (-11%)	1.64 (-11%)
nadir time	[s]	0.77	0.90 (+17%)	0.90 (+17%)
overshoot %	%	1.62	1.60	1.26
overshoot	[Hz]	0.81	0.80 (-1.2%)	0.63 (-22%)
settling time at 100 mHz	[s]	6.78	7.80 (+15%)	6.75 (-0.4%)

with the classical SI control, this excursion decreased by only 1.2% (from 0.81 Hz to 0.80 Hz).

Observing the settling time at 100 mHz, i.e. the time after which the control finally shuts down, entering the frequency dead band, it can be seen that the classical SI control significantly increases the settling time compared to the case without control. The settling time increases from 6.78 s without SI control to 7.8 s with classical SI control, an increase of 15%. This negative aspect of the classical SI control is nullified by the proposed additional control: with the proposed SI control, the settling time is even lower than in the case without SI control, although negligibly so, going from 6.78 s to 6.75 s, corresponding to a reduction of 0.4%.

In Fig.4.6, the set-points generated by the classical SI control and the proposed SI control can be observed. It is evident that with the proposed SI control, the utilized

resource is invoked much less compared to the case where classical SI control is employed. The energy exchanged by the controlled resource through classical SI control would be 0.62 pu·s during the observed transient, whereas it is reduced to 0.27 pu·s with the proposed SI control. The exchanged energy has decreased by 56%, achieving a better frequency response. For clarity, assuming control over a 250 kW BESS, as in the case of the island examined in Chapter 3, such a BESS would be required to exchange 155.8 kWs (43 Wh) with classical SI control, while only 66.4 kWs (18 Wh) with the proposed SI control, in less than 10 seconds of the transient. The exchanged energy values are admittedly negligible, but it is crucial to highlight the short duration within which this energy is exchanged. Moreover, the BESS would experience rapid power variations, shifting from supplying 91 kW to absorbing 54 kW within the first 2 seconds of the transient with classical SI control, only from supplying 91 kW to 0 with the proposed SI control. Furthermore, with the classical SI control, the set-point is subject to the dead-band on frequency deviation. In contrast, the proposed SI control is unaffected by the dead-band on frequency deviation, minimizing set-point oscillations.

4.2 A real-world application in the BLORIN research project framework

As anticipated, the BLORIN (BLOckchain for Renewables INtegration) research project [124], which started on December 2019 and ended on September 2023, focused on the creation of a blockchain platform for the management of solar Smart Communities able to facilitate interactions between small producers, consumers and prosumers and enable them to provide network services. The partners who participated in the development of the BLORIN platform are *Exalto Energy & Innovation*, *Regalgrid Europe Srl*, *S.EL.I.S. Lampedusa S.p.A.*, *SEA Società Elettrica di Favignana S.p.A.*, and *Università degli Studi di Palermo*. The blockchain platform developed has allowed the aggregation of end-users for the distributed provision of Demand Response (DR) and Vehicle-to-Grid (V2G) services with the aim of helping to manage the volatility of demand and especially production from renewable sources. In fact, through DR programs it is possible to address these issues by increasing the flexibility of the electricity system while keeping costs relatively low and facilitating the integration of renewables without the need to expand the electricity grid. Whereas, with V2G programs, in addition to demand flexibility, due to the speed of

response of the charging stations, it is possible to provide frequency regulation services by harnessing the energy in the batteries of electric cars connected to the charging stations for a short period, thus contributing to greater stability of isolated power grids, such as small island grids characterized by low rotational inertia. The BLORIN platform was developed to evaluate the effectiveness of DR on the island of Lampedusa and V2G on the island of Favignana.

The blockchain used is Hyperledger Fabric, a *permissioned* platform that allows participants to access and manage their transactions through purpose-developed smart contracts, which can also be used to validate data. Due to its modular, configurable, and versatile architecture, Hyperledger Fabric has enabled the development of applications in the different use cases envisioned by the project. Being a *permissioned* network, participants are not anonymous. For this reason, the network can only work with a governance model built in such a way as to ensure trust among participants previously authorized by the trusted provider, in this case, the local distributor. The blockchain has enabled versatile and efficient interactions between different actors, creating a unique communication environment (single protocol) that dialogues with local intelligence (such as Energy Management Systems devices) or with measurement systems or even actuators. The use of a proprietary blockchain platform based on HyperLedger Fabric has also given transparency and an equal role to all actors, who have insight into data and the remuneration logic behind business models.

The effectiveness of blockchain for V2G and DR delivery is to date a widely explored topic in the literature. For example, in [126, 127] the authors propose a blockchaian-based transaction system for managing EV charging. While, in [128, 129], the authors propose the use of blockchain for secure authentication of vehicle owners for energy trading in a V2G environment, with the aim of preserving vehicle anonymity and supporting mutual authentication between EVs, charging stations and aggregator. Regarding the provision of network services such as DR, several authors, such as [130–132], propose the use of a blockchain platform to manage, track and remunerate the contribution made by generators/loads to DR in a distributed and secure manner.

The operation of the BLORIN platform for DR is described in [133], the paper [134] describes how the use of blockchain enables end-user involvement in DR service perfectly integrating with the technologies already used for DR, and [135] describes the operation of the BLORIN platform for V2G and how the platform enables privacy among users and secure management of sensitive data.

The project was structured in 11 phases, 3 of which were dedicated to testing DR programs, energy resource management strategies, and V2G energy services. In the experiments, physical Microgrids (MGs) were involved, either emulated/simulated in the laboratory or in a hardware-in-the-loop environment.

The DR and V2G programs developed during the early stages of the project were primarily aimed at supporting the penetration of renewable sources in island systems characterized by low inertia. Later, given the speed of response obtained, frequency regulation scenarios were also developed.

In order to verify the proposed methodologies for FFS by EVs and DR, *University of Palermo* has started a collaboration with *Politecnico di Bari* to emulate the dynamic behavior of these resources by means of the equipment installed at the LabZERO laboratory MG [8]. The control of the emulated devices was then tested in the Power Hardware-in-the-Loop (PHIL) environment [136], which allowed the response of the power components to be coupled with real-time simulations capable of reproducing the dynamic behavior of the power grids under study (Favignana/Lampedusa). At the same time, the cited PHIL emulations were connected to the BLORIN platform to fully simulate the market interaction.

It is important to emphasize that, although the utilization of PHIL for emulating electrical power systems and studying issues arising from specific disturbances or usage scenarios is a well-established practice, the integration of PHIL systems with blockchain platforms remains a relatively underexplored subject.

In this context, only a few papers such as [137] and [138], for example, propose the integration of the two systems, the first one for the implementation of the automated business process within energy communities, while the second one for the market supply of reactive power in a trusted and secure way.

So, the main novelty of this application is the distributed provision of frequency regulation service by involving end-users, rather than centralized and through large producers as is traditionally done, the use of blockchain for its tracking and remuneration and the blockchain connection with a PHIL system for testing.

With the purpose of reporting the application of the additional SI control proposed in this thesis work, only the test part related to the control of V2G EVs in the island of Favignana is discussed in this chapter. The part related to the provision of DR service through detachable loads in the island of Lampedusa is omitted because it is out of context, but its results can be observed in [17].

4.2.1 Dynamic model of Favignana island

To evaluate the impact of distributed generation on frequency transients and what advantages, in terms of RoCoF, maximum under frequency (nadir), settling time, and stability, can be obtained using Fast Frequency Support (FFS) control actions, a network model was developed for the simulation of electromechanical transients, to be applied to the case studies of the islands of Favignana. The dynamic network model was created so that it could be integrated into a PHIL-type real-time simulation. It was developed in the Matlab/Simulink environment to be connected to the Power Hardware-in-the-Loop simulation platform of the Politecnico di Bari based on the use of an OPAL RT5600 real-time simulator.

The created model makes it possible to simulate the behavior of the DR control system, study the influence of control in the charge and discharge cycles of storage systems or V2G EVs, and determine the possible fluctuations of active power exchanged on the system.

Favignana Island is one of the Aegadian Islands, located right off the western coast of Sicily. Although it is relatively close to the mainland (approximately 18 kilometers from the shores of Sicily), the island is not electrically interconnected to the Italian power system. The structure of the MV distribution system on the island of Favignana is shown in Fig. 4.7. The primary distribution is operated at 10 kV. The MV network starts from the 10 kV bus (CE), where the generating power plant is connected. The power plant is located close to the main load source (the town of Favignana and the port). All generating units are connected to the 10 kV bus through their own transformer.

The generating units have a total installed capacity of about 18 MVA, able to cover the summer peak load (about 9 MW) reliably. The MV distribution is organized on three radial feeders, all connected to the main CE bus. Some breakers, normally open, ensure reclosure in case of faults or any maintenance work. The network, as shown in Fig. 4.7, consists of a total of 46 buses, including the CE node to which the power plant is connected. 38 load buses (bus between $N01$ and $N42$), and 7 additional buses representing the disconnector terminals (A, $A1$, $A2$, $A3$, B, $B1$, $B2$). Most of the load buses are connected to a MV/LV transformer to supply power to end users. Only in a few cases, some large end users (such as large hotels and resorts) are connected directly to the MV grid.

The model developed for these tests is aimed to represent, in a real-time simulation, the frequency transients which might be experienced in the island, and to integrate the dynamic behaviour of the power hardware resources at the LabZERO MG [139]. Because of the computational limitations introduced by the real-time simulation requirements, the system

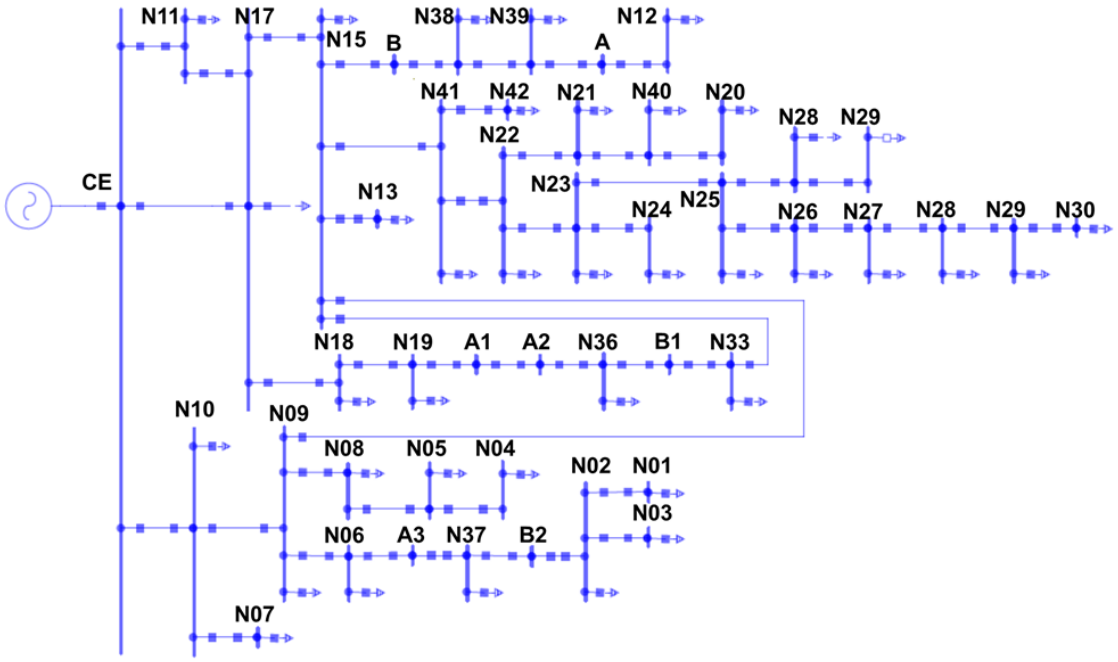


Figure 4.7: MV distribution grid of Favignana

model adopted for simulation must be suitably simplified. The following simplifying hypothesis have been done:

- the generation power plant has been modelled by a single equivalent generator, whose dynamics and actions of the frequency and voltage controllers have been considered. Exciter and governor models have been represented by means of typical literature diagrams;
- the PV power plants installed at MV level are instead modelled taking into account the automatic frequency regulation response set by the Italian grid code CEI 0-16, that regulates the connection of active and passive MV end-users [53];
- in order to avoid computational burden the network model has been reduced: LV circuits have been neglected, and the MV network has been simplified representing some laterals as equivalent MV load;
- main MV disconnecting switches have been represented in order to allow topology changes.

The RES and loads have been modeled using a *three-phase p-q theory-based dynamic load*, proposed by the authors in [12, 16], characterized by a less computation burden than

the *three-phase dynamic load* available in the Simulink's library. Adopting this load model allowed resources to be modeled more accurately, without incurring overruns.

4.2.1.1 Modelling of grid topology and distribution lines

In order to be compatible with the adopted real-time simulation platform (OPAL RT), the grid model was developed using MATLAB/Simulink. As shown in Fig. 4.8, the reduced model consists of 16 MV buses. Some of them results from the aggregation of the downstream nodes of some grid laterals. This kind of simplification allows to reduce the computational burden of the real-time simulations, without heavily affecting the system behaviour.

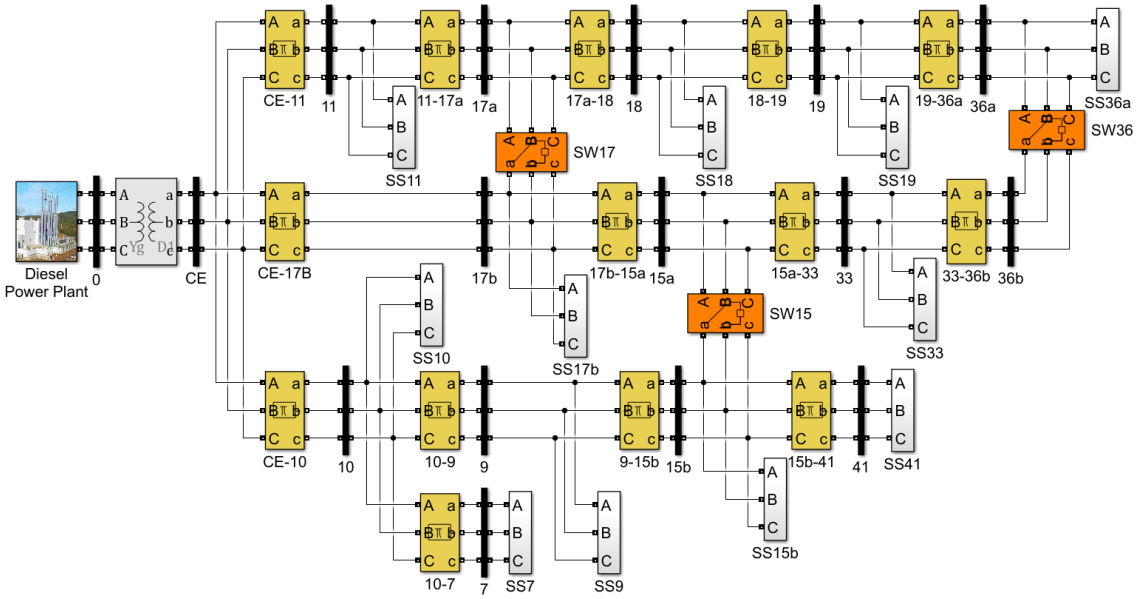


Figure 4.8: Grid model of Favignana

Specifically, model reduction was achieved through the following aggregations:

- the load on bus 15*b* collects the equivalent of nodes 12, 13, 15, 38, and 39;
- the load on bus 41 collects the equivalent of nodes 20, 21, 22, 23, 24, 25, 26, 27, 28, 29, 31, 32, 34, 40, 41, and 42;
- the load on bus 9 collects the equivalent of nodes 1, 2, 3, 4, 5, 6, 8, 9;

Each distribution line has been modelled using the Simulink three-phase PI model (*Three-Phase PI Section Line*). Positive-sequence characteristics have been set accordingly

to the actual data received by the distributor. Each bus in Fig. 4.8 is a subsystem containing a *Three-Phase V-I Measurement block* for the voltage and current measurements.

The equivalent loads and the PV plants have been modelled inside the substation (SS) subsystems, as is visible in Fig. 4.9.

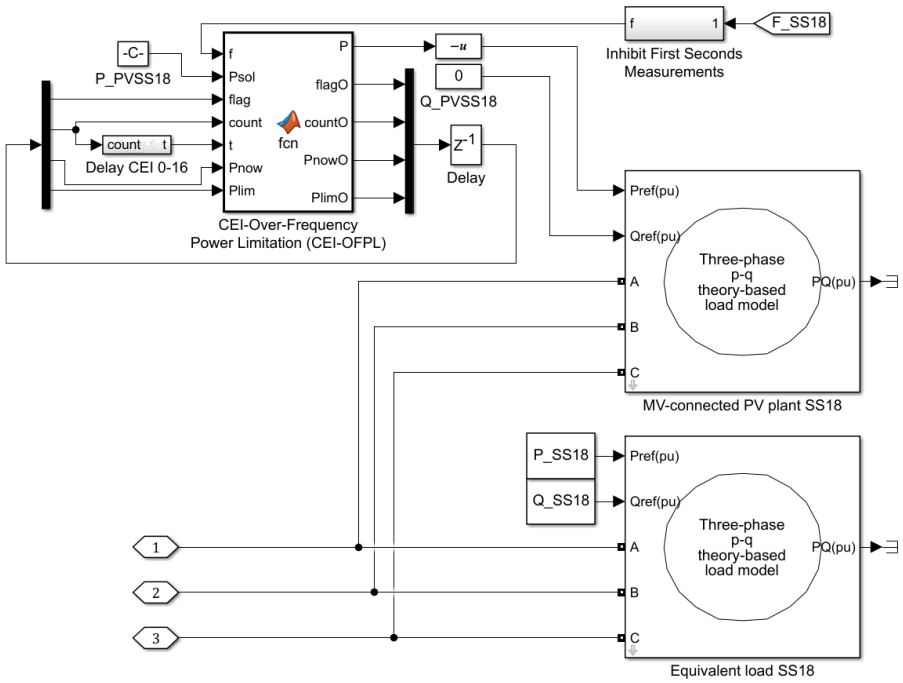


Figure 4.9: Modeling of equivalent load and PV system within a substation subsystem, example of SS18 substation subsystem

With the above simplifying assumptions, the Favignana island grid model, visible in Fig. 4.8, presents a total of 11 equivalent loads, which are directly connected to the MV level. As introduced in 4.2.1, to reduce the computational burden of the model and allow real-time simulations, the *three-phase p-q theory-based dynamic load* model discussed in [12, 16] were used. Since the model is designed to observe the system's response in terms of transient stability, it is not necessary to model the loads as dynamic objects that vary their power consumption over time. Therefore, the loading power can be considered constant during the transient evolution. Thus, the *three-phase p-q theory-based dynamic load* models used have been set as *constant-power loads*. The whole active and reactive consumption for each bus depends of the considered scenario and the entire load consumption of the island. The base case, against which all test scenarios were developed, is characterized by the active and reactive power consumption shown 4.2.

In addition to the equivalent loads, MV-connected PV power plants have been modeled. The PV power plant modeling has already been described in Section 3.2.1.4. Unlike the

Table 4.2: Active and reactive power set in the equivalent loads in the base case

	P [kW]	Q [kvar]
SS7	75,7	17,5
SS9	812,3	205,7
S10	75,4	20,9
S11	86,3	13,5
S15B	1.179,6	278,9
S17B	159,7	19,3
S18	377,9	54,6
S19	518,8	122,3
S33	458,5	111,2
S36A	268,9	96,4
S41	1.427,0	312,0
Total	**5440.2**	**1252.3**

dynamic network model studied in the Chapter 3, IPS was not modeled to lighten the model, as it was interested in observing very short and less burdensome transients than those observed in the Chapter 3.

The diesel generation plant has been modelled as in Section 3.2.1.1 and it is visible in Fig. 3.10. The diesel generation plant has been modelled as an equivalent synchronous generator, connected to the MV grid via a 0.4/10 kV equivalent step-up transformer. Controllers for excitation and governor functions are adapted to the overall equivalent rated power, which depends on the number of active diesel groups. Total inertia is set at 0.5 s, reflecting the system's response characteristics. Additionally, the sizing of the equivalent step-up transformer is directly related to the total rated power of the generating unit, ensuring an accurate representation of the plant's configuration within the simulation framework.

4.2.2 Experimental set-up for FFS validation by V2G electric vehicles

The BLORIN project involved experimental validation of the proposed FFS methodologies. Unfortunately, on the island of Favignana, there are not many EVs and there is not more than one bidirectional charging station. Similarly, only a few loads on the island of Lampedusa have been equipped with the developed Energy Management System (EMS) devices. Due to their low penetration in the islands covered by the project, the contribution to primary regulation provided by V2G and DR would not be assessable, so the assessment

of the contribution of these resources was evaluated through PHIL simulations conducted through the MG and the instrumentation available in the LabZERO laboratory [8], thanks to the collaboration between *Università degli Studi di Palermo* and *Politecnico di Bari*.

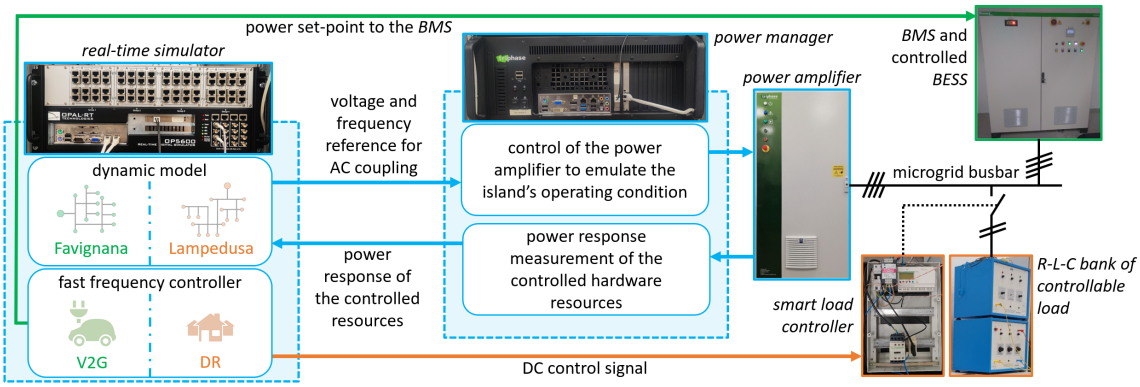


Figure 4.10: Experimental set-up for PHIL simulations: blue indicates the devices and connections used in all tests performed, green indicates the devices and connections used during validation of the V2G action, and orange indicates the devices and connections used during validation of the DR action.

The validation of the V2G and DR actions has been done by defining different scenarios and using different resources connected to the MG during the test. The PHIL set-up used for the experimental validation of the FFS actions concerning the project is shown in Fig. 4.10. In the scheme in Fig. 4.10, blue indicates the devices and connections used in all tests performed, green indicates the devices and connections used during validation of the V2G action, and orange indicates the devices and connections used during validation of the DR action.

It consists of an OPAL RT5600 real-time digital simulator in which dynamic grid models and FFS controllers are simulated in real-time. It is interfaced with a real MG through a power amplifier module managed by a dedicated power manager. The power amplifier is controlled in voltage source mode and leveraged to impose voltage and frequency of a specific point on the simulated grid to the power bus of the real MG. A three-phase $LiFePO_4$ BESS and a set of R-L-C controllable load banks were connected to the MG to carry out the tests. The former is controlled by sending an active power set-point through a wired data network with Modbus TCP/IP protocol and was used to emulate V2G EVs during test scenarios related to Favignana. The latter, on the other hand, is connected to the MG through a smart switch controlled by a 0–12 V DC control signal generated on one of the real-time simulator's analog outputs and was used to emulate the DR during the test scenarios related to Lampedusa.

4.2.3 FFS control scheme for V2G EVs

The FFS control scheme for V2G EVs implemented in this work is shown in Figure 4.11. This control scheme generates a variation (ΔP) on the active power set-point of the V2G EVs. The ΔP generated is characterized by the sum of two separate fast frequency control laws, namely a Fast Frequency Response (FFR) control, and a Synthetic Inertia (SI) control.

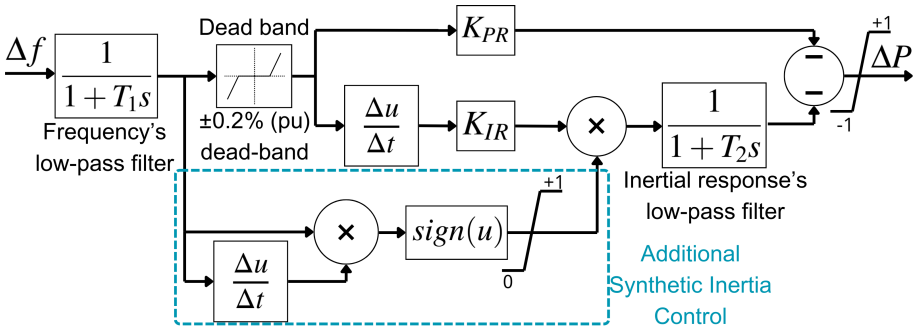


Figure 4.11: V2G Fast Frequency Support Control Scheme

The FFR controller is characterized by a control law proportional to the system frequency deviation, while the SI controller is characterized by a control law proportional to the frequency derivative (RoCoF). The whole control scheme was normalized with respect to the rated power of the controlled resource. A 5% droop was set to the FFR controller (K_{FFR}=20), while the virtual inertia set to the SI controller was 3 s (K_{SI}=6).

The model includes a first low-pass filter needed to filter frequency measurements, and by a second low-pass filter used to avoid sudden changes in the inertial control law. Both filters were chosen first-order with time constants (T_1 and T_2, respectively) set at 40 ms.

In addition to the filters, to avoid disturbance due to frequency measurement errors, a dead-band on the frequency deviation of $\pm 0.2\%$ ($\pm 100\,mHz$) was introduced. This dead band value takes into account the higher frequency volatility in isolated electrical systems with low rotational inertia. The output control signal ΔP, representing the set-point in p.u. to be sent to V2G EVs, was limited between ± 1 p.u..

To improve the effect of SI control, the additional SI control introduced in Section 4.1 was considered. With this additional control, the inertial contribution of the proposed controller is enabled only when the frequency deviation tends to increase, that is, when Δf and its RoCoF are concordant.

As can be seen in Figure 4.11, in fact, the output of the additional SI control goes to multiply the contribution of the SI control. When the sign of the product between the two quantities is positive (+1), the SI control is not altered, while when it is negative (-1), it is

limited inferiorly to 0 and cancels the entire branch of the SI control.

4.2.4 Test scenarios and results in Favignana island

This section describes the scenarios and shows the results of PHIL tests on Favignana island. Due to the capacity of V2G EVs to provide both upward and downward fast frequency support, a winter scenario (where an under-frequency event is experienced) and a summer scenario (where an over-frequency event is experienced). The scenarios used for testing were developed based on data provided by the University of Palermo.

The active power absorbed by each load was calculated by uniformly applying a percentage correction factor to the power value absorbed by the same load in the base case (Table 4.2). Reactive power, on the other hand, was calculated by considering the same power factor as in the base case. A load correction factor (*LCF*) defined by the ratio of the power absorbed by the entire island at that hour of the day to the total power absorbed in the base case was then calculated for each hour of the day. The active and reactive powers absorbed by each equivalent load on the island will then equal the active and reactive powers absorbed during the base case multiplied by the *LCF* coefficient.

Similarly, the active power generated by the island's PV plants was calculated by introducing a generation correction factor (*GCF*) for each hour of each case study. These coefficients were defined as the active power generated by the PV plants on the entire island at a specific time and the base active power chosen. In these tests, the base active power of the island's PV was set equal to 1000 kW. In order to develop a more varied scenario with respect to PV deployment, it was assumed that the total installed power is half due to small systems deployed at the low voltage level, and half due to a single large 500 kWp system directly connected at the MV level. The large 500 kWp plant was connected to a node in the Favignana industrial zone (bus #7).

Since the purpose of the project is to determine what the effects of high levels of distributed generation penetration are and what, if any, countermeasures can be taken to safeguard the security of the grid, it was decided to consider as the most critical time of day, the time of day characterized by the highest production from PV. In both cases (summer and winter) this condition occurs at 11:00 am. High PV production results in a decrease in the net load, and a consequent decrease in the number of synchronous machines and the available rotational inertia during a frequency transient. Below are tables in which the values of *LCF* (Table 4.3) and *GCF* (Table 4.4) used during the tests, derived in the manner just described, were highlighted.

Table 4.3: Load correction factors (*LCF*) for the two scenarios, summer and winter

Total load base case $[kW]$	Time $[h]$	Total load summer scenario $[kW]$	Total load winter scenario $[kW]$	*LCF* summer scenario	*LCF* winter scenario
5440.2	00:00:00	3248.90	825.11	0.5972	0.1517
	01:00:00	3002.71	770.03	0.5519	0.1415
	02:00:00	2802.24	790.11	0.5151	0.1452
	03:00:00	2683.74	817.58	0.4933	0.1503
	04:00:00	2668.49	830.93	0.4905	0.1527
	05:00:00	2708.31	946.79	0.4978	0.1740
	06:00:00	2816.59	1006.82	0.5177	0.1851
	07:00:00	3184.36	1019.07	0.5853	0.1873
	08:00:00	3546.64	1032.96	0.6519	0.1899
	09:00:00	3617.27	995.63	0.6649	0.1830
	10:00:00	3665.55	1017.83	0.6738	0.1871
	11:00:00	**3678.05**	**1090.53**	**0.6761**	**0.2005**
	12:00:00	3777.96	1091.08	0.6945	0.2006
	13:00:00	3817.51	1049.91	0.7017	0.1930
	14:00:00	3676.05	1055.73	0.6757	0.1941
	15:00:00	3609.28	1066.12	0.6634	0.1960
	16:00:00	3805.64	1134.76	0.6995	0.2086
	17:00:00	4248.03	1314.14	0.7809	0.2416
	18:00:00	4679.70	1447.34	0.8602	0.2660
	19:00:00	4974.97	1415.22	0.9145	0.2601
	20:00:00	4868.03	1350.21	0.8948	0.2482
	21:00:00	4470.18	1218.70	0.8217	0.2240
	22:00:00	4154.70	1049.28	0.7637	0.1929
	23:00:00	3838.56	935.26	0.7056	0.1719

In both scenarios, the V2G EVs were supposed at 50% of their SoC and with an exchanged power of 0 kW initially. That hypothesis has been done to better evaluate the effect of the V2G's contribution during frequency events and to keep the same system condition growing the number of connected vehicles. V2G charging stations were assumed to be of 11 kW, one of the most common sizes of charging stations. Furthermore, it was assumed, for simplicity of implementation and to lighten the computational burden of the simulations, that the EVs are all connected to the same equivalent node of the network and can be represented as a single aggregated resource. However, this simplifying assumption is justified by the consideration that most of the EVs on the island will be active in the central area of Favignana, near the port and the town. Moreover, given the small size of the island and its network, it is possible to imagine that the frequency dynamics will be the same at all nodes of the network. In these tests, EVs were assumed to be connected to

Table 4.4: Generation correction factors (*LCF*) for the two scenarios, summer and winter

PV generation base case [kW]	Time [h]	PV generation summer scenario [kW]	PV generation winter scenario [kW]	*LCF* summer scenario	*LCF* winter scenario
1.000.0	00:00:00	0.00	0.00	-	-
	01:00:00	0.00	0.00	-	-
	02:00:00	0.00	0.00	-	-
	03:00:00	0.00	0.00	-	-
	04:00:00	0.00	0.00	-	-
	05:00:00	413.33	0.00	0.4133	-
	06:00:00	199.33	0.00	0.1993	-
	07:00:00	410.33	382.00	0.4103	0.3820
	08:00:00	627.33	612.67	0.6273	0.6127
	09:00:00	807.00	555.33	0.8070	0.5553
	10:00:00	940.00	475.00	0.9400	0.4750
	11:00:00	**1003.00**	**677.00**	**1.0030**	**0.6770**
	12:00:00	975.33	438.67	0.9753	0.4387
	13:00:00	878.00	262.33	0.8780	0.2623
	14:00:00	718.00	350.33	0.7180	0.3503
	15:00:00	509.67	300.33	0.5097	0.3003
	16:00:00	278.67	415.33	0.2787	0.4153
	17:00:00	746.67	0.00	0.7467	-
	18:00:00	0.00	0.00	-	-
	19:00:00	0.00	0.00	-	-
	20:00:00	0.00	0.00	-	-
	21:00:00	0.00	0.00	-	-
	22:00:00	0.00	0.00	-	-
	23:00:00	0.00	0.00	-	-

bus #18.

4.2.5 Winter scenario in Favignana

Initially, at the instant t_0=0^-, the total consumption of the island was 1.091 MW. At that time, the total PV production was 677 kW while the power plant supplied the remaining 414 kW. At the instant t_0=0^+, a cloud cover caused a reduction in generation, from 100 to 10% in 1 s, of the PV system producing the most on the island (339 kW), involving a generation shortfall of 305 kW and, consequently, an under-frequency event.

In Fig. 4.12, the under-frequency transient with and without the action of FFS of V2G EVs can be observed. Due to the FFS contribution, a reduction in frequency excursion of 35.9% was obtained, with the nadir decreasing from 48.27 Hz to 48.89 Hz. A clear

improvement was also obtained regarding the average RoCoF after contingency. The average RoCoF, calculated as the frequency excursion between t_0=0^+ to reaching half of the maximum frequency excursion (0.46 s and 0.48 s, w/o and w/ FFS respectively), was reduced by 38%, from 1.87 Hz/s to 1.16 Hz/s. Also not to be underestimated is the effect that the FFS control made in reducing frequency oscillations during the transient and frequency overshoot, which was completely avoided.

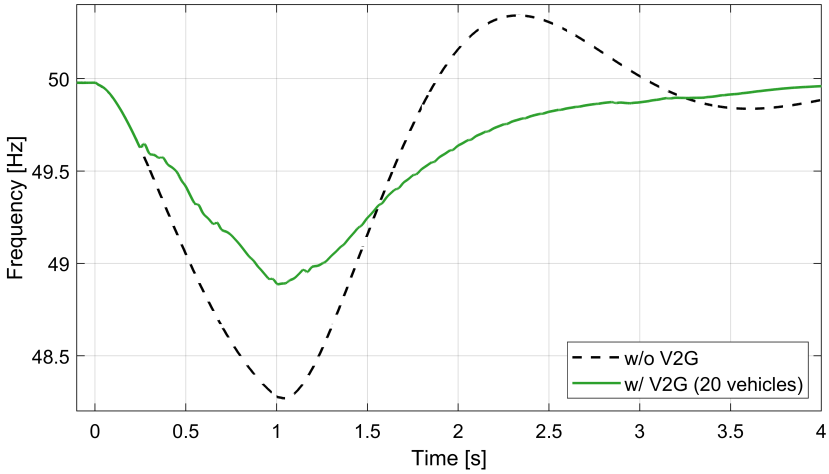


Figure 4.12: Winter scenario on Favignana - Frequency behaviour with and without the FFS contribution of 20 V2G EVs

The active power trends during the transient have also been shown in Fig. 4.13. The power trend of the island's generation plant was also shown both with and without the presence of the FFS contribution. This allows to observe how, under the same contingency conditions, a lower response speed of the diesel generators would be required, as well as lower fuel consumption and consequently lower CO_2 production.

The same scenario was also considered as the number of connected vehicles changed, with the aim of observing how the amount of enabled users affects the frequency transient. In Fig. 4.14, the frequency trend was depicted for an increasing number of enabled vehicles. It can be seen that the improvement was more pronounced as the number of vehicles participating in the adjustment increased. However, starting from 30 vehicles, the frequency trend became distorted due to measurement and component response delays. Despite the oscillations, the system remained stable, partly due to the additional SI control proposed in Section 4.1.

Furthermore, in Fig. 4.15, the frequency trend with and without the additional SI control has been shown for 35 connected vehicles. The additional SI control mitigates the effects of measurement and control delays, facilitating greater penetration of end users

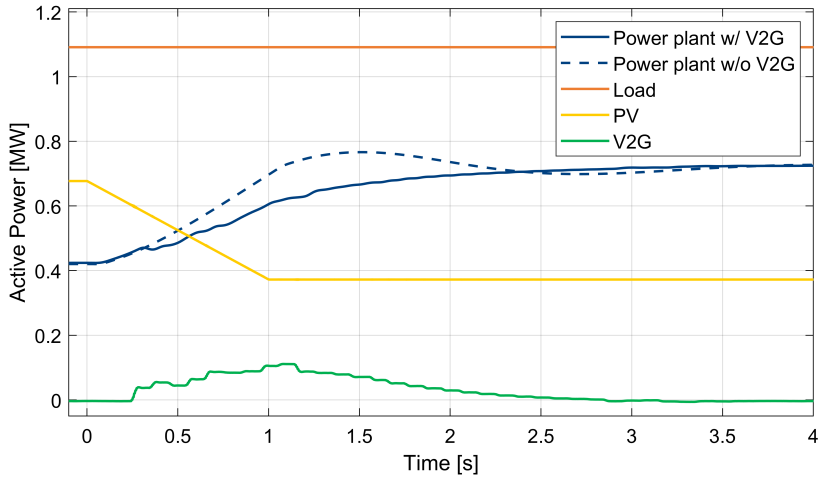


Figure 4.13: Winter scenario on Favignana - Active power behaviours with and without the effect of 20 V2G EVs

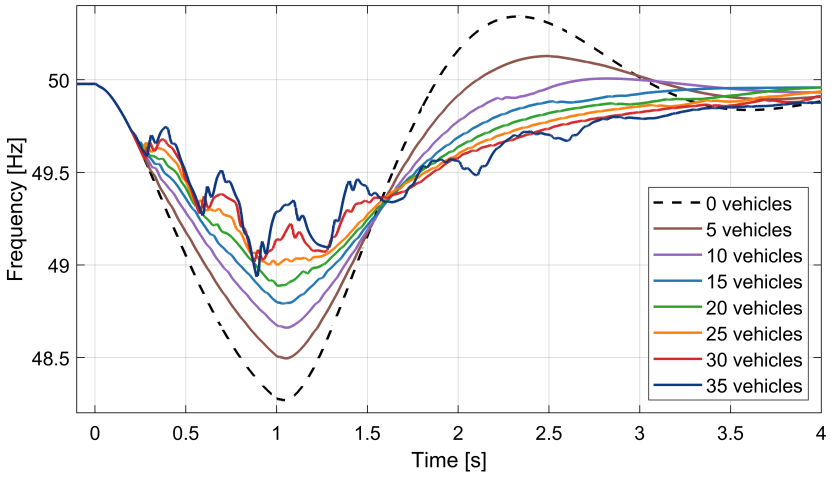


Figure 4.14: Winter scenario on Favignana - Frequency behaviour for different numbers of connected V2G EVs

participating in frequency regulation.

Fig. 4.16 depicted the control law produced by the controller and the power response of a V2G EV, emulated by the controlled BESS in PHIL. The stepped pattern in the response of the controlled component is due to the control architecture used to control the physical component, which assumes control law sampling at a frequency dictated by the speed of asynchronous communication via Modbus TCP/IP. Each step has a duration of about 100 ms, which is equal to the time required to read the set-point produced by the frequency controller and transfer it to the battery BMS. An offset between the control law and the active power output of the battery can also be observed. In fact, a zero control law corresponds to a slight power consumption due to the consumption of the auxiliary circuits

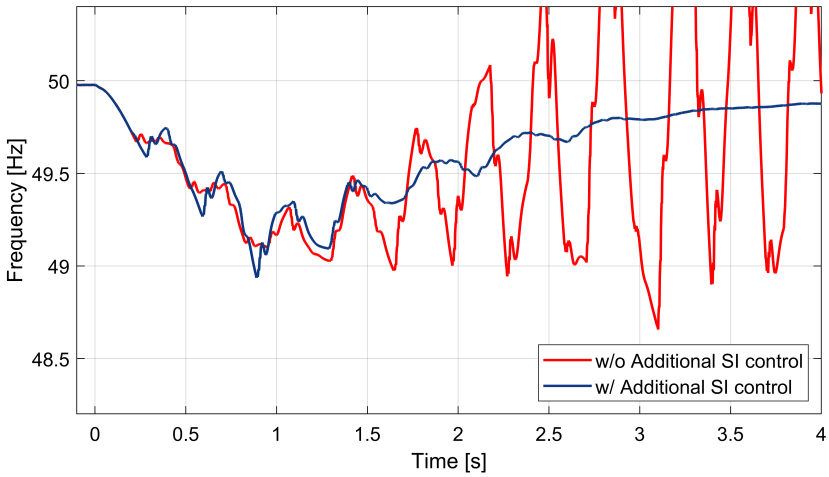


Figure 4.15: Winter scenario on Favignana - Frequency behaviour for 35 connected vehicles on the island, with and without the additional SI control

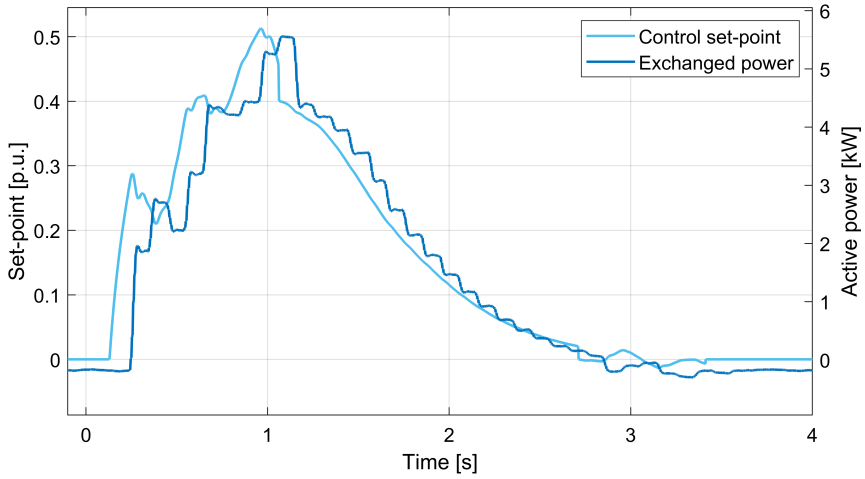


Figure 4.16: Winter scenario on Favignana - Control set-point and exchanged power of a V2G EV

that power the battery and its control system (BMS).

4.2.6 Summer scenario in Favignana

Initially, at the instant t_0=0^-, the total consumption of the island was 3.678 MW. At that time, the total PV production was 1.003 MW while the power plant supplied the remaining 2.587 MW. At the instant t_0=0^+, a protection triggers by going to disconnect part of the island load, generating a step load reduction of about 537 kW and, consequently, an over-frequency event.

In dynamic analyses of this nature, where the aim is to evaluate the impact of certain resources on frequency transients and their necessity, it is crucial to consider every con-

tribution or effect already present in the grid. In this specific scenario characterized by an over-frequency event, it is vital to take into account the effect of the "Active Power Limitation for Over-frequency Transients Originating in the Grid" control, as mandated by the CEI 0-16 national grid code, referred to in this document as CEI-Over-Frequency Power Limitation (CEI-OFPL). Such controls are bound by grid code provisions and will undoubtedly be present in the PV power plants in the Favignana island under study. However, the grid code CEI 0-16 is not very detailed, providing no guidance on how the frequency measurement should take place, how often the measurement should be updated, with what accuracy, etc., offering various possibilities for implementing such actions.

The grid code CEI 0-16 requires that every generation plant reduces its injected power into the grid when an over-frequency event occurs, starting the reduction upon reaching the frequency value of 50.3 Hz. This reduction must have a droop not exceeding 4%, and it must occur within a maximum time period of 10 s. The grid code CEI 0-16 also allows for intentional control delay settings ranging from 0 to 1 second, with a step of 50 ms. However, in low-inertia electrical systems, a 10 s of time period is not acceptable, as it is incompatible with the speed of frequency transients in such systems.

The presence or absence of this control and the speed at which it is implemented can significantly alter the frequency behavior during these transients. To evaluate the effect of V2G EVs' contribution in over-frequency phenomena, 3 different conditions of implementing the CEI-OFPL imposed by the CEI 0-16 grid code have been considered:

- without CEI-OFPL (similar to assuming a 10 s intervention).
- with ideal CEI-OFPL (without any measurement and control delays).
- with real CEI-OFPL (with condition that can be assumed "real", with frequency measurement update and control delay of about 100 ms).

The choice of assuming 100 ms of delay represents a good trade-off between the minimum time for frequency measurement acquisition (about 50 ms [15]) and the period of measurement acquisition at the Point of Interconnection (PoI) from the CCI (200 ms, discussed in Section 1.4). An update time of 100 ms, therefore, represents a rather optimistic measurement acquisition time for the industrial devices that are assumed to be installed together with the grid-following inverters of the island's end-user PVs. This action delay is also compatible with the delay of BESS controlled via Modbus TCP/IP in PHIL simulations. Thus, the two contributions can be considered to be affected by the same delays.

Making this optimistic choice means setting the conditions unfavorably for the evaluation of the effectiveness of the proposed controls and end-user regulation services under analysis. Thus, it is possible to ensure that the benefit from using V2G resources for frequency regulation derived from this study is the minimum that can be achieved. The benefit that will be obtained from the actual implementation of this technology on the Favignana network can only be greater than, or at most equal to, that resulting from this study.

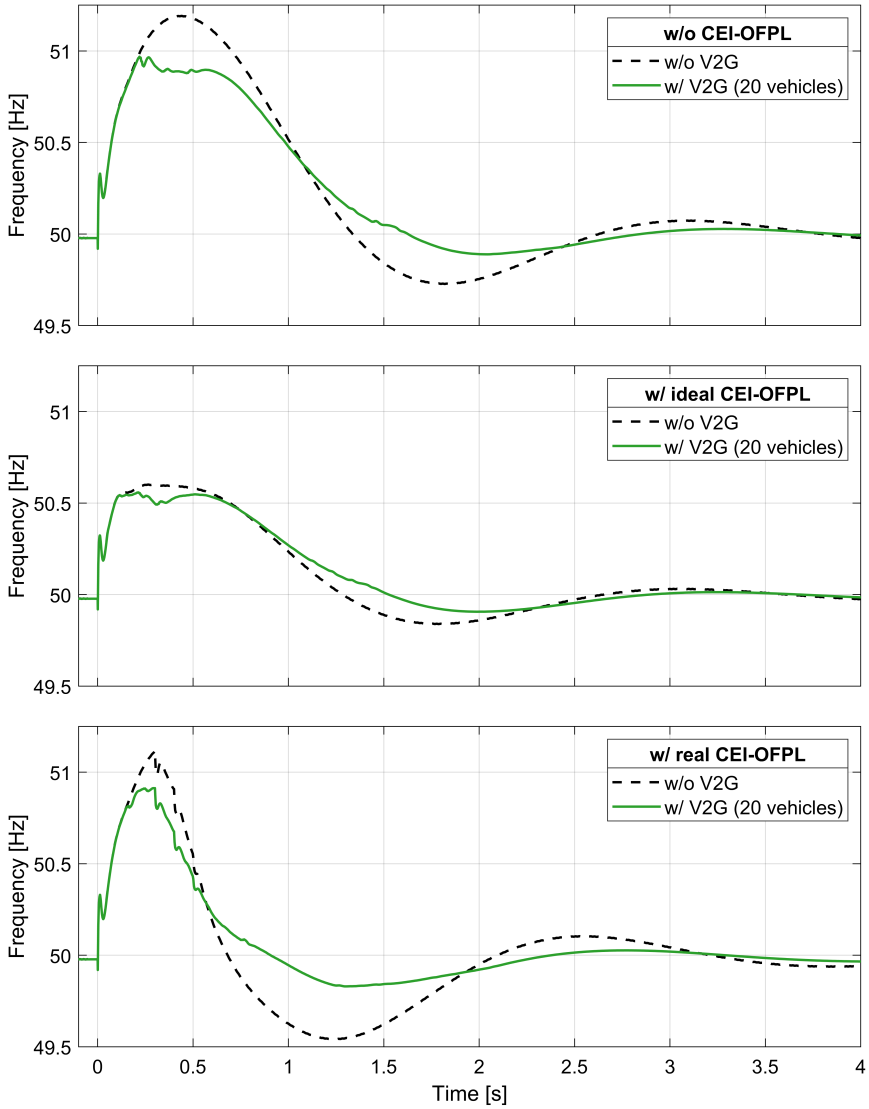


Figure 4.17: Summer scenario on Favignana - Frequency behaviour for 20 connected vehicles on the island w/o CEI-OFPL (upward), w/ ideal CEI-OFPL (middle) and real CEI-OFPL (downward) implemented to the island's PV power plants

In Fig. 4.17, the frequency behavior is illustrated for three different implementations of

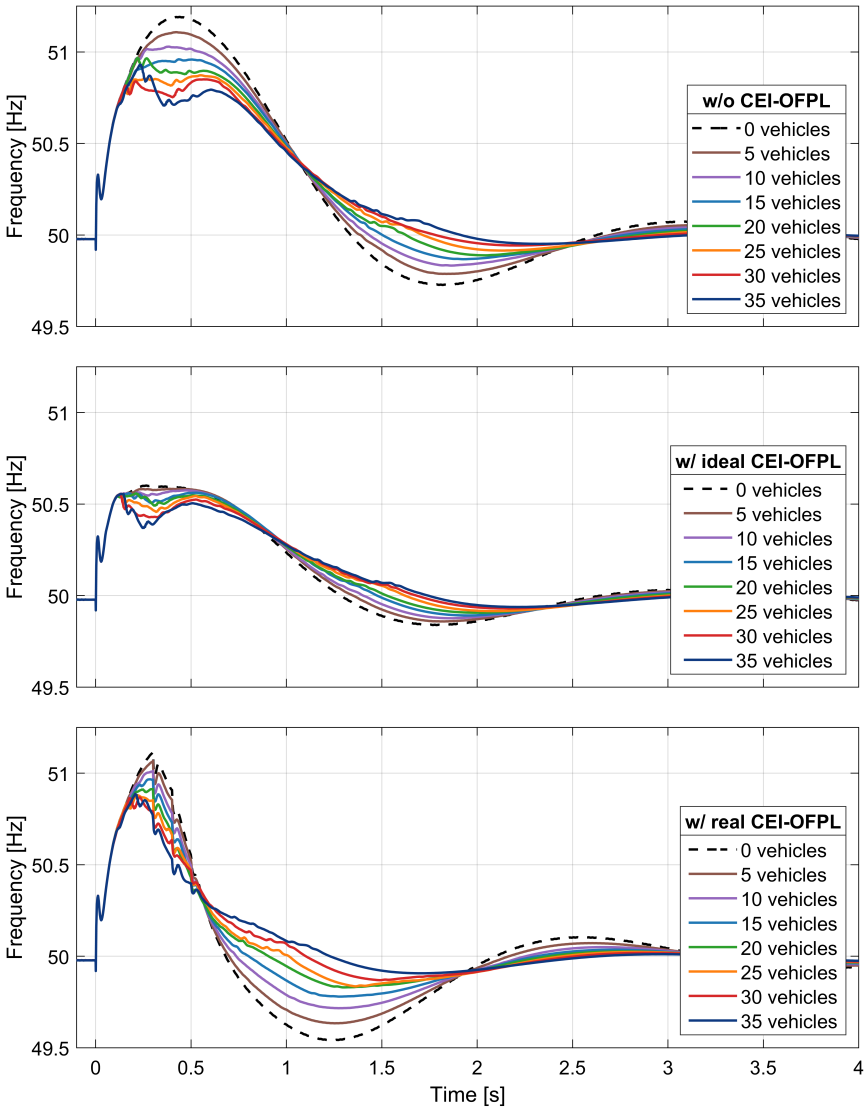


Figure 4.18: Summer scenario on Favignana - Frequency behaviour for different numbers of connected vehicles on the island w/o CEI-OFPL (upward), w/ ideal CEI-OFPL (middle) and real CEI-OFPL (downward) implemented to the island's PV power plants

the CEI-OFPL control, both with and without the effect of the FFS control, considering 20 V2G EVs. In all cases, the FFS contribution reduced the frequency excursion and undershoot during the transient, but had less impact on the average RoCoF, which remained almost identical in all three cases. This is because the RoCoF value was very high, approximately 7 Hz/s, and the nadir was reached very quickly. Due to delays, the vehicle contribution lowered the zenith but did not reduce the RoCoF.

The figure highlights how the effect of the vehicles is more prominent when the CEI-OFPL control is absent, decreasing from a zenith of 51.19 Hz to 50.97 Hz, resulting in a

reduction of the maximum frequency deviation by 18.7%. However, under the assumption of ideal CEI-OFPL control without delays, the contribution of V2G control becomes negligible, lowering the zenith from 50.60 Hz to 50.56 Hz and achieving a modest 7.1% reduction in the maximum frequency deviation. It might seem that the contribution of CEI-OFPL control is slightly better than the contribution of V2G FFS control because the frequency zenith with only CEI-OFPL control is lower than that obtained with only the vehicle contribution, as shown in Fig. 4.17, i.e., 50.60 Hz, w/ ideal CEI-OFPL w/o V2G, compared to 50.97 Hz, w/o CEI-OFPL w/ V2G (20 vehicles). However, unlike ideal CEI-OFPL control, V2G control is real, considering all measurement and control delays through the PHIL.

In the case of real CEI-OFPL, it is observed that the FFS control, despite identical measurement and control delays, is faster than CEI-OFPL limitation. This allows a significant reduction in the frequency zenith, decreasing from 51.12 Hz to 50.91 Hz, with an 18.3% reduction in the maximum frequency deviation during the transient.

The contribution of V2G was also crucial from the point of view of frequency undershoot reduction: without CEI-OFPL the undershoot moved from 49.73 Hz to 49.89 Hz, with a reduction of the maximum under-frequency deviation of 59%, while with the ideal CEI-OFPL the undershoot moved from 49.84 Hz to 49.91 Hz, with a reduction of the maximum under-frequency deviation of 42%. The effect of the FFS control on the undershoot was even more significant in the case of real CEI-OFPL control: the delay of 100 ms considered in the real CEI-OFPL control caused a more pronounced undershoot than in the case without CEI-OFPL (moving from 49.73 Hz w/o CEI-OFPL to 49.54 Hz w/ real CEI-OFPL, maximum under-frequency deviation increased of 74.1%), since the delayed reduction of the power fed into the grid by the island's PV power plants is added to the control of the generating plant. In this case, the V2G EVs' contribution reduced the maximum under-frequency deviation of 63%, moving from a minimum frequency reached during the transient of 49.54 Hz to 49.83 Hz. As in the previous scenario, different numbers of V2G EVs have been considered and, in Fig. 4.18, the frequency trends have been shown.

Fig. 4.19 shows the frequency trends with and without the proposed additional SI control, which had shown a significant improvement in system stability and overshoot reduction in the winter case. In this context, the difference between the two controls is not as obvious, since the reduction in undershoot is mainly attributable to the decrease in zenith (the same for both controls), which defines the amount of power cut-off generated

by PVs as a result of the CEI-OFPL control. Although lower than the winter case, the additional SI control still brings an improvement to the transient, reducing the undershoot. Without the additional SI control, the minimum frequency reached during the transient was 49.79 Hz against 49.83 Hz in the case of additional SI control present. Thus, the additional SI control reduced the maximum under-frequency excursion by about 19%.

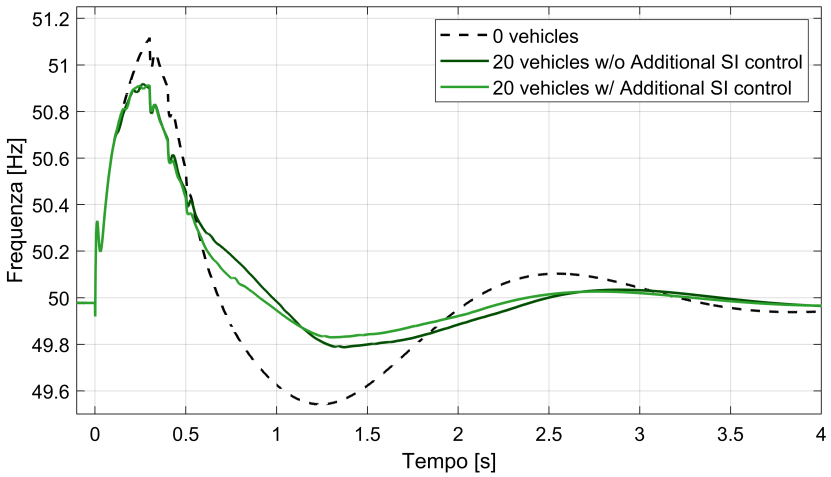


Figure 4.19: Summer scenario on Favignana - Frequency behaviour for 20 connected vehicles on the island, with real CEI-OFPL implemented to the island's PV power plants

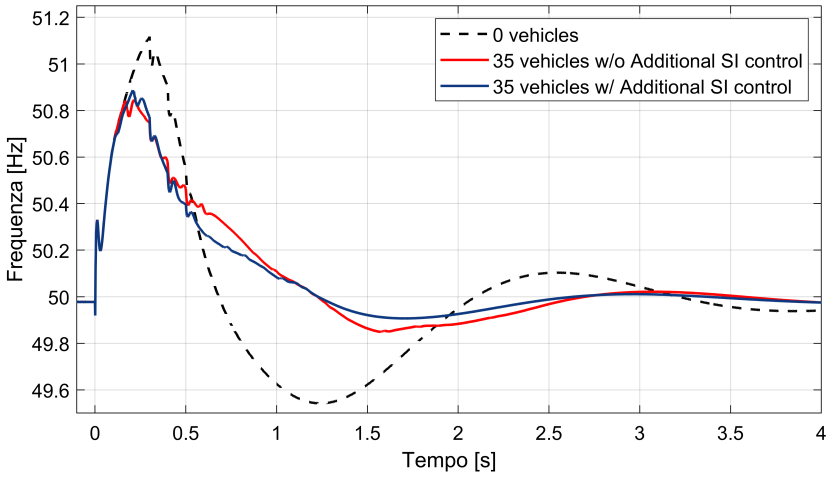


Figure 4.20: Summer scenario on Favignana - Frequency behaviour for 35 connected vehicles on the island, with and without the additional SI control, with real CEI-OFPL implemented to the island's PV power plants

Unlike the winter case, the penetration of 35 vehicles does not cause system instability in summer (Fig. 4.20). This is due to the high load on the island during the summer season, mainly due to tourism, with more diesel generators turned on contributing to system

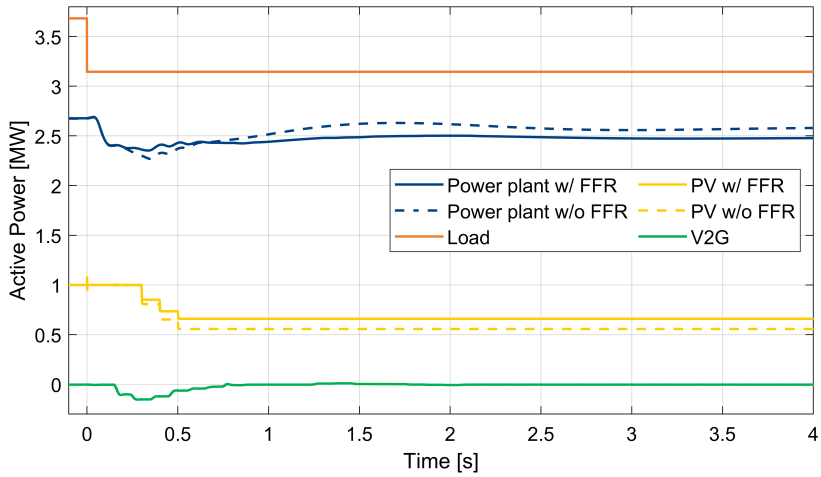


Figure 4.21: Summer scenario on Favignana - Active power behaviours for 20 connected vehicles on the island, with real CEI-OFPL implemented to the island's PV power plants

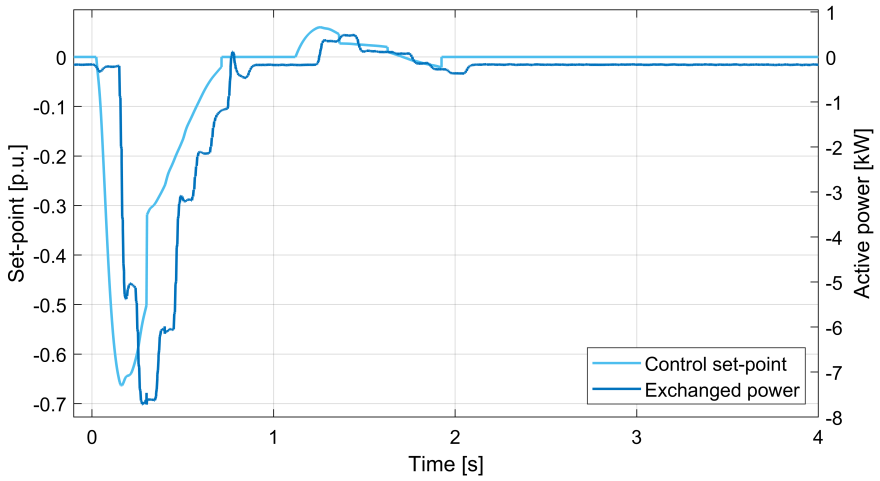


Figure 4.22: Summer scenario on Favignana - Control set-point and exchanged power of a V2G EV

inertia. Moreover, the power exchanged by V2G EVs during the transient (with a peak of 157 kW) compared to the total load consumption (3.141 MW after the step reduction) in this scenario is relatively low (5%) compared to the winter scenario (10.5%, with a peak power exchanged by V2G EVs of 115 kW against 1.091 MW of total load).

In the case of real CEI-OFPL, active power trends of the resources during the transient with 20 connected V2G EVs have been shown in Fig. 4.21. In the figure, the active powers fed into the grid of the diesel power plant and the total PV of the island in the case of 0 connected V2G EVs are also shown. Due to the reduction in frequency zenith during the transient thanks to the effect of V2G EVs, the decrease in PV generation due to CEI-OFPL control was less. This results in reduced fuel consumption and GHG emissions from the diesel power plant, as well as requiring less operating reserve during the grid operation.

The island's PV power generation increased from 556 kW of the case with 0 vehicles to 659 kW of the case with 20 vehicles, thereby reducing the power limitation by about 23%. Because the grid code CEI 0-16 requires that the reduction must be maintained for a time of at least 300 s, 8.3 kWh of cut-off renewable energy was saved in this specific transient.

The control set-point sent and power exchanged by a V2G EV, emulated through the BESS in PHIL, have been reported in Fig. 4.22. Again, the offset due to the consumption of auxiliary services and the delay of about 100 ms due to the measurement and communication of the set-point via Modbus TCP/IP can be observed.

4.3 Fast Frequency Support through LED Street Lighting in Low-Inertia Non-Synchronous Power Systems

In the literature, several authors published works in which they demonstrated how it was possible to provide frequency regulation services through a wide variety of resources. Various approaches have been proposed for secondary frequency control in residential and commercial buildings, utilizing heating, ventilation, and air-conditioning systems [140–142]. Additionally, studies have explored the potential of industrial loads, such as bitumen tanks with adjustable heating power based on grid frequency variations [143]. Several papers have investigated the use of domestic thermal loads like refrigerators/boilers [144–146] and variable-speed heat pumps [147] for providing SI or FFR.

Dimmable lighting systems have emerged as competitive resources for Ancillary Services (AS) in a DR framework, particularly in the context of smart grids [148–150]. Light-Emitting Diode (LED) lamp technologies, in particular, are promising due to their rapid regulation capabilities using remote or local control signals. Numerous studies and projects have showcased the controllability of networked LED street lighting in smart grid frameworks [151], enabling Demand Side Management (DSM) services or optimizing energy use in conjunction with urban energy infrastructures. For instance, initiatives like TeleWatt [152] and EMERA [153] aimed to integrate Electric Vehicle (EV) charging stations with public street lighting systems.

In [154], the authors demonstrated the capability of LED lamps to provide Synthetic Inertia (SI) without the need for significant BESS or Supercapacitor (SC) installation. This was achieved simply by connecting a DC link capacitor to the LED lamps. The utilization of LED lighting systems to support BESS [155] and conventional generators [156] during

primary frequency regulation has also been demonstrated.

A decentralized control strategy for LED lighting systems, designed to offer both primary and secondary frequency regulation, is detailed in [157]. In this approach, each lamp autonomously contributes to frequency response by adjusting power consumption in response to grid frequency excursions. An advanced local control, capable of considering the magnitude and duration of frequency deviations, is presented in [158]. However, it's important to note that implementing a decentralized control requires the installation of local controllers.

This solution is not always feasible and not easy to implement since it needs to aggregate a relevant number of lighting loads to provide a significant amount of flexibility. Nevertheless, this challenge could be addressed by considering clusters of loads controlled through a centralized approach. This is particularly relevant in smart city infrastructures, where resources like public lighting lamps can be aggregated through centralized control to offer grid services [152, 153].

This section assesses the feasibility of providing frequency regulation services, such as SI and FFR, through centralized control of a public street lighting system. The assessment involves testing the response of a real LED lamp and its driver in a Power Hardware-in-the-Loop simulation environment.

Experimental tests were first carried out by assuming a large number of lamps connected to a simple model (single-bus grid model) of a low-inertia power system, then by assuming the installation of these systems on a more accurate model: a typical structure of a small Italian island, the reference island that was described in Section 1.5.1 and was subject of the Chapters 2 and 3.

4.3.1 Flexible Control Resources through LED Street Lamps

With LED technologies getting less and less expensive by the day, LED lamps are progressively substituting all others in both new installations and refurbishment projects. Their competitive performances in terms of efficiency, life expectancy, reliability, controllability and Electromagnetic Compatibility (EMC) impacts make them one of the lead technologies in public street lighting systems.

Anyway, as is pointed out by [159], dimmable lighting systems can be used for DR as long as illuminance variations are adequately controlled and, then, still acceptable by final users. According to the standard [160], if a "Full Adaptive Installation" is employed, the *lighting class* of street lamps can be reduced during low traffic conditions. *Lighting classes*,

as defined by the Part 2 of the European standard EN 13201:2015 [161], determine the road lighting conditions to be ensured to guarantee the safety of road users. Illuminance control actions are allowed, as long as they comply with minimum standard requirements.

Various techniques can be used to easily control and dim LED lamps. For example, the *0-10 V_{DC} protocol* is widely adopted for analog dimming. According to this protocol, the lamp scales its light output so that at a control voltage of 10 V its light intensity corresponds to 100% of its rated value, while below 1 V its light intensity is at its minimum value. However, this control technique is not prone to be extended to control several lamps distributed in a large geographical area, due to the voltage drop on the communication network.

Several protocols, already commercially available, permit to control a larger number of LED drivers. For example, *DALI* controllers allow to manage up to 64 LED lamps, at a maximum distance of about 300 meters. However, time specification of this kind of controllers might not be adequate for applications requiring a very fast device response. The *DMX-512* technology allows instead to control up to 512 networked devices, at a maximum distance of about 300-500 meters, theoretically extendable using repeaters. Since the transmission time for a maximum sized packet with 512 channels is about 20 ms, this protocol is fast enough to be employed for fast modulation of the light output of LED lamps. Clearly, the use of *DMX-512* implies the installation of a wired communication system among all lamps.

The applicability of wireless controllers has been also proved in [151], where each LED lamp in a networked lighting system has been provided due to a receiver that can collect data packages sent via radio transmission at a frequency of about 900 MHz. *GPS* applications for the control of lighting systems are also patented. Large geographical areas are therefore theoretically reachable by the same control system, although the easiest solution could be implementing local frequency measure and control at each lighting control box that usually manages few dozens of street lamps. An example of low-cost SI local controllers has been studied by the authors in [14].

The implementation of these solutions could be prohibitive in practical applications if the infrastructure is implemented only for frequency support, due to the high investment costs associated with the communication infrastructure, especially if implemented over large geographical areas. However, it could be applied to pre-existing infrastructures (without significant additional costs) and to smart grids in which the remote control of DERs if already implemented (e.g. for energy optimal control) and could be extended to

SI and FFR.

In this section, the real-time control of LED street lamps is proposed to harvest flexible resources for fast frequency regulation. Since the most severe part of a frequency transient is usually extinguished within a few seconds from its onset, the time activation of LED lamps control is a crucial aspect in the feasibility of the proposed control. The need of a very fast response introduces for sure some drawbacks in the proposed control scheme, although it also brings some advantages. Given the very short duration of frequency transients, the visual impacts due to this kind of control can be considered comparable to the fluctuations that can be observed during commonly experienced disturbances of power quality such as deep voltage sags or transient voltage interruptions. Due to the very strict requirements in time response, the proposed LED lamp control will be tested in a real-time environment through a Power Hardware-in-the-Loop (PHIL) test bed. Finally, this section presents the experimental results obtained by regulating the power output of an actual LED street lamp according to different frequency-dependant control laws.

4.3.2 Characterization of the LED lamp power regulation response

The first tests were aimed at drawing the control characteristic curve of the LED street lamp. The lamp used for these tests is a commercially available product, which is controlled by a LED driver through a direct current (DC) regulating signal in the range 0–10 V. The higher the voltage, the higher luminous flux is produced by the lamp, and the higher is the electric power absorbed. The control characteristic was obtained through the experimental results collected from the test setup shown in Fig. 4.23. The LED lamp was fed by an AC power source supply, whereas a DC power supply was used to regulate the DC voltage input to the LED driver. The absorbed current was measured using a current probe coupled with a x100 coil to amplify the current signal.

The results obtained by controlling the LED driver with a voltage ranging in the interval 0–10 V have been collected in Table 4.5. These same results are also shown graphically in Fig. 4.24 where the LED lamp power consumption is represented as a function of the DC voltage control input. It can be observed that voltage inputs below 1 V and above 8 V do not produce any significant variation in terms of both absorbed power and luminous flux. Therefore, 1–8 V is the regulating interval that will be used to control the lamp during future tests. In this interval the characteristic curve appears to have almost a linear behavior. In these tests, the lamp was supplied with the nominal voltage 230 V. However, other tests, not shown here for the sake of brevity and carried out by changing the voltage magnitude

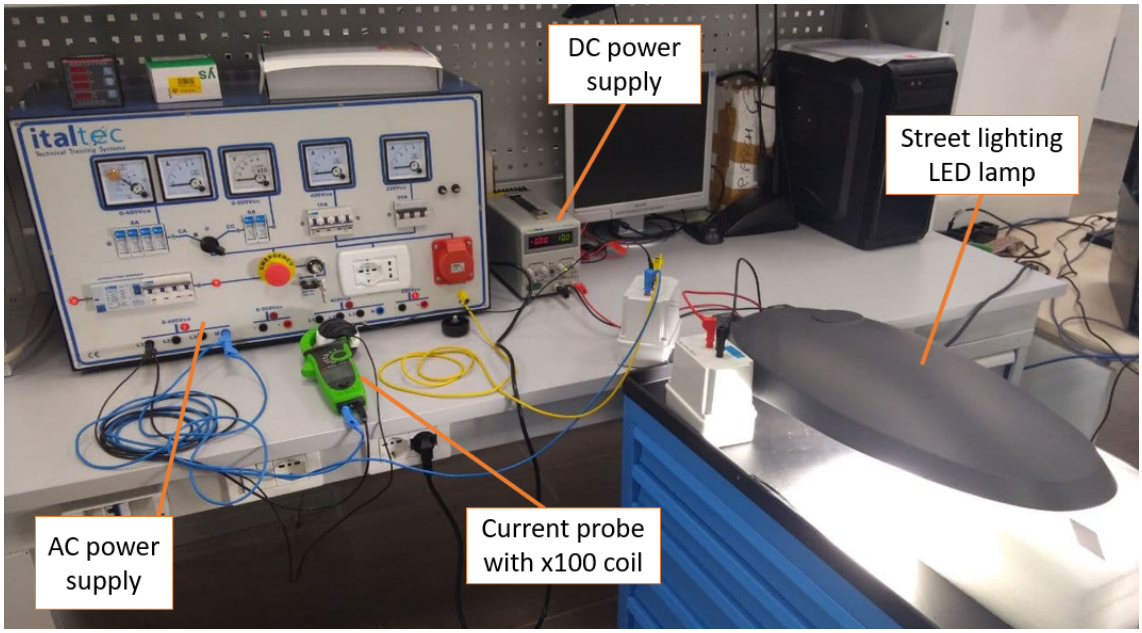


Figure 4.23: Set-up for the LED street lamp characterization tests

of the power supply, showed that the lamp power consumption is scarcely influenced by the voltage within a large confidence interval (200–250 V).

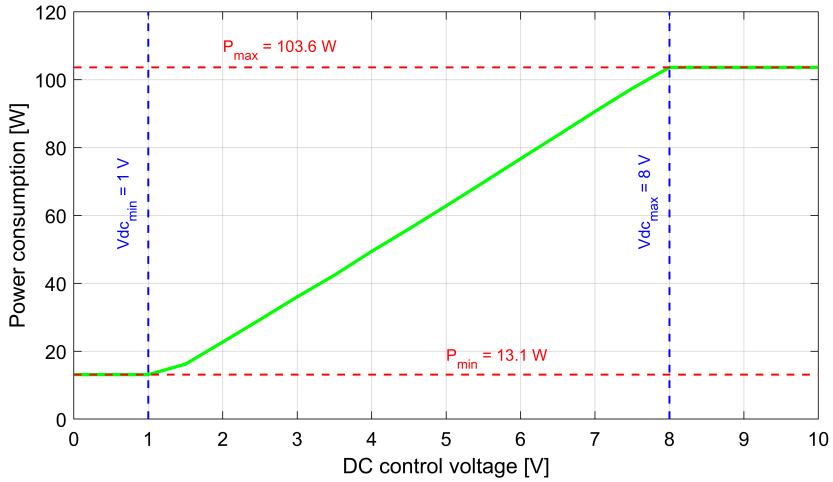


Figure 4.24: Power-Voltage characteristic curve of the LED Street Lamp

According to the experimental results, the lamp under test can be regulated to absorb an electric power ranging from a maximum of 103.6 W to a minimum of 13.1 W. This means that the lamp can be dimmed in order to reduce its consumption by about 90%, when the lamp is operating at full power. Lamps which operate at half capacity, for example in certain periods of the night when the reduced traffic conditions permit to downgrade the lighting class, could instead theoretically provide instantaneous power control for both

upward and downward regulation.

Table 4.5: Test results of LED Street Lamp Characterization

Voltage [V]	**Current [A]**	**Power [W]**
0.0	0.06	13.1
0.5	0.06	13.1
1.0	0.06	13.1
1.5	0.07	16.2
2.0	0.10	22.7
2.5	0.13	29.3
3.0	0.16	36.0
3.5	0.19	42.4
4.0	0.22	49.4
4.5	0.25	56.0
5.0	0.28	62.8
5.5	0.31	69.7
6.0	0.34	76.7
6.5	0.37	83.6
7.0	0.40	90.6
7.5	0.43	97.4
8.0	0.46	103.6
8.5	0.46	103.6
9.0	0.46	103.6
9.5	0.46	103.6
10.0	0.46	103.6

Further tests were carried out in order to characterize the LED lamp time response to a DC control voltage step change, and verify if this control is fast enough to be applied for fast frequency regulation. Fig. 4.25 shows the results obtained by controlling the lamp from one of the extremes of the characteristics curve (Fig. 4.24) to the other, during both upward and downward regulation. In both subplots, the blue curve represents the step-change variation given to the DC control voltage. Each graph contains also multiple active power responses, which almost overlap, obtained repeating the same test multiple times.

The component is clearly characterized by an asymmetrical response, with a faster step-change response observed during upward load regulation. Further tests, not shown here for the sake of brevity, conducted by selecting different step change sizes and initial operating point, showed a more or less constant delay in the 400–500 ms range during upward load regulation, and a delay ranging in the interval 500–1400 ms for downward regulation. The maximum delay was observed when the lamp has to go from maximum to minimum power. This is clearly a critical issue in FFS applications, since the delay

inevitably reduces the effectiveness of the proposed control. However, this behaviour permits to limit the sudden change in illuminance, minimizing the visual disturbances to humans and possible hazards to road safety.

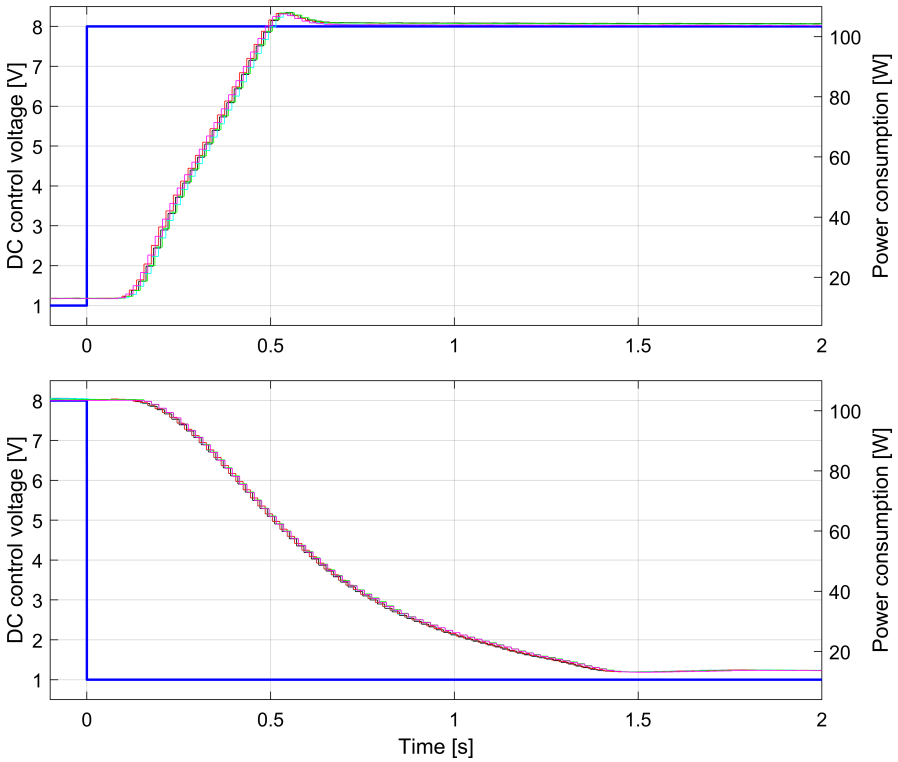


Figure 4.25: Response of Upward and Downward Load Regulation

4.3.3 Synthetic Inertia and Fast Frequency Response Models

To study the support that LED street lamps can provide to improve the frequency behavior of the network, two frequency-dependent control laws have been proposed and compared, namely Synthetic Inertia (SI) and Fast Frequency Response (FFR). These two approaches have never been applied or tested on LED urban lighting systems. An approach somewhat close to what we have proposed was found in [154]. The authors in [154] evaluated the possibility to provide virtual inertia through the energy stored in the capacity of the DC-link that supplies the LED lamp. Due to the limited capability of the DC-link of the lamp driver, this technique can provide a very limited power respect to the SI control proposed in our work that can control up to 90% of the LED lamps rated power (see Subsection 4.3.2). On the other hand, for FFR control, a possible comparison can be done in relation to other primary frequency controls with LED lamps proposed in the literature. The FFR

control law in this work is comparable to the controls in [155] and [158]. In these works, however, the actual response and characteristics of LED lamps and their drivers were not considered. In our work, instead, thanks to the PHIL implementation, the behaviour of an actual (commercially available) LED street lamp, with its driver and control system, was thoroughly taken into account. A different control law is proposed in [157] to provide primary frequency support by LED lighting systems. However, this control introduces a fixed delay to reduce the frequency control activation in addition to a dead-band on the frequency deviation. The introduction of this delay does not permit to obtain a prompt response of the devices for very severe contingencies.

A scheme of the SI/FFR controller used for tests is given in Fig. 4.26 where, through a control switch, it is possible to choose the control law to be adopted. The output of the controller is the amount of load to be curtailed. The curtailed load set-point is converted into a DC control voltage set-point using the look-up table obtained during the characterization tests in Section 4.3.2 (see Fig. 4.23). The DC control voltage obtained in this way is applied to the LED driver to regulate the luminous flux, and therefore the power supplied to the lamps. A detail of the SI and FFR functions blocks in Fig. 4.26 is given in the next subsections. Please note that, for the sake of simplicity, in these tests, it was assumed to allow SI/FFR control of the street lamps only during under-frequency events, when lamps are working at their maximum power and their power output can only be regulated downward. However, it is possible to imagine that a symmetrical control of loading power could be implemented on the lamps that are working at half capacity during reduced road traffic conditions.

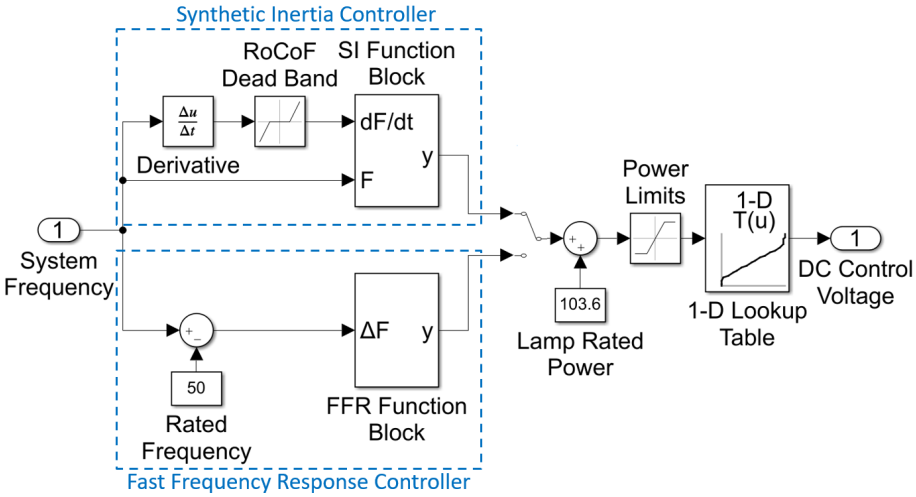


Figure 4.26: Synthetic inertia and FFR control scheme

The SI control adopted in this study is based on the proposed SI control law described in Section 4.1. The SI control law used in this study has been implemented within the *SI Function Block* visible in Fig. 4.26. Assuming F as the frequency sample at the time t and K_{SI} as the applied gain factor, the SI control law implemented in the *SI Function Block* consists of the following *if statement*:

$$\begin{cases} if \quad F \leq F_{rated} \ \ \& \ \ dF/dt < 0.1 \\ \quad y = K_{SI} \cdot dF/dt \\ else \\ \quad y = 0 \end{cases}$$

According to this rule, a non-zero output y of the SI controller is obtained only when the frequency is below its rated value F_{rated} (50 Hz). The gain factor K_{SI} was sized so that the maximum power variation is obtained when a 0.5 Hz/s Rate of Change of Frequency (RoCoF) is reached.

As shown in Fig. 4.26, a Rate of Change of Frequency (RoCoF) dead band has also been introduced in order to avoid unnecessary regulations, due for example to measurement noise. For the single-bus grid model experimental test (Section 4.3.6), where an ideal network model devoid of noise and frequency oscillations was utilized, the dead-band on Rate of Change of Frequency (RoCoF) has been set to ± 10 mHz/s. In the experimental tests on the non-synchronous island model (Section 4.3.9), where frequency dynamics are more prone to oscillations and noise, the Rate of Change of Frequency (RoCoF) dead-band has been set to ± 100 mHz/s. Indeed, Rate of Change of Frequency (RoCoF) calculation can be affected by large errors due to noise on frequency measurement. To further reduce the effect of noise, a low-pass filter can be applied to the frequency measurement. According to the step-change responses shown in Fig. 4.25, the dynamic behaviour of the controlled LED lamp is characterised by a large delay and is therefore inherently less susceptible to noise, making the use of a filter unnecessary. As the FFR controller in the previous application (see Section 4.2.3), the FFR control law in this work aims to provide an active power contribution proportional to the frequency deviation. Even in this case, as for the SI control law, the FFR control law has been implemented in a function block, visible in Fig. 4.26 Assuming ΔF as the measured frequency deviation from the steady-state value, and introducing a 0.1 Hz dead-band to avoid excessive stress to the lamp, the control output y of the *FFR Function Block* in Fig. 4.26 is formulated as follows:

$$\begin{cases} if \quad \Delta F \leq -0.1 \\ \quad y = K_{FFR} \cdot (\Delta F + 0.1) \\ else \\ \quad y = 0 \end{cases}$$

The gain factor K_{FFR} has been set in order to obtain the maximum power contribution with frequency deviations greater than 0.5 Hz.

It may seem that the gains from these controls were chosen exaggeratedly high, but it should not be forgotten that the controlled lamps have very low energy consumption. Even assuming a large amount of lamps capable of regulation, remaining in realistic penetration scenarios, the total controllable power of these systems would remain very limited. The choice to adopt such high gains does not pose problems from the point of view of system stability. Moreover, this choice stems from a desire to make maximum use of these resources to support the frequency.

4.3.4 Power Hardware-in-the-Loop experimental set-up

The PHIL set-up used to investigate the effectiveness of the proposed SI and FFR controls is shown in Fig. 4.27. It consists of a real-time digital simulator (OPAL RT5600), a power amplifier module, managed by an amplifier controller, and a real LED street lamp, whose physical response is applied in PHIL to the simulated power system. The real-time simulator, which was interfaced with the amplifier controller by means of an optical fiber channel, simulated both the grid model (single-bus grid model or small non-synchronous island grid model) and the LED lamp controller. The DC-control voltage signal (0–10 V) sent to the LED driver to control the lamp luminous flux, was generated by the real-time simulator as an analog output, using the *hardware synchronized mode*.

The LED lamp was connected to the LabZERO Microgrid (MG) at the Politecnico di Bari, which was supplied by the programmable power source operating in voltage source control mode. According to this set-up, frequency and voltage signals of the simulated non-synchronous system were communicated to the amplifier controller and, then, physically applied to the MG busbar. The response of the MG (and the LED lamp) to the frequency and voltage variations is measured by the programmable power source and transformed into a PQ signal to be fed back to the real-time simulation.

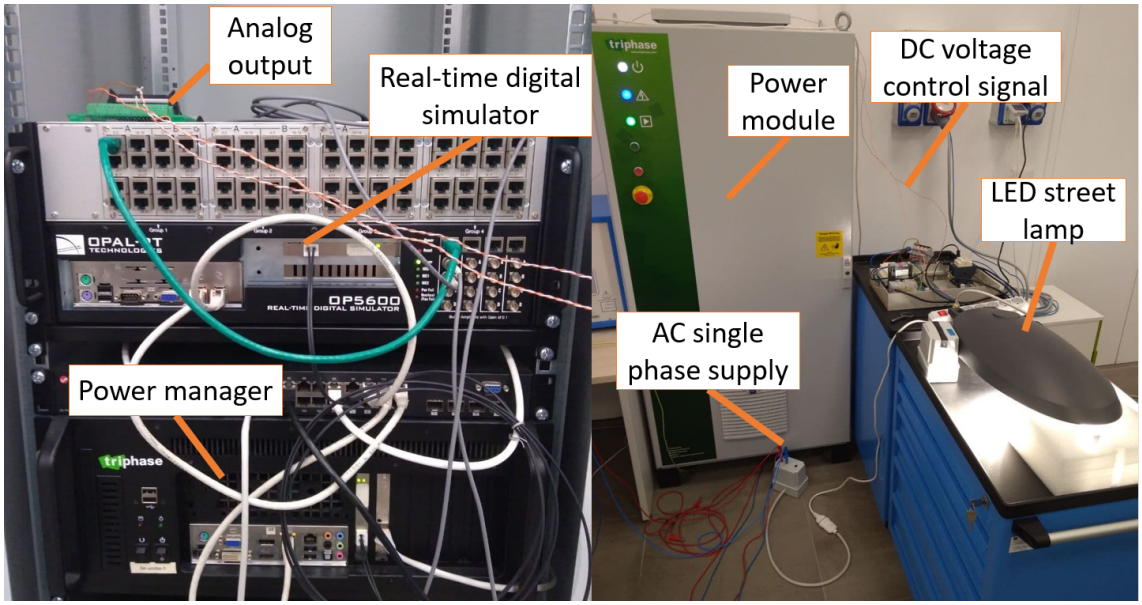


Figure 4.27: Set-up of the Power Hardware-in-the-Loop simulation tests

4.3.5 Single-bus grid model Power Hardware-in-the-Loop experimental tests

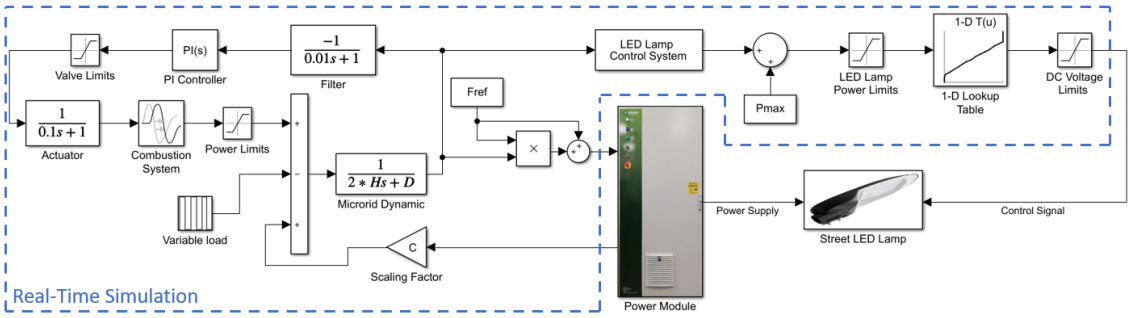


Figure 4.28: Power Hardware-in-the-Loop test bed architecture

In PHIL tests conducted on a single-bus grid model, it has been assumed to provide flexibility and frequency regulation support through the street lighting system of an islanded distribution grid. Within this ideal grid scenario, only the active power exchanged by the real LED lamp was fed back in the PHIL simulations, while the voltage was kept constant and equal to 230 V, which represents the typical voltage of low-voltage distribution networks in Italy. The architecture of the PHIL test bed is schematically depicted in Fig. 4.28. A dynamic frequency response of a typical MG has been simulated into the real-time digital simulator (see Fig. 4.27). In the simulated islanded distribution grid, a diesel generator provides both primary and secondary frequency regulation services. This

generator has been modelled assuming the parameter values suggested in [162], introducing also saturation limits to the opening of the fuel injection valves and to the power output. The PI controller was tuned using a generic PID tuner tool, aiming at obtained a transient response well balanced between aggressive and robust behavior. The proportional and integral constants were set to 2.5 and 1.8, respectively. A delay time of 0.1 s has been set for the combustion process response. In the simulated system, the total inertia (H) was set to 1 s and the damping factor (D) to 0.05 p.u.

As shown in Fig. 4.28, the power consumption of the LED lamp is measured through the power amplifier current signals, and employed to emulate, by means of a scaling factor, the response of an entire street lighting system. This scaling factor was set to 3%, based on the ratio between the Italian annual consumption for street lighting and the overall electric load. In the following tests, it was assumed that LED street lamps can be only controlled to reduce their power output following a low frequency event, caused by a sudden load increase. As in Fig. 4.28, the SI/FFR control law, function of the frequency deviation, is used to generate an active power set-point to be applied to the lighting system. The set-point is converted into a DC voltage set-point through the look-up table obtained during the characterization tests of Section 4.3.2 (see Fig. 4.24), which is sent to the lamp LED driver through the analog outputs of the real-time simulator (see Fig. 4.27).

4.3.6 Test Results on Single-bus grid model

In order to test the proposed control, a load variation of 0.1 p.u. was applied to the grid at time $t = 0$. Fig. 4.29 illustrates the control signal sent to the LED driver and the power response of the controlled device. The frequency nadir was reached in about 1 s, and in correspondence of a 70% reduction of the LED power consumption. As expected, after frequency nadir was reached, the power contribution of the controlled lamp returned to 0 since Rate of Change of Frequency (RoCoF) and frequency deviation assumed different signs.

Fig. 4.30 describes the frequency behaviour with and without SI contribution, whereas Fig. 4.31 describes the active power response of both diesel generator and LED lamp systems. Recorded PHIL trajectories were used as inputs and outputs time series to a transfer function estimator based on Gauss-Newton least square search, showing that inertia had been averagely increased from 1 s to 1.07 s.

Fig. 4.32 depicts the LED lamp power response and the applied control signal to its driver in the presence of the FFR contribution. By comparing the trends in Fig. 4.31 and

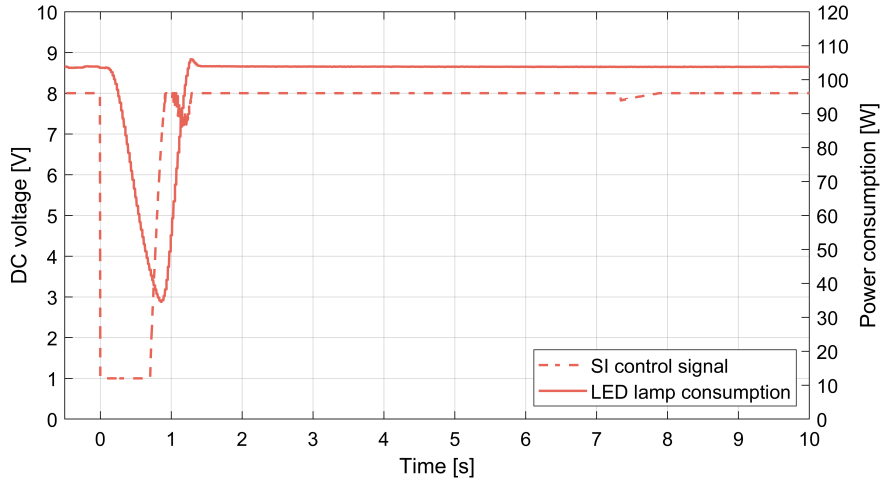


Figure 4.29: LED lamp response with SI control

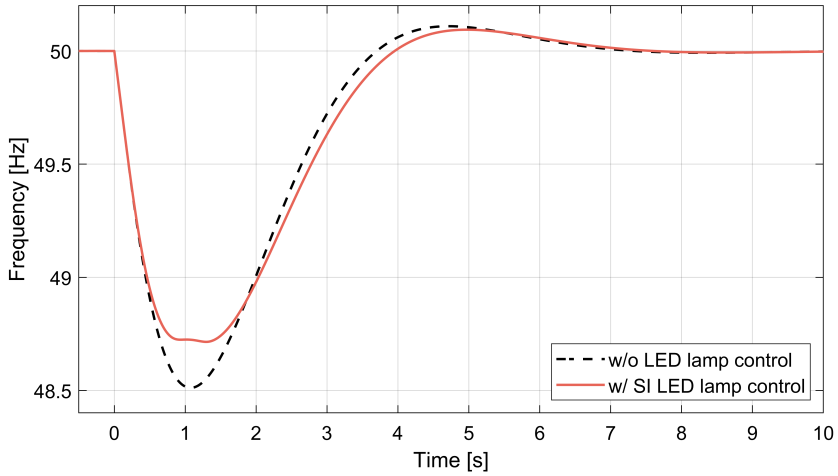


Figure 4.30: Frequency behaviour with and without SI contribution

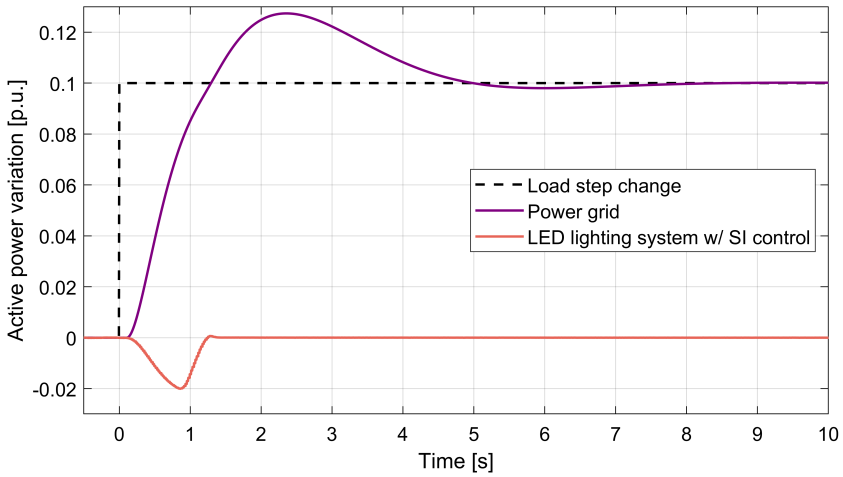


Figure 4.31: Power behaviours with SI contribution

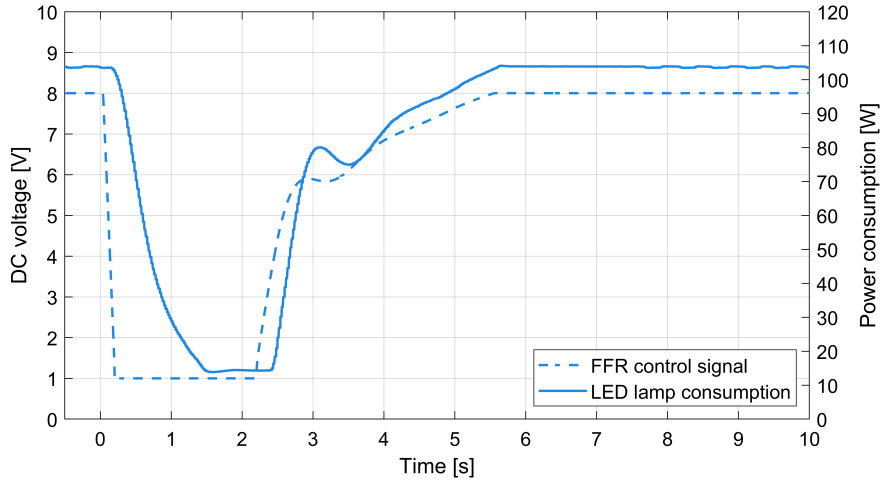


Figure 4.32: LED lamp contribution with FFR control

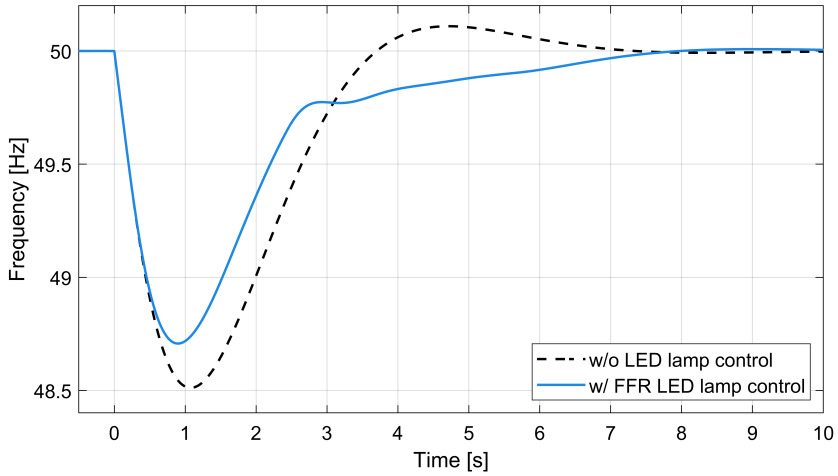


Figure 4.33: Frequency behaviour with and without FFR contribution

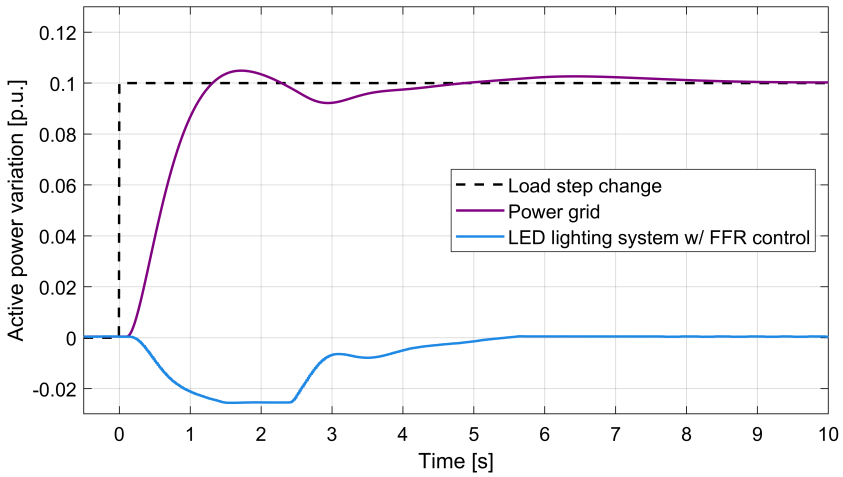


Figure 4.34: Power behaviours with FFR contribution

Fig. 4.34, it becomes evident that the response time with FFR control was longer than that with SI control. It was because, in general, when an imbalance occurs, the Rate of Change of Frequency (RoCoF) reaches its maximum value instantaneously. In addition, the frequency deviation increases at a slower rate than Rate of Change of Frequency (RoCoF) and, therefore, takes longer to exceed the minimum frequency deviation specified by the dead-band (0.1 Hz) and to activate. On the contrary, the FFR control provided frequency support for an extended duration compared to the SI control, persisting even after reaching the nadir point until the frequency stabilized. Consequently, as illustrated in Fig.4.33 and Fig.4.34, the response with FFR control was characterized by a more rapid increase in frequency immediately after the nadir and an extended settling time.

4.3.7 Small Non-Synchronous Island Model Power Hardware-in-the-Loop Experimental Tests

The possibility of providing fast frequency support through LED streetlights was studied preliminary in Section 4.3.6, demonstrating how improvements in frequency behavior can be achieved. The tests were performed by adopting a very simplified electromechanical model of a single-bus network, while in this section a more accurate evaluation is provided through the development of a detailed electrical system model for real-time simulations and PHIL testing. The model proposed for this test is based on the actual MV and LV distribution network supplying the reference small Italian island, introduced in Section 1.5.1 and studied in the Chapters 2 and 3.

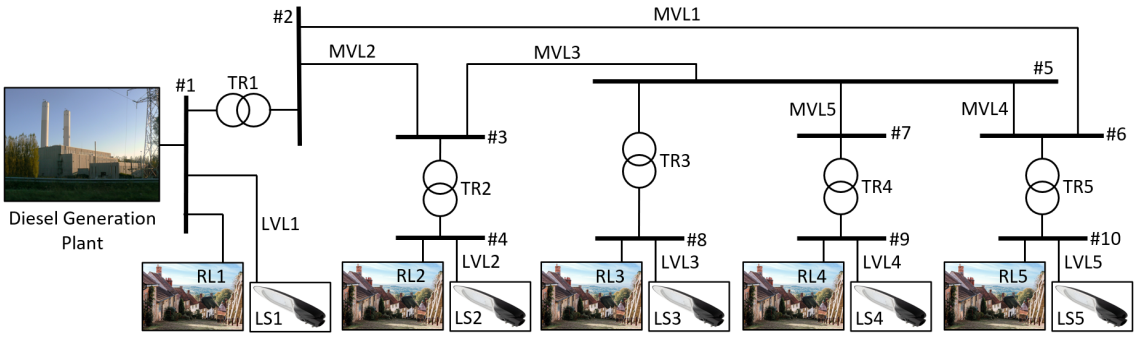


Figure 4.35: Modelled small islanded distribution grid

The modeled distribution grid is structured as in Fig. 4.35. The network has already been extensively described in Section 1.5.1 but in this section a brief description of the network is given for clarity.

It mainly consists of five 10 kV MV buses, each one connected through a transformer to a LV bus. Five distribution lines connect the MV nodes, creating a loop that is normally open during operation. Each LV bus supplies electricity to (mostly) residential customers, which have been represented through the equivalent loads RL1-RL5. The installed load capacity P_n at each node is reported in Table 1.2. One of the LV node (bus #1 in Fig. 4.35) supplies the largest number of customers (RL1) and is connected to a generation plant with a 2.4 MVA rated power and 50 Hz frequency. The plant is based on a set of diesel generating units and supplies electricity to the local load and to the rest of the island via an elevator transformer (TR1). It should be noted that the detailed model of the generating unit has been represented considering all voltage and mechanical power regulators, a detailed model of the synchronous machine and prime mover dynamics.

Since the proposed control is based on the real-time management of the public LED street lighting system, each LV node was also connected to an additional equivalent circuit, which represents a portion of the street lighting system used to light the entire island. More details are given in the subsection below.

The real-time model of the reference grid is is similar to that described in Section 3.2.1. Differently from that model, this model does not include the PV plant and the BESS, as they are not useful for the study. Moreover, as the residential loads (RL1-RL5) do not normally participate in frequency control, they were modeled using a constant PQ model. A dynamic load model was used instead to represent the power consumption at the street lighting system nodes. All system components were modeled using the libraries available in the real-time simulator programming environment. Each component was modeled according to the parameters listed in Table 1.2. These values have been obtained from the data sheets of the components actually installed on the island. Loading levels were set to reproduce conditions of low consumption, usually experienced during the night and far from the tourist season, when the island is more populated. Due to the scarce loading level, the number of active generators is low and the rotational inertia is much reduced. Low inertia conditions can also be due to high Renewable Energy Sources (RES) production and consequent decrease of the number of active synchronous machines.

4.3.8 Model of the LED Street Lighting System

The street lighting system has been modelled according to some assumptions. The installed power of the simulated street lighting system was estimated using aggregated data at national level. According to the statistics in [163], in 2017, the electricity consumption of

public lighting in Italy was about 6000 GWh. Assuming that the public lighting lamps are usually switched on less than half a day (about 4000 hours per year) and that they work almost all times at their rated power, it appeared reasonable to consider that the installed power of the lighting systems in Italy in that year was about 1.5 GW. This value is about 3% of the national load peak (55 GW in 2017, as reported in [164] by the Italian TSO). Applying the same percentage to the simulated system, whose peak power demand is about 1.8 MW, it is possible to assume that the installed power of the public street lighting system in the island is about 54 kW.

Having estimated the overall load for street lighting and the total number of lamps, it was assumed to distribute such load on five subsystems, connected at the LV system nodes. The number of lamps for each subsystem is proportional to the installed load capacity at LV level. As represented in Fig. 4.35, each lighting subsystem is modelled using an equivalent three-phase load (LS1-LS5), supplied by an equivalent low-voltage distribution line (LVL1-LVL5). Table 4.6 shows equivalent power and number of installed lamps for each street lighting subsystem (LS1-LS5).

Table 4.6: Power and number of lamps at each LV node

	LS1	**LS2**	**LS3**	**LS4**	**LS5**
P_{LS} [kW]	24.20	7.76	9.32	4.04	8.69
$N.of\,lamps$	234	75	90	39	84

The equivalent lines LVL1-LVL5 were modelled assuming typical lengths in urban applications and according to the actual data of the urban lighting system in [153]. Cross-section of cables were sized to avoid excessive voltage drops at the terminal of each lighting circuit. The adopted values are summarized in Table 4.7. Please, consider that due to the large number of lamps assigned to LS1, this street lighting system was divided into three parallel sub-circuits, each one supplying one third of the total LS1.

4.3.9 Test Results on Small Non-Synchronous Island Model

The equipment used during the tests was described in Section 4.3.4, while the PHIL set-up used is slightly different from that used for testing with the single-bus network and is shown in Fig. 4.36. In this case, both the frequency and voltage of busbar #1 of the modeled small Italian island network are imposed on the LabZERO MG.

Table 4.7: Characteristics of the equivalent distribution line of the lighting subsystems

	LVL1	**LVL2**	**LVL3**	**LVL4**	**LVL5**
Length [km]	0.81	0.78	0.93	0.42	0.87
N. of circuits	3	1	1	1	1
Cross-sections [mm^2]	4x25	4x25	4x35	4x6	4x25
r_l [Ω/km]	0.99	0.99	0.71	4.21	0.99
x_l [Ω/km]	0.093	0.093	0.089	0.114	0.093

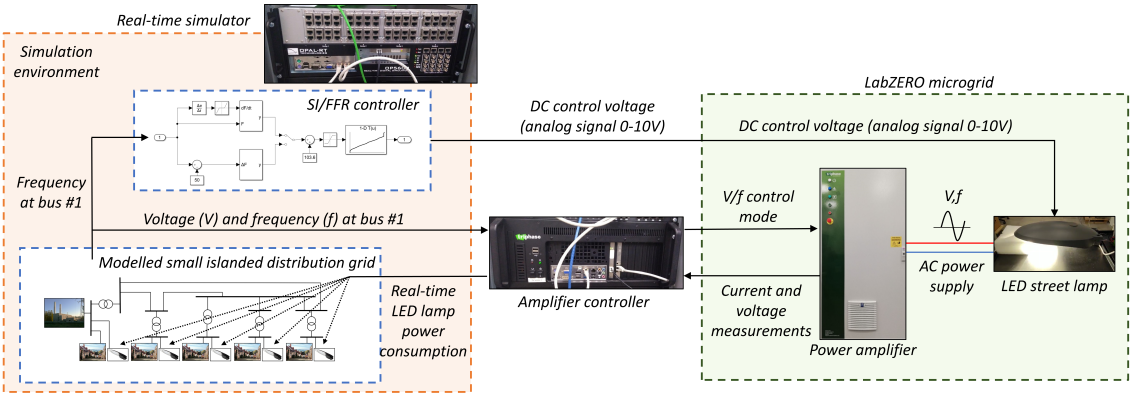


Figure 4.36: Set-up of the Power Hardware-in-the-Loop simulation tests

The active and reactive powers exchanged by the LED lamp, measured through the power amplifier, were suitably scaled to reproduce the response of the five street lighting subsystems connected at different LV nodes. Thanks to the characterization tests, it was proved how LED lamps behavior was not influenced by voltage magnitude in a very large interval. Therefore, the expected response of all simulated lamps can be considered similar to the physical LED lamp as long as the frequency is the same on the entire grid. This condition can be considered true since the system is very small in size and is supplied only by a single power plant.

4.3.9.1 Case 1. SI Control of LED lamps

The proposed SI control was tested applying a sudden load step variation of 180 kW to the simulated grid, in a day characterized by an average power consumption of about 1.25 MW. Given the very low rotational inertia of the diesel power plant (assumed to be 0.3 s with respect to the maximum installed power 2000 kVA), the frequency transient following this disturbance, applied at the generic time $t = 0$ s as in Fig. 4.37, shows a very steep descent with an initial Rate of Change of Frequency (RoCoF) higher than 8 Hz/s, and a

nadir of about 48.3 Hz, much lower than the 49 Hz minimum suggested by the standard EN-50160 for the quality of frequency in systems with no synchronous connection.

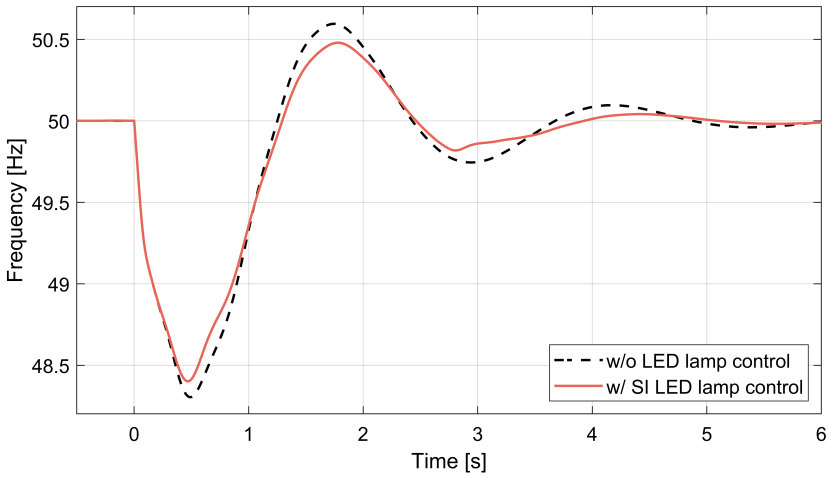


Figure 4.37: Case 1. Frequency response with SI control

Fig. 4.38 shows how the proposed SI controller can generate a DC control signal adjusting the active power consumption of the LED lamps during the frequency transient. The effect of this action control is visible in Fig. 4.37 with a non negligible contribution to the nadir, which is now raised to about 48.4 Hz, a reduction of the frequency overshoot and an overall quicker settling time.

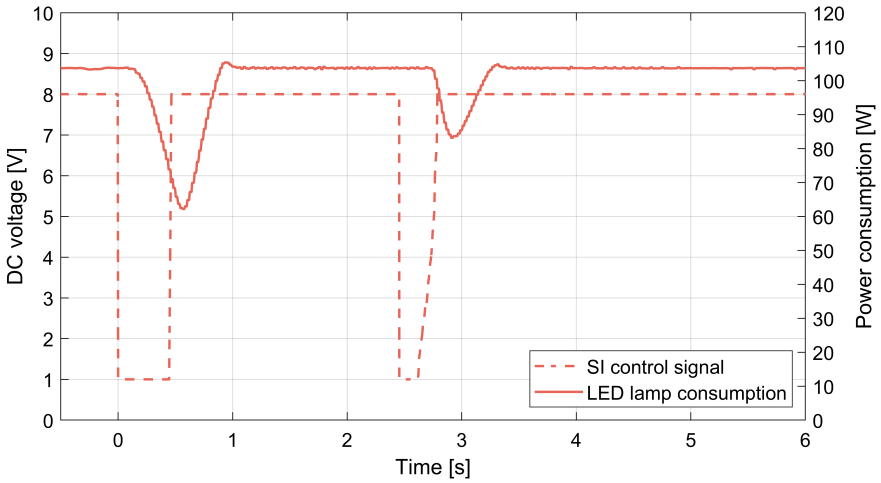


Figure 4.38: Case 1. LED lamp response with SI control

As shown in Fig. 4.38, due to the high Rate of Change of Frequency (RoCoF), a maximum power reduction was instantly asked to the LED lamps. Within a few hundred milliseconds, the LED lamps began to reduce their consumption. The SI controlling signal was stopped after having reached the nadir, and the lamps went back to their regular

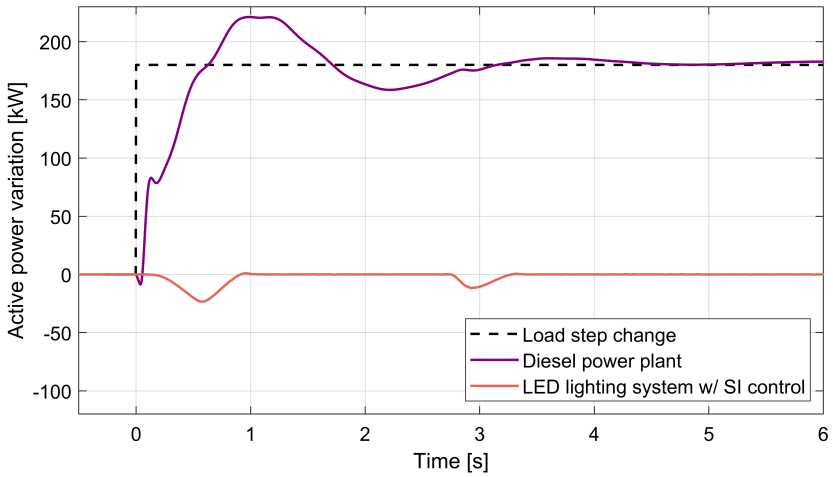


Figure 4.39: Case 1. Active power response with SI control

operating point within a second from the start of the disturbance. Due to the severity of the transient, a second activation of SI was also requested during a second oscillation.

Fig. 4.39 shows how the power response provided by the diesel generation plant derives from a detailed model of the generating units. Its response is clearly much more significant than the LED lamps, whose consumption is in this case only just about 4% of the overall load. Furthermore, due to the high speed of the system response, the contribution of the lamps to the dynamics can be exploited for a short time only. However, it should be observed that these tests were carried out under particularly stressed conditions. In fact, the model of the non-synchronous system was characterized by an extremely low amount of inertia. The frequency support could have been more significant in a system with more inertia and, then, a delayed nadir time. Nevertheless, from another point of view, the limitation in the active power control of the LED lamps guarantees that the visual impact during the transient is very limited.

4.3.9.2 Case 2. FFR control of LED lamps

This second case is equivalent to the previous one, but this time the presence of a FFR control of the LED lamps was assumed. Fig. 4.40 shows the system frequency response with and without the FFR support. The response is quite similar to the previous case, although a better control of the frequency overshoot and settling time is obtained. Fig. 4.41 shows the LED lamp power response and the control signal applied to its driver.

By comparing the two trends in Fig. 4.38 and Fig. 4.41, it is possible to observe that the FFR control strategy is slightly delayed, but allows a longer activation of the LED

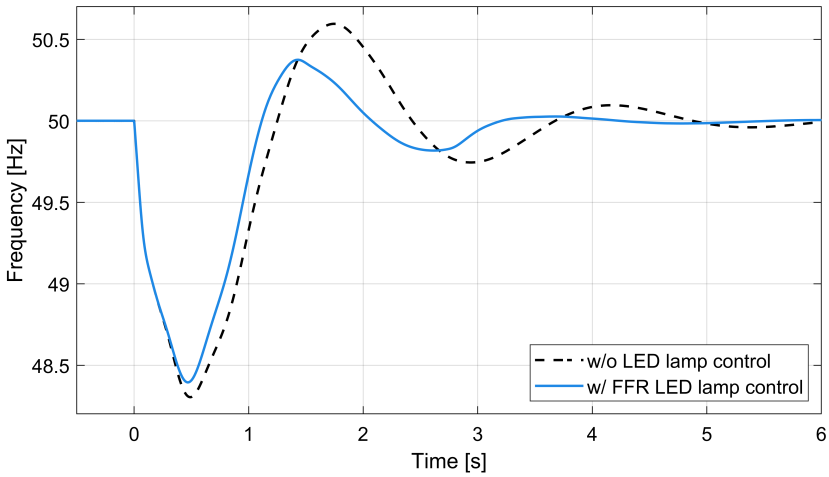


Figure 4.40: Case 2. Frequency response with FFR control

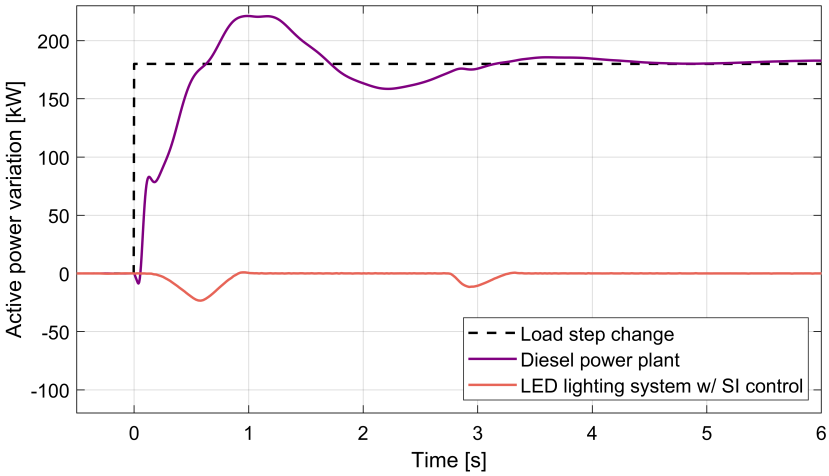


Figure 4.41: Case 2. LED lamp response with FFR control

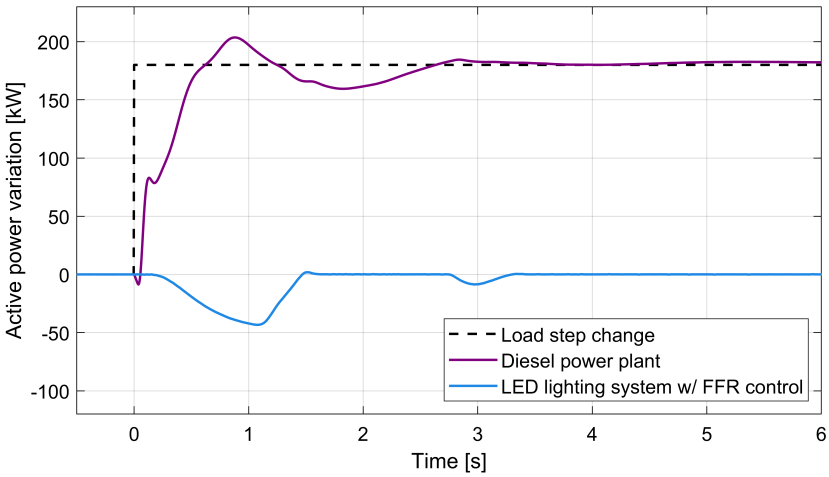


Figure 4.42: Case 2. Active power response with FFR control

lamp active power control. This is due to the fact that, in general, when an imbalance occurs, the Rate of Change of Frequency (RoCoF) (dF/dt) reaches instantaneously its maximum value, saturating the SI control, and goes rapidly to zero when the nadir is reached. Frequency deviation (ΔF), instead, starts from zero and needs more time to reach the saturation threshold of FFR control (set in this case at -0.5 Hz). FFR control is requested until ΔF is brought back within the dead-band limits (i.e. at 49.9 Hz), with an overall activation of about 1 s. In this case, the LED lamps have enough time to curtail almost all of their consumption, ensuring higher damping and a smaller frequency overshoot. Nadir point is comparable to the one reached with SI inertia control, although just slightly lower. Fig. 4.42 shows the active power response of both diesel generation plant and LED street lighting systems.

4.3.9.3 Cases 3-5. Further comparison of SI and FFR control

The previous tests assumed a very severe contingency, with values of Rate of Change of Frequency (RoCoF) and frequency deviations which rapidly saturated either SI or FFR control. Further tests have been carried out in order to investigate the response of SI and FFR control laws in absence of saturation.

Fig. 4.43 allows to compare the system frequency response obtained with SI and FFR control, applying gradually smaller load step variations. The three cases, namely 3, 4 and 5, are characterized by a 3%, 2% and 1% load variation, respectively. In these cases, the SI controller allowed to improve more visibly the response in terms of nadir with respect to the FFR. With the decreasing of the disturbance severity, Rate of Change of Frequency (RoCoF) decreases and the FFR control is activated with larger delays, because of the time necessary for the frequency deviation to reach the dead-band lower limit. In all cases, however, FFR control allows to limit or even avoid the frequency overshoot.

In addition, having imposed a load variation in the system equal to the installed power of the public street lighting system in the island (3% of the total load), the proposed controls allow to reduce the maximum frequency deviation by 20%. This reduction, using the SI control, increases if the load step change has a magnitude lower than the controlled LED lamp power volume. Indeed, SI control, being based on Rate of Change of Frequency (RoCoF), is able to provide a contribution even for very modest contingencies. For this reason, SI controller can be considered preferable as it can provide a better counter-balance for the smaller load variations that most often occur during normal grid operation.

Fig. 4.44 shows the DC control voltage set-points generated by SI and FFR in the

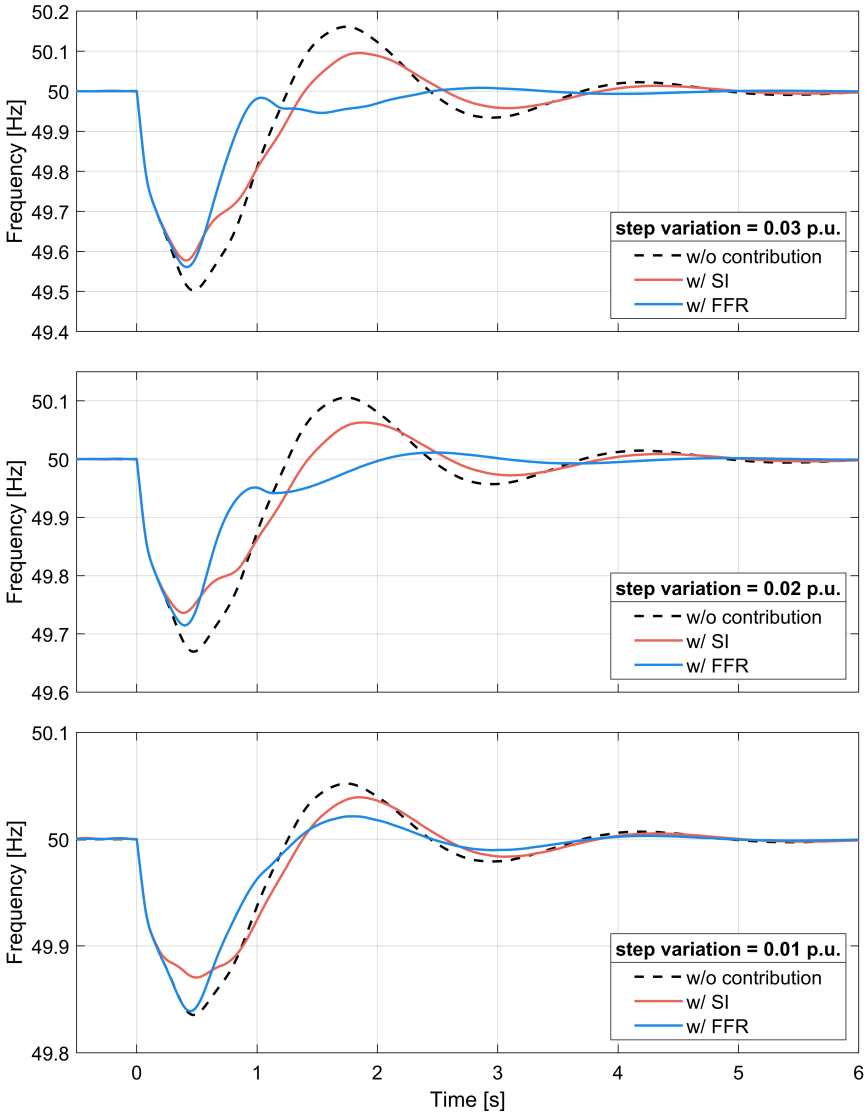


Figure 4.43: Cases 3-5. Frequency response to a 3% (left), 2% (center) and 1% (right) load variation

three cases, together with the LED lamps active power response. It is possible to observe that, due to the extremely low system inertia and the high values of initial Rate of Change of Frequency (RoCoF), even during small disturbances, SI control is still characterized by a sort of on/off behavior. The FFR control signal, instead, changes more smoothly. However, due to the actual delays in the response of the LED lamp, observed during the characterization tests presented in Section 4.3.2, the active power response follows initially about the same trajectory, with just a little delay in the case of FFR. The main difference of the two controls is again found in the longer activation time of the FFR control. As also previously remarked the delayed response of the lamp allows in any case to minimize the

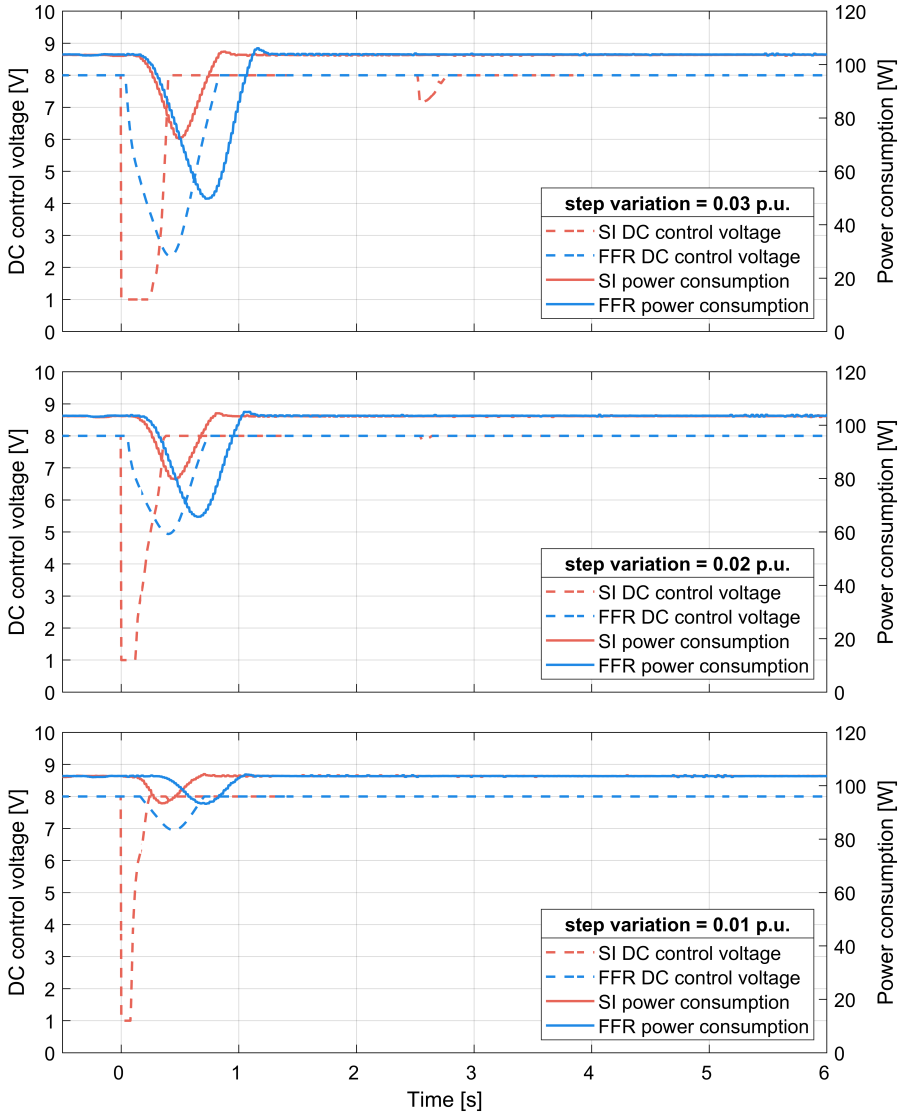


Figure 4.44: Cases 3-5. LED lamp response to a 3% (left), 2% (center) and 1% (right) load variation

visual impacts which can be considered negligible.

4.4 A SOC-feedback Control Scheme for Fast Frequency Support

In this section, a new control scheme that is able to provide fast frequency regulation and SI with Hybrid Energy Storage System (HESS), such as batteries and Supercapacitors (SCs), by modifying the exchanged active power according to the SoC is proposed.

This control reduces the contribution made by the storage systems during frequency transients when their SoC deviates from the reference SoC. In addition, this SOC-Feedback Method (SOCFM) makes it possible to return the SoC of the storage systems to the initial state at the end of the transient.

Similar studies, such as the ones in [165–167] where a SOCFM is discussed, adopt SoC feedback to translate the f-P characteristic of the ESS according to its SoC. However, such methods can only be applied to schemes that control ESS active power with a frequency-proportional control law (as in primary regulation control). The SOCFM proposed, on the other hand, is independent of the type of control with which the set-point of active power requirement to the ESS is generated, and allows for the integration of other fast frequency regulation techniques, such as synthetic inertia.

The SOC-dependent scheme proposed permits to control the active power output of the HESS, introducing a supplementary signal that modifies the active power set-point of the BESS control system, without interfering with the reference signal set by the external controller responsible for SI/FFR frequency support. The proposed scheme can be used to limit the automatic control actions to safeguard the ESS SoC, e.g., limiting the control action during sustained frequency transients.

Furthermore, this study aims to optimally use different storage systems that can work together to improve frequency regulation, while safeguarding their SoC.

4.4.1 SOC-feedback method for fast frequency regulation

In this section, a hybrid storage system consisting of a battery and a supercapacitor, each equipped with a controller for fast frequency regulation, is modeled. This controller adopts at the same time a component proportional to frequency deviation (FFR) and a component proportional to RoCoF (SI), as also proposed in [168]. In addition to FFR/SI control, for each energy storage system, a further control function is introduced to take into account SoC variations during the implementation of fast frequency regulation. Thanks to this additional control, the SoC of energy storage systems is safeguarded during operation. Furthermore, the control allows to restore SoC to a reference value at the end of the frequency event.

The working principle of the proposed SOCFM is similar to the one described in [165–167], where SoC changes result in a translation of the f-P characteristic of the primary regulation control loop (as shown in Fig. 4.45 for a generic BESS). However, such a method is based on applying an offset to the frequency error and cannot be applied

straightforwardly to a fast frequency controller that generates both primary regulation and synthetic inertia control actions. Differently from [165–167], the proposed SoC feedback control scheme is based on the application of a feedback control signal directly to the active power reference used to control the storage unit. This scheme has the advantage of being independent of the adopted fast frequency control scheme and the energy storage technology used. When applied to a single storage system, the overall control scheme can be schematized as in Fig. 4.46.

As shown in Fig. 4.46, the SoC deviation can be calculated by integrating the active power exchanged by the storage system with the power grid over time using the expression (4.1):

$$\Delta SOC_{BESS}(s) = \frac{1}{E_1 \cdot h}\frac{\Delta P_{BESS}(s)}{s} = \frac{1}{K_{E1}s}\Delta P_{BESS}(s) \tag{4.1}$$

where ΔSOC_{BESS} and ΔP_{BESS} represent the SoC deviation and the active power deviation from the initial ones, respectively; K_{E1} is a constant representing the nominal storage capacity expressed in power per second, that is given by the product of the nominal capacity (E_1) in kWh and a conversion factor ($h = 3600$) to convert hours in seconds.

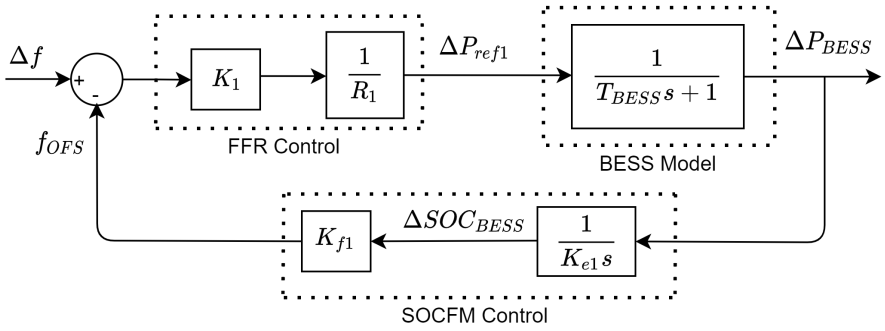


Figure 4.45: SOC-feedback control scheme for primary regulation proposed in literature

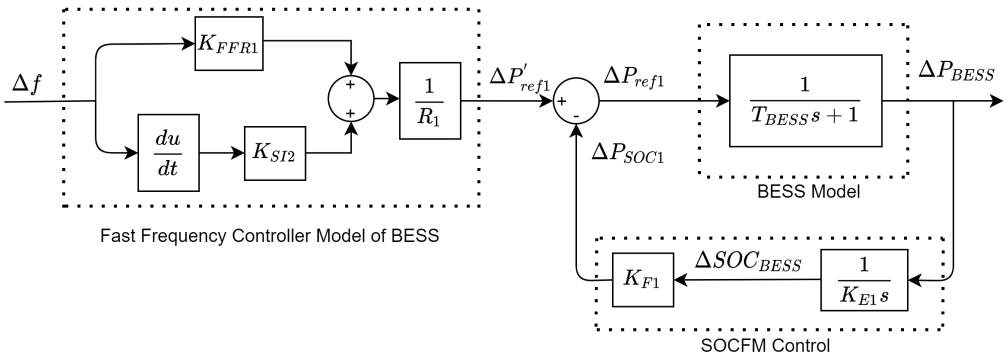


Figure 4.46: Proposed SOC-feedback control scheme for fast frequency regulation

Thanks to the proposed scheme, SoC measurement is not necessary and it is possible to manage the SoC of the energy storage system using only active power measurements. Moreover, differently from the block-diagram in Fig. 4.45 proposed in literature [165–167], where the constant K_F allows to obtain an off-set frequency correction from SoC variation, the proposed SOC-feedback method applies a correction to the reference active power output:

$$\Delta P_{SOC1}(s) = K_{F1} \cdot \Delta SOC_{BESS}(s) \tag{4.2}$$

In such a way, this control limits the active power required by the storage system as the SoC deviates from the initial value. The control also reestablishes the initial SoC when the control action of the fast frequency control system ceases. The relationship between the SoC deviation and the additional reference active power deviation is given in (4.2), where K_f is the coefficient linking them. A graphical reconstruction of the K_f ratio and the control operating margin is shown in Fig. 4.47.

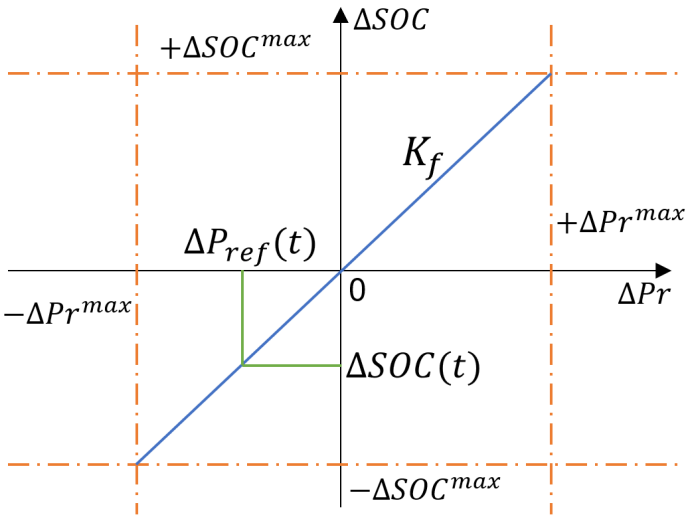


Figure 4.47: Graphical determination of additional reference active power deviation

In this study, the proposed SOC-feedback method is applied to analyze the response of a hybrid energy storage system during fast regulation actions. The hybrid system consists of a BESS and a SC that can be controlled separately to provide fast frequency regulation services.

The overall model of a controlled BESS/SC hybrid energy storage system is shown in Fig. 4.48. The dynamic response of the two energy storage systems is modeled through first-order transfer functions. The output active power (ΔP_{BESS} and ΔP_{SC}) is used to calculate the SoC variation (ΔSOC_{BESS} and ΔSOC_{SC}) and the active power reference deviation

(ΔP_{SOC1} and ΔP_{SOC2}). The output active power set-point of the fast frequency controllers ($\Delta P'_{ref1}$ and $\Delta P'_{ref2}$) is the result of the sum of two contributions: the first contribution is proportional to the frequency deviation while the second contribution is proportional to the frequency derivative (RoCoF). Coefficients K_{FFR1}, K_{SI1} and K_{FFR2}, K_{SI2}, used for the fast frequency controller of BESS and SC, permit to split the control action into two different contributions. As also proposed in [168], the sum of each pair of coefficients can be set equal to 1.

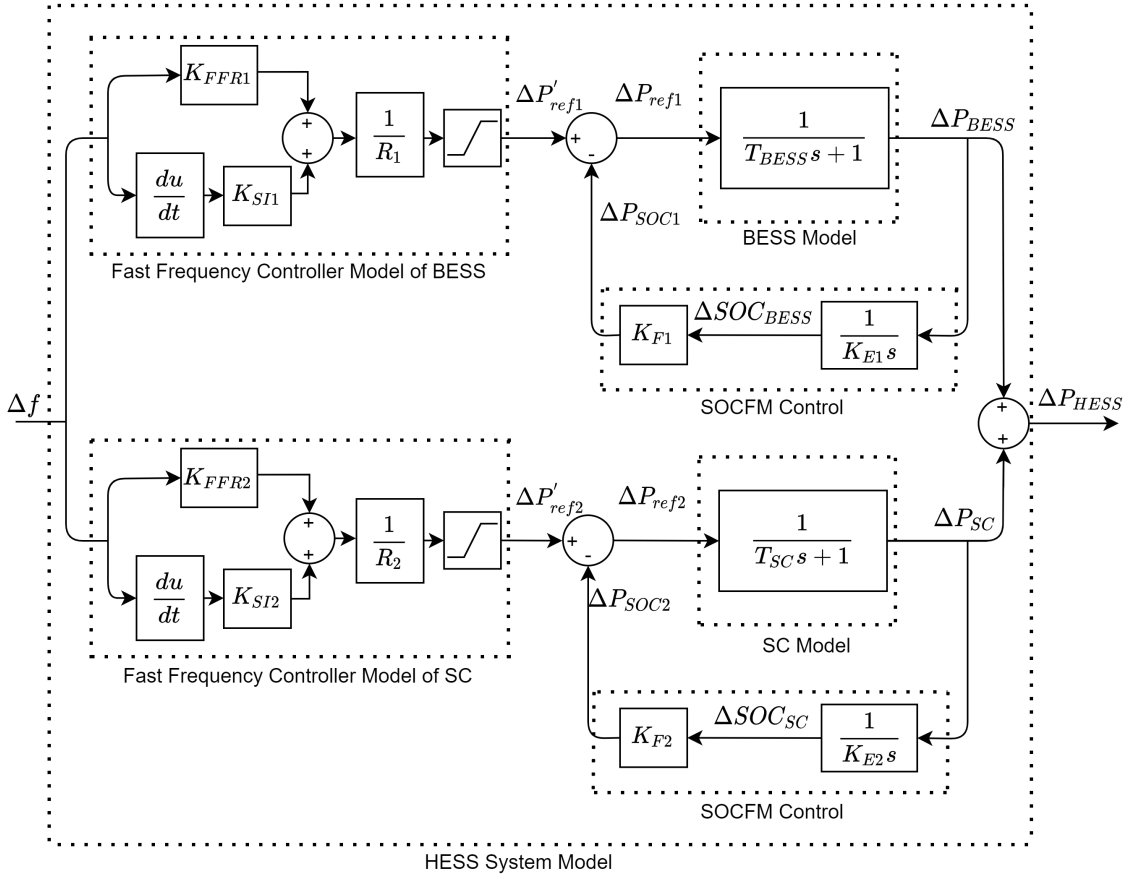


Figure 4.48: Proposed SOC-feedback control scheme applied to a Hybrid Energy Storage System

4.4.2 Open-loop test of the proposed controller

The response of the proposed control scheme was tested using as input of the model in Fig. 4.48 the frequency transient experienced during a real severe contingency. The transient used in this test, represented in Fig. 4.49 was reconstructed from the frequency trend described in [169]. In this test, all parameters were set as in Table 4.8.

The rated active power of each energy storage system was assumed to be 0.05 $p.u.$ of

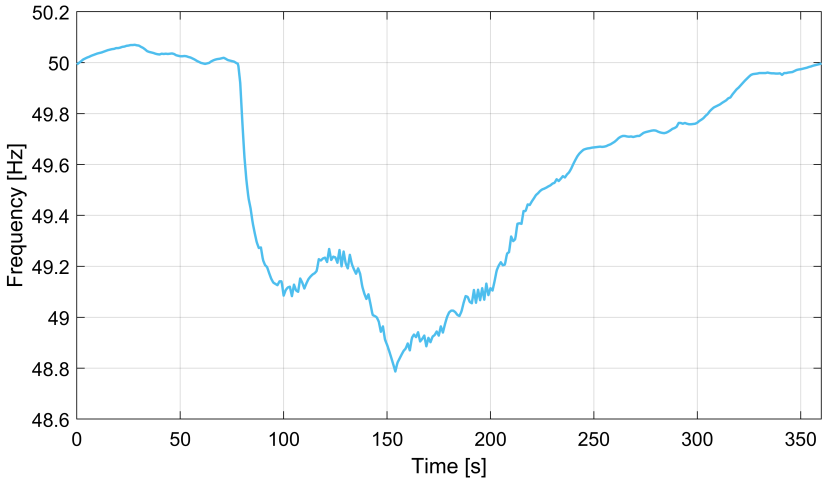


Figure 4.49: Frequency transient experienced during the Aug. 9th 2019 Great Britain power system disruption event

Table 4.8: Base parameters of the proposed SOC-feedback control scheme

R_1	T_{BESS}	K_{E1}	K_{FFR1}	K_{SI1}	K_{F1}
0.05	0.1	180	0.8	0.2	0.167

R_2	T_{SC}	K_{E2}	K_{FFR2}	K_{SI2}	K_{F2}
0.05	0.04	3	0.2	0.8	0.1

the entire power grid. The rated active represents also the maximum active power deviation for both devices ($\Delta P^{max}_{SOC1} = \Delta P^{max}_{SOC2} = 0.05$). The energy capacity of BESS and SC, was set so that, starting from a 100% SoC, the devices can fully discharge at the rated active power in one hour and one minute, respectively. Coefficients K_{E1} and K_{E2} can be calculated according to (4.1).

A maximum ΔSOC^{max}_{BESS} deviation of 30% has been assumed for the BESS, whereas a ΔSOC^{max}_{SC} of 50% was considered for the SC. According to (4.2), coefficients K_{F1} and K_{F2} have been chosen in such a way that the maximum power rate corresponds to the maximum SoC deviation.

The active power references exiting the fast-frequency controllers, $\Delta P'_{ref1}$ and $\Delta P'_{ref2}$, are limited by ΔPr^{max}_{BESS} and ΔPr^{max}_{SC}, respectively. This limit is represented by a saturation block and is necessary because the power reference actually sent to the device (ΔP_{ref1} and ΔP_{ref2}), given by the difference between the power reference arriving from the fast-frequency controller and the additional active power reference, must be able to reach zero when the SoC of the component has reached the assumed minimum or maximum SoC

deviation.

Given the higher energy capacity, a greater weight has been set to the contribution proportional to the frequency deviation (higher K_{FFR1}) than the contribution proportional to the frequency derivative (lower K_{SI1}) in the fast frequency controller of the BESS. On the contrary, since the SC is a device capable of providing higher power density, a higher weight has been set in its fast frequency controller to the contribution proportional to the RoCoF (higher K_{SI2}) than to the contribution proportional to the frequency deviation (lower K_{FFR2}).

In Figs. 4.50 and 4.51 are shown the active power response and SoC behaviour of the two controlled energy storage devices for the frequency event in Fig. 4.49.

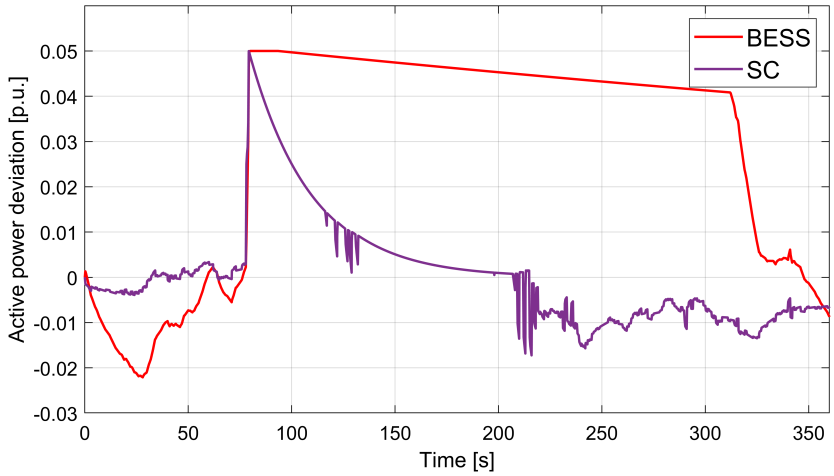


Figure 4.50: Active power responses of the HESS model for open-loop response analysis

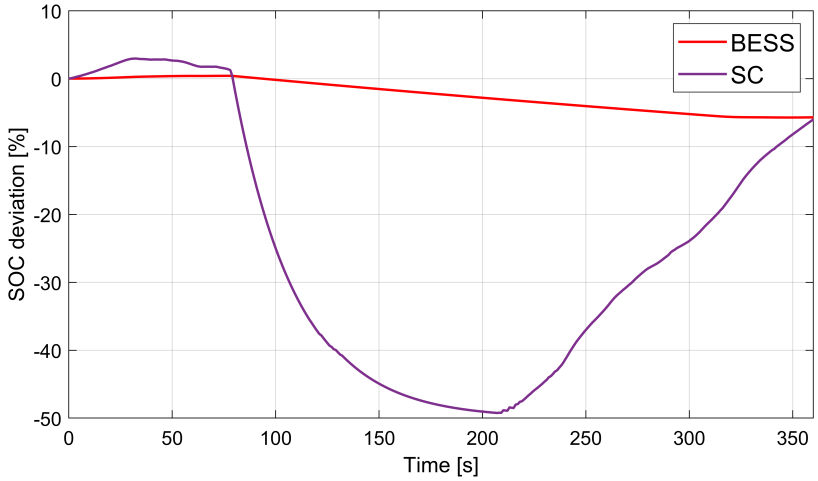


Figure 4.51: SoC behaviours of the HESS model for open-loop response analysis

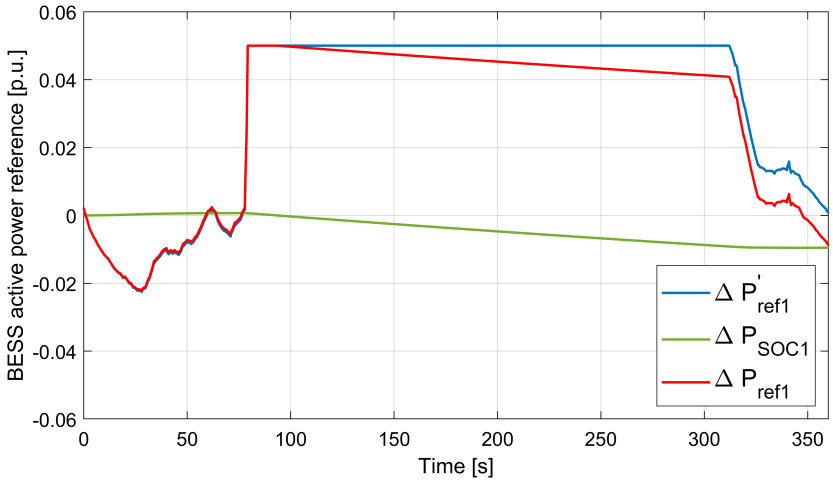


Figure 4.52: BESS active power references for open-loop response analysis

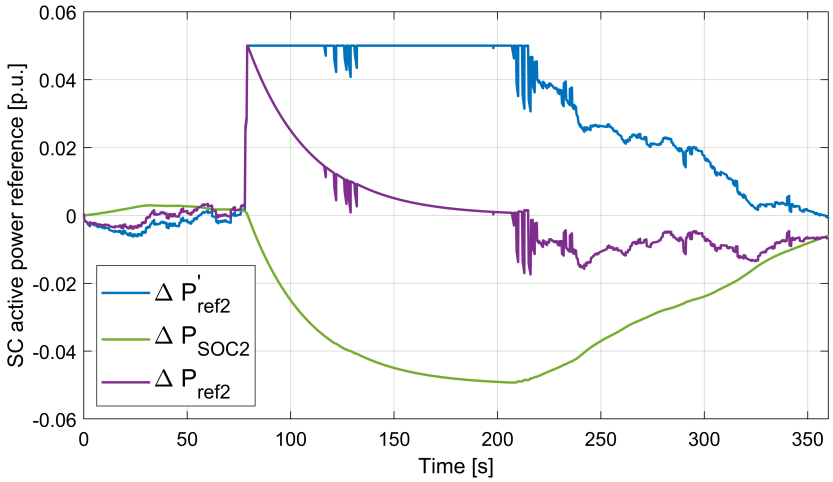


Figure 4.53: SC active power references for open-loop response analysis

As it can be observed in Fig. 4.50, for the BESS fast frequency regulator, the proportional contribution to the frequency deviation is preponderant over the proportional contribution to the frequency derivative. For this reason, a noticeable active power absorption of the BESS can be observed in the moments before the failure where a slight over-frequency was detected. On the other hand, the supercapacitor fast frequency regulator generates a SI contribution preponderant with respect to the FFR. SC behavior is slightly affected by the absolute frequency value, where as it is heavily affected by fast frequency changes and RoCoF.

The SoC responses are shown in Fig. 4.51. The BESS, endowed with a much larger capacity than the SC, varies its SoC only slightly during the transient. In this case the SoC feedback control does not affect significantly the BESS response. On the contrary, the SoC

of the SC varies considerably and, for this reason, the active power contribution is limited in the interval from about $t = 80\,\text{s}$ to $t = 200\,\text{s}$, as it can be observed in Fig. 4.50. The effect of the SOC-Feedback Method on the active power reference sent to BESS and SC is more explicitly recognizable in Figs. 4.52 and 4.53, where it is possible to separate the frequency regulation from the SOC-Feedback Method (SOCFM) correction.

The values shown in these figures are described in Fig. 4.48. The values shown in these figures are the output active power reference from the fast frequency regulators ($\Delta P'_{ref1}$, $\Delta P'_{ref2}$), the additional output active power reference from the SOC-Feedback Method (SOCFM)s (ΔPr_{BESS}, ΔPr_{SC}) and the resulting active power references sent to the storage systems (ΔP_{ref1}, ΔP_{ref2}), for the BESS and SC, respectively.

4.4.3 Closed-loop response analysis and controller parameters optimal tuning

In order to test the aforementioned control system performance, further simulation tests have been carried out. These simulations are aimed to study the behavior of the overall power system with additional frequency support provided by HESS. An aggregated hybrid storage system, that includes batteries and supercapacitors, has been integrated into the power system model, to provide fast frequency regulation. The overall model used is shown in Fig. 4.54.

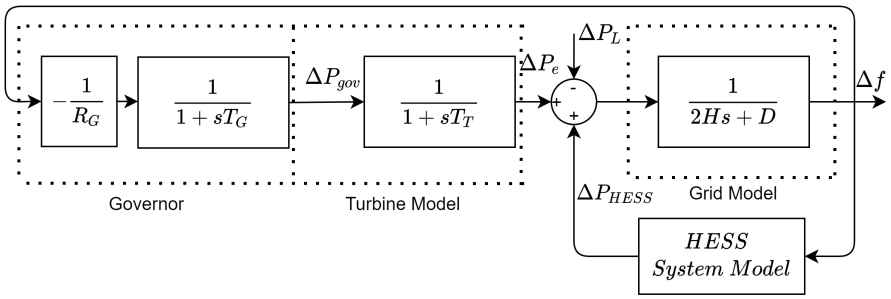


Figure 4.54: Power system model with hybrid storage connected

The modeled system involves the simulation of the frequency dynamics in a power grid when a load variation occurs, considering only the contribution of primary frequency regulation. The contribution of secondary frequency regulation is not brought into account because this study is focused on observing the first moments following a load change and how the contribution to frequency regulation of storage systems changes when the frequency is held at a value away from the steady state value for an indefinite time.

In all tests, the system parameters were set as follows: generator droop $R_G = 5\%$, generator time constant $T_G = 0.2\,s$, turbine time constant $T_T = 0.3\,s$, total system inertia $H = 2.5\,s$, dumping factor $D = 2\%$.

The coefficients considered in the model have been initially chosen following the existing literature approaches [167, 168], and from the operating conditions of the devices assumed in the model. However, the gain coefficients of the fast frequency controllers (K_{FFR1}, K_{SI1}, K_{FFR2}, K_{SI2}) and the gains K_{F1} and K_{F2} can be optimally tuned by means of a generic optimization algorithm. The problem to be solved minimized a generically nonlinear function of all system variables

$$\min_{\boldsymbol{u}} \int^{T} f(\boldsymbol{x}(t), \boldsymbol{u}, d) \cdot dt \tag{4.3}$$

subject to the differential set of equations

$$\mathbf{h}(\boldsymbol{x}(t), \boldsymbol{u}, d) = 0 \tag{4.4}$$

that can be expressed in the form

$$\dot{\boldsymbol{x}} = A(\boldsymbol{u}) \cdot \boldsymbol{x}(t) + B(\boldsymbol{u}) \cdot d \tag{4.5}$$

$$\begin{aligned} \boldsymbol{x} &\in \boldsymbol{X} \\ \boldsymbol{u} &\in \boldsymbol{U} \end{aligned} \tag{4.6}$$

where

$$\boldsymbol{u}^T = [K_{FFR1}, K_{SI1}, K_{FFR2}, K_{SI2}, K_{F1}, K_{F2}] \tag{4.7}$$

$$\boldsymbol{x}^T = [\Delta P_e(t), \Delta f(t), \Delta P_{gov}(t), \Delta P_{BESS}(t), \Delta P_{SC}(t), \Delta SOC_{BESS}(t), \Delta SOC_{SC}(t)] \tag{4.8}$$

and where d represents the disturbance ΔP_L applied at $t = 0$, $\boldsymbol{X}$ takes into account all physical constraints and $\boldsymbol{U}$ limits the control variables. In (4.8), ΔP_{gov} and ΔP_e represent the active power variation output from the governor and turbine model blocks, respectively. Δf represents the change in frequency output from the power grid, ΔP_{BESS} and ΔP_{SC} are

respectively the changes in active power output from the BESS and SC, and ΔSOC_{BESS} and ΔSOC_{SC} represent the respective changes in SoC. The formulation of matrices A,B and C is given below:

$$A = \begin{bmatrix} -1 & 0 & 1 & 0 & 0 & 0 & 0 \\ 1 & -D & 0 & -1 & -1 & 0 & 0 \\ 0 & -1 & Rg & 0 & 0 & 0 & 0 \\ \frac{K2}{M} & K1 - \frac{D \cdot K2}{M} & 0 & -\frac{K2}{M} + R1 & -\frac{K2}{M} & -R1 \cdot Kf1 & 0 \\ \frac{K4}{M} & K3 - \frac{D \cdot K4}{M} & 0 & -\frac{K4}{M} & -\frac{K4}{M} + R2 & 0 & -R2 \cdot Kf2 \\ 0 & 0 & 0 & \frac{1}{Ke1} & 0 & 0 & 0 \\ 0 & 0 & 0 & 0 & \frac{1}{Ke2} & 0 & 0 \end{bmatrix} \tag{4.9}$$

$$B = \begin{bmatrix} 0 & -1 & 0 & -\frac{K_2}{2H} & -\frac{K_4}{2H} & 0 & 0 \end{bmatrix} \tag{4.10}$$

$$C = \begin{bmatrix} \frac{1}{T_T} & 0 & 0 & 0 & 0 & 0 & 0 \\ 0 & \frac{1}{2H} & 0 & 0 & 0 & 0 & 0 \\ 0 & 0 & \frac{1}{R_G T_G} & 0 & 0 & 0 & 0 \\ 0 & 0 & 0 & \frac{1}{T_{BESS} R_1} & 0 & 0 & 0 \\ 0 & 0 & 0 & 0 & \frac{1}{T_{SC} R_2} & 0 & 0 \\ 0 & 0 & 0 & 0 & 0 & 1 & 0 \\ 0 & 0 & 0 & 0 & 0 & 0 & 1 \end{bmatrix} \tag{4.11}$$

Through discretization the dynamic problem formulated by eqs. (4.3)-(4.8) can be converted into a static nonlinear problem in the discrete time domain:

$$\min_{\boldsymbol{u}} F(\hat{\boldsymbol{x}}, \boldsymbol{u}, d) \tag{4.12}$$

subject to

$$\mathbf{H}(\hat{\boldsymbol{x}}, \boldsymbol{u}, d) = 0 \tag{4.13}$$

$$\begin{aligned} \hat{\boldsymbol{x}} &\in \boldsymbol{X} \\ \boldsymbol{u} &\in \boldsymbol{U} \end{aligned} \tag{4.14}$$

$$\hat{\boldsymbol{x}}^T = [\hat{\boldsymbol{x}}_1^T,\ \hat{\boldsymbol{x}}_2^T,\ ...,\ \hat{\boldsymbol{x}}_{nstep}^T] \tag{4.15}$$

$$\hat{\boldsymbol{x}}_k^T = [\Delta P_e^k, \Delta f^k, \Delta P_{gov}^k, \Delta P_{BESS}^k, \Delta P_{SC}^k, \Delta SOC_{BESS}^k, \Delta SOC_{SC}^k] \tag{4.16}$$

where $\mathbf{H}$ is the set of discretized differential equations, $\hat{\boldsymbol{x}}_k$ represents the state variables at the k_{th} time step and $\hat{\boldsymbol{x}}$ is the state variables' simulated trajectory. The multi-objective

optimization problem given by (4.12)-(4.16) is a nonlinear problem due to the combination of $\mathbf{u}$ and $\hat{\boldsymbol{x}}$ in (4.13) and the effect of saturation blocks in (4.14). However, the problem can be easily solved through any meta-heuristic method or through dynamic programming. In this study, a Genetic Algorithm (GA) method, where each particle in the population is represented by a vector with six real components in (4.7), is used to solve the problem. The function F is a multi-objective function given by a weighted sum of six different objective functions. The suggested multi-objective function that has been employed to reach the desired performance is:

$$F(\hat{\boldsymbol{x}},\boldsymbol{u},d) = \sum_{i=1}^{6} \alpha_i J_i(\hat{\boldsymbol{x}},\boldsymbol{u},d) = \min_{\boldsymbol{u}}(\alpha_1 J_1(\boldsymbol{u}) + \alpha_2 J_2(\boldsymbol{u}) + \alpha_3 J_3(\boldsymbol{u}) + \\ + \alpha_4 J_4(\boldsymbol{u}) + \alpha_5 J_5(\boldsymbol{u}) + \alpha_6 J_6(\boldsymbol{u})) \tag{4.17}$$

The six objective functions in (4.17) have been made explicit in eq. (4.18)-(4.23). The objective functions have been normalized to have comparable values.

$$J_1 = \frac{1}{nstep} \cdot \sum_{k=1}^{nstep} \left(\frac{f^k - f^{k-1}}{f_n} \right)^2 \tag{4.18}$$

$$J_2 = \left(\frac{max|f^k - f_n|}{f_n} \right)^2 \tag{4.19}$$

$$J_3 = \frac{1}{nstep} \cdot \sum_{k=1}^{nstep} \left(\frac{P_{BESS}^k \cdot \Delta t}{E_{BESS}} \right)^2 \tag{4.20}$$

$$J_4 = \frac{1}{nstep} \cdot \sum_{k=1}^{nstep} \left(\frac{P_{SC}^k \cdot \Delta t}{E_{SC}} \right)^2 \tag{4.21}$$

$$J_5 = \frac{1}{nstep} \cdot \sum_{k=1}^{nstep} \left(\frac{P_{BESS}^k - P_{BESS}^{k-1}}{P_{BESS}^{max}} \right)^2 \tag{4.22}$$

$$J_6 = \frac{1}{nstep} \cdot \sum_{k=1}^{nstep} \left(\frac{P_{SC}^k - P_{SC}^{k-1}}{P_{SC}^{max}} \right)^2 \tag{4.23}$$

where f^k represents the system frequency at the k_{th} time step, f_n represents the nominal system frequency, P_{BESS}^k, E_{BESS} and P_{SC}^k, E_{SC} represent the active power output at the k_{th}

time step and the energy capacity of the BESS and the SC, respectively. Δt is the size of the adopted time step and $nstep$ is the number of time steps into which the optimization window has been divided. In this case, a time window of 5 seconds and a time step Δt of 0.002 s have been chosen, obtaining a $nstep$ of 2500. P_{BESS}^{max} and P_{SC}^{max} represent the maximum active power output of the BESS and the SC, respectively.

Eq. (4.18) minimizes the sum of the frequency variations for each time step, while eq. (4.19) minimizes the maximum deviation of the frequency from the initial value (i.e. the nadir). These two functions are aimed to improve the system transient behaviour.

Eq. (4.20) and eq. (4.21) take into account the energy provided by the components, BESS and SC, in relation to their maximum capacity. These equations take into account the component wear cost, in relation to the energy throughput. Eq. (4.22) and eq. (4.23) minimize the sum of the active power variations delivered by the BESS and SC, respectively. Therefore, these functions allow during the optimization, to dampen the active power variation dynamic required from the batteries, reducing the stress on the component.

4.4.4 Test results

The cases studied and shown below are aimed to optimize the response of the system in Fig. 4.54 following at a load step variation ΔP_L of 0.1 $p.u.$ This load step was chosen equal to the the available HESS flexibility ($0.05 + 0.05$ $p.u.$), in other to better observe the effects of the optimization on the HESS response. However, in actual operation, the optimization could be calculated on-line with respect to updated dynamic parameters (for example a new estimate of the power system total inertia) and to an assumed worst possible contingency (for example the loss of the highest generation unit or the sudden disconnection of the highest load).

Although the functions (4.18)-(4.23) were normalized, the weights α can be chosen in such a way as to emphasize a specific target. For example, during alert or vulnerable conditions (for example when inertia is below a specific security threshold), components' safekeeping can be sacrificed with respect to power system security. The effects of these choices are presented in the test results. Desirable settings of weights can be obtained through extensive off-line simulations.

4.4.4.1 Case 1

In Case 1, the weight α_1 was set relatively high ($\alpha_1 \gg 1$), in order to induce the optimization algorithm to choose a set of the parameters $\boldsymbol{u}$ such that the RoCoF is reduced as much as possible. All other weights have been set to 1.

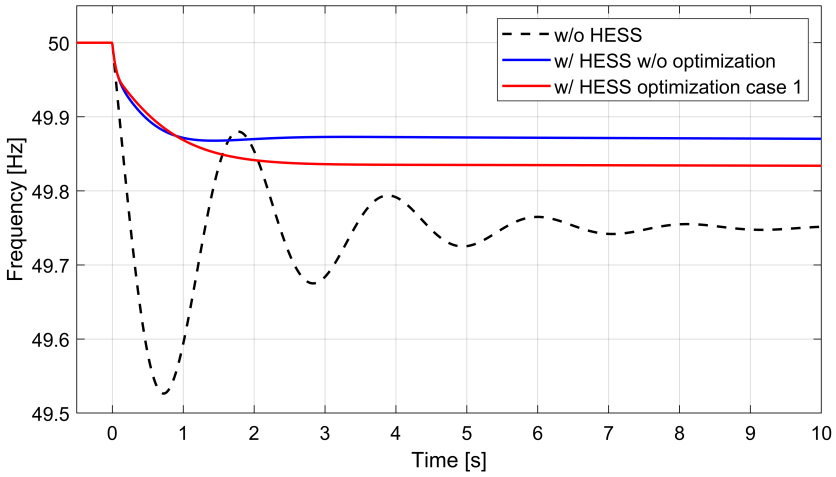


Figure 4.55: Frequency behaviour with RoCoF optimization

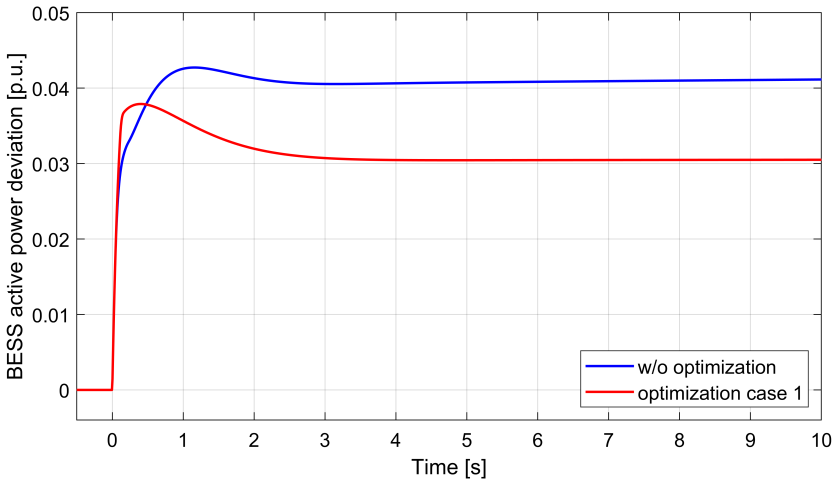


Figure 4.56: Battery active power response with RoCoF optimization

The coefficients set $\boldsymbol{u}$, resulting from the optimization, is given in (4.24).

$$\boldsymbol{u}^T = [0.463, 0.537, 0.084, 0.916, 0.171, 0.100] \tag{4.24}$$

In Fig. 4.55 the frequency behavior in the first seconds after the step load change can be observed and compared to the case with the non-optimized parameters (i.e. the values

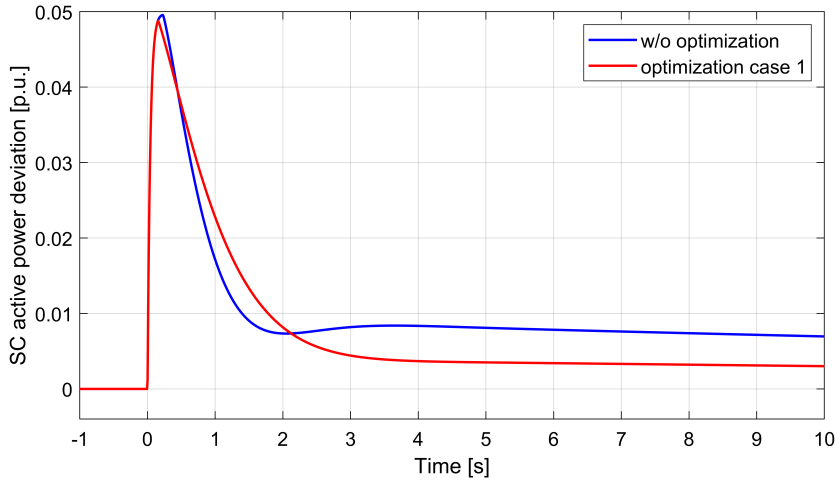


Figure 4.57: Supercapacitor active power response with RoCoF optimization

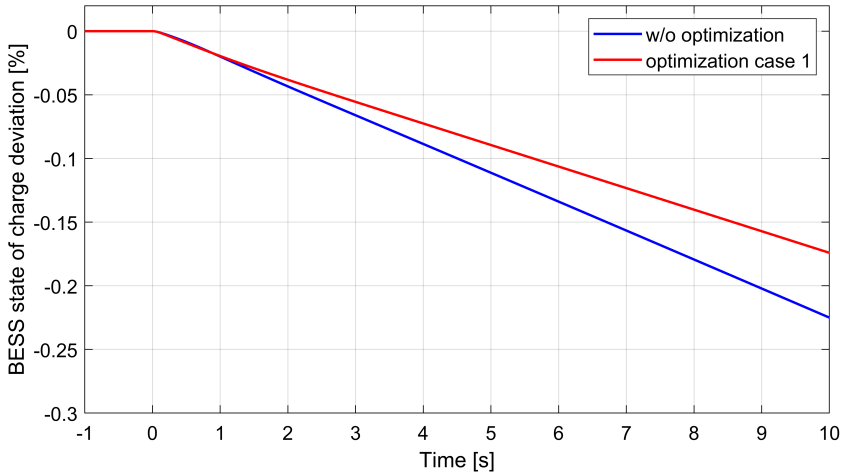


Figure 4.58: Battery SoC behaviour with RoCoF optimization

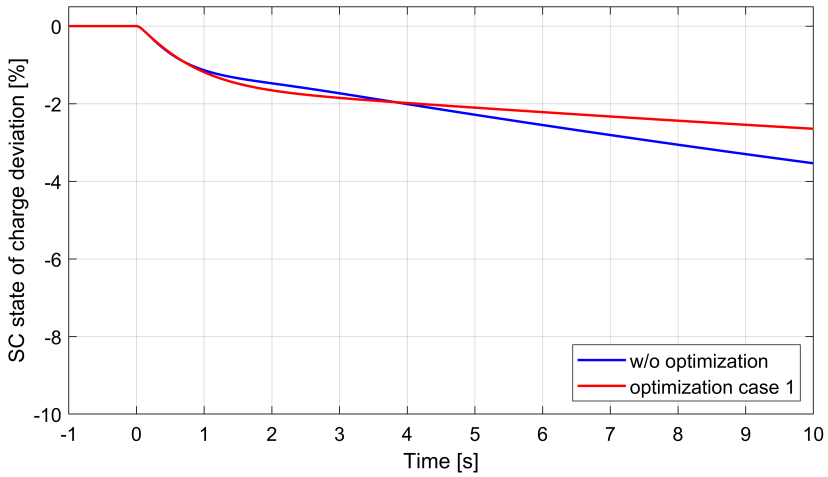


Figure 4.59: Supercapacitor SoC behaviour with RoCoF optimization

in Table 4.8), and the case without the HESS contribution. In any case, the contribution provided by the HESS allows a clear improvement in the frequency response of the system. Compared to the non-optimized case, adopting the optimized set $\boldsymbol{u}$ in (4.24), the frequency reaches a larger frequency nadir but has a reduced RoCoF.

In Fig. 4.56 and Fig. 4.57, it can be observed that the active power provided by the BESS during the transient is lower than in the non-optimized case, so that the stress on the component is reduced. On the other hand, similarly to the non-optimized case, the SC power capability is exploited at the rated value (0.05 p.u.) in the very first instants following the disturbance, when maximum RoCoF is experienced. Shortly after this maximum, when the nadir is approached, the SC active power contribution rapidly decreases.

The SoC of BESS and SC drops only slightly as it can be observed in Figs. 4.58 and 4.59. The effect of the SOC-Feedback Method (SOCFM) is therefore only slightly noticeable in the represented time window (first 10 seconds) that shows the response of primary regulation. However, if the storage power capacity is exploited for a longer period, for example also during secondary regulation, the SOC-Feedback Method (SOCFM) control can smoothly reduce the contribution required by the storage resources, avoiding a sudden triggering of storage SOC-based protections.

4.4.4.2 Case 2

In this second case, higher importance is given to preserving BESS lifetime by avoiding fast active power variations.

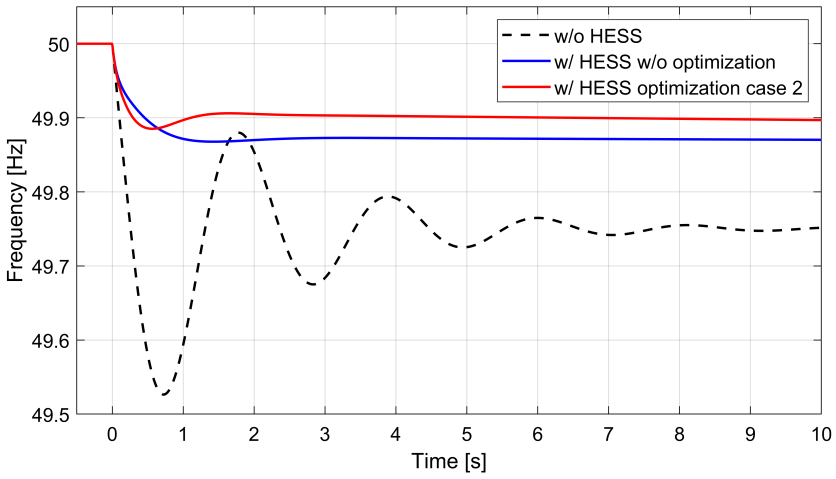


Figure 4.60: Frequency behaviour with battery response optimization

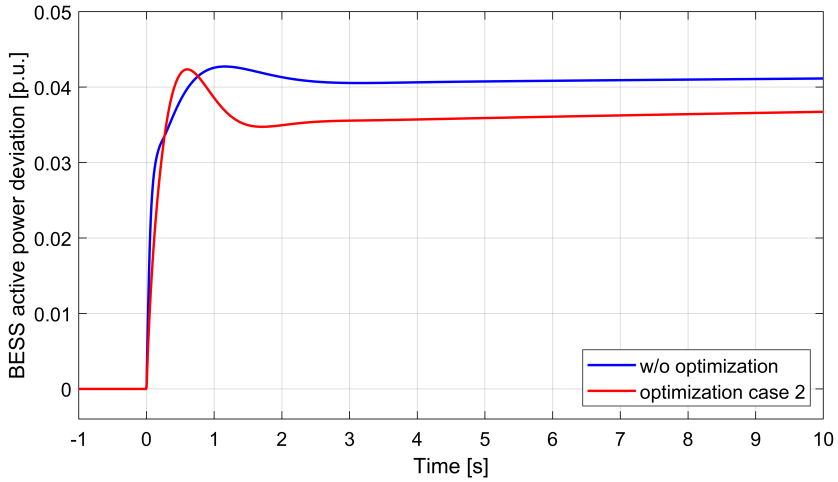


Figure 4.61: Battery active power response with battery response optimization

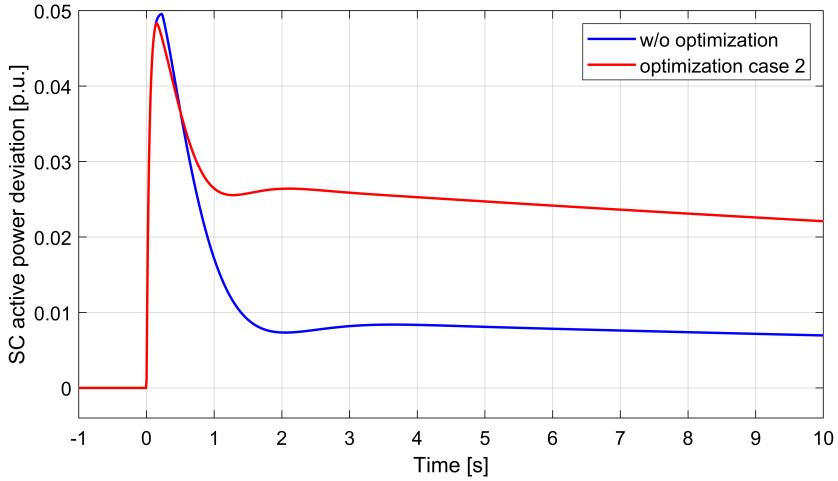


Figure 4.62: Supercapacitor active power response with battery response optimization

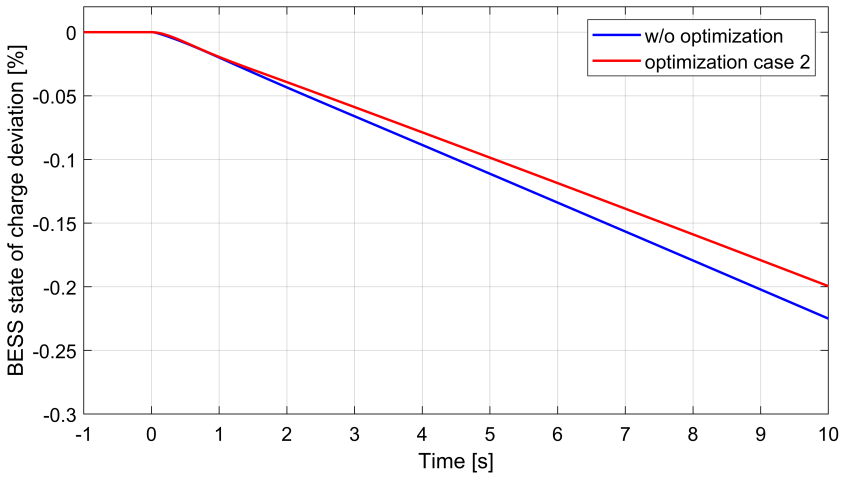


Figure 4.63: Battery SoC behaviour with battery response optimization

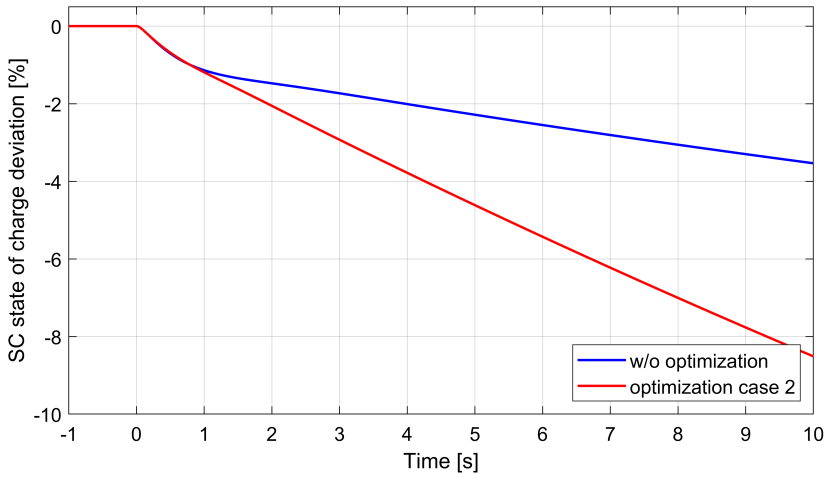


Figure 4.64: Supercapacitor SoC behaviour with battery response optimization

Stress on the battery was limited increasing the weight of function J_5. In this test a $\alpha_5 \gg 1$ was considered. All other weights were set to 1, obtaining the new solution:

$$\boldsymbol{u}^T = [0.931, 0.068, 0.742, 0.258, 0.829, 0.101] \tag{4.25}$$

By assigning a higher weight to J_5, the algorithm selected $\boldsymbol{u}$ in such a way as to reduce the variations in the active power delivered by the BESS without trying to severely constrain the RoCoF. Indeed, as can be seen in Fig. 4.60, the RoCoF is less contained compared to the non-optimized case. On the other hand, the frequency nadir is more contained.

The reason can be observed in Figs. 4.61, where it is shown how the BESS provides less active power than the optimized Case 1 in the first instants after the contingency, but provides more active power during the remaining part of the transition. Similarly, even the power contribution provided by the SC after the nadir is higher than in case 1 and the non-optimized case.

This effect is due to the higher values of K_{FFR1} and K_{FFR2} resulting from this second optimization. These high values of K_{FFR1} and K_{FFR2} are obtained because the weight assigned to function J_1 is no longer predominant with respect to the others. This condition gives a higher nadir but faster component discharge in cases where the frequency remains at a value other than the reference value after the disturbance. Indeed, it can be seen from Figs. 4.63 and 4.64 how the SoC of the two components decreases more than in Case 1.

4.5 Conclusion

This chapter has presented innovative solutions to optimize and maximize the utilization of DERs in fast frequency support services, aiming to make the process smoother and easily implementable in a future energy services market. The proposed approaches mainly focus on the challenges associated with the increasing integration of DERs, principally interfaced through grid-following inverters and with no inertia. These solutions represent improvements over controls recently introduced in the literature.

In Section 4.1, a control law for providing SI through DERs interfaced via grid-following inverters is introduced. This control enhances the performance of classical SI control, requiring less energy and reducing stress on the controlled resource. Simultaneously, it improves the frequency response compared to using classical SI control. The proposed SI control includes an additional component compared to classical SI control, allowing the cancellation of the inertial contribution from the controlled resource when not needed.

In Section 4.2, the effectiveness of a FFS contribution provided by DERs, specifically V2G EVs, is thoroughly analyzed within the BLORIN research project framework. The SI control proposed in Section 4.1 has been considered in the FFS controller used to assess the impact of V2G vehicles on frequency support during transients on the island of *Favignana*. The island's electrical network was modeled in MATLAB/Simulink and the V2G vehicles were emulated by a real $LiFePO_4$ battery connected to the modeled grid through a PHIL test setup. During these analyses, it was demonstrated that the proposed SI control ensured greater system stability during frequency transients and allowed for a higher penetration of end-users' resources enabled for frequency support services on the island.

Analyses were conducted for transients related to a rapid decrease in power produced by the island's PV systems and for transients caused by protection interventions leading to the disconnection of substantial load sections. In both cases, the contribution of V2G vehicles proved significant, reducing frequency excursion, average RoCoF, and oscillation amplitude during the transients. In evaluating these contributions in the case of over-frequency phenomena, various implementations of "Active Power Limitation for Over-frequency Transients Originating in the Grid" control (i.e. CEI-OFPL), imposed by the Italian grid code CEI 0-16, were considered.

Section 4.3 explored the idea of using LED public street lighting systems to obtain an extra grid support in scenarios characterized by very low rotational inertia. The capability

of providing a very fast active power regulation, without disconnecting the lamps, was investigated through a real Light-Emitting Diode (LED) lamp connected to a simulated power grid via Power Hardware-in-the-Loop tests.

First, a simplified single-bus network characterized by low inertia was considered for PHIL tests, then a more complex and precise network of a typical structure of a small Italian island, the same reference small island described in Section 1.5.1.

In both cases, the proposed LED lamp control was tested in a scenario characterized by an extreme reduction of inertia, allowing to prove how a non-negligible contribution to frequency support can be obtained exploiting these controllable resources.

The support for frequency transients provided by the hypothesized Light-Emitting Diode (LED) street lighting system in these studies was achieved through two different controllers, FFR control, and SI control, analyzing the differences in the use of each. In this application, similar to the analyses conducted in Section 4.2, the SI control used was based on the SI control proposed in Section 4.1. However, in this case, envisioning a nocturnal scenario, the lamps could only reduce their power consumption and contribute to cases of under-frequency transients.

The PHIL tests showed that FFR control, in case of severe contingencies, allows a more pronounced contribution to enhance the frequency behavior but causes a longer drop in the illumination flux, which has a higher visual impact. On the other hand, SI control has the advantage of reducing impacts on illumination levels, due to a shorter activation time of the dimming control. For this reason, the SI control is preferable with regard to the use of Light-Emitting Diode (LED) street lighting systems to provide ancillary services. In both cases, however, the visual impacts due to the control can be considered negligible and comparable to the same disturbances that can be observed during commonly power quality events, such as deep voltage sags or transient voltage interruptions, which happen hundreds of times in a year (more often than frequency events).

In Section 4.4, a SoC-feedback control mechanism is introduced to prevent abrupt reductions in the SoC and restore the device's charge to the pre-disturbance condition following a transient event. This control is designed to alleviate stress on a generic ESS component (in this study, a Hybrid Energy Storage System (HESS) consisting of a BESS and a SC was hypothesized) during the delivery of fast frequency support services. The proposed SoC-feedback control can be applied independently of the implemented frequency regulation control law, as it modulates the set-point provided by a generic FFS controller based on the component's SoC.

It has been shown how, through targeted optimization of control parameters, it is possible to derive controller parameters to achieve an improvement in frequency response and/or avoid excessive component stress. The results demonstrate how giving more weight to battery protection rather than reducing RoCoF during a disturbance visibly changes the frequency behaviour. Furthermore, the SoC control permits safeguarding of the state of charge without limiting the action of the components during frequency transients.

Conclusion

In this thesis, various tools and methodologies have been proposed to facilitate the implementation of Microgrid (MG)s (MGs) in power systems, with a particular focus on increasing the hosting capacity of Renewable Energy Sources (RES) in isolated or weakly connected power systems.

The study addressed the challenges faced by small Italian islands characterized by high operational costs and heavy dependence on fossil fuels. The elevated fuel costs and fuel supply expenses not only pose management challenges but also contribute to higher energy costs for the entire population of a country.

Moreover, achieving decarbonization and reducing greenhouse gas emissions in these regions is a challenging task. Finding solutions to decarbonize these vulnerabilities in a country's electricity system landscape is a significant step forward.

Enabling greater penetration of renewables into these systems is complex. It requires a comprehensive examination of all aspects of controlling these systems, ensuring that there are resources that can sustain the low inertia of these systems and sufficient operating reserves to compensate for unexpected, although frequent, variations in renewable energy production.

This thesis has proposed technical and methodological advancements across several aspects of isolated MG management. Firstly, an operational system planning algorithm was introduced, aiming to minimize operational costs and cuts in load and renewable production over a time scale ranging from 15 minutes to 24 hours.

Subsequently, a real-time algorithm was suggested, operating on a time scale from 1 minute to 15 minutes, evaluating and managing the real-time operating reserve available in the system. Its goal is to make the system resilient to sudden load/generation variations.

Finally, advancements were proposed for frequency support during transients, observing and supporting the network in the earliest moments of a contingency, making the network dynamically strong enough to withstand significant load and renewable production

oscillations occurring within seconds.

The methodologies presented in this thesis are only a part of the activities conducted during the doctoral journey, involving in-depth modeling of dynamic networks to study trends, criticalities, and the impact of the proposed methodologies.

In all aspects and methodologies presented in this thesis, further studies and improvements can be pursued. The effect of the presence and absence of a Battery Energy Storage System (BESS), as well as its size, in islanded MGs can be analyzed through the approaches and methodologies discussed in Chapter 2. This will allow us to observe how the various approaches are sensitive to the size of the BESS. Moreover, these approaches can also be used to optimally size energy resources of an isolated MG, not only the BESS size but also the number and the size of the installed Photovoltaic (PV) plants. Further studies may also be conducted on the real-time algorithm proposed in Chapter 3, by analyzing how the presence or absence of a Microgrid Controller (MGC) on isolated distribution networks influences the hosting capacity of these systems, not only conceptually but also analytically, by deriving the maximum penetration of renewable energy generation on the grid as the parameters of the MGC change, with and without certain functions of it. Improvements in the stability of islanded systems due to the innovative methodologies proposed in Chapter 4 can be further analyzed by hypothesizing different control methodologies distributed in the network and how they influence each other.

Additionally, various activities, including power hardware in the loop and remote power hardware in the loop experiments, were performed to validate some methodologies. These activities encompassed the control architecture mentioned in Chapter 3 and the frequency regulation services remuneration of the tests shown in Chapter 4.2 related to the BLORIN project.

Furthermore, extensive modeling and testing efforts were undertaken to create computationally lightweight network and electrical load models. These were used during the tests described in this thesis, allowing real-time simulation of the modeled networks and the aforementioned power hardware in the loop co-simulations.

Through computationally lightweight load modeling and real-time co-simulations, the next step in this work emerges. Starting from this research, it will be necessary to consider all the described methodologies, adapt them to coexist, and test the control structure of an isolated MG in its entirety. These tools offer the ability to test the complete network control across all time scales without having to build a prototype on a real island, which is invasive for residents, as well as expensive, and challenging to get public authorities to

authorize.

In conclusion, with this work, it is hoped to contribute to the technological advancement of these themes, facilitating the rapid integration of renewable sources into isolated systems, thereby reducing energy costs for users and emissions of polluting gases.

By increasing the stability and reliability of MGs operating in island mode, the aim is to enable the integration of these systems into interconnected grids. Future studies include a further generalization of the methodologies proposed in this thesis to make them suitable for interconnected MGs and multi-MG systems. Advancements in these studies could consider the possibility for nested MGs to communicate with each other and collectively provide support for the security of the national power system even during severe contingencies. Among the various contributions that a collection of dispersed MGs can provide to the main grid, envisioning the re-powering of parts of the system after a blackout, reducing downtime and improving the quality of electrical service. In a future power system composed of various interconnected MGs, the resolution of numerous power system management issues through the use of MG resources is possible. It would no longer be a stringent constraint to keep the entire grid interconnected, allowing for solutions to optimal network reconfiguration or optimal power flow problems where parts of the system are isolated. By increasing the range of possible network management solutions, a reduction in network management costs can be achieved, resulting in lower MG implementation costs and lower electric energy costs for end users.

References

[1] S. Bruno, G. Giannoccaro, C. Iurlaro, M. L. Scala, and C. Rodio, "A Low-cost Controller to Enable Synthetic Inertia Response of Distributed Energy Resources," in *2020 IEEE International Conference on Environment and Electrical Engineering and 2020 IEEE Industrial and Commercial Power Systems Europe (EEEIC / I&CPS Europe)*, 2020, pp. 1–6.

[2] S. Bruno, G. Giannoccaro, C. Iurlaro, M. L. Scala, L. Notaristefano, and C. Rodio, "Mapping Flexibility Region through Three-phase Distribution Optimal Power Flow at TSO-DSO Point of Interconnection," in *2021 AEIT International Annual Conference (AEIT)*, 2021, pp. 1–6.

[3] S. Bruno, G. De Carne, C. Iurlaro, C. Rodio, and M. Specchio, "A SOC-feedback Control Scheme for Fast Frequency Support with Hybrid Battery/Supercapacitor Storage System," in *2021 6th IEEE Workshop on the Electronic Grid (eGRID)*, 2021, pp. 1–8.

[4] S. Bruno, G. Giannoccaro, C. Iurlaro, M. L. Scala, C. Rodio, and R. Sbrizzai, "Fast Frequency Regulation Support by LED Street Lighting Control," in *2021 IEEE International Conference on Environment and Electrical Engineering and 2021 IEEE Industrial and Commercial Power Systems Europe (EEEIC / I&CPS Europe)*, 2021, pp. 1–6.

[5] S. Bruno, G. Giannoccaro, C. Iurlaro, M. L. Scala, and M. Menga, "Predictive Optimal Dispatch for Islanded Distribution Grids considering Operating Reserve Constraints," in *2022 IEEE 21st Mediterranean Electrotechnical Conference (MELECON)*, 2022, pp. 518–523.

[6] S. Bruno, C. Iurlaro, M. L. Scala, and M. Menga, "Integration of Operating Reserve Constrains in the Predictive Optimal Dispatch of Energy and Storage Resources

in Small Islands," in *2022 IEEE International Conference on Environment and Electrical Engineering and 2022 IEEE Industrial and Commercial Power Systems Europe (EEEIC / I&CPS Europe)*, 2022, pp. 1–6.

[7] M. M. Islam, S. Bruno, C. Iurlaro, and M. La Scala, "Robust adaptive integral backstepping control of FC-SC-battery and traction motor based hybrid electric vehicles," in *2022 AEIT International Annual Conference (AEIT)*, 2022, pp. 1–6.

[8] S. Bruno, G. Giannoccaro, M. Muzammal Islam, C. Iurlaro, M. La Scala, M. Menga, and C. Rodio, "Control and Power Hardware-in-the-Loop tests for low-inertia power systems," in *2022 AEIT International Annual Conference (AEIT)*, 2022, pp. 1–6.

[9] S. Bruno, C. Iurlaro, M. L. Scala, M. Menga, and M. Semeraro, "A Dynamic Model of the Favignana Island Non-Synchronous Power System for Power Hardware-in-the-Loop Tests," in *2022 Workshop on Blockchain for Renewables Integration (BLORIN)*, 2022, pp. 107–112.

[10] S. Bruno, G. Giannoccaro, M. M. Islam, C. Iurlaro, M. L. Scala, M. Menga, and C. Rodio, "Predictive Control Based Energy Management of a Residential Hybrid AC-DC Nanogrid," in *2022 4th International Conference on Electrical Engineering and Control Technologies (CEECT)*, 2022, pp. 1183–1187.

[11] C. Iurlaro, L. Barbato, G. Bianco, S. Bruno, G. Ceneri, M. La Scala, L. Mascolo, M. Menga, C. Micillo, F. Renna, and G. Sapienza, "Control Architecture and Algorithms for Isolated Microgrids," in *CIRED 2023 - The 27th International Conference and Exhibition on Electricity Distribution*, Rome, Italy, 2023.

[12] K. Rajashekaraiah, G. De Carne, C. Iurlaro, M. Semeraro, and S. Bruno, "P-q theory-based dynamic load modelling in short-circuit analysis," in *2023 8th IEEE Workshop on the Electronic Grid (eGRID)*, 2023, pp. 1–5.

[13] L. Barbato, G. Bianco, L. Mascolo, M. Menga, F. Renna, G. Sapienza, C. Micillo, S. Bruno, C. Iurlaro, and M. L. Scala, "Power hardware-in-the-loop tests of a control architecture for isolated microgrids in a co-simulation framework," in *2023 8th IEEE Workshop on the Electronic Grid (eGRID)*, 2023, pp. 1–6.

[14] S. Bruno, G. Giannoccaro, C. Iurlaro, M. La Scala, and C. Rodio, "Power Hardware-in-the-Loop Test of a Low-Cost Synthetic Inertia Controller for Battery Energy Storage System," *Energies*, vol. 15, no. 9, 2022.

[15] S. Bruno, G. Giannoccaro, C. Iurlaro, M. L. Scala, M. Menga, C. Rodio, and R. Sbrizzai, "Fast Frequency Support Through LED Street Lighting in Small Non-Synchronous Power Systems," *IEEE Transactions on Industry Applications*, vol. 59, no. 2, pp. 2277–2287, 2023.

[16] K. Rajashekaraiah, C. Iurlaro, S. Bruno, and G. De Carne, "Modelling of 3-Phase p-q Theory-Based Dynamic Load for Real-Time Simulation," *IEEE Open Access Journal of Power and Energy*, vol. 10, pp. 654–664, 2023.

[17] G. Sciumè, C. Iurlaro, S. Bruno, R. Musca, G. Zizzo, E. R. Sanseverino, and M. La Scala, "An integrated architecture for power hardware-in-the-loop environment and blockchain for fast frequency response tracking and remuneration," *to be submitted for publication to Electric Power Systems Research (EPSR)*, 2024.

[18] U.S. Energy Information Administration (EIA), "International energy outlook 2016," 2016, license: CC BY 4.0. [Online]. Available: https://www.eia.gov/outlooks/ieo/pdf/0484(2016).pdf

[19] International Energy Agency (IEA), "World energy investment outlook," 2014, license: CC BY 4.0. [Online]. Available: https://www.iea.org/reports/world-energy-investment-outlook

[20] European Commission, "Directive (EU) 2018/2001 of the European Parliament and of the Council of 11 December 2018 on the promotion of the use of energy from renewable sources," Official Journal of the European Union, Brussels, Belgium, 2018.

[21] ——, "Communication from the commission to the european parliament, the council, the european economic and social committee and the committee of the regions: The european green deal," COM(2019) 640 final, Brussels, Belgium, 2019.

[22] ——, "Delivering the european green deal," COM(2021) 640 final, Brussels, Belgium, 2021.

[23] ——, "Communication from the commission to the european parliament, the council, the european economic and social committee and the committee of the regions: Repowereu plan," COM(2022) 230 final, Brussels, Belgium, 2022.

[24] ——, "Proposal for a council regulation on a temporary emergency measure to streamline permit-granting procedures for renewable energy projects and facilitate power purchase agreements," COM(2022) 640 final, Brussels, Belgium, 2022.

[25] Council of the European Union, "Council regulation (eu) 2022/230 of 22 december 2022 on a temporary emergency measure to streamline permit-granting procedures for renewable energy projects and facilitate power purchase agreements," Official Journal of the European Union, Brussels, Belgium, 2022.

[26] European Commission, "European Green Deal: EU agrees stronger legislation to accelerate the rollout of renewable energy," Press release, Brussels, Belgium, 2023.

[27] M. Carpintero-Rentería, D. Santos-Martín, and J. M. Guerrero, "Microgrids literature review through a layers structure," *Energies*, vol. 12, no. 22, p. 4381, 2019.

[28] D. T. Ton and M. A. Smith, "The u.s. department of energy's microgrid initiative," *The Electricity Journal*, vol. 25, no. 8, pp. 84–94, 2012. [Online]. Available: https://www.sciencedirect.com/science/article/pii/S1040619012002254

[29] N. Hatziargyriou, *Microgrids: architectures and control*. John Wiley & Sons, 2014.

[30] CIGRÉ WG C6.22, *Microgrids 1 Engineering, Economics, & Experience*. Paris, France: CIGRÉ, 2015.

[31] S. Parhizi, H. Lotfi, A. Khodaei, and S. Bahramirad, "State of the art in research on microgrids: A review," *IEEE Access*, vol. 3, pp. 890–925, 2015.

[32] F. Martin-Martínez, A. Sánchez-Miralles, and M. Rivier, "A literature review of microgrids: A functional layer based classification," *Renewable and Sustainable Energy Reviews*, vol. 62, pp. 1133–1153, 2016. [Online]. Available: https://www.sciencedirect.com/science/article/pii/S1364032116301356

[33] International Electrotechnical Commission, "IEC TS 62898-1:2017 Microgrids—Part1:Guidelines for Microgrid Projects Planning and Specification," IEC Publications, Geneva, Switzerland, Technical Specification, 2017.

[34] IEEE, "IEEE Standard for the Specification of Microgrid Controllers," *IEEE Std 2030.7-2017*, pp. 1–43, 2018.

[35] G. Joos, J. Reilly, W. Bower, and R. Neal, "The need for standardization: The benefits to the core functions of the microgrid control system," *IEEE Power and Energy Magazine*, vol. 15, no. 4, pp. 32–40, 2017.

[36] J. F. Castro, R. A. Roncolatto, A. R. Donadon, V. E. Andrade, P. Rosas, R. G. Bento, J. G. Matos, F. A. Assis, F. C. Coelho, R. Quadros *et al.*, "Microgrid applications and technical challenges—the brazilian status of connection standards and operational procedures," *Energies*, vol. 16, no. 6, p. 2893, 2023.

[37] A. Mohammed, S. S. Refaat, S. Bayhan, and H. Abu-Rub, "Ac microgrid control and management strategies: Evaluation and review," *IEEE Power Electronics Magazine*, vol. 6, no. 2, pp. 18–31, 2019.

[38] M. Barnes, A. Dimeas, A. Engler, C. Fitzer, N. Hatziargyriou, C. Jones, S. Papathanassiou, and M. Vandenbergh, "Microgrid laboratory facilities," in *2005 International Conference on Future Power Systems*, 2005, pp. 6 pp.–6.

[39] IEEE, "IEEE Standard for the Testing of Microgrid Controllers," *IEEE Std 2030.8-2018*, pp. 1–42, 2018.

[40] ——, "IEEE Standard for Interconnection and Interoperability of Distributed Energy Resources with Associated Electric Power Systems Interfaces," *IEEE Std 1547-2018 (Revision of IEEE Std 1547-2003)*, pp. 1–138, 2018.

[41] International Electrotechnical Commission, "IEC TS 62898-2:2018 Microgrids—Part1:Guidelines for Operation," IEC Publications, Geneva, Switzerland, Technical Specification, 2018.

[42] ——, "IEC TS 62898-3-1:2020 Microgrids—Part 3-1: Technical requirements - Protection and dynamic control," IEC Publications, Geneva, Switzerland, Technical Specification, 2020.

[43] A. Canova, L. Giaccone, F. Spertino, and M. Tartaglia, "Electrical impact of photovoltaic plant in distributed network," *IEEE Transactions on industry applications*, vol. 45, no. 1, pp. 341–347, 2009.

[44] B. Tamimi, C. Cañizares, and K. Bhattacharya, "System stability impact of large-scale and distributed solar photovoltaic generation: The case of ontario, canada," *IEEE Transactions on Sustainable Energy*, vol. 4, no. 3, pp. 680–688, 2013.

[45] K. Kawabe and K. Tanaka, "Impact of dynamic behavior of photovoltaic power generation systems on short-term voltage stability," *IEEE Transactions on Power Systems*, vol. 30, no. 6, pp. 3416–3424, 2015.

[46] G. Artale, A. Cataliotti, V. Cosentino, D. Di Cara, S. Guaiana, N. Panzavecchia, and G. Tinè, "Real-time power flow monitoring and control system for microgrids integration in islanded scenarios," *IEEE Transactions on Industry Applications*, vol. 55, no. 6, pp. 7186–7197, 2019.

[47] T. Lu, Z. Wang, Q. Ai, and W.-J. Lee, "Interactive model for energy management of clustered microgrids," *IEEE Transactions on Industry Applications*, vol. 53, no. 3, pp. 1739–1750, 2017.

[48] H. K. Nguyen, A. Khodaei, and Z. Han, "Incentive mechanism design for integrated microgrids in peak ramp minimization problem," *IEEE Transactions on Smart Grid*, vol. 9, no. 6, pp. 5774–5785, 2018.

[49] S. Marzal, R. Salas, R. González-Medina, G. Garcerá, and E. Figueres, "Current challenges and future trends in the field of communication architectures for microgrids," *Renewable and Sustainable Energy Reviews*, vol. 82, pp. 3610–3622, 2018.

[50] R. Madani, M. Ashraphijuo, J. Lavaei, and R. Baldick, "Power system state estimation with a limited number of measurements," in *2016 IEEE 55th Conference on Decision and Control (CDC)*, 2016, pp. 672–679.

[51] A. Ahmed and M. Khalid, "A review on the selected applications of forecasting models in renewable power systems," *Renewable and Sustainable Energy Reviews*, vol. 100, pp. 9–21, 2019. [Online]. Available: https://www.sciencedirect.com/science/article/pii/S1364032118306932

[52] F. Salvadori, C. S. Gehrke, A. C. de Oliveira, M. de Campos, and P. S. Sausen, "Smart grid infrastructure using a hybrid network architecture," *IEEE Transactions on Smart Grid*, vol. 4, no. 3, pp. 1630–1639, 2013.

[53] CEI Italian Standard, "CEI 0-16:2022-03 - Reference technical rules for the connection of active and passive consumers to the HV and MV electrical networks of distribution Company," 2022.

[54] TERNA S.p.A. Piano di difesa del sisteme elettrico. [Online]. Available: https://download.terna.it/terna/Allegato%20A.9_8d7c12172fe7836.pdf

[55] L. Cassin, P. Melindi-Ghidi, and F. Prieur, "Confronting climate change: Adaptation vs. migration in small island developing states," *Resource and Energy Economics*, vol. 69, p. 101301, 2022.

[56] E. Ali, W. Cramer, J. Carnicer, E. Georgopoulou, N. Hilmi, G. Le Cozannet, and P. Lionello, "Cross-chapter paper 4: Mediterranean region," *Climate change*, pp. 2233–2272, 2022.

[57] "Climate change 2022: Impacts, adaptation and vulnerability," contribution of Working Group II to the Sixth Assessment Report of the IPCC. [Online]. Available: https://www.ipcc.ch/report/ar6/wg2/

[58] I. Kougias, S. Szabó, A. Nikitas, and N. Theodossiou, "Sustainable energy modelling of non-interconnected mediterranean islands," *Renewable Energy*, vol. 133, pp. 930–940, 2019. [Online]. Available: https://www.sciencedirect.com/science/article/pii/S096014811831293X

[59] D. C. Major, P. Blaschke, V. Gornitz, E. Hosek, M. Lehmann, J. Lewis, H. Loehr, G. A. Major-Ex, M. Pedersen Zari, M. J. Vásquez Vargas, E. Watterson, and A. Wejs, "Adaptation to climate change in small island settlements," *Ocean & Coastal Management*, vol. 212, p. 105789, 2021. [Online]. Available: https://www.sciencedirect.com/science/article/pii/S0964569121002726

[60] United Nations Framework Convention on Climate Change, "Paris agreement," 2015. [Online]. Available: https://unfccc.int/process-and-meetings/the-paris-agreement/the-paris-agreement

[61] "NESOI | New Energy Solutions Optimized for Islands." [Online]. Available: https://www.nesoi.eu/

[62] Clean energy for EU islands secretariat. [Online]. Available: https://euislands.eu/index.php/.

[63] G. Frydrychowicz-Jastrzębska, "El hierro renewable energy hybrid system: A tough compromise," *Energies*, vol. 11, no. 10, 2018. [Online]. Available: https://www.mdpi.com/1996-1073/11/10/2812

[64] R. Godina, E. Rodrigues, J. Matias, and J. Catalão, "Sustainable energy system of el hierro island," in *International conference on renewable energies and power quality (ICREPQ'15)*, 2015, pp. 46–51.

[65] G. Jastrzębska, "El hierro—the first energetically self-sufficient region," in *Proceedings of the 17th International Multidisciplinary Scientific Geoconference SGEM Energy and Clean Technologies*, Vienna, Austria, 2017, pp. 651–658.

[66] A. Mena-Nieto, C. Estay-Ossandon, and S. P. Dos Santos, "Will the balearics and the canary islands meet the european union targets for municipal waste? a comparative study from 2000 to 2035," *Science of the Total Environment*, vol. 783, p. 147081, 2021.

[67] D. Curto, S. Favuzza, V. Franzitta, R. Musca, M. A. N. Navia, and G. Zizzo, "Evaluation of the optimal renewable electricity mix for lampedusa island: The adoption of a technical and economical methodology," *Journal of cleaner production*, vol. 263, p. 121404, 2020.

[68] J. R. S. Doorga, "Climate change and the fate of small islands: The case of mauritius," *Environmental Science & Policy*, vol. 136, pp. 282–290, 2022.

[69] F. Battistelli, A. Messina, L. Tomassetti, C. Montiroli, E. Manzo, M. Torre, P. Tratzi, M. Segreto, C.-Y. Chu, V. Paolini, A. Corsini, and F. Petracchini, "Assessment of Energy, Mobility, Waste, and Water Management on Italian Small Islands," *Sustainability*, vol. 15, no. 15, 2023. [Online]. Available: https://www.mdpi.com/2071-1050/15/15/11490

[70] E. Commission and D.-G. for Energy, *Clean energy for EU islands – Technology solutions booklet*. Publications Office of the European Union, 2021.

[71] Sustainable Islands - observatory on smaller Italian islands, "Energy, water, mobility, circular economy, sustainable tourism - Challenges for smaller islands and best practices from the world - Issue 2022," Tech. Rep., 2022.

[72] ——, "The challenges of ecological transition in the smaller islands - Issue 2023," Tech. Rep., 2023.

[73] Ministry of Economic Development. Ministerial Decree of 14 February 2017. [Online]. Available: https://www.mise.gov.it/.

[74] Z. Movahediyan and A. Askarzadeh, "Multi-objective optimization framework of a photovoltaic-diesel generator hybrid energy system considering operating reserve," *Sustainable Cities and Society*, vol. 41, pp. 1–12, 2018.

[75] M. A. Matos and R. J. Bessa, "Setting the operating reserve using probabilistic wind power forecasts," *IEEE Trans. Power Syst.*, vol. 26, no. 2, pp. 594–603, 2011.

[76] X. Yan, B. Francois, and D. Abbes, "Operating power reserve quantification through pv generation uncertainty analysis of a microgrid," in *2015 IEEE Eindhoven PowerTech*. IEEE, 2015, pp. 1–6.

[77] X. Yan *et al.*, "Day-ahead optimal operational and reserve power dispatching in a pv-based urban microgrid," in *18th European Conference on Power Electronics and Applications (EPE'16 ECCE Europe)*. IEEE, 2016, pp. 1–10.

[78] N. Ortega-Vazquez, Miguel A. Costilla-Enriquez, E. Ela, and A. Tuohy, "Risk-based reserve procurement," in *2020 PMAPS*, 2020, pp. 1–7.

[79] C. Rahmann, A. Heinemann, and R. Torres, "Quantifying operating reserves with wind power: towards probabilistic–dynamic approaches," *IET Gener*, vol. 10, no. 2, pp. 366–373, 2016.

[80] M. Thilekha, K. Siriwardana, N. Siebel, D. Waslathanthri, N. Lidula, T. Siyambalapitiya, and A. Wickramasinghe, "Impact of large-scale wind and solar power integration on operating reserve requirements of an islanded power system," in *2018 Moratuwa Engineering Research Conference (MERCon)*, 2018, pp. 589–594.

[81] IRENA, "Tranforming Small-Island Power Systems: Technical planning studies for the integration of variable renewables," International Renewable Energy Agency, Abu Dhabi, Tech. Rep., 2018.

[82] B. H. Vu and I.-Y. Chung, "Optimal generation scheduling and operating reserve management for pv generation using rnn-based forecasting models for stand-alone microgrids," *Renewable Energy*, vol. 195, pp. 1137–1154, 2022.

[83] D. Groppi, F. Feijoo, A. Pfeifer, D. A. Garcia, and N. Duic, "Analyzing the impact of demand response and reserves in islands energy planning," *Energy*, vol. 278, p. 127716, 2023.

[84] A. van Stiphout, K. De Vos, and G. Deconinck, "The impact of operating reserves on investment planning of renewable power systems," *IEEE Trans. Power Syst.*, vol. 32, no. 1, pp. 378–388, 2016.

[85] Q. Ma and H. Lu, "Wind energy technologies integrated with desalination systems: Review and state-of-the-art," *Desalination*, vol. 277, no. 1, pp. 274–280, 2011.

[86] M. Ma, H. Huang, X. Song, F. Peña-Mora, Z. Zhang, and J. Chen, "Optimal sizing and operations of shared energy storage systems in distribution networks: A bi-level programming approach," *Applied Energy*, vol. 307, p. 118170, 2022. [Online]. Available: https://www.sciencedirect.com/science/article/pii/S0306261921014410

[87] A. Sobu and G. Wu, "Dynamic optimal schedule management method for microgrid system considering forecast errors of renewable power generations," in *2012 IEEE POWERCON*. IEEE, 2012, pp. 1–6.

[88] S. Bruno, M. Dassisti, M. La Scala, M. Chimienti, C. Cignali, and E. Palmisani, "Predictive dispatch across time of hybrid isolated power systems," *IEEE Trans Sustain Energy*, vol. 5, no. 3, pp. 738–746, 2014.

[89] S. Bruno, G. Giannoccaro, and M. La Scala, "A demand response implementation in tertiary buildings through model predictive control," *IEEE Trans. Ind. Appl.*, vol. 55, no. 6, pp. 7052–7061, 2019.

[90] J. Sachs and O. Sawodny, "A two-stage model predictive control strategy for economic diesel-pv-battery island microgrid operation in rural areas," *IEEE Trans Sustain Energy*, vol. 7, no. 3, pp. 903–913, 2016.

[91] S. Bruno, G. Giannoccaro, and M. La Scala, "Predictive control of demand and storage for residential prosumers," in *2017 IEEE PES ISGT-Europe*, 2017, pp. 1–6.

[92] J. P. Fossati, A. Galarza, A. Martín-Villate, J. M. Echeverría, and L. Fontán, "Optimal scheduling of a microgrid with a fuzzy logic controlled storage system," *Int. J. Electr. Power Energy Syst.*, vol. 68, pp. 61–70, 2015.

[93] Y. Dvorkin, D. S. Kirschen, and M. A. Ortega-Vazquez, "Assessing flexibility requirements in power systems," *IET Gener. Transm. Distrib.*, vol. 8, no. 11, pp. 1820–1830, 2014.

[94] S. Bruno, G. Dellino, M. L. Scala, and C. Meloni, "A microforecasting module for energy consumption in smart grids," in *2018 IEEE EEEIC / I&CPS Europe*, 2018, pp. 1–6.

[95] A. Nespoli, , E. Ogliari, S. Leva, A. Massi Pavan, A. Mellit, V. Lughi, and A. Dolara, "Day-ahead photovoltaic forecasting: A comparison of the most effective techniques," *Energies*, vol. 12, no. 9, p. 1621, 2019.

[96] P. E. Black, "Greedy algorithm," *Dictionary of Algorithms and Data Structures*, vol. 2, p. 62, 2005.

[97] T. Huld, R. Müller, and A. Gambardella, "A new solar radiation database for estimating pv performance in europe and africa," *Solar energy*, vol. 86, no. 6, pp. 1803–1815, 2012.

[98] Italian Regulatory Authority for Energy, Networks and Environment. Delibera 558/2018/R/efr. [Online]. Available: https://arera.it/it/docs/18/558-18.htm

[99] ——. Delibera 07 settembre 2021 370/2021/R/eel. [Online]. Available: https://www.arera.it/it/docs/21/370-21.htm

[100] P. Pinceti, *Scada per sistemi elettrici*. Franco Angeli, 2003.

[101] M. S. Thomas and J. D. McDonald, *Power system SCADA and smart grids*. CRC press, 2017.

[102] E. Buraimoh and I. E. Davidson, "Laboratory procedure for real-time simulation experiment of renewable energy systems on opal-rt digital simulator," in *2022 10th International Conference on Smart Grid (icSmartGrid)*, 2022, pp. 221–226.

[103] J. LeSage, "Systems-level microgrid simulation from simple one-line diagram," https://www.mathworks.com/matlabcentral/fileexchange/67060-systems-level-microgrid-simulation-from-simple-one-line-diagram, 2024, accessed: 2024-01-08.

[104] SICES, *Parallel functions manual Series ENG*, 2022, accessed: 2024-01-10. [Online]. Available: https://www.sices.eu/parallel-functions-manual-series-eng/

[105] R. H. Tan and G. K. Tinakaran, "Development of battery energy storage system model in matlab/simulink," *Int. j. smart grid clean energy*, vol. 9, pp. 180–188, 2020.

[106] S. Impram, S. Varbak Nese, and B. Oral, "Challenges of renewable energy penetration on power system flexibility: A survey," *Energy Strategy Reviews*, vol. 31, p. 100539, 2020. [Online]. Available: https://www.sciencedirect.com/science/article/pii/S2211467X20300924

[107] J. Song, X. Zhou, Z. Zhou, Y. Wang, Y. Wang, and X. Wang, "Review of low inertia in power systems caused by high proportion of renewable energy grid integration," *Energies*, vol. 16, no. 16, 2023. [Online]. Available: https://www.mdpi.com/1996-1073/16/16/6042

[108] A. Ulbig, T. Borsche, and G. Andersson, "Impact of low rotational inertia on power system stability and operation," *IFAC Proceedings Volumes (IFAC-PapersOnline)*, vol. 19, 12 2013.

[109] P. Tielens and D. Van Hertem, "The relevance of inertia in power systems," *Renewable and Sustainable Energy Reviews*, vol. 55, pp. 999–1009, 2016. [Online]. Available: https://www.sciencedirect.com/science/article/pii/S136403211501268X

[110] ENTSO-E, "Need for synthetic inertia (SI) for frequency regulation," ENTSO-E, Brussels, Tech. Rep., mar 2017.

[111] A. Ulbig, T. S. Borsche, and G. Andersson, "Impact of low rotational inertia on power system stability and operation," in *IFAC Proceedings Volumes (IFAC-PapersOnline)*, vol. 19, dec 2014, pp. 7290–7297.

[112] P. Daly, H. W. Qazi, and D. Flynn, "RoCoF-Constrained Scheduling Incorporating Non-Synchronous Residential Demand Response," *IEEE Transactions on Power Systems*, vol. 34, no. 5, pp. 3372–3383, 2019.

[113] Terna S.p.A., "Regolamento per la fornitura del servizio di regolazione primaria della frequenza per il tramite di unità di produzione integrate con sistemi di accumulo." p. 11, 2018.

[114] J. Fang, R. Zhang, Y. Tang, and L. Hongchang, "Inertia Enhancement by Grid-Connected Power Converters with Frequency-Locked-Loops for Frequency Derivative Estimation," in *2018 IEEE Power Energy Society General Meeting (PESGM)*, 2018, pp. 1–5.

[115] T. Kerdphol, F. S. Rahman, M. Watanabe, Y. Mitani, D. Turschner, and H. Beck, "Enhanced Virtual Inertia Control Based on Derivative Technique to Emulate Simultaneous Inertia and Damping Properties for Microgrid Frequency Regulation," *IEEE Access*, vol. 7, pp. 14 422–14 433, 2019.

[116] I. Martínez-Sanz, B. Chaudhuri, A. Junyent-Ferré, V. Trovato, and G. Strbac, "Distributed vs. concentrated rapid frequency response provision in future great britain system," in *2016 IEEE Power and Energy Society General Meeting (PESGM)*, 2016, pp. 1–5.

[117] H. R. Chamorro, A. C. Sanchez, A. Verjordet, F. Jimenez, F. Gonzalez-Longatt, S. Member, and V. K. Sood, "Distributed Synthetic Inertia Control in Power Systems," in *Proceedings of 8th International Conference on Energy and Environment: Energy Saved Today is Asset for Future, CIEM 2017*, 2017, pp. 74–78.

[118] R. Eriksson, N. Modig, and K. Elkington, "Synthetic inertia versus fast frequency response: a definition," *IET Renewable Power Generation*, vol. 12, no. 5, pp. 507–514, 2018.

[119] ENTSO-E, "Future System Inertia 2," techreport, 2018. [Online]. Available: https://www.entsoe.eu/Documents/Publications/SOC/Nordic/2018/System-inertia.zip

[120] M. Rezkalla, A. Zecchino, M. Pertl, and M. Marinelli, "Grid frequency support by single-phase electric vehicles employing an innovative virtual inertia controller," in *2016 UPEC Conference*, 2016, pp. 1–6.

[121] M. Rezkalla, A. Zecchino, S. Martinenas, A. M. Prostejovsky, and M. Marinelli, "Comparison between synthetic inertia and fast frequency containment control based on single phase EVs in a microgrid," *Applied Energy*, vol. 210, pp. 764–775, 2018.

[122] L. Meng, J. Zafar, S. K. Khadem, A. Collinson, K. C. Murchie, F. Coffele, and G. M. Burt, "Fast Frequency Response From Energy Storage Systems—A Review of Grid Standards, Projects and Technical Issues," *IEEE Transactions on Smart Grid*, vol. 11, no. 2, pp. 1566–1581, 2020.

[123] D. Ochoa and S. Martinez, "Fast-Frequency Response Provided by DFIG-Wind Turbines and its Impact on the Grid," *IEEE Transactions on Power Systems*, vol. 32, no. 5, pp. 4002–4011, 2017.

[124] "Blorin project," https://www.blorin.energy/progetto/.

[125] H. R. Chamorro, R. Torkzadeh, M. Eliassi, P. Betancourt-Paulino, M. Rezkalla, F. Gonzalez-Longatt, V. K. Sood, and W. Martinez, "Analysis of the Gradual Synthetic Inertia Control on Low-Inertia Power Systems," in *2020 IEEE ISIE Conference*, vol. 2020-June, 2020, pp. 816–820.

[126] J. Hong, E. Oh, Y. Yang, K. Roh, M. Oh, and J. Kim, "Consortium blockchain-based v2g energy trading system using tokens," in *2020 International Conference on Information and Communication Technology Convergence (ICTC)*, 2020, pp. 677–682.

[127] M. Kim, J. Lee, J. Oh, K. Park, Y. Park, and K. Park, "Blockchain based energy trading scheme for vehicle-to-vehicle using decentralized identifiers," *Applied Energy*, vol. 322, p. 119445, 2022. [Online]. Available: https://www.sciencedirect.com/science/article/pii/S0306261922007723

[128] S. Garg, K. Kaur, G. Kaddoum, F. Gagnon, and J. J. P. C. Rodrigues, "An efficient blockchain-based hierarchical authentication mechanism for energy trading in v2g environment," in *2019 IEEE International Conference on Communications Workshops (ICC Workshops)*, 2019, pp. 1–6.

[129] S. Aggarwal, N. Kumar, and P. Gope, "An efficient blockchain-based authentication scheme for energy-trading in v2g networks," *IEEE Transactions on Industrial Informatics*, vol. 17, no. 10, pp. 6971–6980, 2021.

[130] M. Samadi, H. Schriemer, S. Ruj, and M. Erol-Kantarci, "Energy blockchain for demand response and distributed energy resource management," in *2021 IEEE International Conference on Communications, Control, and Computing Technologies for Smart Grids (SmartGridComm)*, 2021, pp. 425–431.

[131] A. Lucas, D. Geneiatakis, Y. Soupionis, I. Nai-Fovino, and E. Kotsakis, "Blockchain technology applied to energy demand response service tracking and data sharing," *Energies*, vol. 14, no. 7, 2021. [Online]. Available: https://www.mdpi.com/1996-1073/14/7/1881

[132] X. Zhu, Y. Liu, Y. Cao, and Z. Jiao, "Demand response scheduling based on blockchain considering the priority of high load energy enterprises," *Energy Reports*, vol. 9, pp. 992–1000, 2023, 2022 The 3rd International Conference on Power Engineering. [Online]. Available: https://www.sciencedirect.com/science/article/pii/S2352484723007874

[133] M. L. Di Silvestre, P. Gallo, G. Restifo, E. R. Sanseverino, G. Sciumè, and G. Zizzo, "A blockchain platform for demand response in mediterranean islands: a smart contract for remuneration," in *IECON 2022 – 48th Annual Conference of the IEEE Industrial Electronics Society*, 2022, pp. 1–6.

[134] A. Augello, P. Gallo, E. R. Sanseverino, G. Sciumè, and M. Tornatore, "A coexistence analysis of blockchain, scada systems, and openadr for energy services provision," *IEEE Access*, vol. 10, pp. 99 088–99 101, 2022.

[135] A. Augello, P. Gallo, E. Sanseverino, G. Sciabica, and G. sciumè, "Certifying battery usage for v2g and second life with a blockchain-based framework," *Computer Networks*, vol. 222, p. 109558, 02 2023.

[136] G. Lauss, M. O. Faruque, K. Schoder, C. Dufour, A. Viehweider, and J. Langston, "Characteristics and design of power hardware-in-the-loop simulations for electrical power systems," *IEEE Transactions on Industrial Electronics*, vol. 63, pp. 1–1, 01 2015.

[137] M. Galici, M. Mureddu, E. Ghiani, and F. Pilo, "Blockchain-based hardware-in-the-loop simulation of a decentralized controller for local energy communities," *Energies*, vol. 15, no. 20, 2022. [Online]. Available: https://www.mdpi.com/1996-1073/15/20/7623

[138] S. Häselbarth, O. Winkels, and K. Strunz, "Blockchain-based market procurement of reactive power," *IEEE Access*, vol. 11, pp. 36 106 – 36 119, 04 2023.

[139] G. De Carne, S. Bruno, M. Liserre, and M. La Scala, "Distributed online load sensitivity identification by smart transformer and industrial metering," *IEEE Transactions on Industry Applications*, vol. 55, no. 6, pp. 7328–7337, 2019.

[140] E. Vrettos and G. Andersson, "Scheduling and Provision of Secondary Frequency Reserves by Aggregations of Commercial Buildings," *IEEE Transactions on Sustainable Energy*, vol. 7, no. 2, pp. 850–864, 2016.

[141] C.-M. Chu and T.-L. Jong, "A Novel Direct Air-Conditioning Load Control Method," *IEEE Transactions on Power Systems*, vol. 23, no. 3, pp. 1356–1363, 2008.

[142] R. Zhang, X. Chu, W. Zhang, and Y. Liu, "Active Participation of Air Conditioners in Power System Frequency Control Considering Users' Thermal Comfort," *Energies*, vol. 8, no. 10, pp. 10 818–10 841, 2015.

[143] M. Cheng, J. Wu, S. J. Galsworthy, C. E. Ugalde-Loo, N. Gargov, W. W. Hung, and N. Jenkins, "Power System Frequency Response From the Control of Bitumen Tanks," *IEEE Transactions on Power Systems*, vol. 31, no. 3, pp. 1769–1778, 2016.

[144] F. Conte, M. C. Di Vergagni, S. Massucco, F. Silvestro, E. Ciapessoni, and D. Cirio, "Synthetic Inertia and Primary Frequency Regulation Services by Domestic Thermal Loads," in *Proceedings - 2019 IEEE EEEIC/I&CPS Europe*, 2019.

[145] F. Conte, M. Crosa di Vergagni, S. Massucco, F. Silvestro, E. Ciapessoni, and D. Cirio, "Performance analysis of frequency regulation services provided by aggregates of domestic thermostatically controlled loads," *International Journal of Electrical Power & Energy Systems*, vol. 131, p. 107050, 2021.

[146] V. Trovato, I. M. Sanz, B. Chaudhuri, and G. Strbac, "Advanced Control of Thermostatic Loads for Rapid Frequency Response in Great Britain," *IEEE Transactions on Power Systems*, vol. 32, no. 3, pp. 2106–2117, 2017.

[147] I. Ibrahim, C. O'Loughlin, and T. O'Donnell, "Virtual Inertia Control of Variable Speed Heat Pumps for the Provision of Frequency Support," *Energies*, vol. 13, no. 8, 2020.

[148] F. M. Rubinstein and S. Kiliccote, "Demand Responsive Lighting: A Scoping Study," Lawrence Berkeley Nat. Lab., Berkeley, CA, USA, Tech. Rep., 2007.

[149] F. Rubinstein, L. Xiaolei, and D. Watson, "Using Dimmable Lighting for Regulation Capacity and Non-Spinning Reserves in the Ancillary Services Market. A Feasibility Study," Lawrence Berkeley Nat. Lab., Berkeley, CA, USA, techrep, 2010.

[150] O. Ma, N. Alkadi, P. Cappers, P. Denholm, J. Dudley, and E. al., "Demand Response for Ancillary Services," *IEEE Transactions on Smart Grid*, vol. 4, no. 4, pp. 1988–1995, 2013.

[151] M. Shahidehpour, C. Bartucci, N. Patel, T. Hulsebosch, P. Burgess, and N. Buch, "Streetlights are getting smarter: Integrating an intelligent communications and control system to the current infrastructure," *IEEE Power and Energy Magazine*, vol. 13, no. 3, pp. 67–80, 2015.

[152] M. Alvarado-Ruiz, F. Abi Abdallah, M. Gagnaire, and Y. Lascaux, "TeleWatt: An innovative electric vehicle charging infrastructure over public lighting systems," 2013, pp. 741–746.

[153] S. Bruno, G. Giannoccaro, M. La Scala, G. Lopopolo, and C. Rodio, "A Microgrid Architecture for Integrating EV Charging System and Public Street Lighting," in *2019 IEEE EEEIC/I&CPS Europe*, 2019.

[154] E. Waffenschmidt, "Virtual inertia grid control with LED lamp driver," in *2016 IESC Conference*, 2016, pp. 1–6.

[155] M. Bagheri-Sanjareh, M. H. Nazari, and G. B. Gharehpetian, "A novel and optimal battery sizing procedure based on mg frequency security criterion using coordinated application of bess, led lighting loads, and photovoltaic systems," *IEEE Access*, vol. 8, pp. 95 345–95 359, 2020.

[156] W. Wang, X. Chu, and K. Xiao, "A distributed economic agc strategy integrating dynamic demand response," in *2018 IEEE Power & Energy Society General Meeting (PESGM)*. IEEE, 2018, pp. 1–5.

[157] K. Xiao, X. Chu, and Y. Liu, "LED lighting loads actively participating in power system frequency regulation," in *2016 IEEE Power Energy Society Innovative Smart Grid Technologies Conference (ISGT)*, 2016, pp. 1–5.

[158] J. Liu, W. Zhang, and Y. Liu, "Primary Frequency Response From the Control of LED Lighting Loads in Commercial Buildings," *IEEE Transactions on Smart Grid*, vol. 8, no. 6, pp. 2880–2889, 2017.

[159] G. R. Newsham, S. Mancini, and R. G. Marchand, "Detection and Acceptance of Demand-Responsive Lighting in Offices with and without Daylight," *LEUKOS*, vol. 4, no. 3, pp. 139–156, 2008.

[160] UNI Technical Committee, "UNI 11248:2016 - Road lighting - Selection of lighting classes," pp. 1–38, 2016.

[161] European Committee For Standardization, "EN 13201:2015 - Road lighting - Part 2: Performance requirements," 2015.

[162] T. Theubou, R. Wamkeue, and I. Kamwa, "Dynamic model of diesel generator set for hybrid wind-diesel small grids applications," in *2012 25th IEEE Canadian Conference on Electrical and Computer Engineering (CCECE)*, 2012, pp. 1–4.

[163] C. Cottarell, C. Valdes, D. Bonata, F. Falchi, and R. Furgoni, "Illuminazione pubblica: spendiamo troppo," Università del Sacro Cuore - Osservatorio CPI, techreport, may 2018.

[164] Terna S.p.A. e Gruppo Terna, "Dati statistici sull'energia elettrica in Italia," Terna, Tech. Rep., 2017.

[165] T.-A. Nguyen-Huu, V. T. Nguyen, K. Hur, and J. W. Shim, "Coordinated control of a hybrid energy storage system for improving the capability of frequency regulation and state-of-charge management," *Energies*, vol. 13, no. 23, 2020. [Online]. Available: https://www.mdpi.com/1996-1073/13/23/6304

[166] J. W. Shim, G. Verbič, N. Zhang, and K. Hur, "Harmonious integration of faster-acting energy storage systems into frequency control reserves in power grid with high renewable generation," *IEEE Transactions on Power Systems*, vol. 33, no. 6, pp. 6193–6205, 2018.

[167] J. W. Shim, G. Verbič, H. Kim, and K. Hur, "On droop control of energy-constrained battery energy storage systems for grid frequency regulation," *IEEE Access*, vol. 7, pp. 166 353–166 364, 2019.

[168] L. Toma, M. Sanduleac, S. A. Baltac, F. Arrigo, A. Mazza, E. Bompard, A. Musa, and A. Monti, "On the virtual inertia provision by bess in low inertia power systems," in *2018 IEEE International Energy Conference (ENERGYCON)*, 2018, pp. 1–6.

[169] BEIS - Department for Business, Energy & Industrial Strategy, "GB Power System Disruption - 9 August 2019," Tech. Rep., 2019.

Acronyms

AC Alternating Current. 12, 16, 189

AMR Automatic Meter Reading. 20

BC Breaker Controller. 20, 78, 79, 83, 88, 91, 114

BESS Battery Energy Storage System. v, vi, ix, 41, 45, 46, 48–52, 56, 63–69, 71, 72, 74, 75, 77, 81–83, 85–87, 89, 92–94, 96, 102, 104, 107–109, 111, 117–121, 123, 125–139, 141–152, 154, 164, 172, 178, 180, 186, 201, 210, 212–217, 219, 222, 225, 227, 229, 232

CCI Controllore Centrale d'Impianto. iv, 20–24, 79, 82, 83, 93, 94, 116, 180

CEI Comitato Elettrotecnico Italiano. 20, 22, 79, 82, 83, 102, 106–108, 110, 134, 168, 180, 186, 228

CEI-OFPL CEI-Over-Frequency Power Limitation. viii, 83, 86, 110, 116, 149–152, 180–185, 228

CEI-SFPR CEI-Storage Frequency Power Regulation. v, 82, 108, 109, 142–144, 146, 149, 151

CI Confidence Interval. 62, 65, 71, 72, 74

CLR Closed-Loop Routine. 44, 60–62, 64, 65, 69–72, 74, 75

DC Direct Current. 12, 172

DER Distributed Energy Resource. 14–17, 156, 160, 161, 188, 228

DG Distributed Generation. 10, 18–20, 37

DOR Downward Operating Reserve. 43, 45, 47, 49, 53–55, 60, 65, 81, 85–87, 89, 91–93, 98–102, 121, 123, 131–133, 137–140, 145, 149, 151

DR Demand Response. vii, 41, 156, 164–167, 171, 172, 186, 187

DSO Distribution System Operator. iv, 18–21, 28, 29, 82, 104, 114, 115

EMS Energy Management System. 16, 171

ESS Energy Storage System. 16, 18–20, 210

EU European Union. 10, 11, 24

EV Electric Vehicle. vii, viii, 157, 165–167, 171–180, 182, 183, 185, 186, 228

FCR Frequency Containment Reserve. 155, 156

FFR Fast Frequency Response. viii, ix, 6, 156, 157, 173, 186, 187, 189, 192–195, 197, 199, 200, 205–208, 210, 216, 229

FFS Fast Frequency Support. vii, 157, 166, 167, 171–173, 176, 177, 182, 183, 228, 229

FP Functional Performances. 21

GP General Protection. 21

GPRS General Packet Radio Service. 20–22

GSM Global System for Mobile communication. 20–22

HESS Hybrid Energy Storage System. ix, 209, 210, 215, 217, 222, 225, 229

IEA International Energy Agency. 10

IEC International Electrotechnical Commission. 16

IoT Internet of Things. 20

IPCC Intergovernmental Panel on Climate Change. 24

IPS Interface Protection System. 21, 105, 108, 110, 114, 116, 171

LED Light-Emitting Diode. viii, ix, 186–201, 203–209, 228, 229

LLC Local Level Controller. 78

LV Low Voltage. 10, 11, 18, 19, 79, 104, 154, 167, 168

MDRB Minimum Downward Regulation Bandwidth. 85, 89, 92, 93, 118, 131, 133, 139, 140, 148, 153, 154

MG Microgrid. iv, v, 6–9, 11–19, 41, 42, 77, 78, 81, 84–86, 153, 166, 167, 172, 195, 196, 202, 231–233

MGC Microgrid Controller. v, vi, xi, 78, 79, 81–91, 93–97, 99, 109, 112–114, 116, 117, 120–123, 125–154, 232

MILP Mixed-Integer Linear Programming. 50

MIQP Mixed-Integer Quadratic Programming. 44

MPP Main Power Plant. v, 28, 29, 56, 81, 82, 86–89, 91–94, 96, 102, 104, 105, 110–114, 118, 120, 121, 123, 125–142, 144, 146, 147, 149, 151, 153

MSD Mercato dei Servizi di Dispacciamento. 20, 21

MV Medium Voltage. vii, 10, 11, 19, 20, 79, 93, 104, 109, 111, 154, 167–171, 174

OLR Open-Loop Routine. 44, 46, 60–62, 65, 69–72, 74, 75

PCU Plant Control Unit. 79

PDFs Probability Distribution Functions. 39

PHIL Power Hardware-in-the-Loop. vii, 102, 166, 167, 172, 174, 178, 180, 183, 186, 189, 193, 195–197, 200, 202, 228, 229

PLC Programmable Logic Controller. 80, 81

PoD Point of Delivery. 21–23

PoI Point of Interconnection. 19, 180

PV Photovoltaic. iv–viii, 25, 27, 37–39, 41–43, 53, 56, 57, 60–62, 64, 65, 69, 70, 72–75, 81, 83, 86, 87, 91–94, 97, 102, 104, 109–111, 116–118, 121, 128–133, 138, 140–142, 144, 146, 149–152, 154, 168, 170, 174, 176, 179–186, 201, 228, 232

RES Renewable Energy Sources. 10–13, 18, 19, 24, 27, 39–43, 45–47, 50–53, 55, 60, 61, 74, 75, 103, 104, 154, 201, 231

RoCoF Rate of Change of Frequency. vii, ix, 102, 155–162, 167, 173, 177, 182, 194, 197, 200, 203, 204, 207, 208, 210, 213, 215, 216, 223–225, 227, 228, 230

RTA Real-Time Algorithm. v, 77, 80, 81, 83, 84, 87, 89, 99, 101, 102, 104, 118, 121, 127, 141, 152, 153

SC Supercapacitor. ix, 186, 209, 212–217, 219, 222, 225, 227, 229

SI Synthetic Inertia. vii–ix, 6, 156–164, 166, 173, 174, 177, 179, 183, 184, 186–189, 192–195, 197, 198, 200, 203–205, 207–210, 216, 228, 229

SoC State of Charge. ix, 44, 48, 63, 65, 77, 117–121, 128, 133, 138, 142, 144, 146, 149, 151, 157, 209–212, 214–216, 219, 224–227, 229, 230

SOCFM SOC-Feedback Method. 210, 217, 225

TSO Transmission System Operator. 21

UOR Upward Operating Reserve. 43, 45, 47, 49, 53–55, 60, 65, 69, 81, 87–89, 91, 92, 94, 98–102, 112, 113, 121, 123, 125–127, 129, 130, 132–135, 138, 140, 142, 144–146, 148

V2G Vehicle-to-Grid. vii, viii, 157, 164–167, 171–183, 185, 186, 228